

Micro-Opto-Mechanical Switching and Tuning for Integrated Optical Systems

by

Gregory Nolan Nielson

B.S., Utah State University (1998)

S.M., Massachusetts Institute of Technology (2000)

Submitted to the Department of Mechanical Engineering
in partial fulfillment of the requirements for the degree of


Doctor of Philosophy in Mechanical Engineering

at the

MASSACHUSETTS INSTITUTE OF TECHNOLOGY

September 2004

© Massachusetts Institute of Technology 2004. All rights reserved.

Author 

 ✓

Department of Mechanical Engineering

July 6, 2004

Certified by .

George Barbastathis

Assistant Professor

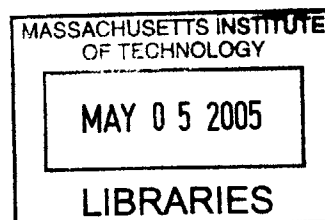
Thesis Supervisor

Accepted by

.....

Ain A. Sonin

Chairman, Department Committee on Graduate Students



BARKER

Micro-Opto-Mechanical Switching and Tuning for Integrated Optical Systems

by

Gregory Nolan Nielson

Submitted to the Department of Mechanical Engineering
on July 6, 2004, in partial fulfillment of the
requirements for the degree of
Doctor of Philosophy in Mechanical Engineering

Abstract

Integrated optical circuits have the potential to lower manufacturing and operating costs and enhance the functionality of optical systems in a manner similar to what has been achieved by integrating electronic circuits. One of the basic optical elements required to enable integrated optical circuits is an integrated optical switch, analogous to transistor switches used in integrated electronic circuits. An ideal switch for integrated optical circuits would provide wavelength-selective switching. Wavelength-selective behavior is an important characteristic for devices intended for networking applications as wavelength division multiplexing (WDM) of optical signals has become the accepted standard.

A major contribution of this thesis is the design, fabrication, and experimental demonstration of a wavelength-selective, integrated optical switch. This switch operates by combining a microring resonator filter with a microelectromechanical system (MEMS) device that allows the normally static ring resonator filter to be switched on and off. This represents the first demonstration of a wavelength-selective integrated optical MEMS switch.

Additional contributions of this work include a new study of dielectric charging, analysis of the use of titanium nitride as structural material for MEMS, two new MEMS actuation techniques that lead to higher speed and/or lower actuation voltage, and a feasibility analysis for wavelength tuning using a generalized version of the switch design. A model for the evolution of dielectric charging during the actuation of MEMS devices was developed to address a deviation of the experimentally fabricated devices from the theoretical predictions according to older models. The new model predicts the experimental voltage versus displacement behavior of the wavelength selective switch accurately, and offers new insights into the physics of dielectric charging. The use of titanium nitride as a MEMS material was conceived as a solution to residual stress problems that are common in cantilever-type of actuators in general, including the wavelength-selective switch. Specific details on MEMS implementation using titanium nitride are discussed in the thesis. To address CMOS compatibility and speed challenges, two new complementary MEMS switch actuation techniques

were developed. The new methods require less voltage and energy for actuation while at the same time reducing the switching time of the device to levels unachievable with current MEMS actuation techniques. Preliminary theoretical and experimental results are presented and discussed. Finally, the thesis covers the feasibility analysis of a version of the switch design where the motion is analog and, hence, can be used for tuning of resonant integrated optical structures. The analysis shows that the required positional accuracy is achievable with on-chip capacitive position sensing and feedback control, and points to a promising new direction for mechanically tunable integrated photonics.

While these contributions are all outgrowths of work directed towards realizing an integrated optical circuit, they are also significant for applications such as radio-frequency (RF) MEMS switching and free-space optical MEMS devices (i.e. micro-mirror arrays for projection displays).

Thesis Supervisor: George Barbastathis
Title: Assistant Professor

Acknowledgments

It is difficult to believe that it has been six years since my wife, Emily, and I moved to Cambridge for graduate school. I have had countless experiences during these years that have influenced me deeply, both professionally and personally. At this time, I would like to acknowledge and thank everyone who has contributed to my graduate student experience.

First of all, I would like to thank and recognize my advisor, Professor George Barbastathis. His fingerprint is very much on this thesis as well as on my professional development. It has been a real pleasure to work with, and learn from George over the years.

I would also like to acknowledge the efforts of the professors who served on my thesis committee; Professor Sang-Gook Kim, Professor Martin Schmidt, and Professor Henry Smith. I very much appreciate the time they took to meet with me and discuss and critique my work. Their input was extremely valuable as my work progressed and took shape.

I also had the unique opportunity to work with a number of other professors who contributed significantly to my thesis and my graduate experience in general. These professors include Professor Harry Tuller, Professor Hermann Haus, Professor Lionel Kimerling, Professor Franz Kaertner, Professor David Parks, Professor Stephen Senturia, and Professor Erich Ippen. It was a great pleasure to associate with and learn from each of these professors.

I need to also acknowledge the efforts of my fellow students and colleagues. In particular I would like to mention Dilan Seneviratne, Francisco Lopez-Royo, Peter Rakich, Milos Popović, Mike Watts, Tymon Barwicz, Peter Vandre, and Wei-Chuan Shih. It was a lot of fun to work with all of you and I really appreciate your contributions to this work!

As a final professional acknowledgement, I would like to thank the staff of MIT's Microsystems Technology Laboratories (MTL) and Nanostructures Laboratory (NSL). The staff of both labs were invaluable to me in helping me fabricate the devices de-

scribed in this thesis. In particular, I'd like to mention Vicky Diadiuk, Bob Bicchieri, Kurt Broderick, Dennis Ward, Gwen Donahue, Bernard Alamariu, Jim Carter, Jim Daley, Donal Jamieson, Dave Terry, Paul Tierney, and Paudely Zamora.

As far as personal acknowledgements, first and foremost I want to acknowledge my wife, Emily. I can't begin to describe the impact Emily has had on me and my work during my time in graduate school. She has supported and sustained me during this challenging time and has always stood with me. Emily, I love you and love what we have created together. I am thrilled at the prospect of standing together throughout this life and in the eternities to come!

I also want to acknowledge my children, Madeline and Joel, as well as the new baby who will be joining our family soon. There is nothing like a big hug from my children to make the stress of graduate student life melt away.

I'd like to thank the different communities that Emily and I have been a part of. The members of our church congregation have truly been our family away from home and have helped us tremendously over the years. The Eastgate community has been a wonderful "neighborhood" for our family for the last five years. Finally, The professors and students of the Music Department at UMass-Boston, where Emily finished her degree, also brought much joy to our lives.

I would be profoundly ungrateful if I didn't acknowledge and thank that Being who created this world and made my life, and all others, possible. So far this life has been a tremendous experience for me and I want to express my thanks to my Heavenly Father who continues to lead me and my family on wonderful, exciting paths.

I would like to dedicate this thesis to my parents, Nolan and Linda Nielson, whose example of hard work and selfless service continues to inspire me to this day. If all people had parents as good as mine, the world would be a dramatically better and happier place. I hope I can live up to the example they have set for me.

Contents

1	Introduction	29
1.1	Optical switching	32
1.1.1	Free-space MEMS switching	32
1.1.2	Waveguide based optical MEMS switching	35
1.1.3	Electro-optic optical switching	37
1.1.4	Liquid crystal optical switching	39
1.1.5	Thermo-optic switching	41
1.1.6	Wavelength selective switching	41
1.2	Filter Tuning	44
1.2.1	Thermal tuning	44
1.2.2	Liquid crystal tuning	44
1.2.3	Electro-optic tuning	45
1.2.4	Piezoelectric strain tuning	45
1.3	Thesis objectives	45
1.4	Outline of Thesis	46
1.5	Thesis contributions and applications	48
2	Optical ring resonator MEMS switch design	51
2.1	Optical ring resonator filters	52
2.2	MEMS optical ring resonator switch description	56
2.3	Design requirements	57
2.4	MEMS parallel plate electrostatic actuation	59
2.5	Switch Design	64

2.5.1	Optical Design	64
2.5.2	Electro-mechanical Design	66
2.5.3	Performance analysis	70
2.6	Reliability	74
2.6.1	Stiction	74
2.6.2	Dielectric charging	75
3	Optical ring resonator MEMS switch fabrication	77
3.1	Fabrication Process Design	77
3.2	Fabrication details	81
3.2.1	Sacrificial material	81
3.2.2	Release etch	82
3.2.3	Lossy bridge material	82
3.2.4	Wafer dicing	83
3.2.5	Packaging	83
4	Optical ring resonator MEMS switch fabrication results and testing	87
4.1	Fabrication results	87
4.1.1	Lithographic resolution	88
4.1.2	Residual stress	89
4.1.3	Surface roughness	96
4.1.4	Alignment	99
4.1.5	Aluminum undercut	100
4.2	Testing	101
4.2.1	Actuation voltage and dielectric charging	102
4.2.2	Optical Performance - spectral	112
4.2.3	Optical Performance - temporal	117
4.3	Discussion of results	120
5	Residual stress manipulation and control	123
5.1	Residual stress in aluminum films	123

5.2	Titanium nitride for MEMS applications	127
5.2.1	Titanium nitride versus other MEMS materials	128
5.3	Fabrication techniques for titanium nitride	128
5.3.1	Deposition	128
5.3.2	Etching	129
5.3.3	Residual stress management	130
5.3.4	Sacrificial materials	130
5.4	Fabrication process	131
5.5	Experimental characterization of titanium nitride	133
5.5.1	Titanium nitride anneal	133
5.6	Discussion	136
6	Dynamic pull-in	139
6.1	System Model	140
6.1.1	Parallel Plate Model	141
6.1.2	Torsional Model	144
6.2	Step voltage response and pull-in	146
6.2.1	Step Voltage System Response - Parallel Plate Case	147
6.2.2	Step Voltage System Response - Torsional motion	148
6.3	Modulated voltage system response and pull-in	152
6.3.1	Modulated Voltage System Response - Parallel Plate Case	153
6.3.2	Modulated Voltage System Response - Torsional Case	154
6.3.3	Discussion	158
6.4	Conclusions	160
7	Strain-energy MEMS switching	163
7.1	Current parallel plate MEMS switching	164
7.2	Strain-energy actuation technique	165
7.2.1	Strain-energy switch implementations	167
7.3	Modelling of strain-energy switching	172
7.3.1	Lumped parameter model	172

7.3.2	Hold voltage	174
7.3.3	Actuation voltage	175
7.3.4	Switch initialization	179
7.3.5	Switching speed	179
7.4	Strain-energy prototype switch design and fabrication	180
7.4.1	Prototype design	180
7.4.2	Fabrication	183
7.4.3	packaging	186
7.4.4	Control electronics	188
7.5	Fabrication and experimental results	191
7.5.1	Fabrication results	192
7.5.2	Device resistance	193
7.5.3	Pull-in/hold voltages and dielectric charging	193
7.5.4	Discussion of results	199
7.6	Applications of strain energy switching	199
7.6.1	Optical switching	200
7.6.2	Radio Frequency (RF) switching	200
8	MEMS tuning of Optical ring resonator filters	203
8.1	Design Requirements	204
8.2	Device Description	205
8.3	Device modelling and design	206
8.3.1	Noise sources	210
8.3.2	Feedback control system	211
8.3.3	Capacitive sensing	214
8.3.4	System performance	216
8.4	Nonlinear control	217
8.5	Discussion	218
9	Conclusions and future work	221
9.1	Future work	223

A	Material Property Tables	225
B	List of Symbols	231
B.1	List of Symbols	231
C	Residual stress gradient measurements	237
D	Linear dielectric charging model	239
E	Thermal-mechanical noise amplification in parallel plate actuators	241

List of Figures

1-1	Soref's vision of an optical integrated circuit (OIC) in 1993 [131]. Note the absence of wavelength selective components. Wavelength division multiplexing (WDM) was just beginning to be developed in 1993. . .	30
1-2	An image of one micro-mirror from the micro-mirror array developed by Lucent. This mirror is tiltable on two axes allowing a beam to be pointed to any of a 2D array of output fibers. (Image courtesy of Lucent Technologies Inc.)	33
1-3	A schematic representation of how a diffractive grating MEMS device operates. (A) shows the device cross-section with all of the grating beams as the same level which essentially acts as a mirror. (B) shows the device with every other grating beam displaced downward. In this position, the grating will diffract the light into a variety of optical orders.	34
1-4	Schematic representation of the micro-bubble optical switch. When the heater is on and the bubble is present in the trench, the light is routed to the drop waveguide (as shown). When the heater is off and the bubble is not present, the light is routed to the through waveguide.	35
1-5	Schematic representation of the mirror based integrated optical switch. The position of the mirror controls whether the input light is directed toward the drop waveguide or the through waveguide.	36

1-6	Illustration of a electro-optic “Y” switch. To direct the input light to one of output waveguides, power is applied to the opposite electro-optic region. The index in that electro-optic region is reduced and thus makes that leg of the Y splitter appear like cladding material rather than a waveguide.	37
1-7	Illustration of a electro-optic coupling switch. To direct the input light to one of the two output waveguides, the coupling between the input and the output waveguides is controlled by applying power to the electro-optic regions.	37
1-8	Illustration of a electro-optic ring resonator switch. To direct the input light to the either the through or the drop port, the index of the ring resonator is changed to cause the input to either resonate in the ring or not. If the input light is resonant, the light will couple to the drop waveguide, if the light is non-resonant it will pass by the ring unaffected and exit through the through waveguide.	38
1-9	Illustration of a electro-optic Mach-Zehnder filter switch. To direct the input light to one of the two output waveguides, the electro-optic region is used to change the path length between the two legs of the interferometer. In this way the light is cause to constructively interfere in one of the output waveguides and destructively interfere in the other output waveguide.	39
1-10	Illustration of a liquid crystal optical switch. The liquid crystal elements steer the input light to the desired output fiber [44].	40
1-11	Illustration of the required arrangement to achieve wavelength selective switching with most of the optical switches currently available.	42
1-12	Illustration of the response of a filter tuning based to a WDM input spectrum. Note that going from the first state to the second state switches two wavelengths between the drop and through ports, in opposing directions, rather than just a single wavelength.	43

2-1	Schematic representation of an optical ring resonator filter showing its static wavelength selective behavior.	53
2-2	Schematic representation of an optical ring resonator filter switch showing its (A) resonant behavior with the lossy material membrane up and (B) its non-resonant behavior with the lossy material membrane down.	56
2-3	RF MEMS switches using electrostatic parallel plate actuators. A) was developed at the University of Michigan [107]. B) was developed at the University of Illinois [15]. C) was developed at Northeastern University and Analog Devices and is currently licensed to Radant MEMS [92]. D) was also developed at the University of Michigan [112].	61
2-4	Simplified lumped parameter model of a parallel plate electrostatic actuator.	62
2-5	Quasi-static equilibrium curve for the parallel plate actuator from Equation 2.7. The arrows indicating the evolution of the equilibrium positions for increasing and decreasing voltage illustrate the bifurcation in the system. When the pull-in voltage is reached, the movable plate tries to jump to the equilibrium position to the right of the fixed electrode position. The isolation layer between the two electrodes will, of course, limit the plate's displacement so it won't reach the theoretical equilibrium position. The thickness of the isolation layer determines the voltage required to maintain the movable plate in the pulled-in state, referred to as the "hold" voltage [22].	63
2-6	Schematic drawing of the cross-sectional view of the waveguides. (Note, drawing not to scale.)	65
2-7	Schematic drawing of the side view of the wavelength-selective MEMS switch structure. (Note drawing not to scale.)	67
2-8	Optical micrographs of prototype bridges that were fabricated to evaluate different design concepts.	68
2-9	CAD image of the layout of the device showing the optical waveguides and the MEMS bridge structure.	69

3-1	Cross-section illustration of the fabrication process of the waveguides and ring resonators. (A) $3\ \mu\text{m}$ of low-temperature oxide (LTO) was deposited for the bottom side cladding. (B) $0.33\ \mu\text{m}$ of silicon rich silicon nitride was deposited for the waveguide core material. (C) The silicon nitride was patterned and etched using e-beam direct-write lithography and reactive ion etching (RIE).	78
3-2	Image from a ring resonator device fabricated using the process described in Figure 3.1. This device was completely fabricated at MIT and is the work of T. Barwicz [6]	78
3-3	Fabrication process for the MEMS structure. (A) the poly-silicon sacrificial layer is deposited using low-pressure chemical vapor deposition (LPCVD). (B) the poly-silicon is patterned and etched using contact photolithography and reactive ion etching (RIE). (C) the bridge material (aluminum) is deposited by sputtering. (D) the aluminum is patterned and etched using contact photolithography and wet etching. (E) the structure is released by isotropically etching away the poly-silicon using a gas phase xenon difluoride etch.	79
3-4	Image of the packaged optical MEMS switches evaluated in the Zygo profilometer system.	84
3-5	Picture of a die with an array of MEMS bridges. The probe tips can be seen in contact with one of the contact pads for the optical switch devices.	85
4-1	Optical micrograph of a fabricated wavelength selective switch.	88
4-2	CAD layout of the suspended series of cantilever beams used to determine the residual stress gradient in the aluminum film.	91
4-3	Diagram showing the important dimensions and geometric relationships used in the residual stress gradient derivation from the cantilever beam array.	92

4-4	Finite element analysis showing the Mises stress in the anchor resulting from the residual stress in the aluminum film. Where the Mises stress exceeds the yield stress of aluminum, the structure will plastically deform, causing the anchor to rotate inward as indicated.	95
4-5	Comparison between the experimentally measured bridge profile and the bridge profiles calculated using an elastic finite element model as well as a finite element model that compensated for the plastic deformation that was experienced by the structure.	96
4-6	SEM image of a portion of the MEMS bridge over the top of the optical ring resonator filter.	97
4-7	SEM image showing one of the anchored sides of the MEMS bridge. Note that the suspended section of the aluminum bridge has much greater roughness than the aluminum anchored to the silicon oxide layer. This is a result of the roughness of the poly-silicon sacrificial layer. 98	
4-8	Schematic drawing showing the evolution of an isotropically etched film beginning with (A) and proceeding through (B), (C), and (D) showing the resulting undercut.	100
4-9	Displacement as a function of voltage for the wavelength selective switch device. Note the pull-in at 24 volts.	102
4-10	Finite element pull-in analysis compared with the experimental testing results. Note the finite element analysis predicts that pull-in shouldn't occur since the pull-in point is below the surface of the insulating oxide film.	103
4-11	Schematic representation of the model used to for the analysis of the effect of dielectric charging on the wavelength selective switch.	104
4-12	Schematic drawing showing the relationship between the trapped charge on the dielectric surface and the resulting induced charges on the two electrodes.	105
4-13	Results of fitting the lumped parameter model with no charging to the results of the finite element pull-in analysis.	109

4-14 Comparison of the results of the experimental actuation results with the finite element actuation model and the lumped parameter model that takes into account dielectric charging using the second order dielectric charging model.	110
4-15 Evolution of the top electrode charge and the trapped charge versus the applied voltage for the lumped parameter dielectric charging simulation.	111
4-16 Illustration of the set-up to test the spectral response of the wavelength selective switch.	113
4-17 Image of the test set-up used to couple light into the input waveguide of the device and image the output light coming from the through and drop ports.	114
4-18 Image of the edge of the chip. The bright spot of light is the waveguided light coming out of the end facet of the waveguide at the edge of the chip. The lighter area above the bright spot is the surface of the chip, while the darker area below the bright spot is the chip edges.	115
4-19 Spectral response of the drop port of the wavelength selective switch for both states of the switch.	115
4-20 Spectral response of the through port of the wavelength selective switch for both states of the switch.	116
4-21 Spectral response of both the through port and the drop port of the wavelength selective switch for both states of the switch.	117
4-22 Illustration of the test set-up for testing the temporal response of the switch.	118
4-23 Temporal response of the through port of the wavelength selective switch.	119
4-24 Temporal response of the drop port of the wavelength selective switch.	119
4-25 Temporal response of both the through port and the drop port of the wavelength selective switch.	120

5-1	Illustrations of the dislocation pile-up experienced by the aluminum film during thermally induced plastic deformation. (A) illustrates the film prior to plastic deformation. (B) illustrates the film after deforming plastically due to temperature increase. (C) illustrates the film after deforming plastically due to a temperature decrease.	126
5-2	Illustration of the fabrication process used to create the titanium nitride MEMS bridges. (A) A silicon oxide film is first grown, followed by deposition of a polysilicon film. (B) The poly-silicon sacrificial layer is patterned and etched with contact photolithography followed by reactive ion etching (RIE). (C) The titanium nitride film is deposited by sputtering. (D) The titanium nitride film is patterned and etched using contact photolithography and etched by RIE. (E) The sacrificial poly-silicon layer is removed using a gas phase xenon difluoride etch. .	131
5-3	Optical micrographs of a variety of prototype titanium nitride bridges structures.	134
5-4	Plot of the titanium nitride film stress as a function of temperature during the anneal process.	135
5-5	Contours along the center and edge (as illustrated in (A)) of an unannealed and an annealed titanium nitride bridge. The deformation of the annealed bridge is much less than that of the unannealed bridge. .	137
6-1	Lumped parameter model of a parallel plate actuator.	142

6-2	Quasi-static equilibrium curve for the parallel plate actuator from Equation 6.2. The arrows showing the evolution of the equilibrium positions for increasing and decreasing voltage indicate the bifurcation in the system. When the pull-in voltage is reached, the movable plate tries to jump to the equilibrium position to the right of the fixed electrode position. The isolation layer between the two electrodes will, of course, limit the plate's displacement so it won't reach the theoretical equilibrium position. The thickness of the isolation layer determines the voltage required to maintain the movable plate in the pulled-in state, referred to as the "hold" voltage [22].	143
6-3	Lumped parameter model for a torsional electrostatic actuator.	144
6-4	Quasi-static equilibrium curve for the torsional actuator from Equation 6.5. The arrows showing the evolution of the equilibrium positions for increasing and decreasing voltage indicate the bifurcation in the system. When the pull-in voltage is reached, the movable plate tries to jump to the equilibrium position to the right of the fixed electrode position. The isolation layer between the two electrodes will, of course, limit the plate's rotation so it won't reach the theoretical equilibrium position. The thickness of the isolation layer determines the voltage required to maintain the movable plate in the pulled-in state, referred to as the "hold" voltage [22].	145
6-5	Plot of the required voltage for a given maximum overshoot for various levels of damping (Q values). As the quality factor of the system decreases, the step pull-in voltage moves from the ideal step pull-in voltage with no damping to the quasi-static pull-in voltage value. . .	149
6-6	Plot of the required voltage for a given maximum overshoot for various levels of damping (Q values) for the torsional actuator. As the quality factor of the system decreases, the step pull-in voltage moves from the ideal step pull-in voltage with no damping to the quasi-static pull-in voltage value.	151

6-7	Numerical and analytical curves of the modulated voltage required for particular limit cycle amplitudes for parallel plate systems with quality factors of 10, 100, and 1000. The analytical solutions, from Equation 6.27, are the solid lines. The numerical simulation results are given by the data points. For $Q = 10$, the numerical and analytical solution show some discrepancy due to the sinusoidal motion assumption used in the analytical derivation. For comparison, the quasi-static equilibrium curve (Equation 6.2) and the step response curve (Equation 6.12) are also plotted. The peak of each curve defines that curve's pull-in voltage and position.	155
6-8	Numerical results showing the response of the parallel plate actuator to a modulated input voltage. In A) and B) the applied voltage level is below the modulated pull-in voltage. The system is seen converging to a limit cycle. C) and D) show the system pulling in with an applied voltage just above the modulated pull-in voltage level.	156
6-9	Numerical and analytical curves of the modulated voltage required for particular limit cycle amplitudes for torsional systems with quality factors of 10, 100, and 1000. The analytical solutions, from Equation 6.33, are the solid lines. The numerical simulation results are given by the data points. For $Q = 10$, the numerical and analytical solution show some discrepancy due to the sinusoidal motion assumption used in the analytical derivation. For comparison, the quasi-static equilibrium curve (Equation 6.5) and the step response curve (Equation 6.18) are also plotted. The peak of each curve defines that curve's pull-in voltage and position.	158
6-10	V_{spi} and V_{mpi} as a function of the quality factor for a parallel plate electrostatic actuator. For all values of Q greater than one, the modulated pull-in voltage is less than the step pull-in voltage.	159

6-11	V_{spi} and V_{mpi} as a function of the quality factor for a torsional electrostatic actuator. For all values of Q greater than one, the modulated pull-in voltage is less than the step pull-in voltage.	160
7-1	Switching voltage versus switching speed for a number of RF MEMS switches that have been developed [111].	164
7-2	Schematic diagram of one possible implementation of the ultra-fast switch. (A) shows the movable electrode in its equilibrium state with no applied voltage. (B) and (C) show the movable electrode in its two switch states during normal operation.	166
7-3	Comparison of the switching speed and actuation voltage of a number of RF MEMS switches with switch designs that utilize the strain-energy switching technique.	167
7-4	Schematic diagram of a torsional implementation of the ultra-fast switching technique. (A) shows the movable electrode in its equilibrium state with no applied voltage. (B) and (C) show the movable electrode in the two switch states used during normal operation.	169
7-5	Schematic diagram of a side-to-side motion implementation of the ultra-fast switching technique. (A) shows the movable electrode in its equilibrium state with no applied voltage. (B) and (C) show the movable electrode in the two switch states used during normal operation.	170
7-6	Schematic diagram of the side-to-side motion implementation with electrodes that are shaped to match the mode shape of the movable electrode. (A) shows the movable electrode in its equilibrium state with no applied voltage. (B) and (C) show the movable electrode in the two switch states used during normal operation.	171
7-7	Lumped parameter model for the strain-energy actuation technique. Note the switch is designed to be symmetric, therefore the two resistors have the same resistance R and the two parasitic capacitors have the same capacitance C_p	173

7-8	Curve of the minimum required quality factor for a given effective dielectric thickness normalized by the total effective gap that allows switching by the use of a voltage no higher than the hold voltage. . .	177
7-9	Curve of the minimum required actuation voltage for a system with the dimensionless quantity $RC\sqrt{\frac{k}{m}}$, comparing the effect of the RC time constant relative to the resonant frequency of the mechanical structure.	178
7-10	Cross-sectional view of the fabrication process used for the strain-energy switching prototype. (A) fabrication process begins with an SOI wafer. (B) thermal oxide is grown on the wafer. (C) thermal oxide is patterned with photolithography and RIE. (D) silicon device layer is etched with Deep RIE (DRIE). (E) thermal oxide mask and oxide sacrificial layer are etched away with BOE. (F) thermal oxide layer is grown to create dielectric layer to separate electrodes. (G) thermal oxide is patterned and etched with photolithography and BOE to provide access to bond pads. (H) thin aluminum film is deposited by electron-beam evaporation.	184
7-11	Schematic illustration of the wafer bonding vacuum packaging approach. (A) device wafer and capping wafer prior to bonding. (B) wafer stack after bonding. (C) individual chips after bonding and dicing.	187
7-12	Schematic illustration of the thin film vacuum packaging approach. (A) device wafer with the fabricated MEMS devices. (B) wafer after deposition and patterning of the packaging sacrificial material. (C) wafer after deposition and patterning of the first capping thin film. (D) wafer after the removal of the sacrificial material and the deposition of the final capping film. (E) final chips after dicing.	189
7-13	Schematic drawing of the switching circuit for the strain-energy actuation technique.	190
7-14	Timing of the control voltages for the strain-energy switch circuit for a switch operation where the movable electrode moves from being pulled-in to fixed electrode one to being pulled-in to fixed electrode two. . .	191

7-15	Pull-in and hold voltages for a series of switching cycles of device “C.” The + and - signs above the bars indicate the polarity of the iterations. These pull-in and release iterations were performed in air. Note the strong dielectric charging effects.	196
7-16	Pull-in and hold voltages for a series of switching cycles of device “K.” The + and - signs above the bars indicate the polarity of the iterations. In this case, the polarity is reversed with each cycle and the pull-in and hold voltages for the different polarities appear to be converging to a constant value.	197
7-17	Pull-in and hold voltages for a series of switching cycles using the second fixed electrode of device “K” (Figure 7-16 used the first fixed electrode of device “K”). The same polarity cycling strategy was used in this case as in Figure 7-16 and the results are similar. This indicates that the symmetry of device “K” is good.	198
7-18	Pull-in and hold voltages for a series of switching cycles of device “K.” The + and - signs above the bars indicates the polarity used for that pull-in and release cycle. These pull-in and release tests were conducted in a vacuum within the chamber of an SEM. The dielectric charging seen in Figures 7-15, 7-16, and 7-17 is not observed in these tests. (The release voltages of iterations 6 and 18 were not recorded.)	198
8-1	Illustration of the operation of the MEMS ring resonator tuning device. (A) and (B) show the ring resonator tuned to drop different channels (wavelengths).	205
8-2	Schematic of the MEMS structure, including both the control and sens- ing electrodes, integrated with the optical ring resonator.	206
8-3	Schematic of the lumped parameter model based on the MEMS struc- ture illustrated in Figure 8.2.	207
8-4	Block diagram of the feedback control system used for the tunable ring resonator filter.	213

8-5	PID controller circuit [103].	214
8-6	Capacitive sensing circuit [7].	215
D-1	Comparison of the results of the experimental actuation results with the finite element actuation model and the lumped parameter model that takes into account dielectric charging using the linear dielectric charging model.	240

List of Tables

2.1	Switching speed requirements for different applications within optical networking [110].	58
2.2	Dimensions of the optical ring resonator that was integrated into the wavelength selective switch devices.	65
2.3	Results of the electromechanical analysis of the bridge structure design compared with the design requirements and the actual experimental results of the fabricated switch prototypes.	73
3.1	Process flow for the fabrication of the MEMS structures on top of the optical ring resonator structures. The process begins after the fabrication of the ring resonator structures.	79
4.1	Parameters used with the nonlinear dielectric charging lumped parameter model.	108
5.1	Fabrication process for the titanium nitride prototype bridge structures.	132
7.1	Design details of prototype switch structures.	182
7.2	Fabrication process for the prototype MEMS switch based on the strain-energy technique.	185
7.3	Resistance measurements and calculations for the prototype strain-energy switching structures.	194
7.4	Pull-in and hold voltage results of several of the switch prototypes.	195

8.1	Mechanical parameters for the ring resonator tuning lumped parameter model.	210
8.2	Parameters for the capacitive sensing circuit.	215
8.3	Simulation results of open-loop and feedback control of the ring resonator tuning structure.	216
8.4	PID controller parameters used in closed-loop simulations.	217
A.1	Aluminum (Al) Material Properties	226
A.2	Silicon (Si) Material Properties	227
A.3	Silicon Oxide (SiO ₂) Material Properties	228
A.4	Silicon Nitride (Si ₃ N ₄) Material Properties	229
A.5	Titanium nitride (TiN) Material Properties	229
A.6	Properties of air (at standard temperature and pressure).	230
C.1	Radius of curvature, residual stress gradient measurements, and stress difference between top and bottom of aluminum film	237
D.1	Parameters used with the linear dielectric charging lumped parameter model.	240

Chapter 1

Introduction

Optical integrated circuits (OICs) promise to enable faster and cheaper optical communications networks, optical computer interconnects for extremely fast data transfer between chips, and even all-optical computing. The vision for these OICs is a chip that brings together lasers, modulators, amplifiers, filters, and optical switches all in an integrated package that is both highly functional and inexpensive. The expectation is that this type of optical integrated circuit will be able to provide an impact similar to what was experienced when electronics moved from being a collection of discrete components to integrated electronics. A conceptual idea of a possible IOC is shown in Figure 1-1 [131].

For the purposes of this work, optical integrated circuits are defined as optical systems where all of the devices are integrated together on one substrate in a compatible material system where the light is completely guided (i.e. no free-space transmission of light). This definition reflects the integration concepts that have proven to be successful for integrated electronic circuits.

Research into OICs has been ongoing since the 1970's [113] and although significant progress has been made towards a functional OIC, the vision and value of OICs have yet to be realized. Probably the most significant reason OICs have not yet been widely deployed is that the components needed for an OIC have not yet all been developed in a single compatible material system. Another reason is that in some cases the best performing optical components are not integrated devices. A good example

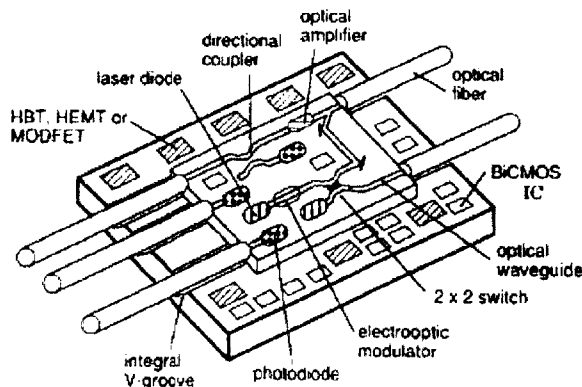


Figure 1-1: Soref's vision of an optical integrated circuit (OIC) in 1993 [131]. Note the absence of wavelength selective components. Wavelength division multiplexing (WDM) was just beginning to be developed in 1993.

of such a device is the lithium niobate optical modulators that are currently used in optical communications networks [110]. These modulators are currently the best performing products at modulating light for high-speed communications but they are not integrated devices in the sense that they could be integrated with other optical devices in the same material system on the same substrate.

One important consideration in the development of OICs, as with any new technology is whether the problem the technology is meant to solve can be adequately solved using current technology. In telecommunications, where OICs would have a tremendous impact, electronic integrated circuits have so far been able to keep up with switching and routing needs of the optical networks by the use of optical to electrical to optical (OEO) conversion of the signals being transmitted. In this arrangement, optical signals coming from optical fiber into switching hubs are converted into electrical signals by photodetectors. The signals are routed in the electrical domain and then are resent into the appropriate output fiber using a laser and an optical modulator.

By using OEO switching and routing, the needs of optical networking has been adequately addressed. However, with the desire to put more and more data across optical networks through the use of wavelength division multiplexing (WDM), where many different wavelengths (channels) are sent down a single fiber, as well as other

methods; the ability to switch and route signal using OEO conversion is becoming difficult to do at both the cost and speed required.

If an OIC could be developed that had the capability to route individual wavelengths of light from a single input waveguide into a variety of output waveguides, the need for OEO would be eliminated and the cost savings on equipment ranging from photodetectors, electronics, lasers, and modulators that would no longer be needed at all of the switching nodes would be enormous.

If the OIC was manufactured in an inexpensive material system for microfabrication, such as silicon CMOS, the OIC would enable inexpensive high speed networking that could potentially connect every house and business in a way that is not possible with current technology.

This thesis is aimed towards the development of an OIC that has the capability to route individual wavelengths of light to various output waveguides. Specifically, this work focuses on the development of tunable and switchable integrated optical elements for OICs in a CMOS compatible material system. This work combined with other recent developments in the use of silicon for optical applications [113] have brought the vision of OICs much closer to reality. As the cost and speed of electronic switches, routers, and interconnects are becoming restrictive; these technological developments make OICs very attractive. The key contribution of this thesis is to advance the practicality of using OICs in communications networks and interconnects by demonstrating switchable and adaptive capabilities. These will be crucial for utilizing OICs in these contexts.

One particular device that is a fundamental component of an OIC is an integrated optical switch. This thesis will describe a unique integrated optical switch that is based on enabling or disabling an optical ring resonator filter. The switching is accomplished by a microelectromechanical system (MEMS) moving a lossy material into and out of the evanescent field of the optical ring resonator [144]. The results of the design, fabrication, and testing of this device are described in Chapters 2, 3, and 4. This switch has the very unique capability of wavelength selective switching.

A second device that will also be explored in this thesis is a tunable ring resonator

filter where a MEMS device moves a dielectric material within the evanescent field of an optical ring resonator. The design of this device is developed in Chapter 8 with particular emphasis on controlling the dielectric material position with sufficient accuracy to make the tuning function a viable element for real life OIC networks.

1.1 Optical switching

An integrated optical switch is a fundamental building block of almost any OIC. A number of different approaches have been taken in developing an optical switch. These approaches include MEMS switching, electro-optic switching, liquid crystal switching, and thermo-optic switching. To date, nearly all of the switches that have been developed lack intrinsic wavelength selective switching capabilities. There have been some devices that nominally demonstrate wavelength selective switching [30, 56, 140], however, these devices are based on changing the resonant frequency of a ring resonator filter. This provides wavelength switching in a sense but the “switching” operation would affect adjacent optical channels making them unsuitable for WDM applications.

1.1.1 Free-space MEMS switching

The bulk of the work done in the space of MEMS-based optical switching has been for free-space optical switching. This type of optical switch wouldn’t be useful in OICs; however, it is worthwhile to review the work done in this area to give context to the work presented in this thesis.

There have been two main approaches to free-space optical MEMS switching. The best approach in terms of optical losses is in using reflective MEMS devices. An alternative approach uses diffractive elements.

A good example of a reflective MEMS device used for switching is Lucent’s micro-mirror array used in their Wavestar™Lambdarouter product. The mirrors are tiltable on two axes allowing each mirror to be used to reflect light from an incoming fiber to any of a two-dimensional array of output fibers. The actuation voltage required for

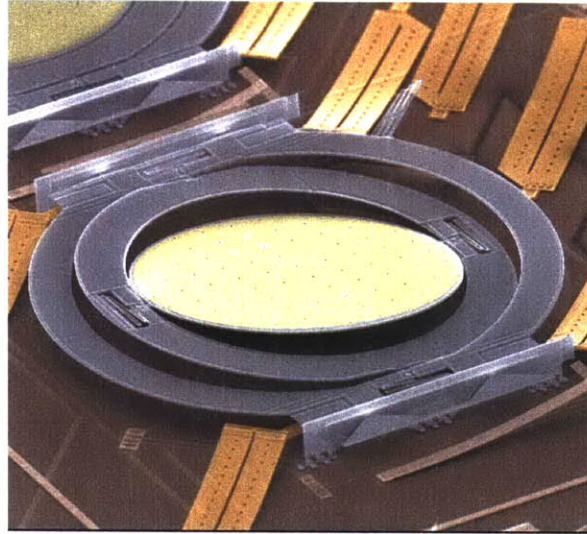


Figure 1-2: An image of one micro-mirror from the micro-mirror array developed by Lucent. This mirror is tiltable on two axes allowing a beam to be pointed to any of a 2D array of output fibers. (Image courtesy of Lucent Technologies Inc.)

the device is 200 volts, with a response time of 5 to 50 ms [3,69]. Lucent's mirrors were operated with an open-loop control system, yet they still exhibited remarkable stability over time. Figure 1-2 shows an image of one micro-mirror from a micro-mirror array developed by Lucent.

In addition to the Lucent micro-mirror device, there have been a number of other tiltable micro-mirror based devices fabricated for optical switching purposes [8,35,84,97].

There have also been several MEMS optical gratings that have been demonstrated for free space optical applications [11,126,127,130,148]. In theory, these devices have the capability to switch light but since they are based on diffraction, they intrinsically have high insertion losses - making them inappropriate for switching in optical networking applications.

The most "switch-like" of the MEMS optical gratings is the device by Solgaard et al. developed initially at Stanford University and then at Silicon Light Machines, where the elements comprising the grating switch from one position to another [130]. The device can produce either a flat, mirror-like surface or a grating with a period that

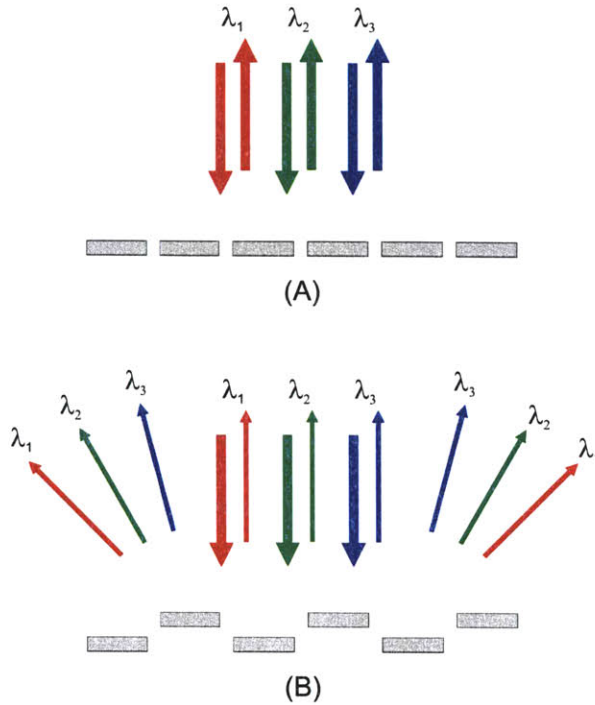


Figure 1-3: A schematic representation of how a diffractive grating MEMS device operates. (A) shows the device cross-section with all of the grating beams as the same level which essentially acts as a mirror. (B) shows the device with every other grating beam displaced downward. In this position, the grating will diffract the light into a variety of optical orders.

is twice the width of the grating beams. Because the diffraction angle of the grating is wavelength dependent, the grating can produce wavelength selective switching. The grating is designed to produce a displacement of one quarter of the operating wavelength for optimal switching contrast. Figure 1-3 shows a schematic illustration of this device in its two switch positions.

Other diffractive MEMS devices reported on provide a wide range of positions for the elements comprising the gratings and thus operate in an analog rather than binary fashion [11,127,148]. These devices could also be used for wavelength selective switching.

For telecommunications wavelengths of light, these devices switch at speeds ranging from a few microseconds up to hundreds of microseconds and require anywhere from a few volts up to several tens of volts for actuation. Since these devices are

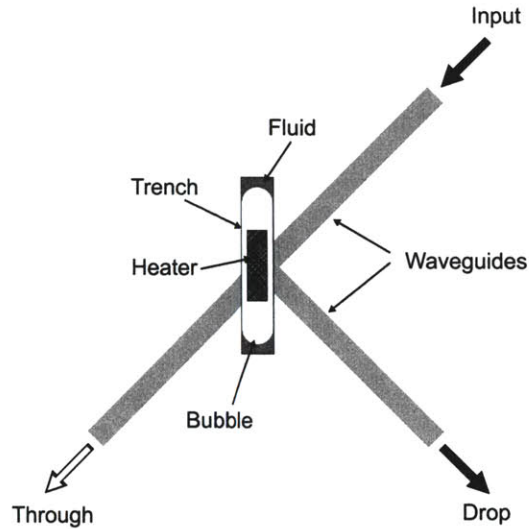


Figure 1-4: Schematic representation of the micro-bubble optical switch. When the heater is on and the bubble is present in the trench, the light is routed to the drop waveguide (as shown). When the heater is off and the bubble is not present, the light is routed to the through waveguide.

all based on either electrostatic or piezoelectric actuation, the devices have very low currents and thus require very little operating energy - on the order of micro-Watts.

1.1.2 Waveguide based optical MEMS switching

Agilent (HP) developed a MEMS optical switch using micro-bubbles to create a reflective surface at the liquid-gas interface. This device can be thought of as a hybrid between a free-space optical switch and an integrated optical switch. Waveguides lead light to a small gap where the bubble is formed or removed to create the optical switching effect. Switching speeds from 100 μs to 7 ms have been reported for this approach [37, 38, 51, 142, 143]. Figure 1-4 illustrates the operation of the micro-bubble switch.

Another hybrid device that uses a MEMS mirror is described in [17]. This device also guides light with waveguides/fibers with only a small free-space path where the mirror is moved in and out of. This device demonstrated switching speeds of 400 to 600 μs with an actuation voltage of 20 volts and an insertion loss of 0.7dB (not

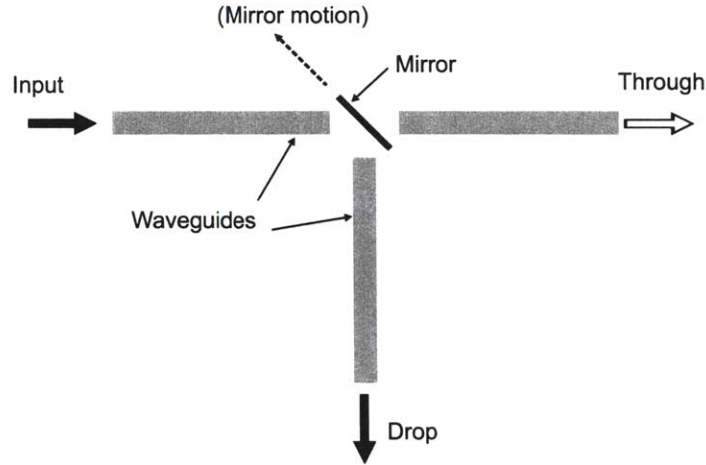


Figure 1-5: Schematic representation of the mirror based integrated optical switch. The position of the mirror controls whether the input light is directed toward the drop waveguide or the through waveguide.

including the coupling losses). A similar device that operates at 30 volts with a switching speed of $100 \mu\text{s}$ is described in [80]. The insertion loss for this switch is quite high at 10dB, due to excessive roughness on the mirror surface. Figure 1-5 illustrates the switching concept used for these devices.

Another hybrid device where a waveguide is pointed to one of two different output waveguides is described in [104]. This device has insertion losses of 1.5dB when an index matching gel is used in the gap between the waveguides. The switching time is 1 ms and the actuation voltage is 70 volts. A theoretical design of a similar hybrid device where a waveguide is either pointed to output waveguides or is coupled to output waveguides is described in [108].

The device described in [23] maintains the light in the waveguides throughout the entire switch structure. This device works by controlling the evanescent coupling between the waveguides to switch the light. Experimental results were not reported for this switch but a similar attenuator device described in the same reference reported a switching time of 1ms with an actuation voltage of between 40 and 85 volts.

Another switch where the light is maintained in waveguides throughout the length of the device is described in [29]. Switching is accomplished by an electrostatically actuated structure that interacts with the evanescent field of the integrated waveguide.

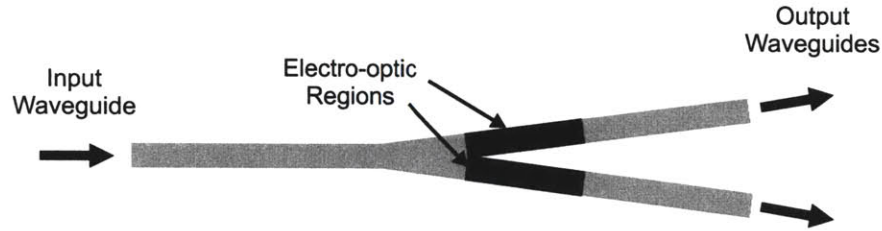


Figure 1-6: Illustration of a electro-optic “Y” switch. To direct the input light to one of output waveguides, power is applied to the opposite electro-optic region. The index in that electro-optic region is reduced and thus makes that leg of the Y splitter appear like cladding material rather than a waveguide.

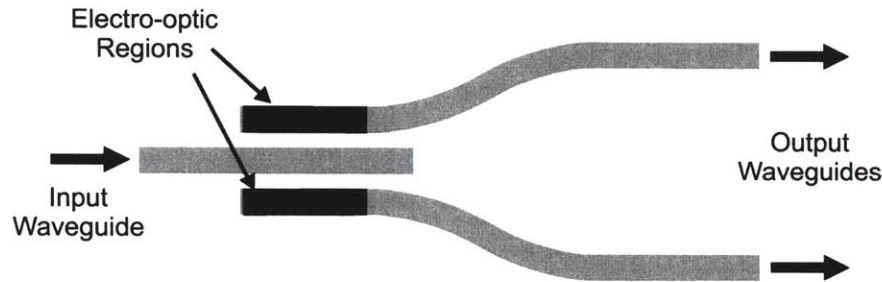


Figure 1-7: Illustration of a electro-optic coupling switch. To direct the input light to one of the two output waveguides, the coupling between the input and the output waveguides is controlled by applying power to the electro-optic regions.

The MEMS structure is not fabricated on the same substrate as the waveguides. It is fabricated on a different wafer, die-sawed into individual elements and then bonded to the waveguide chips. The actuation voltage was comprised of a DC bias voltage coupled with an additional control voltage. The bias voltage ranged from 7 volts up to 200 volts while the control voltage signal was only a few volts. Reported switching times were about 50 μ s.

1.1.3 Electro-optic optical switching

Electro-optic switching is most often demonstrated in waveguide based systems where the waveguide core and/or cladding material have DC-field dependent index of refraction and/or absorption. Typically, electro-optic switch structures are based on “Y” splitters (see Figure 1-6 or waveguide coupling (see Figure 1-7). Some recent electro-optic switches have been created by tuning microring resonator and Mach-Zehnder

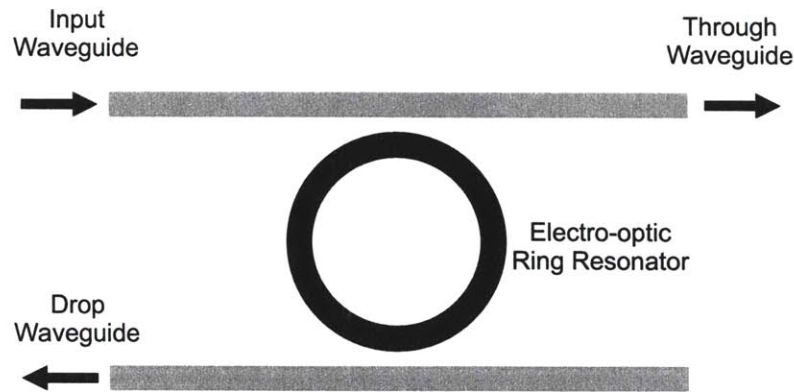


Figure 1-8: Illustration of a electro-optic ring resonator switch. To direct the input light to the either the through or the drop port, the index of the ring resonator is changed to cause the input to either resonate in the ring or not. If the input light is resonant, the light will couple to the drop waveguide, if the light is non-resonant it will pass by the ring unaffected and exit through the through waveguide.

filters (see Figures 1-8 and 1-9, respectively).

Electro-optic switches have been demonstrated in silicon and silicon germanium waveguides [28,78,79,89,90], in III-V semiconductors (InP, InGaAsP, etc.) [2,30,56,57, 100,140], and in perovskite crystals such as lithium niobate [101]. The semiconductor based switches use the refractive index change resulting from carrier injecting, either due to a electrical current or an optical pump signal. The injected carriers also cause absorption in the waveguides which can lead to high insertion losses. Lithium niobate experiences an index change due to the application of an electric field, hence requiring much less power to operate than the semiconductor based switches; however, the required electric field can be high, thus requiring high voltages (relative to IC voltage levels).

Electro-optic switches based on “Y” splitters, coupling, or Mach-Zehnder filters require anywhere from 200 to 600 mW up to several watts for silicon and silicon germanium based switches while tens of milliwatts are required for III-V based switches. Lithium niobate switches have been demonstrated with applied voltages as low as 8 volts with very low power since the current is very small. Switching times of tens of nanoseconds are common. Insertion losses for these switches have been demonstrated to be as low as 8.2 dB for silicon switches, 3 dB for silicon germanium switches, 2

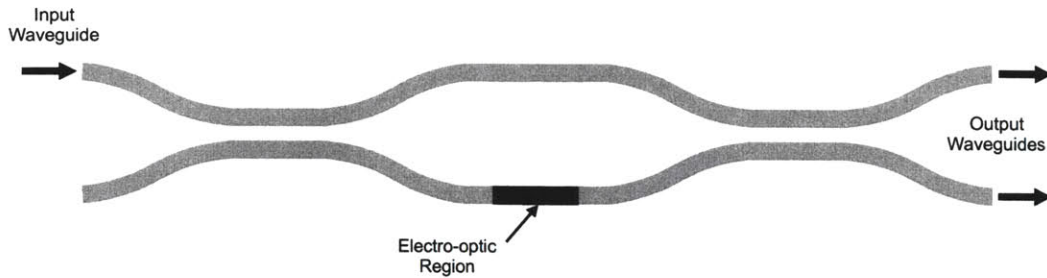


Figure 1-9: Illustration of a electro-optic Mach-Zehnder filter switch. To direct the input light to one of the two output waveguides, the electro-optic region is used to change the path length between the two legs of the interferometer. In this way the light is cause to constructively interfere in one of the output waveguides and destructively interfere in the other output waveguide.

dB for III-V semiconductor switches, and 7.2 dB for lithium niobate switches. The length of these switches is usually on the order of a few millimeters to centimeters [2, 28, 78, 79, 89, 90, 100, 101].

A second group of electro-optic switches use integrated optical ring resonators fabricated out of III-V semiconductors. The ring resonators are switched by carrier injection induced by either an electrical current [30] or by optical pumping [56, 57, 140]. These devices work by detuning the resonance of the rings off the particular wavelength (channel) of interest. In a WDM setup, this approach is troublesome because the new resonant channel will be switched in the opposite direction as the initial resonant channel, which is typically not desired.

The power required for switching or tuning of these ring resonator based switches is generally less than that required for other electro-optic switches because optical resonance in the ring amplifies the effect of the index change. A few milliwatts of power is typically sufficient for switching. Switching speeds can be as fast as tens of picoseconds. Insertion losses for these switches weren't reported [30, 56, 57, 140].

1.1.4 Liquid crystal optical switching

Most liquid crystal based switches operate on light in free-space [44, 96, 114, 115] although some devices that use a waveguide based switching approach have also been reported [5, 146, 150].

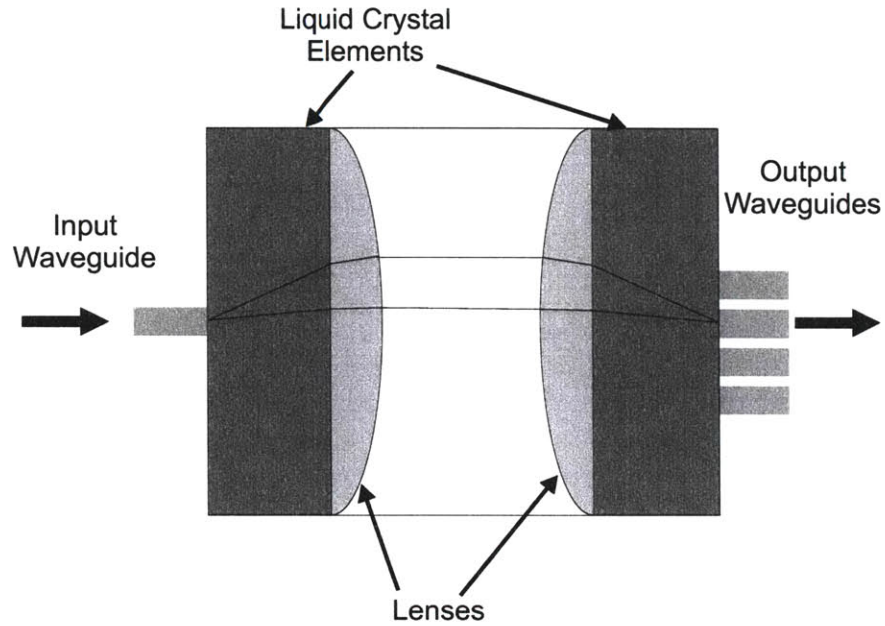


Figure 1-10: Illustration of a liquid crystal optical switch. The liquid crystal elements steer the input light to the desired output fiber [44].

These liquid crystal switches have a wide variety of implementations. Figure 1-10 shows one implementation that uses liquid crystals as beam steering elements to direct the light from an input fiber to one of an array of output fibers. Regardless of the optical system, the actuation of the liquid crystals requires that the liquid crystals be sandwiched between two electrodes that can apply an electric field. When the electric field is applied the liquid crystals line up and create an optically anisotropic media. It is this effect that is used to create liquid crystal switches.

Liquid crystal based switches have switching times from as good as $20 \mu\text{s}$ up to tens of milli-seconds. The fastest switching times were achieved by heating the liquid crystals to reduce their viscosity. Actuation voltages are reported from 10 volts up to 20 volts. Insertion losses as low as 5 dB have been reported¹ [5,44,96,114,115,146,150].

¹The insertion losses reported for these devices typically include coupling losses since the input and output fibers are usually an integral part of the switch.

1.1.5 Thermo-optic switching

Thermo-optic switches are integrated, waveguide based switches. They can be fabricated out of CMOS compatible materials such as silica [31, 122, 129] although they are often fabricated out of polymers [45, 53, 62, 128] to reduce the amount of power needed for switching. The silica based devices tend to have lower losses. One particular device uses a hybrid silica and polymer scheme to take advantage of the properties of both materials [65].

Thermo-optic switches tend to be similar to electro-optic switches. There are thermo-optic switches based on “Y” splitters (see Figure 1-6) and coupled waveguides (see Figure 1-7) as well as Mach-Zehnder (see Figure 1-9) and ring resonator filter (see Figure 1-8) devices. These devices require the integration of a heating element to provide the energy for actuation.

Thermo-optic switches have switching times of a few milli-seconds, at best. The actuation power required is tens to hundreds of milliwatts with insertion losses as low as 2 dB. These devices typically have sizes of a few to tens of millimeters [31, 45, 53, 62, 65, 88, 122, 128, 129].

1.1.6 Wavelength selective switching

Most of the devices described so far do not have the capability to selectively switch individual wavelengths of light. To achieve wavelength selective functionality, these switches would have to be coupled with some additional demultiplexing and multiplexing devices, as illustrated in Figure 1-11. Among the devices described above, there are a few examples of that approach [31, 84, 114, 115, 122].

A few integrated switches do have intrinsic wavelength selectivity. These switches are all based on tuning ring resonators or Mach-Zehnder interferometers [30, 56, 110, 140]. While this approach provides wavelength selectivity, its utility in a WDM network is limited. By tuning the filter passband away from a particular wavelength to switch it between output ports, one inadvertently switches the adjacent wavelength, as illustrated in Figure 1-12. To avoid interfering with adjacent channels, the channels

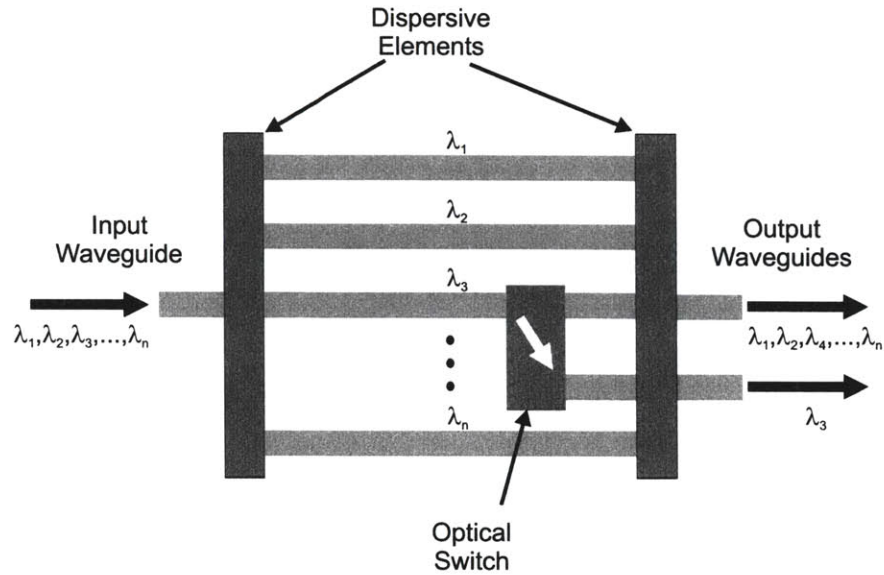


Figure 1-11: Illustration of the required arrangement to achieve wavelength selective switching with most of the optical switches currently available.

would need to be widely spaced so the drop band of the filter can be placed in between the channels, or the number of channels would need to be limited so that the drop band can be moved outside of the frequency band of the channels where the channels reside. Either of these methods places limitations on the bandwidth that can be sent using WDM.

These switches would work well in a system that contains only a single wavelength of light, however, in that type of system their effective functionality would be no different than the broadband optical switches described in the previous sections.

An ideal wavelength selective switch would provide the capability to switch a single wavelength or channel between two output waveguides without affecting any other wavelengths. Prior to the wavelength selective switch described in this thesis, this capability was not available in an optical switch.

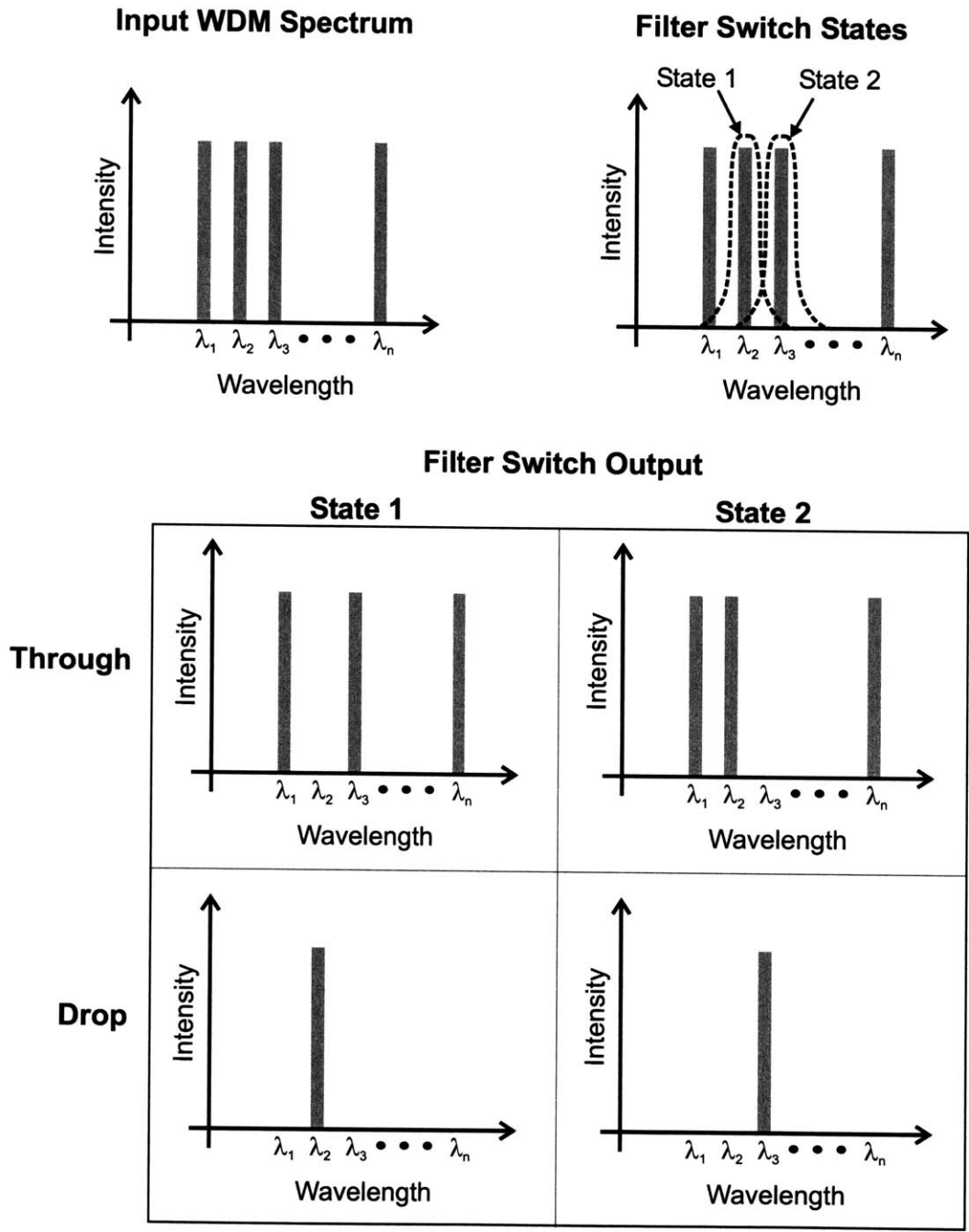


Figure 1-12: Illustration of the response of a filter tuning based to a WDM input spectrum. Note that going from the first state to the second state switches two wavelengths between the drop and through ports, in opposing directions, rather than just a single wavelength.

1.2 Filter Tuning

Integrated tunable filters are another important element for integrated optical circuits used in WDM applications. The techniques that are used to tune integrated optical filters include thermal tuning, electro-optic tuning, liquid crystal tuning, and piezoelectrically induced strain tuning. These devices have essentially the same functionality as the filter tuning switches illustrated in Figure 1-12, except that ideal tunable filters would have the capability to tune to any of the channels in the WDM input signal rather than have just two states.

The integrated filters elements that have been used in tunable filters include ring resonator filters, one-dimensional photonic bandgap crystal filters, and Mach-Zehnder filters. The tuning is accomplished by using some technique that changes either the core or cladding index of the waveguides comprising the filter, or by changing the physical dimensions of the filter. These changes create a change in the optical path length of the device and, therefore, a change in the spectral position of the passband of the filter.

1.2.1 Thermal tuning

Thermal tuning is achieved by the thermo-optic effect where the index of a particular material changes with temperature [49, 85]. Thermal tuning can take several Watts of power and tends to be slow. The fastest response times of these devices are on the order of milliseconds. The tuning range can be fairly wide, if high temperatures are acceptable in the devices. The vernier effect has been used with two coupled tunable ring resonator filters to achieve a very large tuning range [85]².

1.2.2 Liquid crystal tuning

Liquid crystal based filter tuning has been demonstrated by using liquid crystal material as the top and side cladding of a ring resonator [94]. When the liquid crystal is

²Using the vernier effect to create a tunable filter puts significant constraints on the utility of a device in a WDM network.

subjected to an electric field, its index changes which causes the resonant frequency of the ring resonator to change. The tuning range of this device was quite limited, showing a change in resonance of only 0.22 nm with an applied voltage of 20 volts. Response time wasn't reported, however, it is expected that it would be no faster than tens of microseconds, similar to what is possible with other liquid crystal devices.

1.2.3 Electro-optic tuning

Electro-optically tunable ring resonators have already been discussed as switches in section 1.1.3. These devices use carrier injection resulting from either a current flow [30] or an optical pump [56,57,140] to change the index of the ring resonator waveguide core, which is comprised of a III-V semiconductor material. While these devices can have very fast response times, on the order of tens of picoseconds, the injected carriers introduces additional optical loss into the rings. This additional loss is readily seen even with a small change in resonance. This additional loss creates higher insertion losses and alters the shape of the filter passbands. Tuning of up to about 5 nm has been shown with tens of mW of input power.

1.2.4 Piezoelectric strain tuning

The tunable filter that utilized piezoelectric strain tuning utilized a one-dimensional photonic bandgap crystal structure within a waveguide to create the optical filter [148]. The waveguide was suspended between integrated piezoelectric actuators which, when actuated, introduced strain into the photonic bandgap waveguide. The strain changed the length of the resonant cavity and thus introduced a shift in the response of the filter. Tuning of up to 1.8 nm was observed.

1.3 Thesis objectives

The topic of this thesis is MEMS switching and tuning of optical ring resonator filters for integrated optical applications. The integration of MEMS devices with

ring resonator filters is a new application for MEMS. For this reason, the focus of this research is to analyze and demonstrate the feasibility of operating ring resonator filters with MEMS switching and tuning. This thesis will address the system impact of these architectures from the point of view of fundamental optical and mechanical/material properties.

The first part of this thesis describes the design, fabrication, and demonstration of an integrated MEMS-switchable ring resonator device where the micromechanism effectively couples the resonator in and out of the optical circuit to accomplish wavelength-selective response. The performance of our first demonstrated prototype will be compared the requirements of integrated optical systems and shown to have unique advantages in terms of functionality, actuation voltage, and operating power.

The second portion of this thesis builds off of the results of the prototype switching device. A detailed exploration of the dynamic performance of parallel plate MEMS actuators is given. From this analysis, two new MEMS switching approaches are derived. The new switching methods allow a significant reduction in actuation voltage as well as much faster switching speeds compared to what is currently possible with standard MEMS parallel plate actuators.

The third portion of this thesis will explore the tuning of optical ring resonator filters by MEMS. This is a much more complex device with some very strict performance requirements. The effort in this area is in the design and analysis of the device to determine its feasibility and if this type of device can meet the strict performance requirements of integrated optical systems. The answer turned out to be positive, but the experimental demonstration of the device was outside the scope of this thesis.

1.4 Outline of Thesis

Chapter 1 described the vision of an integrated optical circuit and reviews the relevant literature related to integrated optical switches and integrated tunable filters.

Chapter 2 describes the design for the integrated wavelength selective switch based on integrating a high-index-contrast ring resonator filter with a MEMS parallel plate

structure.

Chapter 3 describes the fabrication process used to create the MEMS ring resonator switch designed in Chapter 2 and discusses material and packaging considerations for this type of device.

Chapter 4 describes the results of a series of experiments to characterize the structure and performance of MEMS ring resonator switches that were fabricated at MIT's Microsystem Technology Laboratories (MTL). The experiments were designed to test both the optical and mechanical performance of the device. In addition, a model for dielectric charging is proposed that allows accurate modelling of the electro-mechanical pull-in characteristics of the device.

Chapter 5 addresses the problem of residual stress seen in the wavelength selective optical switch device. The difficulties associated with using aluminum as the MEMS bridge material are detailed. In addition, the use of titanium nitride (TiN) as an electro-mechanical material for MEMS applications is proposed and characterized based on the properties of this material and the telecommunications requirements for integrated optical systems. TiN has some very unique properties (i.e. high stiffness, electrically conductive, high strength, low surface adhesion energy, wear resistance, etc.) that make it a preferred material over many of the current standard MEMS materials (silicon, silicon oxide, silicon nitride, etc.).

Chapter 6 describes a new technique that allows the operation of the wavelength-selective switch (and other parallel plate and torsional MEMS actuators) at a much lower voltage. This chapter first analyzes the system dynamics of these actuators to get a more full view of the actuation of these MEMS devices. By using these dynamic motion insights, an actuation technique is proposed that can significantly reduce the required voltage from the high actuation voltages that are currently used in these devices.

Chapter 7 describes a new actuation method for MEMS switching that has the potential to lead to significantly lower actuation voltages, lower operating energy (on a per-switching event basis), and significantly higher speed than any other MEMS actuation technique. The key innovation is the use of stored elastic potential energy

to drive the switching motion while an electrostatic hold voltage maintains the switch in its two states.

Chapter 8 describes the design and analysis of an integrated tunable optical filter. This filter is also based on a high-index-contrast ring resonator filter integrated with a MEMS device. In this case, the MEMS device moves a dielectric slab within the evanescent field of the ring resonator in such a way as to tune the resonance of the ring to drop the desired channel out of a WDM input signal. The position of the dielectric slab in the evanescent field determines the effective index of the ring resonator, and therefore the optical path length and the resonant wavelength of the ring. It is shown that although the required positional stability tolerances are tight, the device should be able to perform within the specifications.

Chapter 9 is a final discussion of the thesis, its impact, and suggestions for related future work.

1.5 Thesis contributions and applications

This thesis contributes to both IOC technology and MEMS technology. The contributions to IOC technology are the development and demonstration of an integrated wavelength-selective switch as well as the design and analysis of a new tunable integrated optical filter. Both of these devices are important to a wide variety of potential applications of IOCs including telecommunications, optical computing, optical interconnects, and optical bio-sensing.

The key contributions to MEMS technology include:

- The development of a dielectric charging model that accurately predicts the effects of dielectric charging during actuation.
- The use of titanium nitride as a material for MEMS applications.
- The development of a new actuation technique for parallel plate and torsional actuators that significantly reduces the voltage needed to pull-in the structure.

- The development of a second complementary actuation technique that allows for low voltage and extremely fast actuation - faster than any other current MEMS actuation technique.

These contributions have many potential applications. Dielectric charging is present to some degree in virtually any MEMS device where an electric field is present in combination with an air/dielectric boundary. The model proposed and developed in Chapter 4 predicts the evolution of the charge on the dielectric surface as a function of the applied voltage and the bridge displacement. This provides the capability to model the response of the bridge throughout the actuation process, rather than just predict the increased pull-in voltage due to dielectric charging [147, 151].

As mentioned previously, titanium nitride has a number of appealing properties for MEMS including high stiffness, high strength, electrical conductivity, low surface adhesion energy, high wear resistance, chemical stability, low temperature processing, CMOS compatibility, and low temperature annealing. These properties make titanium nitride a material that is uniquely suited for a wide variety of MEMS applications.

The two new actuation techniques described in this thesis allows MEMS switching at speeds that are currently unavailable through any other MEMS actuation technique. In addition, the low voltage and low power required by these techniques allows direct integration of MEMS devices based on these techniques into both electronic and optical integrated circuits.

The low voltage, low energy, and high speed capabilities of these actuation techniques enables many very exciting MEMS switching applications. These techniques can, of course, be used in integrated optical switching devices, both broadband and wavelength selective, as described in this thesis. Another exciting application of these actuation techniques is in radio-frequency (RF) MEMS switching.

RF MEMS switches have been an area of active research since the early 1990's. These switches provide much lower insertion loss and isolation than semiconductor based switches that are currently used in RF applications. However, the RF MEMS switches have typically required high voltages to actuate and are much slower than

semiconductor switches. By applying these new actuation techniques to an RF MEMS switch, a low-voltage high-speed RF MEMS switch is possible that would have the very appealing insertion loss and isolation characteristics that have been demonstrated by other RF MEMS, but would still provide the low-voltage and high speed actuation that is provided by semiconductor RF switches. This kind of RF MEMS switch could be used in phased array radar systems, satellite communications, RF test equipment, cell phones, wireless internet access, base stations, and a variety of other RF applications as a direct replacement for RF semiconductor switches.

Chapter 2

Optical ring resonator MEMS switch design

This chapter describes the design of the MEMS based wavelength selective integrated switch. The switching function is based on the introduction of loss into an optical ring resonator to significantly weaken the resonance of the ring to point where the quality factor is very small. With a small quality factor, the ring is effectively detached from the circuit and the light in the input waveguide passes by the ring unaffected [87,144]. Using this loss-based approach for optical ring resonator switching provides wavelength selective switching without affecting adjacent wavelength channels¹.

The loss based approach requires a significant amount of loss to be introduced into the ring, much more than can be reasonably achieved using carrier injection. The idea of using an electrostatic MEMS device to move a lossy material membrane into and out of the evanescent field of the optical ring resonator to introduce the necessary loss for switching was first proposed theoretically in [144]. This thesis is the first experimental demonstration to date.

The switch described here provides a number of advantages. The first advantage is that it provides a completely integrated wavelength selective switch within a material system that is CMOS compatible, thus allowing direct integration into an

¹Other ring resonator “switching” devices that make use of detuning as the switching mechanism will affect adjacent channels, see Section 1.1.6 in Chapter 1.

opto-electronic integrated circuit. Secondly, the ring resonator and MEMS device are both extremely small occupying a total area of $160\ \mu\text{m} \times 30\ \mu\text{m}$, occupying the smallest chip real estate of any wavelength selective switch currently available. Thirdly, electrostatic MEMS devices require very little energy for operation², unlike electro-optic switches based on carrier injection or thermo-optic switches. Finally, because the switching mechanism isn't doesn't depend on the waveguide material, as is the case with carrier injection based switches which require semiconductor core and/or cladding material, the ring resonator can be fabricated out of any material. Allowing the designer to select the best performing waveguide materials for a particular application without constraints imposed by the switching mechanism.

2.1 Optical ring resonator filters

Ring resonator filters have been shown to be very effective static integrated optical elements [24, 25, 55, 86]. By coupling MEMS devices with the rings, microring resonators can become active elements in an integrated optical circuit for routing optical channels within the circuit.

Figure 2.1 illustrates the static operation of a typical optical ring resonator. A number of wavelengths (channels) are directed into the input waveguide. The resonant wavelength couples into the drop waveguide via the ring resonator while the non-resonant wavelengths do not couple into the ring resonator and propagate through unaffected.

Optical ring resonators operate very much like Fabry-Perot resonators. The coupling between the bus waveguides (the input, through, and drop waveguides) and the ring resonator is very small, on the order of 1% or less. The small fraction of light that does couple into the ring from the input waveguide propagates around the ring. After one round trip, the resonant wavelength interferes *constructively* with the light currently coupling into the ring. At the same time, some of this light also

²Electrostatic parallel plate actuators require only a few μW of power during the switching process, and essentially no power while in either switch state.

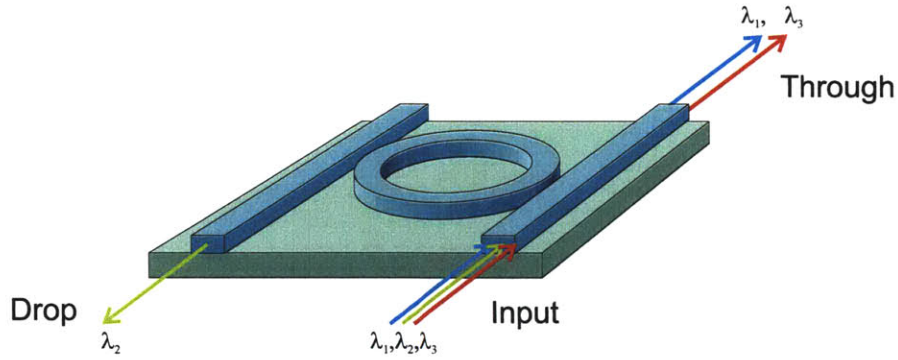


Figure 2-1: Schematic representation of an optical ring resonator filter showing its static wavelength selective behavior.

couples back into the input/through waveguide. The interference at the through port is *destructively*; hence after a sufficient number of roundtrips there is no light at the resonant wavelength propagating in the through port. The resonant wavelength also couples weakly into the drop port. However, due to the resonance and since the drop port is the only pathway for the optical energy to escape the ring resonator (with the exception of intrinsic losses), all of the resonant light will wind up being coupled into the drop port.

For non-resonant wavelength channels, the light that couples into the ring resonator and propagates around the ring will interfere *destructively* with the light that is currently coupling into the ring and *constructively* with the light that has remained in the through waveguide. In this way, the non-resonant wavelengths are transmitted to the through port experiencing essentially no effect due to the presence of the ring resonator.

The wavelengths that resonate in a particular ring resonator are determined by the ring's radius r , and refractive index n , according to

$$\lambda = \frac{2\pi r n}{N}, \quad (2.1)$$

where λ is a resonant wavelength, and N is an integer value. Equation 2.1 is a result of calculating the distance required for the resonant wavelengths to constructively interfere after propagating around the ring.

The free spectral range (FSR) of a resonator is the spectral distance between two resonant wavelengths and is calculated according to

$$\text{FSR} = \frac{2\pi rn}{N(N+1)}. \quad (2.2)$$

Ideally, the FSR of the resonator should equal or exceed the spectral band of interest so that only one resonant wavelength resides in the spectral band of interest.

To increase the FSR of a ring resonator, the radius of the ring must be decreased. However, as the radius of the ring resonator decreases the curvature of the ring increases which increases the bend loss from the ring waveguides. When a waveguide is bent, there is a certain amount of light lost depending on the sharpness of the bend. To reduce bend losses, the optical index contrast between the waveguide core and cladding material can be increased. Higher index contrasts creates strong total internal reflection (TIR) inside the waveguide which more tightly confines the light and reduces bending loss.

The amount loss in the ring resonator is critical in that it determines the quality factor of the resonator. The quality factor is defined as

$$Q_{\text{opt}} = 2\pi \frac{\text{Total energy stored in resonator}}{\text{Energy lost per roundtrip}}. \quad (2.3)$$

Although the desired quality factor for a particular resonator filter depends on the specific filtering application, usually a higher quality factor is more desirable. The loss in the ring is a combination of the bending losses, intrinsic material loss (absorption), scattering loss due to waveguide surface roughness. The coupling of the light from the ring resonator to the bus waveguides (input/through and drop ports) is also considered a "loss" for calculating the quality factor of the ring resonator. Strong coupling between the ring resonator and the bus waveguides will decrease the quality factor of the ring resonator, while weak coupling will increase the quality factor.

The key design parameters for optical ring resonators include the waveguide and cladding materials, the radius of the ring resonator, the cross-sectional shape of the waveguides, the amount of coupling between the bus waveguides and the ring res-

onator, and the number of cascaded ring resonators. The waveguide and cladding materials are used to determine the index contrast and the material losses of the ring resonator. The radius and index of the core determines the resonant wavelengths and the FSR. The index contrast and the radius determine the bending losses.

The waveguide shape determines whether the waveguide is single-mode or multi-mode, and also if the waveguide is polarization sensitive [73]. To limit the effects of dispersion and to improve the performance of the ring resonator (decrease optical losses), single mode waveguides are normally used. Because the waveguides have rectangular cross-sections (due to constraints of microfabrication), rather than round cross-sections like optical fibers, the waveguides are polarization sensitive. Nevertheless, optical telecommunications systems require that the performance be insensitive to polarization, even for randomly polarized light entering the system through the input fiber. Therefore, the incoming light needs to be converted to the polarization state which is optimal for the designed waveguides. One possible way of achieving the conversion of the polarization of the incoming light is described in [144].

The strength of the coupling between the ring resonator and the waveguides affects the quality factor of the device and therefore the bandwidth of the filter. The two dimensional parameters affecting the coupling are the gap between the ring and the bus waveguides and the radius of the ring resonator. Ring resonators with larger radii have longer coupling lengths than ring resonators with smaller radii. This means that for a fixed amount of coupling, a smaller ring will need to be closer to the bus waveguides than a larger ring.

The filter shape provided by the ring resonator can be modified by cascading several ring resonator filters together. In this way, filters with flat tops and sharp roll-off can be designed [55]. These are desirable for preserving the quality of transmitted information in high-bandwidth channels (10GHz and above). The number of rings used does not significantly affect the switch design since the MEMS bridge structure can be easily modified to switch any number of rings cascaded together.

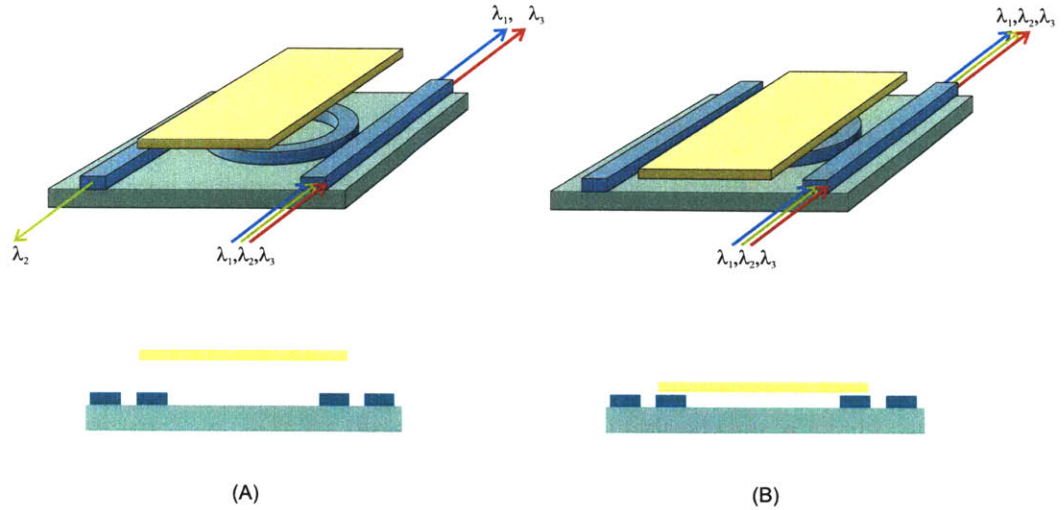


Figure 2-2: Schematic representation of an optical ring resonator filter switch showing its (A) resonant behavior with the lossy material membrane up and (B) its non-resonant behavior with the lossy material membrane down.

2.2 MEMS optical ring resonator switch description

Figure 2.2 shows a schematic drawing of how the optical ring resonator switch operates. The switch is composed of a standard optical ring resonator filter with a lossy material membrane suspended above it. When the lossy material is up and away from the ring resonator, the ring resonator is unaffected by the material and behaves in its standard static fashion. When the lossy material is brought down on top of the ring resonator, the optical resonance is killed due to optical loss (damping). Without the benefit of the resonance in the ring, the formerly resonant wavelengths of light are no longer able to couple from the input waveguide to the drop waveguide. Thus, by controlling the position of the lossy material membrane, the resonant wavelength can be switched between the drop waveguide and the through waveguide.

The lossy material membrane is controlled by a MEMS parallel plate electrostatic actuator. MEMS parallel plate actuators are often used as switching structures because of the pull-in effect resulting from the nonlinearities of the system [4,67,99,111]. Pull-in is the term used to describe a phenomena where the movable plate of the elec-

trostatic actuator snaps down to the fixed plate when the displacement of the movable plate is roughly a third of the original gap between the plates [125]. Pull-in gives a binary, switch-like, operation to parallel plate actuators.

2.3 Design requirements

While the primary goal of this work is to prove the concept of MEMS based ring resonator optical switching, it is important to look forward to the requirements of a product based on this kind of device.

This device is intended to be used in integrated optical circuits for a variety of applications. To be useful as part of an integrated circuit, the switch needs to meet certain requirements. Different applications would have different operating requirements. This list of requirements is based on using these devices as part of IOCs for telecommunications networks. The requirements are:

- IC level voltage operation (~ 5 volts)
- CMOS compatible fabrication
- Switching time of less than one microsecond
- Insertion loss of less than 1-2dB per switch
- Switch footprint should be less than $100\mu\text{m} \times 30\mu\text{m}$
- Heat generation of less than 1mW per switch
- Temperature range of operation -25°C to 85°C
- Operating lifetime of ten to twenty years.

The switch is intended to be integrated together with standard CMOS circuitry as well as optical circuitry. For this reason, the switch should operate at IC level voltages (~ 5 volts). The switch will also need to be compatible with CMOS fabrication.

Table 2.1: Switching speed requirements for different applications within optical networking [110].

Application	Switching Time Required
Lightpath Provisioning	1-10 ms
Protection Switching	1-10 μ s
Packet Switching	1-10 ns
Modulation	1-10 ps

For different applications in optical networking, different switching speeds are required. Table 2.1 gives some switching speed requirements for different applications that come out of optical networking standards [110, 116]. With a switching speed of one microsecond, the switch will be suitable for both lightpath provisioning and protection switching.

It is expected that in an IOC, many of these switches would be cascaded together in typical circuit style. For this to be possible, the switches are required to have very low optical losses. While the specific loss requirement depends on the particular application and the number of switches in the circuit, a good assumption is that the losses need to be less than 1-2dB per switch.

A additional requirement resulting from the switch being integrated together with a number of elements, and because of the cost benefit of small devices in microfabrication, the size of the switch should be minimized [116].

A related integration issue is the amount of energy that is dissipated as heat from the device. For the device to be successfully integrated with a number of devices, the heat production of each device needs to be low, less than 1mW. If too much heat is produced, the microring resonators resonant frequencies will drift from the desired resonance.

To be used in optical networking, these devices will need to withstand a wide range of environments. For this reason, the temperature range of operation of the

switch should be large³.

Finally, the lifetime of the switch needs to be adequate for the particular application. For some consumer applications, the lifetime may be only three to five years. For commercial applications, such as in optical communication networks, the lifetime requirement may be anywhere from ten to twenty years [116].

2.4 MEMS parallel plate electrostatic actuation

There are a number of actuation techniques currently used in MEMS devices . They include piezoelectric, thermal, shape-memory, magnetic, and electrostatic [125]. The characteristics of these actuation techniques are widely varied. Depending on the particular application, one actuation technique is often preferable over others. For the ring resonator switch, electrostatic actuation is the best candidate based on actuation speed, CMOS compatibility, and actuation energy.

Actuation speed is a key requirement of the wavelength selective switch. Of all the actuation techniques available, parallel plate actuators have proven to be the fastest for this type of switching device [111].

Parallel plate actuators can very easily meet the CMOS compatibility requirement. Piezoelectric, shape-memory, and magnetic actuation all use non-CMOS compatible materials.

Additional advantages that electrostatic actuation has over thermal, magnetic, and shape-memory actuation is that the energy required for switching is several orders of magnitude less and that no additional energy is needed to maintain the switch in the switched state. This is not true of thermal and magnetic actuators. Because very little energy is dissipated by the electrostatic device, the thermal load on the overall system that comes from the switch is very low. This is an important consideration when integrating a number of these devices together in a circuit to implement crossbar

³The temperature range is limited more by the ring resonator's sensitivity to temperature than that of the MEMS device. To maintain a consistent resonant wavelength, the ring resonator will need to be maintained at a rather narrow temperature range. To achieve the requirement of a large temperature operation range means that some active packaging will be required to maintain the proper operating temperature for the device.

switching, for example.

The actuation voltage also needs to be low for integration with standard CMOS circuitry. This tends to be difficult for electrostatic actuation where a high pull-in voltage is usually required for parallel plate actuators. In spite of this, some parallel plate devices have been demonstrated that require voltages as low as 6 volts [107]. However, the low actuation voltage comes at the price of slow switching speeds and reliability concerns.

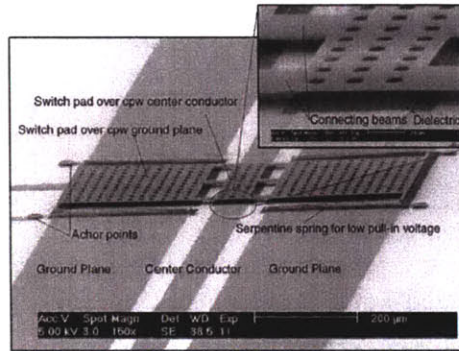
MEMS parallel plate actuators consist of a fixed electrode or plate, a movable plate, and a suspension system that holds the movable plate over the fixed plate. When a voltage difference is applied between the two plates, the plates act as a capacitor, with each plate taking on an opposite signed charge. The charges on the two plates exert an electrostatic force that tends to pull the two plates together. The electrostatic force is resisted by the stiffness of the suspension system. Figure 2-3 shows some images of some MEMS parallel plate actuators used in RF MEMS switches [15, 92, 107, 112].

Parallel plate actuators are often modelled as a mass (the movable plate), damper, and spring (the suspension system) over a fixed plate, as in Figure 2.4. For actuation, a voltage source is connected between the two plates. The equation of motion that is derived from this lumped parameter model is

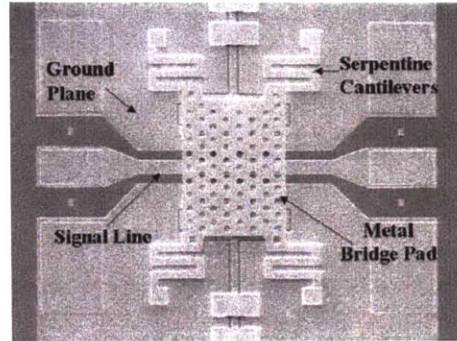
$$m\ddot{x} + b\dot{x} + kx = \frac{\epsilon_0 AV^2}{2(d_0 - x)^2}, \quad (2.4)$$

where x is the displacement of the movable plate, m is the mass of the movable plate, b is the damping coefficient, k is the spring constant of the suspension system, A is the overlap area of the fixed and movable electrodes, V is the voltage applied across the plates, ϵ_0 is the permittivity of air, and d_0 is the initial effective gap between the fixed and movable electrodes.

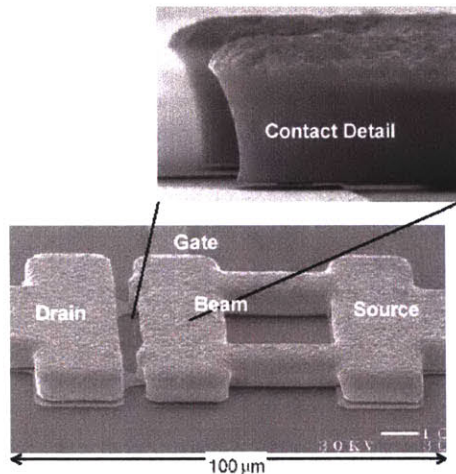
The effective gap d_0 is a combination of the air gap d_a and the effective thickness of the dielectric material that maintains electrical isolation between the plates. The



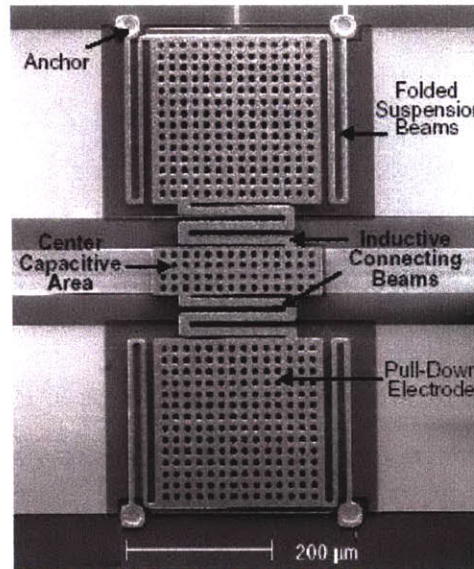
(A)



(B)



(C)



(D)

Figure 2-3: RF MEMS switches using electrostatic parallel plate actuators. A) was developed at the University of Michigan [107]. B) was developed at the University of Illinois [15]. C) was developed at Northeastern University and Analog Devices and is currently licensed to Radant MEMS [92]. D) was also developed at the University of Michigan [112].

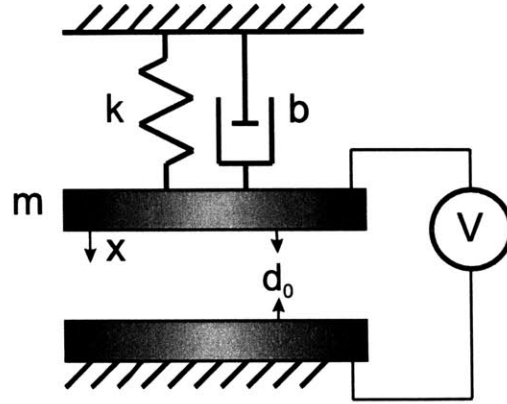


Figure 2-4: Simplified lumped parameter model of a parallel plate electrostatic actuator.

effective gap is thus

$$d_0 = d_a + \frac{t_d}{\epsilon_d}, \quad (2.5)$$

where t_d is the actual thickness of the dielectric material, and ϵ_d is the relative permittivity of the dielectric material.

Because of the nonlinear nature of Equation 2.4, quasi-static conditions ($\ddot{x} \approx \dot{x} \approx 0$) are usually assumed to simplify the equation and provide some insight into the system. This approximation gives

$$kx = \frac{\epsilon_0 AV^2}{2(d_0 - x)^2}. \quad (2.6)$$

Solving for the applied voltage gives

$$V = \sqrt{\frac{2kx}{\epsilon_0 A}}(d_0 - x), \quad (2.7)$$

which provides the equilibrium curve of voltage versus displacement shown in Figure 2-5.

In the domain $0 < x < d_0$, Equation 2.7 has a maximum that occurs at $x = d_0/3$. This is often referred to as the pull-in position. The equilibrium voltage associated with this point is called the pull-in voltage, since application of higher voltages will cause the system to experience a bifurcation to an equilibrium point located at $x > d_0$. Of course, this jump cannot be fully realized due to the fixed electrode and dielectric

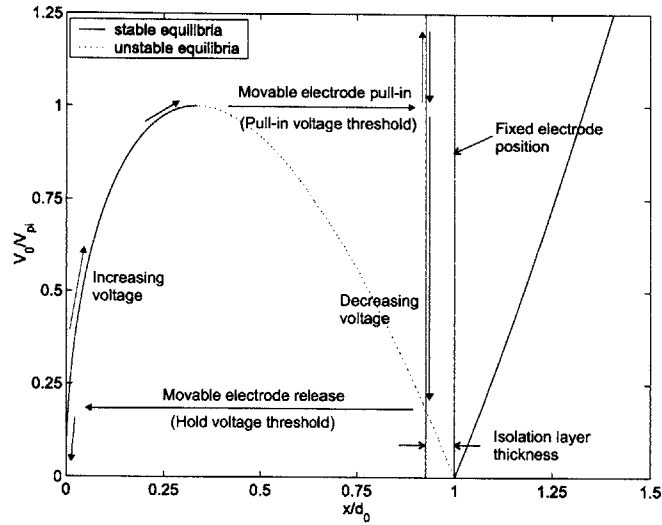


Figure 2-5: Quasi-static equilibrium curve for the parallel plate actuator from Equation 2.7. The arrows indicating the evolution of the equilibrium positions for increasing and decreasing voltage illustrate the bifurcation in the system. When the pull-in voltage is reached, the movable plate tries to jump to the equilibrium position to the right of the fixed electrode position. The isolation layer between the two electrodes will, of course, limit the plate's displacement so it won't reach the theoretical equilibrium position. The thickness of the isolation layer determines the voltage required to maintain the movable plate in the pulled-in state, referred to as the "hold" voltage [22].

layer; instead, the moving electrode is jumps to and is held at the dielectric layer. Figure 2-5 illustrates the “pull-in” bifurcation experienced by parallel plate actuators. The pull-in voltage is found to be

$$V_{\text{pi}} = \sqrt{\frac{8kd_0^3}{27\epsilon_0 A}}. \quad (2.8)$$

The minimum voltage to hold the moving electrode in the pulled-in state is called the hold voltage and is

$$V_h = \sqrt{\frac{2k \left(d_0 - \frac{t_d}{\epsilon_d} \right) t_d}{\epsilon_0 A \epsilon_d}}. \quad (2.9)$$

As with any model, there are a number of assumptions associated with this model. These assumptions are discussed in detail in Section 6.1.

In designing a MEMS parallel plate electrostatic actuator, the main parameters that can be varied are the stiffness, k , and the overlap area, A . The initial gap, d_0 , is usually fixed by the particular application of the device (as is the case for the integrated wavelength selective switch).

2.5 Switch Design

The design of the wavelength selective switch consisted of the optical design of the ring resonator filter and the electro-mechanical design of the MEMS structure to be integrated together with the ring resonator. The goal of the device design described in this section is to first of all demonstrate MEMS switching of a ring resonator filter. Secondly, an effort will be made to meet, or at least approach, the design requirements discussed in Section 2.3.

2.5.1 Optical Design

One of the compelling characteristics of this MEMS-based approach to ring resonator switching is that it is applicable to virtually all of the many ring resonator filter designs that have been proposed, including the higher order filter designs [24, 25, 55, 86]. For

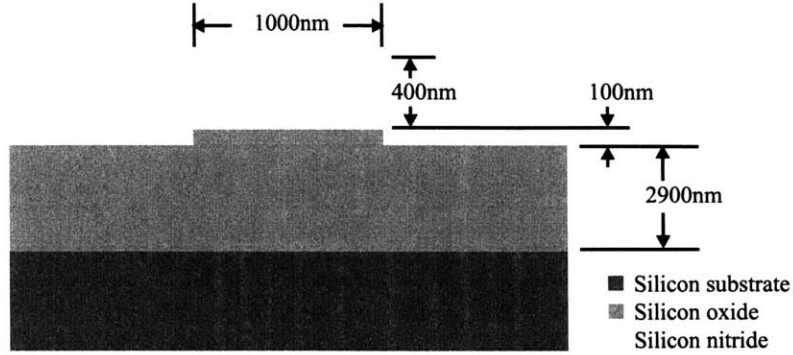


Figure 2-6: Schematic drawing of the cross-sectional view of the waveguides. (Note, drawing not to scale.)

Table 2.2: Dimensions of the optical ring resonator that was integrated into the wavelength selective switch devices.

Outside Diameter (μm)	28.96
Inside Diameter (μm)	26.94
Gap (nm)	185

this reason, and since the goal of this work is to experimentally demonstrate loss based switching of a ring resonator filter, the actual performance of the filter, in terms of bandwidth and filter shape is somewhat arbitrary. A simple single ring resonator design was used to create the prototype wavelength selective switch.

The ring resonator and bus waveguides were composed of a core material of silicon-rich silicon nitride, with an index of 2.0. The cladding was silicon oxide (index 1.44) on the bottom, and air cladding on the top and sides (index 1.0). The dimensions of the waveguide cross-section are shown in Figure 2-6.

The inside and outside diameter of the ring and the gap between the ring and the bus waveguides is given in Table 2.2.

As mentioned before, the ring resonator design does not strongly effect the MEMS design. There is, however, one exception; the required separation between the lossy material membrane and the ring resonator must be chosen so as to not induce loss

in the ring resonator. This distance is primarily a function of the material system of the ring. The index of the lossy material also has a secondary effect on the required separation. For the silicon nitride/silicon oxide material system used for the ring resonators in this prototype, the initial gap needs to be at least $1.1 \mu\text{m}$ for an aluminum bridge [145]. Aluminum was selected as the lossy material for the prototype switch.

2.5.2 Electro-mechanical Design

There are a number of considerations in designing the MEMS structure for the switch. They are:

- There needs to be a membrane of optically lossy material that covers the ring resonator
- There needs to be a suspending structure that provides the proper elastic stiffness for the system
- There needs to be adequate overlap area between the top movable electrode and the fixed bottom electrode for actuation
- The input, through, and drop waveguides need to be kept away from the lossy material comprising the MEMS device.

The optically lossy material membrane is simple to construct in this case because the suspended electrode, or bridge, is itself constructed of a conductive material, which, in almost all cases, means the material is also optically lossy. This allows the bridge to act both as the suspended electrode for the actuator and the optically lossy material membrane used to switch the optical ring resonator. This significantly simplifies the design and fabrication of the device.

A very simple MEMS bridge structure that allows integration with ring resonator filters is shown in Figure 2-7. The bridge uses one conformal film deposition step to define the suspended bridge as well as the anchors that attach the bridge to the silicon oxide layer. The silicon substrate acts as the bottom fixed electrode.

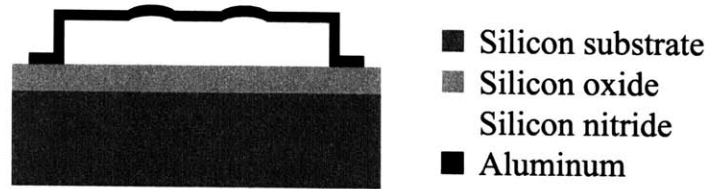


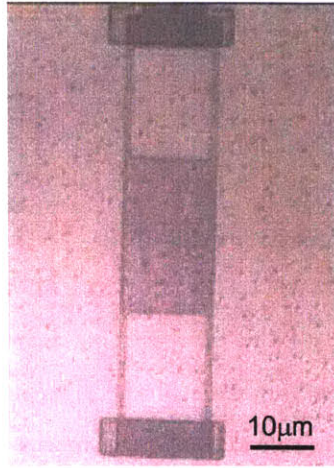
Figure 2-7: Schematic drawing of the side view of the wavelength-selective MEMS switch structure. (Note drawing not to scale.)

In designing the bridge, the two key characteristics that we have control over are the mechanical stiffness of the structure and the overlap area of the top and bottom electrodes. Because of the dimensional constraints imposed by the waveguide structures, the primary dimensions that can be controlled to vary the stiffness and overlap area are the length and the thickness of the bridge. One possible way to decrease the stiffness without increasing the overlap area of the structure is to use thin flexures to suspend the membrane over the ring resonator. The overall stiffness of the bridge actuator in this case is a combination of the stiffness of the plate and the flexures that suspend the plate.

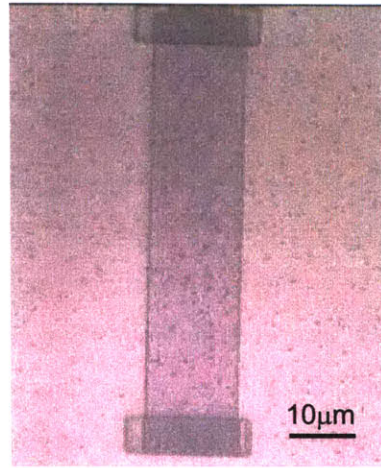
To develop insight into the design and fabrication of MEMS bridge structures, a wide range of prototype bridge structures were designed and fabricated. Figure 2-8 shows images of some of the prototypes. The bridge structures covered a wide range of designs. Straight flexure, serpentine flexure, and solid (no flexure) design concepts were all explored. Within each of the different flexure designs, widths were varied from $8\ \mu\text{m}$ to $30\ \mu\text{m}$ and lengths were varied from $30\ \mu\text{m}$ to $150\ \mu\text{m}$. These bridge prototype designs were analyzed using finite element analysis⁴. The theoretical range of the pull-in values for these prototype bridges extended from about 3V up to more than 80V.

In characterizing the fabricated prototype bridges, it was found that the bridge structures with flexures (both serpentine and straight) were more susceptible to the effects of residual stress. The solid (no flexure) bridge structures tended to be flatter and straighter. In addition, for the solid bridges, it was found that the wide structures tended to amplify the effects of residual stress gradients (i.e. by bending up or down

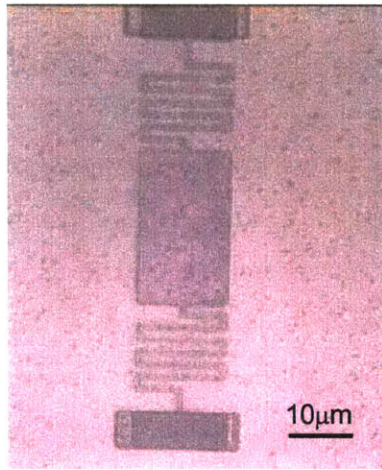
⁴Finite element analysis was performed using the Coventorware MEMS analysis software package.



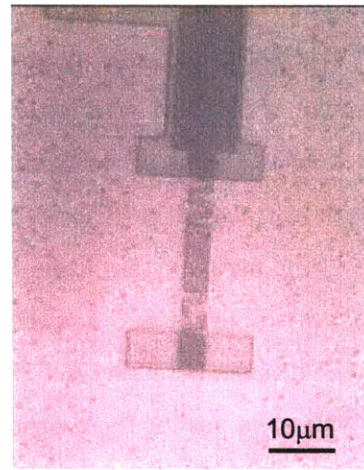
(A)



(B)



(C)



(D)

Figure 2-8: Optical micrographs of prototype bridges that were fabricated to evaluate different design concepts.

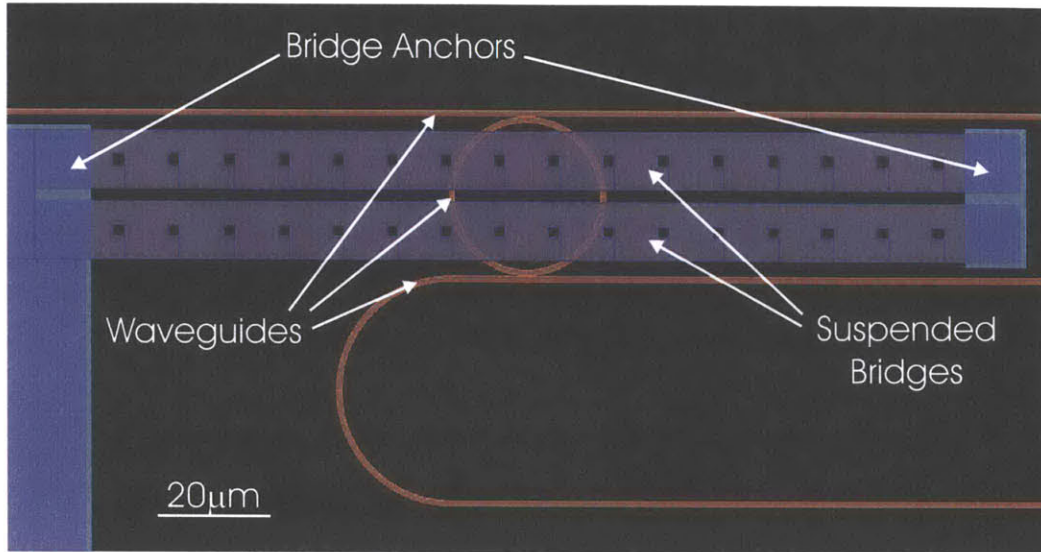


Figure 2-9: CAD image of the layout of the device showing the optical waveguides and the MEMS bridge structure.

at the free edges).

Taking into account the lessons learned from the prototype bridge structures, the bridge structure to be integrated with the optical ring resonator was designed to be tolerant to some amount of residual stress. In addition, while the eventual goal of this project is to create an optical switch that utilizes integrated circuit level voltages, it was decided based on the results of the initial prototype bridge structures that in the first demonstration prototype, a higher actuation voltage would create a device that would be more robust relative to process variations. For this reason, an actuation voltage of between 12 and 15 volts was targeted in the design. The final bridge structure design for the wavelength selective switch prototype is shown in Figure 2-9.

The bridge structure over the top of the ring resonator was designed as two separate bridges. This technique was employed to minimize the width of the bridges and thus minimize the effect of residual stress gradients. Also, in this design, no flexures were used. This choice was also motivated by the desire to minimize the effects of residual stresses in the bridge material.

Figure 2-9 shows that etch holes were included in the bridge design. The bridge structure is quite narrow and would allow a very quick release etch, even without the

etch holes. The etch holes were included to minimize the exposure time of the silicon nitride waveguides to the release etchant (xenon difluoride). In etch selectivity tests performed on silicon and silicon-rich silicon nitride, it was found that the selectivity of xenon difluoride to silicon nitride versus the polysilicon sacrificial material was 1:550. While this is very good selectivity, the exposed surfaces of the waveguides would still have been etched by as much as 20nm without the use of etch holes, which was unacceptable. By introducing the etch holes, the etching of the waveguides is kept to under 10nm.

The bridge structure has a length of $160\mu\text{m}$, a width of $10.5\mu\text{m}$, and a thickness of $0.35\mu\text{m}$. There are 16 etch holes in the bridge that are each $2\mu\text{m} \times 2\mu\text{m}$. The gap between the bridge and the substrate (which acts as the fixed electrode) is $1.1\mu\text{m}$ of air and $3\mu\text{m}$ of silicon oxide. This is the same as an effective gap of $2.6\mu\text{m}$ of air for the electrostatic actuation calculations, due to the differences in permittivity of air and silicon oxide.

2.5.3 Performance analysis

The response of the bridge structure to an applied voltage is rather complex for a number of reasons. For instance, the stepped-up anchors used in the design of the bridge do not match typical end conditions used in analytical beam analysis. The etch holes in the bridge also create a more complex mechanical response than a solid bridge [109]. Finally, the effects of residual stress on the bridge structure are significant. Finite element analysis is the only option that allows these effects on the electromechanical response of the bridge to be modelled. The structure was therefore modelled and analyzed using the finite element tools in the Coventorware package. From this analysis, the resonant frequency f_n , generalized mass m , pull-in voltage V_{pi} , pull-in displacement, and maximum Mises stress⁵ were all calculated.

The finite element model utilized 692 quadratic hexahedral elements. The mesh was highly refined at the bridge anchors, which experience the largest values of stress

⁵Mises stress is a yield criterion comprised of all the components of stress. If the Mises stress exceeds the yield stress of the material, plastic deformation will result.

and strain and therefore require the highest mesh refinement.

By combining the results of the finite element response with an analytical estimate of the damping of the structure, analytical predictions of the damped dynamic response of the structure were found.

The dynamic response of the switch is complex due to the nonlinearity of the electrostatic actuation. An estimate of the pull-in time, t_{pi} , upon the application of the actuation voltage is given by the equation [112]

$$t_{pi} \approx 3.67 \frac{V_{pi}}{V f_n}. \quad (2.10)$$

A value of 1.2 was used for the ratio V/V_{pi} for the calculation of the pull-in time. Typically, electrostatic actuators are operated at 1.1 to 1.3 times the pull-in voltage [111].

The rise time was calculated using standard second-order system response techniques [103]. This is because, upon the removal of the actuation voltage, the system behaves essentially like a second order system. It should be noted that the squeeze film damping effect present in the system does add some nonlinearities.

The first step in determining the response of a second order system is determining if the system is underdamped, overdamped, or critically damped. To determine this, an estimate of the damping present in the system is needed. For this device, the damping will be dominated by the squeeze film effects of the air trapped between the bridge and the substrate. A rough estimate of the damping resulting from the squeeze film effect can be found in [125] which gives the damping constant, b , as

$$b = \frac{96\mu L W_e^3}{\pi^4 d_a^3}, \quad (2.11)$$

where μ is the viscosity of the fluid, L is the length of the bridge, and d_a is the air gap beneath the bridge. W_e is the distance the air molecules need to travel to get out from under the bridge. Because of the presence of the etch holes, the value used for W_e in this calculation is $5\mu\text{m}$. (The viscosity of air is given in Table A.6 in Appendix A.)

Equation 2.11 is derived assuming small displacements of the suspended bridge, which is not the case when the bridge is pulled-in or when it releases. For this reason, this is only a rough estimate of the damping of the system and should be treated as such. In reality, the effects of the squeezed-film damping are nonlinear in nature and require computational fluid dynamic techniques for a proper large displacement analysis.

With the damping constant calculated from Equation 2.11 and the system values obtained from the finite element analysis, the damping ratio is found by

$$\zeta = \frac{b}{2\omega_n m}. \quad (2.12)$$

This value of ζ obtained indicates that the system is underdamped. For an underdamped second order system, the rise time t_r is

$$t_r = \frac{\pi - \arccos \zeta}{\omega_d}, \quad (2.13)$$

where the damped natural frequency ω_d is

$$\omega_d = \omega_n \sqrt{1 - \zeta^2}. \quad (2.14)$$

One other system parameter of interest is the mechanical quality factor, Q , of the system. The quality factor is calculated as

$$Q = \frac{m\omega_n}{b}. \quad (2.15)$$

Table 2.3 summarizes the results of the finite element and analytical analysis of the bridge design. The results are compared with the design requirements as well as the fabricated prototype test results discussed in 4.

Table 2.3: Results of the electromechanical analysis of the bridge structure design compared with the design requirements and the actual experimental results of the fabricated switch prototypes.

Parameter	Required	Design	Actual
Pull-in Voltage V_{pi} (V)	5	12.8	24
Pull-in Displacement (μm)	1.1	1.1	0.34
Resonant Frequency f_n (kHz)	NS	69.9	NM
Switching Time t_{pi} (μs)	1.0	7.0	60*
Switching Time t_r (μs)	1.0	5.5	16*
Damping Constant b (N·s/m)	NS	2.64×10^{-7}	NM
Generalized Mass m (kg)	NS	6.08×10^{-13}	NM
Damped Natural Frequency f_d (kHz)	NS	60.8	NM
Damping Ratio ζ	NS	0.5	NM
Mechanical Quality Factor Q	NS	1.0	NM

NS - Not specified.

NM - Not measured.

* Test equipment limited. Faster equipment should allow faster switching.

2.6 Reliability

The wavelength selective switch needs to be highly reliable to be appropriate for use in fiber optic networks. The requirement would be for the product to work reliably over a period of ten to twenty years with potentially billions of switching cycles. This has been an area of intense research for parallel plate electrostatic MEMS devices. RF MEMS switches based on parallel plate actuators in particular have been put through rigorous reliability tests with mixed results.

There are a number of reasons for failure of switching devices utilizing parallel plate electrostatic actuation. The two main failure mechanisms are stiction [9, 137] and dielectric charging [15, 151]. Both failure mechanisms are of concern for the wavelength selective switch presented here.

2.6.1 Stiction

Stiction in parallel plate actuators occurs when the moving electrode becomes stuck in the pulled-in position with no voltage applied [9, 137]. This is a result of the mechanical stiffness of the structure being insufficient to overcome the adhesion forces of the surfaces in contact. There are a number of techniques to minimize the effects of stiction. The most obvious is to increase the stiffness of the system. Another method is reducing the surface area of contact, which reduces the overall surface adhesion force. A third technique is using contact surfaces with low surface adhesion energy. This can be achieved by coating the contact surfaces with thin layers of materials with low surface adhesion energy, such as teflon.

The natural approach for our switch is to reduce the contact area. The bridge only needs to come into contact with the ring resonator, which has a very small surface area compared to the parallel plate actuator. This method requires the planarization of the sacrificial layer, which was not done in the initial prototype but is straightforward to do in subsequent devices.

2.6.2 Dielectric charging

Dielectric charging describes a situation where the dielectric material separating the two plates of the parallel plate actuator accumulates charges [151]. Because the material is a dielectric, the charges are trapped and cannot move or dissipate. The field that these trapped charges creates can affect the performance of the electrostatic actuator. Effects of dielectric charging include an increased actuation voltage, slower switching speeds, failure to actuate, or holding the structure in a pulled-in state.

The best way to remove this failure mechanism is to reduce the amount of dielectric material between the plates [15]. Another option is to heat up the dielectric material, which tends to allow the charges in the dielectric to disperse. Yet another technique is to reduce the electric field that the dielectric material experiences. This decreases the charging effect but usually involves lowering the mechanical stiffness of the system which can then lead to problems with stiction.

In the case of the wavelength selective switch, the ring resonator is used as a mechanical stop, therefore, there is no need for additional dielectric material between the two parallel plates. This should allow significant improvements in reliability relative to dielectric charging [15].

Chapter 3

Optical ring resonator MEMS switch fabrication

In MEMS, the design of the device is strongly coupled with the fabrication process. In Chapter 2, the design of the wavelength-selective integrated optical switch was described, and an analysis of its predicted performance was given. In this chapter the design and implementation of the fabrication process for the Optical ring resonator MEMS switch is described.

3.1 Fabrication Process Design

The fabrication process of the switch consists of two distinct parts. The fabrication of the waveguides and ring resonators, and the fabrication of the MEMS structure. This further indicates the ability of the MEMS structure to be integrated together with a wide range of ring resonator devices to produce a wide range of wavelength selective switches.

The fabrication process of the waveguides and ring resonators is shown in Figure 3.1. For the ring resonator devices that were integrated with the MEMS structure, steps (A) and (B) in Figure 3.1 were done in MIT's Microsystems Technology Laboratories (MTL). Step (C) was done at Pirelli Labs in Milan, Italy. Other preliminary test rings were fabricated completely at MIT (see Figure 3-2). For these rings the

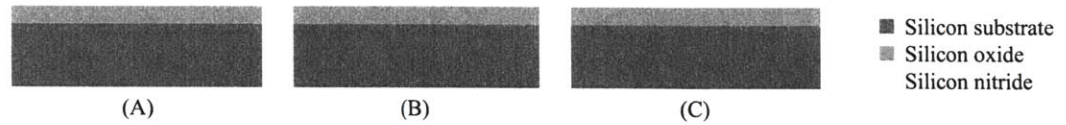


Figure 3-1: Cross-section illustration of the fabrication process of the waveguides and ring resonators. (A) $3 \mu\text{m}$ of low-temperature oxide (LTO) was deposited for the bottom side cladding. (B) $0.33 \mu\text{m}$ of silicon rich silicon nitride was deposited for the waveguide core material. (C) The silicon nitride was patterned and etched using e-beam direct-write lithography and reactive ion etching (RIE).

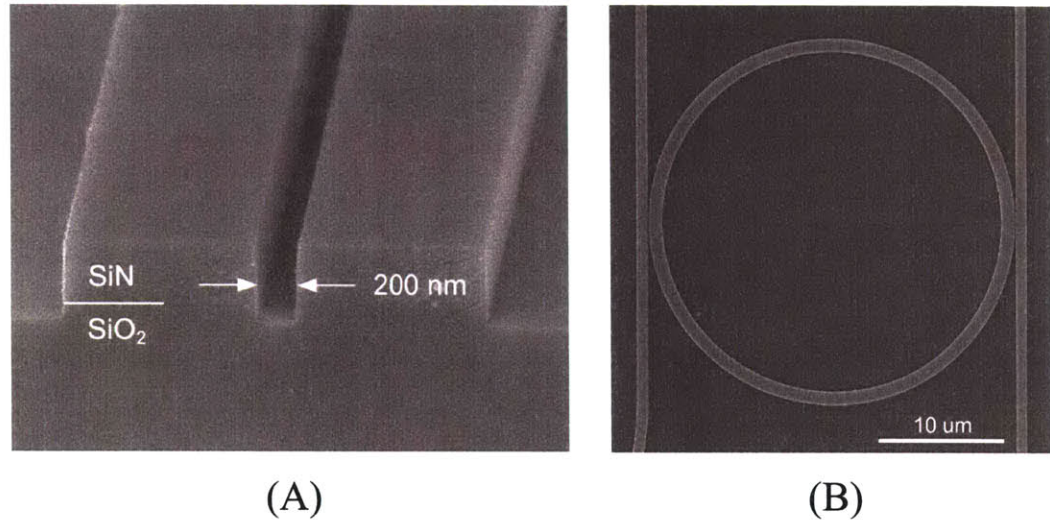


Figure 3-2: Image from a ring resonator device fabricated using the process described in Figure 3.1. This device was completely fabricated at MIT and is the work of T. Barwicz [6]

film depositions were done in MTL while the lithography and etching was done in MIT's Nano-Systems Laboratory (NSL).

Figure 3-2 is an image of a ring resonator fabricated at MIT using the process described in Figure 3.1. The fabrication of the ring resonators was not part of this thesis project. For more details on this fabrication process see [6].

The fabrication process for the MEMS structure is shown in Figure 3-3. The entire process flow is described in detail in Table 3.1.

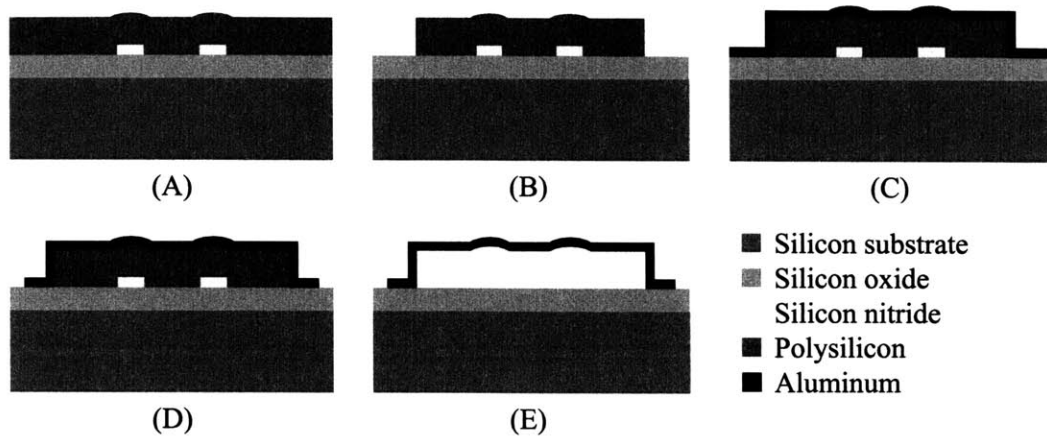


Figure 3-3: Fabrication process for the MEMS structure. (A) the poly-silicon sacrificial layer is deposited using low-pressure chemical vapor deposition (LPCVD). (B) the poly-silicon is patterned and etched using contact photolithography and reactive ion etching (RIE). (C) the bridge material (aluminum) is deposited by sputtering. (D) the aluminum is patterned and etched using contact photolithography and wet etching. (E) the structure is released by isotropically etching away the poly-silicon using a gas phase xenon difluoride etch.

Table 3.1: Process flow for the fabrication of the MEMS structures on top of the optical ring resonator structures. The process begins after the fabrication of the ring resonator structures.

Step	Machine	Process Notes
1	Wet station	RCA clean
2	Low-pressure diffusion tube	LPCVD deposition of $1.1 \mu\text{m}$ of polysilicon
3	HMDS oven	Vapor phase deposition of Hexamethyldisilazane (HMDS) (photoresist adhesion promoter)
4	Spin coater	Coat wafer with $1.3 \mu\text{m}$ of photoresist
5	Oven	Pre-bake photoresist for 30 min. at 90°C

continued on next page

Table 3.1: *continued*

Step	Machine	Process Notes
6	EV620 Aligner	Align mask and expose photoresist
7	Wet station	Develop photoresist
8	Oven	Post-bake photoresist for 30 min. at 120°C
9	Lam 490B	Reactive ion etch (RIE) polysilicon
10	Oxygen plasma asher	Strip photoresist
11	Wet station	Piranha clean and HF dip
12	Endura 5500	Sputter 350nm of Aluminum
13	HMDS oven	Vapor phase deposition of HMDS
14	Spin coater	Coat wafer with 1.0 μ m of photoresist
15	Oven	Pre-bake photoresist for 30 min. at 90°C
16	EV620 Aligner	Align mask and expose photoresist
17	Wet station	Develop photoresist
18	Oven	Post-bake photoresist for 30 min. at 120°C
19	Wet station	Etch aluminum with PAN etchant
20	Oxygen plasma asher	Strip photoresist
21	HMDS oven	Vapor phase deposition of HMDS
22	Spin coater	Coat wafer with 8 μ m of photoresist
23	Oven	Pre and post-bake photoresist for 90 min. at 90°C
24	Die saw	Cut through 80% of wafer <i>from backside</i>
25		Cleave through remaining wafer thickness
26	Solvent hood	Soak in acetone to remove photoresist
27	Solvent hood	Rinse with isopropyl
28	Xenon difluoride etcher	Release aluminum bridges with isotropic etch

continued on next page

Table 3.1: *continued*

Step	Machine	Process Notes
		of polysilicon

3.2 Fabrication details

While there are number of fairly standard microfabrication steps in the process shown in Table 3.1, there are a few steps that require some additional explanation about the motivation for the process and/or the process itself. These steps include the use of polysilicon as the sacrificial material, the material selection and process for the aluminum bridge structures, the release etch, the unique die-saw and cleave technique for dicing the wafer, and the subsequent packaging steps.

3.2.1 Sacrificial material

For suspended metal MEMS structures, it is very common to use some type of polymer as the sacrificial layer [111]. Polymers allow for low temperature processing which is important for integrating MEMS devices with optical and CMOS circuitry. For this reason, the use of polyimide as a sacrificial material was initially explored. However, the polyimide was found to be difficult to planarize. In addition, the high vacuum system used to sputter aluminum is incompatible with polymers. For these two reasons, polyimide was abandoned as the sacrificial material.

Amorphous silicon was next explored as a potential low-temperature sacrificial material. Some prototype bridge structures were fabricated using the amorphous silicon. Amorphous silicon was also subsequently abandoned, mostly due to machine contamination issues. The machine used to deposit the amorphous silicon is gold contaminated, which then bars the wafers from further processing in the CMOS machines in MTL. If this process were to be commercialized, low temperature deposition of the amorphous silicon would be a very appealing process for the sacrificial material.

To maintain CMOS compatibility in MIT's MTL, polysilicon deposited in a LPCVD tube was finally settled on as the sacrificial material. This has the disadvantage of being a rather high temperature process, which limits its ability to be included in an integrated process. However, for the demonstration prototype, this proved to be the best available option.

3.2.2 Release etch

In conjunction with the selection of silicon (poly or amorphous) as the sacrificial material came the selection of the release etch. The release etch needed to be an isotropic etch that, ideally, was a dry etch. A dry etch is desirable in that it avoids the stiction problems that are experienced with wet release etches. In addition, the etch needed to selectively etch silicon relative to the silicon oxide bottom cladding, the silicon nitride waveguide core, and the aluminum comprising the MEMS bridge structure. Finally, the machine used for the etch needed to accept metals (aluminum).

The etch that matched all of these constraints was determined to be a gas-phase xenon difluoride etch. The xenon difluoride is highly selective to all of the materials comprising the structure of the switch, etches silicon rapidly, and is a dry etch [91].

3.2.3 Lossy bridge material

The optically lossy bridge material was selected to be aluminum due to a couple of constraints. First, the preferred deposition technique was sputtering, which gives a fairly good conformal coating and is a low temperature process. Secondly, the material needed to be resistant to being etched by xenon difluoride.

In the machines and materials available at MTL, aluminum and titanium nitride both matched the conditions mentioned above. Aluminum was selected as the material for the prototype bridge based on aluminum having been used successfully in other MEMS devices [35].

3.2.4 Wafer dicing

The dicing of the wafer is a critical step in the wavelength selective switch process because the end facets of the waveguides need to come right to the edge of the chip and be optically flat. This can be accomplished by dicing the wafer using a typical die saw procedure and then polishing the edge of the chip until a nice flat end facet is achieved. For the MEMS process, this approach was not acceptable because the release of the MEMS devices could not occur before the polishing step (the bridges would have been destroyed by the polishing) and after the polishing step, the chips would not be allowed back into the fab for subsequent processing.

An alternative technique that relies on the brittle nature of the silicon nitride waveguides is to cleave the wafer and allow the fracture of the silicon nitride to produce a nice flat end facet for the waveguide. This would work quite well except that cleaving the wafer does not provide the necessary accuracy for the optical test chips.

To overcome these challenges, a combined die-saw and cleave process was used. This involved die sawing the wafer through 90% of the thickness from the backside of the wafer. To protect the devices on the frontside of the wafer, which is in contact with Kapton tape and the wafer chuck, a thick layer of photoresist was applied to the frontside of the wafer.

Once the wafer was die sawed, the wafer was very carefully removed from the Kapton tape and cleaved along the lines defined by the die saw. This technique produced very accurate cleaved surfaces that provided a fairly high yield (75%) of good quality waveguide end facets. With process refinement, higher yields are very likely possible.

3.2.5 Packaging

Two different packaging techniques were used for the device. One package was optimized for electromechanical testing with the Zygo profilometer system. This setup was used for measuring displacement with applied voltage, which required optical



Figure 3-4: Image of the packaged optical MEMS switches evaluated in the Zygo profilometer system.

access to the top of the device. Because the objective lens comes very close to the device, probes could not be used to apply the actuation voltage. For this reason, a simple test package was used with gold wire-bonds connecting the device bond-pads to the package connector pins. Figure 3-4 shows a packaged device that was tested in the Zygo profilometer.

For testing the optical performance of the device, access needed to be provided to the input and output edges of the chip where the end facets of the waveguides were located. In this case, the test package used in the Zygo profilometer was not acceptable. However, in the optical test setup, the top of the device was available for access by probes to allow the introduction of the control voltage. The chip was mounted to a small pedestal that was inserted into the optical test set-up. The chip substrate was grounded to the pedestal while the control voltage was applied through probes, as shown in Figure 3-5. This technique allowed the necessary introduction of the actuation voltage as well as maintained the optical pathway to the edge of the device to couple the light into and out of the waveguides.

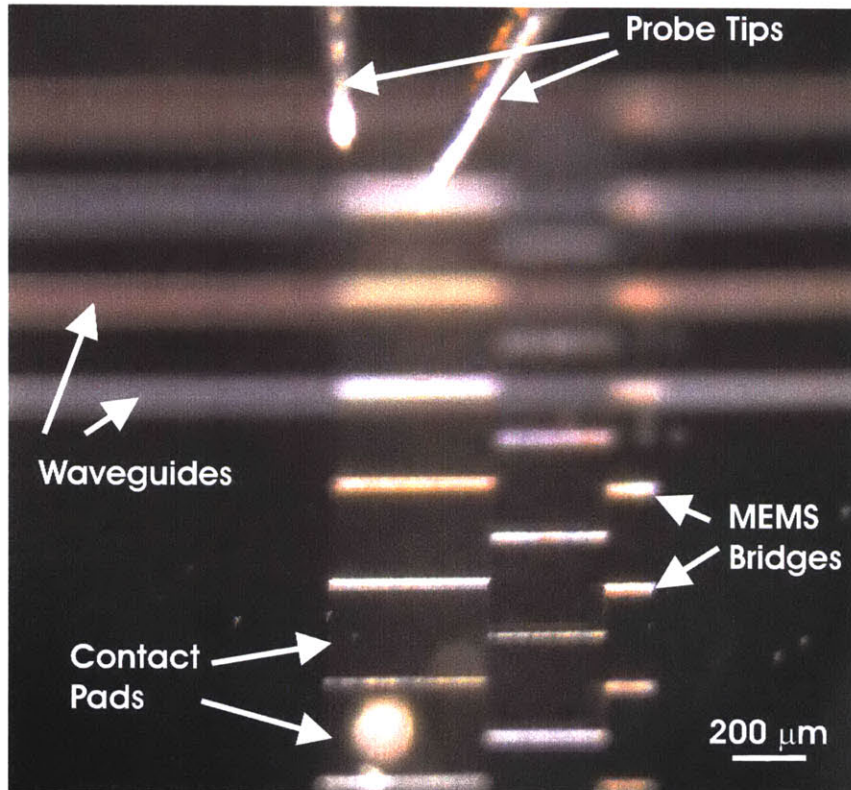


Figure 3-5: Picture of a die with an array of MEMS bridges. The probe tips can be seen in contact with one of the contact pads for the optical switch devices.

Chapter 4

Optical ring resonator MEMS switch fabrication results and testing

After fabrication, the devices were subjected to a series of mechanical and optical tests. Some of these tests were metrological to determine how well the fabricated devices matched the design. Other tests evaluated electro-mechanical performance of the device and the actual optical switching performance. This chapter reports on the results of these tests. In addition, further modelling of the performance of the device is provided based on information extracted from the experimental testing.

4.1 Fabrication results

The MEMS structures resulting from the fabrication process were analyzed using an optical microscope, a white light Zygo interferometer, and an scanning electron microscope (SEM). The results of this analysis indicated that the structures were affected by lithographic resolution, residual stress, surface roughness, mask alignment, and over-etching. The effects of these issues caused deviations from both the designed geometry as well as from the expected optical performance. Nevertheless, the switch functioned and thus demonstrated the first-ever switching on and off of an integrated

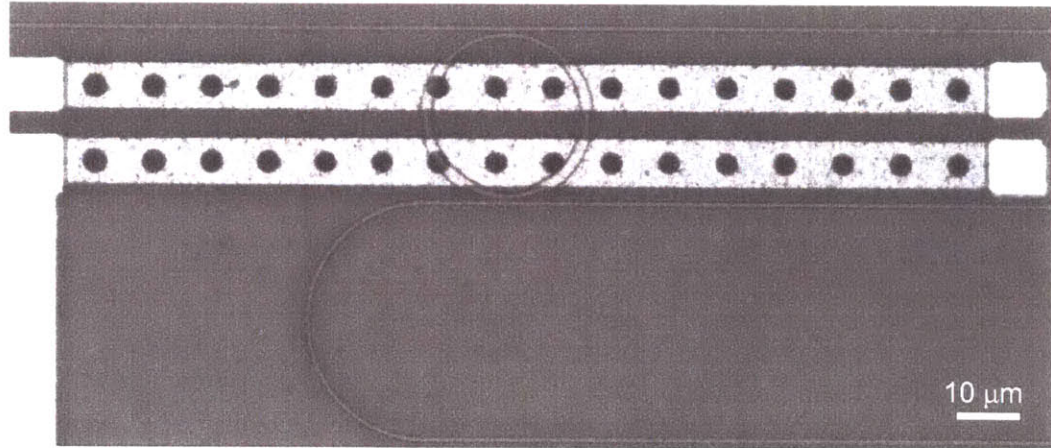


Figure 4-1: Optical micrograph of a fabricated wavelength selective switch.

microring optical resonator by a MEMS device.

4.1.1 Lithographic resolution

The diameter of the etch-holes in the MEMS bridge structures was almost equal to the resolution limit ($2\mu\text{m}$) of the contact lithography equipment used for the patterning of the bridge structures. The result of this was that in some areas on the wafer, the etch holes were not imaged into the photoresist and thus no etch holes were transferred into the aluminum bridge structure. In the bridges where the etch holes were patterned the limited resolution caused the corners of the the etch holes to be rounded to the point that the etch holes assumed a circular shape, as seen in Figure 4-1.

The rounding of the corners of the etch holes was anticipated and desired since rounded corners produce lower stress concentrations in deforming structures. The complete disappearance of the etch holes was undesirable and indicates that greater care needs to be exercised during the patterning of the aluminum layer. However, the bridge structures without etch holes actually proved to be useful in the mechanical displacement measurements because they provided better experimental results from the optical profilometer as compared with the bridge structures with etch holes. The limited lateral resolution combined with the small features resulting from the etch

holes in the bridges produced noisy results when the bridges with the etch holes were tested in the optical profilometer.

The bridge structures with etch holes were used for the optical testing since the etch time to release the bridges was less and therefore the etching of the silicon nitride waveguides was also minimized. Somewhat surprisingly, the pull-in voltage for both bridges with and bridges without etch holes was about 24 volts. The reason for this is that the pull-in voltage of the bridge was actually more strongly controlled by dielectric charging rather than the stiffness of the bridge structure, as explained in Section 4.2.1.

4.1.2 Residual stress

Residual stress within the MEMS structures significantly reduced the optical performance of the MEMS devices. Through measurements with the Zygo white light interferometer, it was found that residual stress in the MEMS structure reduced the gap between the optically lossy material in the MEMS bridge from the required 1.1 μm down to 0.34 μm . This caused the optically lossy MEMS bridge to interact with the evanescent field in its unactuated position more strongly than desired, and enhanced the insertion loss in the drop waveguide and reduced the switching contrast in the through waveguide.

To assist in the analysis of the stress in the unreleased aluminum film, it is helpful to think of the stress in the film as a combination of a constant stress, or mean stress, and a stress gradient. In this analysis, the stress gradient will be assumed to be constant (i.e. linear stress variation through the thickness of the beam).

To determine the value of the stress gradient in the aluminum film, release structures were incorporated into the mask set that allowed the determination of the stress gradient due to the deformation of the structures. Similar techniques have been reported on in the past [18, 26, 27, 33, 34, 98, 105, 139].

For the particular method used here, a series of cantilever beams of different lengths were fabricated, similar to [26, 27, 139]. Cantilever beams were selected because they allow the mean stress in the beam to relax through the expansion or

contraction of the beam. The beam also bends up or down due to the stress gradient. This decouples the mean stress from the stress gradient. While the relaxation of the mean stress due to the beam contracting or expanding can not be measured, the deformation (bending) due to the stress gradient is measurable, from which the stress gradient can be calculated.

By using a series of beams with a fixed difference in length, the only measurement required of each beam is the gap between the tip of the beam and the substrate. This measurement is best done with a non-contact profilometer. In the testing of the wavelength selective switch, a Zygo white-light interferometer was used successfully.

From the measurement of the gaps between beam tips and the substrate of subsequent beams, the radius of curvature of the deformed beams can be found. The stress gradient of the unreleased film is directly related to the radius of curvature of the released beams. Figure 4-2 shows the layout of the series of cantilevers used to determine the stress gradient in the aluminum film.

In addition to the unknown stress gradient, there is an unknown amount of rotation about the beam anchor introduced by the deformation of the anchor resulting from the residual stress. This means that at least three beams (providing two relative tip displacement measurements) are required to find the unknown stress gradient.

The radius of curvature of the beams is constant and equal if there is no variation in the stress state of the film comprising the beams in any plane parallel to the substrate plane. Because of the small size of the beams and the close proximity of the individual beams, variation in the film stress in this manner is unlikely to cause a problem. By using the measured tip displacement values along with the known difference in beam lengths, the radius of curvature can be calculated. Figure 4-3 shows the important dimensions and geometric relationships for the calculation.

The cantilever beams in the array have a constant change in length ΔL between adjacent beams. After the sacrificial release etch, the beams bend due to the residual stress gradient in the film. Because they are only attached at one end, the beams assume a circular shape with a constant radius of curvature. The length ΔL , has now

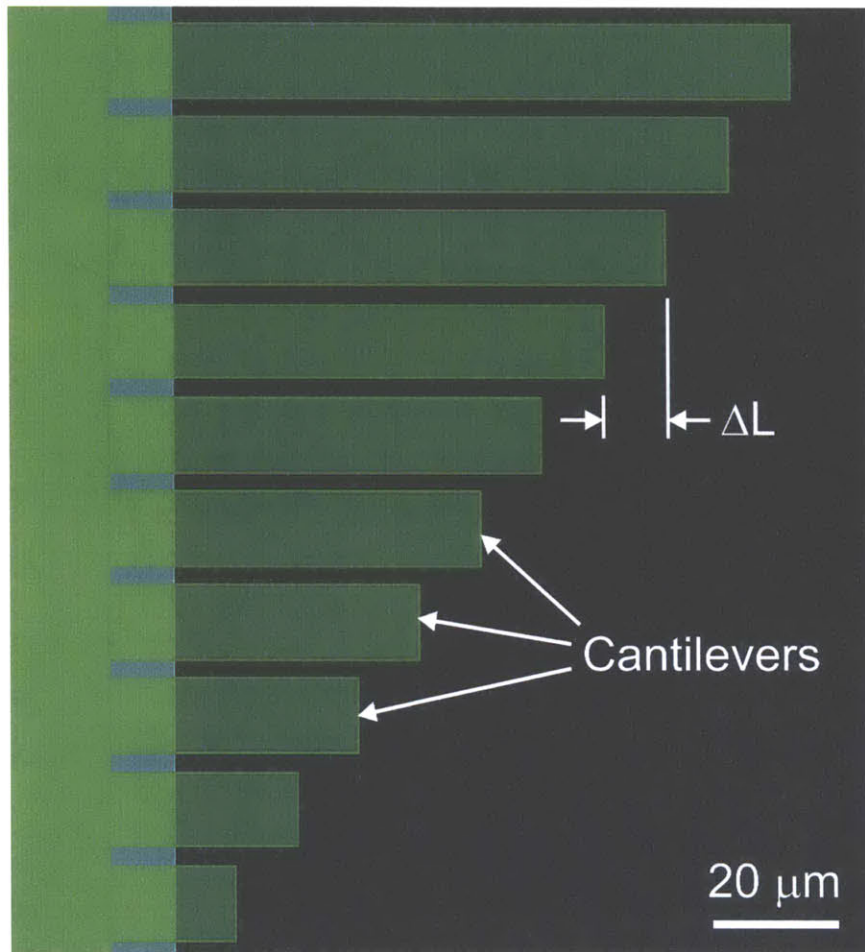


Figure 4-2: CAD layout of the suspended series of cantilever beams used to determine the residual stress gradient in the aluminum film.

• Cantilever Beam Tips

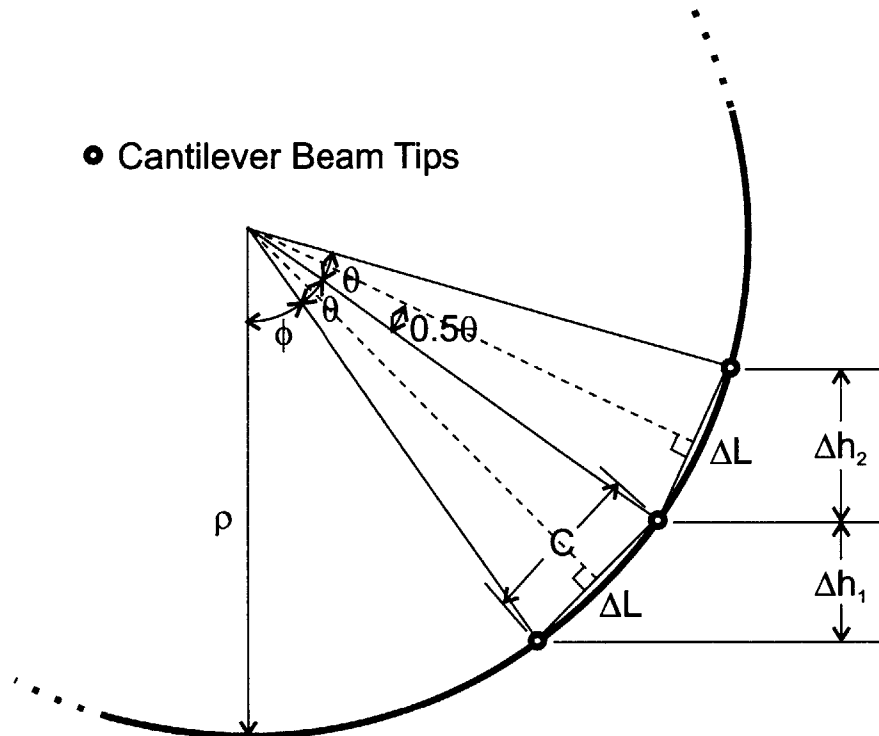


Figure 4-3: Diagram showing the important dimensions and geometric relationships used in the residual stress gradient derivation from the cantilever beam array.

become an arc on the circle defined by the deformed beams. The relationship

$$\rho\theta = \Delta L \quad (4.1)$$

between the radius ρ , the arc length ΔL , and the angle subtended by the arc θ , therefore holds.

In addition, equations relating the change in end height (Δh_1 , Δh_2) and chord length, C , of subsequent cantilever beams with the angles ϕ and θ as defined in Figure 4-3 can be written as

$$\frac{\Delta h_1}{C} = \sin\left(\phi + \frac{\theta}{2}\right) \quad (4.2)$$

$$\frac{\Delta h_2}{C} = \sin\left(\phi + \frac{3\theta}{2}\right). \quad (4.3)$$

If the angle θ is small, then the arc length ΔL , and the chord length C , are approximately equal¹. By using this assumption, Equations 4.2 and 4.3 can be rearranged and combined to eliminate ϕ , leaving θ as the only unknown.

$$\theta \approx \arcsin\left(\frac{\Delta h_2}{\Delta L}\right) - \arcsin\left(\frac{\Delta h_1}{\Delta L}\right) \quad (4.4)$$

Equation 4.4 can be combined with Equation 4.1 to allow the direct calculation of the radius of curvature of the cantilever beams.

$$\rho \approx \frac{\Delta L}{\arcsin\left(\frac{\Delta h_2}{\Delta L}\right) - \arcsin\left(\frac{\Delta h_1}{\Delta L}\right)} \quad (4.5)$$

The relationship between the radius of curvature and the bending moment, M , of a beam is [41]

$$\frac{1}{\rho} = -\frac{M}{EI_a}, \quad (4.6)$$

where E is the Young's modulus of the beam material² and I_a is the area moment of

¹The size of the angle θ is controlled by the magnitude of ΔL . Therefore, the ΔL value that is selected in the design of the cantilever beams should be such that θ is small to simplify the calculation of the residual stress gradient.

²For beams with a width greater than about ten times the thickness, the biaxial modulus, $\frac{E}{1-\nu}$,

inertia of the beam cross-section.

The relation between bending moment and stress at any particular point through the thickness of the beam is [41]

$$\sigma_{xx} = \frac{My}{I_a}, \quad (4.7)$$

where σ_{xx} is the stress in the beam at the position y , and y is measured from the neutral axis of the beam. For the case of beams of rectangular cross-section composed of a single material, the neutral plane is at the center of the thickness of the beam.

By taking the spatial derivative of Equation 4.7 and combining it with Equations 4.6 and 4.5, the residual stress gradient is found as

$$\frac{\partial \sigma_{xx}}{\partial y} \approx -E \frac{\arcsin\left(\frac{\Delta h_2}{\Delta L}\right) - \arcsin\left(\frac{\Delta h_1}{\Delta L}\right)}{\Delta L} \quad (4.8)$$

Using this technique, the aluminum film was found to have a residual stress gradient of 63.1 ± 16.8 MPa/ μm (for a 95% level of certainty)³. This indicates that for the aluminum film with thickness 350nm, the stress difference between the top and bottom of the film was 22.1 ± 5.9 MPa.

If we set the stress at the bottom of the aluminum film at 100 MPa, then the stress at the top of the film will be 122.1 MPa. The average stress through the thickness of the aluminum is therefore 111.0 MPa. This constant background stress level is consistent with reported values of average residual stress levels in the aluminum films deposited on silicon substrates [54, 71, 72] and is further validated by the results of the finite element modelling of the experimental results of the fixed-fixed bridge structures.

Using the stress values for the film described above, the bridge structure used to switch the optical ring resonator on and off was modelled using finite element analysis (FEA) with a linear elastic material model. The analysis indicated that the Mises

should be used in place of the Young's modulus to account for the Poisson effect in the beam which tends to stiffen the beam.

³Appendix C lists the results of the individual measurements of the radius of curvature and the residual stress gradient.

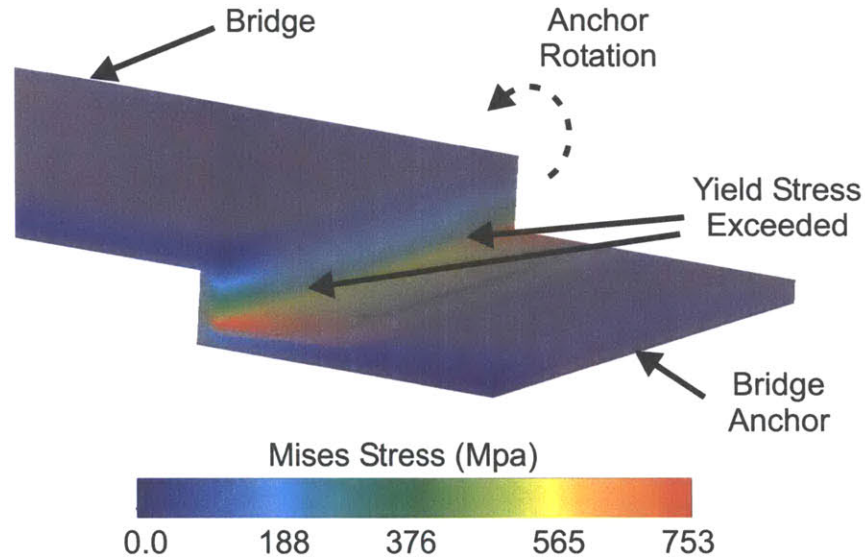


Figure 4-4: Finite element analysis showing the Mises stress in the anchor resulting from the residual stress in the aluminum film. Where the Mises stress exceeds the yield stress of aluminum, the structure will plastically deform, causing the anchor to rotate inward as indicated.

stress where the anchors rise up into the bridge structure greatly exceeds the yield stress of aluminum (see Figure 4-4). This result indicates that the upright portion of the anchors will experience significant plastic deformation. The result of the plastic deformation is that the anchor rotates inward, giving the bridge structure an initial downward slope. This is observed experimentally in the profilometry tests of the bridge structure.

The Coventorware finite element package does not provide a material model that allows plastic deformation. However, the rotation in the anchors resulting from the plastic deformation can still be captured in the model by reducing the stiffness of the anchor. This was done in the model by reducing the thickness of the anchor and thus allowing more bending and rotation of the anchor.

Figure 4-5 shows an experimental measurement of the profile of the bridge compared with both the strictly elastic and the plastic deformation compensated finite element models. When the plastic deformation is taken into account, the finite element model predicts quite well the deformation experienced by the bridge using the

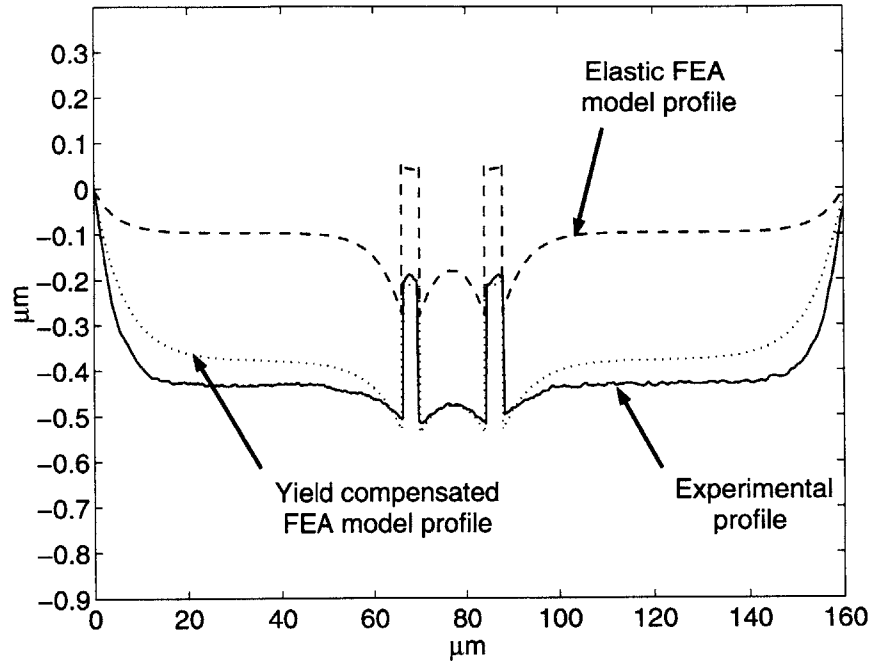


Figure 4-5: Comparison between the experimentally measured bridge profile and the bridge profiles calculated using an elastic finite element model as well as a finite element model that compensated for the plastic deformation that was experienced by the structure.

residual stress values of the aluminum bridge as determined above. This plastic deformation compensated finite element model will be used again in Section 4.2.1 to model the actuation of the MEMS bridge.

4.1.3 Surface roughness

Figures 4-6 and 4-7 are SEM images of an aluminum bridge structure over the ring resonator and bridge anchor, respectively. Significant roughness can be seen on both the top surface as well as the edges (sidewalls) of the aluminum bridge. For the switching application, the roughness is not a significant concern. In fact, the roughness likely increases the optical loss introduced into the ring resonator when the MEMS bridge is pulled down due to the roughness inducing scattering losses. However, for other applications, such as ring resonator MEMS tuning (see Chapter 8), the roughness of the surface must be avoided.

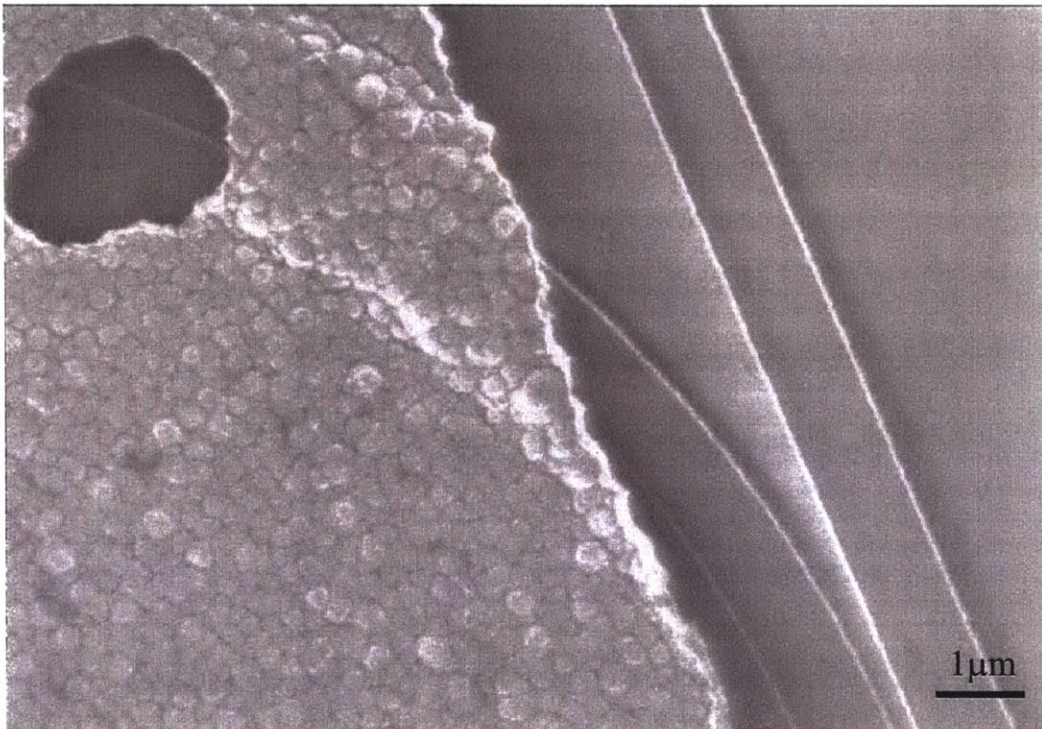


Figure 4-6: SEM image of a portion of the MEMS bridge over the top of the optical ring resonator filter.

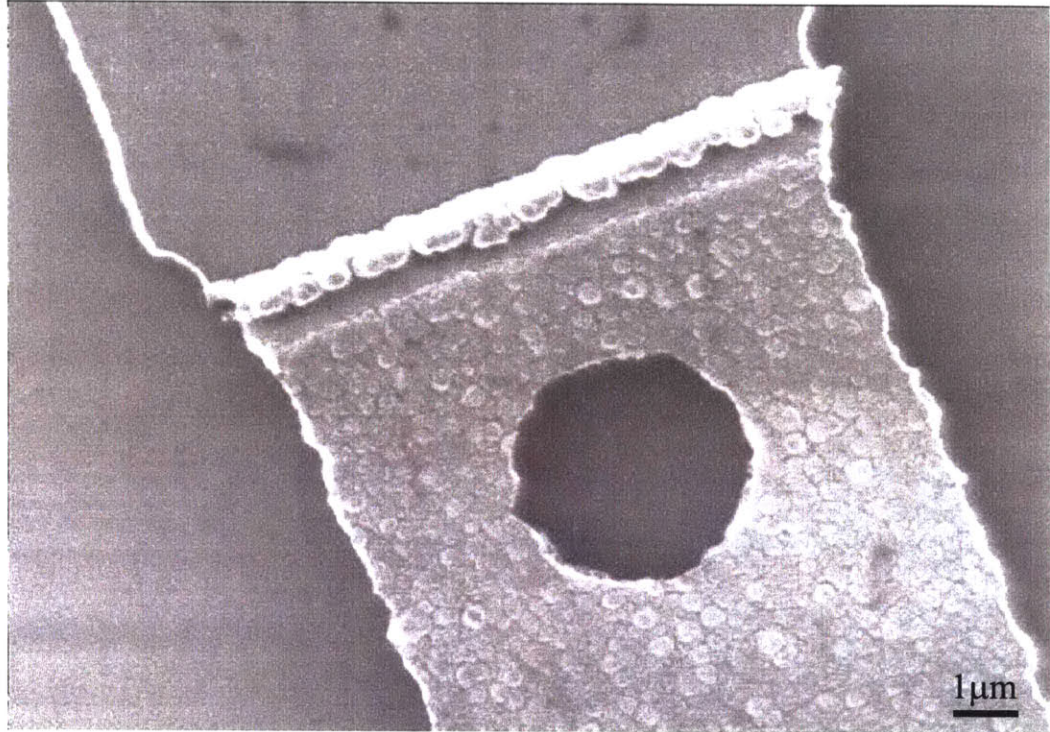


Figure 4-7: SEM image showing one of the anchored sides of the MEMS bridge. Note that the suspended section of the aluminum bridge has much greater roughness than the aluminum anchored to the silicon oxide layer. This is a result of the roughness of the poly-silicon sacrificial layer.

The surface roughness of the aluminum bridge is due to the roughness of the underlying poly-silicon sacrificial layer. The poly-silicon develops a rough surface by the preferential growth of certain orientations of silicon crystal grains in the poly-silicon film. The deposited aluminum film conforms to the shape of the poly-silicon grains and in so doing assumes the roughness of the poly-silicon film. The effect of the roughness of the poly-silicon layer on the aluminum bridge is very clear in Figure 4-7, where the suspended aluminum is quite rough while the aluminum that is affixed to the silicon oxide layer is smooth.

To reduce the roughness induced by the sacrificial poly-silicon layer, a chemical-mechanical polishing (CMP) step should be included after the deposition of the poly-silicon film to reduce the surface roughness of the poly-silicon film. The CMP step would also eliminate the rounded bump in the aluminum film over the top of the waveguides comprising the ring resonator (see Figure 4-6).

The sidewall roughness of the aluminum bridge is due to the aluminum etchant preferentially etching certain aluminum crystal grain orientations. Because some grains are etched more quickly than others, this leaves a ragged edge on the aluminum bridge. While this edge roughness does not have any significant effect on the ring resonator switching device or the ring resonator tuning device, it could be somewhat reduced by using anisotropic reactive ion etching (RIE) rather than the wet (PAN) etch that was used in our process.

4.1.4 Alignment

The alignment of the fabricated devices was off by 3 to $4\mu\text{m}$ along the length of the bridge and $1.5\mu\text{m}$ along the width of the bridge. Rotational misalignment was not observed. Even though these misalignments are relatively large, the most critical requirement on the alignment of the bridge to the ring resonator structures was met, which was keeping the bridge structure well outside of the evanescent field of the bus waveguides.

The misalignment did place some of the etch holes above the waveguides comprising the ring resonator structure, as can be seen in Figures 4-1 and 4-6. The

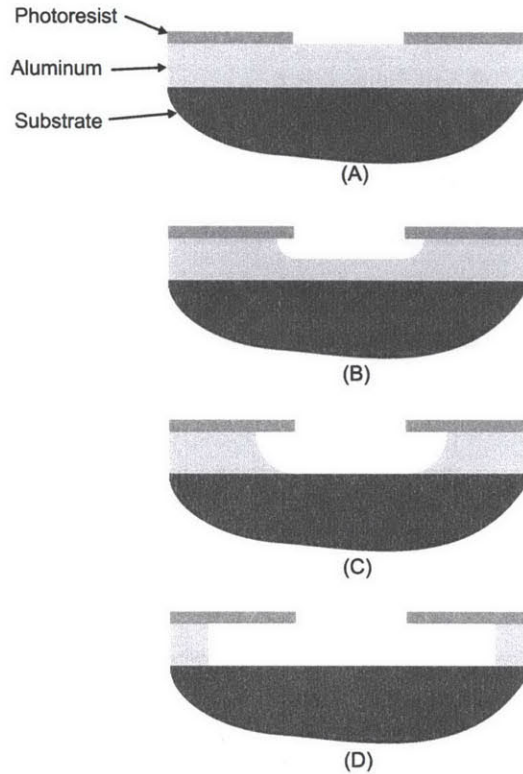


Figure 4-8: Schematic drawing showing the evolution of an isotropically etched film beginning with (A) and proceeding through (B), (C), and (D) showing the resulting undercut.

misalignment of these etch holes decreased the coverage of the ring resonator by the MEMS structure. This led to a decrease in the absorptive loss introduced to the optical ring resonator and thus to decreased switching contrast.⁴

4.1.5 Aluminum undercut

To pattern the aluminum bridge structure, a wet aluminum etch (PAN etch) was used. This etchant is isotropic for aluminum, meaning that it etches in all directions at the same rate. Figure 4-8 shows a schematic representation of an isotropic etch.

To ensure that the aluminum layer was completely etched through, the aluminum etch was allowed to proceed for approximately twice the time duration nominally

⁴The decreased loss from absorption caused by the misalignment of the etch holes may actually be compensated by increased scattering losses due to the edges of the etch holes creating changes in the effective index of the ring resonator.

required to etch through the film thickness. This was expected to, and did, introduce an undercut of approximately twice the thickness of the film. The undercut was measured using SEM images and was found to be $0.82\mu\text{m}$. This decreased the bridge width by $1.64\mu\text{m}$, while the etch holes increased from $2.0\mu\text{m}$ up to $3.64\mu\text{m}$.

The undercut effected both the optical and mechanical performance of the switch. In the mechanical domain, the undercut tends to reduce the stiffness and mass, thus altering the resonant frequency and switching speed. In the optical domain, the undercut reduces the coverage of the ring resonator by the bridge from⁵ 58% to 41%, resulting in smaller absorptive optical loss being introduced into the ring resonator when the bridge is in the lowered state.

4.2 Testing

The switch was tested both electro-mechanically and optically to evaluate its performance. The purpose of electro-mechanical testing was to determine the pull-in voltage of the structure. The mechanical measurements consisted of applying a constant voltage and measuring the displacement of the MEMS bridge. The results of the mechanical testing fit very well with a proposed model that takes into account the effects of dielectric charging (see Section 4.2.1).

Optical testing demonstrated functionality of the device as a wavelength selective switch. The spectral wavelength response of the switch was measured for both the through and drop ports, in both states of the switch. The temporal response of the switch was also measured by applying a square-wave actuation signal to the device and simultaneously measuring the optical response of both the through and drop ports at a fixed wavelength.

⁵This coverage value also takes into account the reduction in coverage due to the misalignment of the bridge structure which resulted in some of the etch holes residing over the ring resonator.

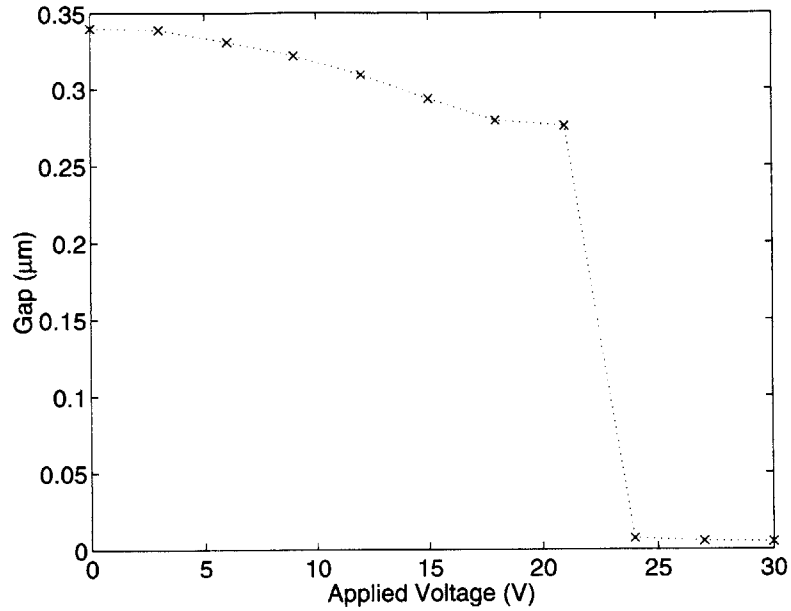


Figure 4-9: Displacement as a function of voltage for the wavelength selective switch device. Note the pull-in at 24 volts.

4.2.1 Actuation voltage and dielectric charging

The displacement with applied voltage of the wavelength selective switch was evaluated using a Zygo white light interferometer system to measure the profile of the device as it was being actuated by an applied voltage. The profile change with applied voltage was used to determine the change in the gap at the center of the bridge structure as a function of applied voltage. The results of this test are shown in Figure 4-9. It can be seen that the bridge pulls in between 21 and 24 volts. This was a surprising result. A pull-in analysis using the finite element model of the bridge developed in Section 4.1.2 predicts that pull-in should occur only after the bridge is in contact with the dielectric material (i.e. the bridge should be blocked from ever actually experiencing pull-in by the dielectric material). The results of the finite element pull-in analysis are compared with the experimental results in Figure 4-10. During optical testing, the same pull-in effect of the bridge was also observed in that there was little effect on the optical output of the switch until a voltage of 24 volts was reached. At this point a very abrupt change in the optical output was observed.

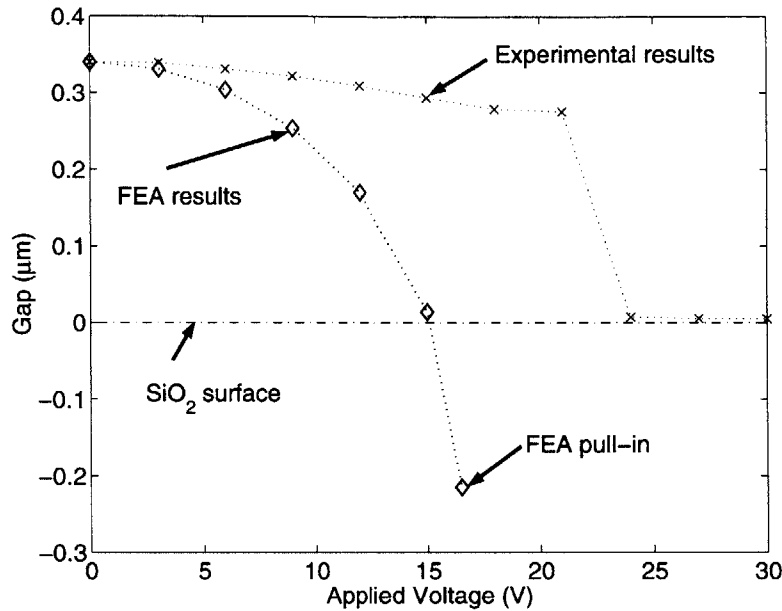


Figure 4-10: Finite element pull-in analysis compared with the experimental testing results. Note the finite element analysis predicts that pull-in shouldn't occur since the pull-in point is below the surface of the insulating oxide film.

The anomalous pull-in of the MEMS device seen in the experimental testing is due to trap charges building up on the surface of the dielectric material between the MEMS bridge and the substrate. This charging up of the dielectric surface is referred to as dielectric charging. The charges are trapped in charge trap sites of the dielectric material when an electric field is applied. The charge trap sites are the result of imperfections in the microstructure of dielectric materials. The charge traps can retain the trapped charges for a significant time duration after the removal of the electric field, anywhere from the order of seconds to days [111,147].

A simple model predicting the effect of dielectric charging on parallel plate actuators has been proposed previously [147,151] that predicts an increase in the pull-in voltage due to dielectric charging. A revised version of this model is used here to predict and explain the experimental displacement results of the wavelength selective switch throughout the actuation process.

A schematic of the model used for the dielectric charging analysis is shown in Figure 4-11. The charges on the parallel plate electrodes are, of course, on the two

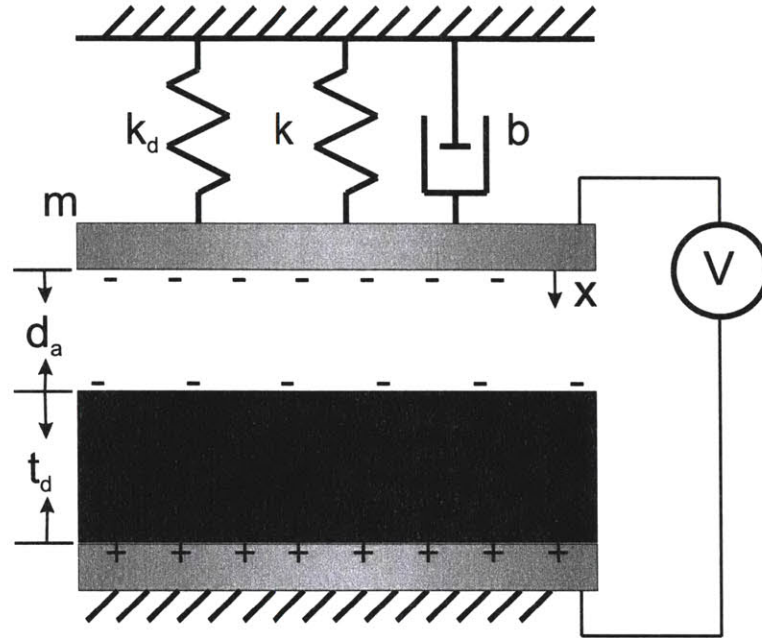


Figure 4-11: Schematic representation of the model used to for the analysis of the effect of dielectric charging on the wavelength selective switch.

opposing surfaces of the electrodes. The trapped charges on the dielectric material are also located on the surface of the dielectric layer.

In the MEMS bridge model, a nonlinear spring was used. The nonlinear spring is required because the bridge is fixed at both ends which introduces a nonlinear spring effect due to stretching. The nonlinear spring used to model the stretching of the bridge is a Duffing spring. The spring also has a linear component resulting from the bending of the bridge.

The equation of motion for this model is

$$m\ddot{x} + b\dot{x} + kx + k_d x^3 = F_{el}(V, x, Q_0,), \quad (4.9)$$

where $F_{el}(V, x, Q_0)$ is the electrostatic force due to the combined effects of the parallel plate actuator and the charged dielectric layer, and is a function of the applied voltage V , the displacement x , and the charge trapped on the dielectric surface Q_0 .

The total charge on the top and bottom electrodes is a combination of the charge

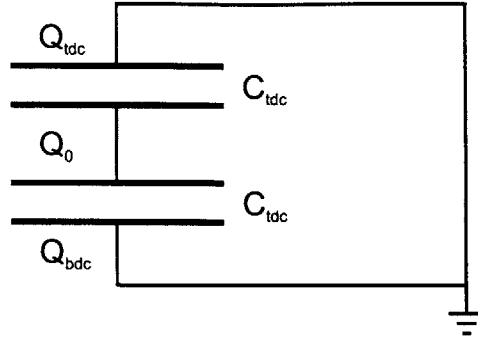


Figure 4-12: Schematic drawing showing the relationship between the trapped charge on the dielectric surface and the resulting induced charges on the two electrodes.

due to the applied voltage and the charge induced by the charged dielectric surface. By superposition, the effective charges of the top and bottom plates can be written as

$$Q_t = Q_{ta} + Q_{tdc}, \quad (4.10)$$

$$Q_b = Q_{ba} + Q_{bdc}, \quad (4.11)$$

where Q_t and Q_b are the total charges on the top and bottom electrodes, respectively. Q_{ta} and Q_{ba} are the charges on the top and bottom electrodes, respectively, due to the voltage applied across the electrodes. Q_{tdc} and Q_{bdc} are the charges induced on the top and bottom electrodes, respectively, by the charge on the dielectric surface.

The charge on the electrodes due to the applied voltage is straightforward to calculate, and is

$$Q_{ba} = -Q_{ta} = \frac{\epsilon_d \epsilon_0 AV}{\epsilon_0 t_d + \epsilon_d (d_a - x)}, \quad (4.12)$$

where ϵ_d is the relative permittivity of the dielectric material.

To calculate the charge induced on the electrodes by the trapped dielectric charge, it is helpful to think of the system as two capacitors in series where the trapped charge is located on two connected plates as in Figure 4-12.

Two equations are needed to determine the induced charges on the two electrodes. The first equation comes from the fact that the sum of the induced charges on the

electrodes and the trapped charge on the dielectric is zero.

$$Q_{tdc} + Q_{bdc} + Q_0 = 0. \quad (4.13)$$

The second equation relating the induced charges results from applying Kirchhoff's voltage law to the circuit of Figure 4-12 and using the basic definition of capacitance. This gives

$$\frac{Q_{tdc}}{C_{tdc}} = -\frac{Q_{bdc}}{C_{bdc}}. \quad (4.14)$$

By combining Equations 4.13 and 4.14 with the geometric dependence of the capacitances,

$$C_{tdc} = \frac{\epsilon_0 A}{d_a - x}, \quad (4.15)$$

$$C_{bdc} = \frac{\epsilon_d \epsilon_0 A}{t_d}, \quad (4.16)$$

we can find both Q_{tdc} and Q_{bdc} as functions of the trapped charge Q_0 and the displacement x as

$$Q_{tdc} = \frac{Q_0 \epsilon_0 t_d}{\epsilon_d \epsilon_0 (d_a - x) - \epsilon_0 t_d}, \quad (4.17)$$

$$Q_{bdc} = -\frac{Q_0 \epsilon_d \epsilon_0 (d_a - x)}{\epsilon_d \epsilon_0 (d_a - x) - \epsilon_0 t_d}. \quad (4.18)$$

The amount of charge on the surface of the dielectric material varies widely due to a number of parameters. The trapped charge varies strongly with the strength of the applied electric field, but is also affected by the composition, pressure, and temperature of the atmosphere within the gap. During the testing of the wavelength selective switch, the atmosphere was relatively constant but the electric field certainly changed. To capture this dependence of the trapped charge on the strength of the

electric field, the following model is proposed

$$Q_0 = \begin{cases} \alpha_0 \frac{V\epsilon_0 A}{(d_a - x) + \frac{\epsilon_0 t_d}{\epsilon_d}} + \alpha_1 \left[\frac{V\epsilon_0 A}{(d_a - x) + \frac{\epsilon_0 t_d}{\epsilon_d}} \right]^2 & \text{for } Q_0 < Q_{\text{sat}} \\ Q_{\text{sat}} & \text{otherwise} \end{cases} \quad (4.19)$$

This contains a linear term and a second order term that makes the trapped charge a nonlinear function of the applied voltage. This model is based on the physics behind dielectric charging, where the amount of ionization of the gas molecules in the gap is nonlinearly dependent on the electric field [43, 111, 151]. In addition, the trapped charge saturation Q_{sat} included in this model represents the fact that realistic dielectrics have a maximum trap density for charges with a fixed energy. Beyond this density, no additional charging is experienced.

With all of the charges in the system now known, it is possible to calculate the electrostatic force F_{el} on the suspended electrode. The most straightforward method to calculate the force resulting from the various charges is to calculate the electric field at the position of the top electrode and use that to find the force on the electrode due to its own charge. This gives

$$F_{el} = \frac{(Q_{ta} + Q_{tdc})(Q_{ba} + Q_{bdc} + Q_0)}{2\epsilon_0 A}. \quad (4.20)$$

The system model described in the Equations 4.9 through 4.20 was implemented in Simulink. The first step in using this model to predict the pull-in behavior seen in the experimental results is to calibrate the model to the results of the finite element model pull-in analysis. For the calibration, the dielectric charging effects in the lumped parameter model were set to zero. The finite element model was used for the calibration based on the assumption that the finite element model provides an accurate prediction of the pull-in characteristics of the device in the absence of dielectric charging. Judging from the fit achieved between the experimental profilometer results and the finite element model, this assumption is likely good to within a few percent.

Table 4.1: Parameters used with the nonlinear dielectric charging lumped parameter model.

Parameter	No Charging	Nonlinear Charging
m (kg)	6.08×10^{-13}	6.08×10^{-13}
b (N·s/m)	4.8×10^{-7}	4.8×10^{-7}
k (N/m)	5.23	5.23
k_d (N/m ³)	1.3×10^{13}	1.3×10^{13}
A (m ²)	1.42×10^{-9}	1.42×10^{-9}
d_a (m)	3.4×10^{-7}	3.4×10^{-7}
t_d (m)	3.0×10^{-6}	3.0×10^{-6}
α_0 (N·s/m)	0.0	0.2
α_1 (N·s/m)	0.0	8.4×10^{11}
Q_{sat} (C)	0.0	1.05×10^{-13}

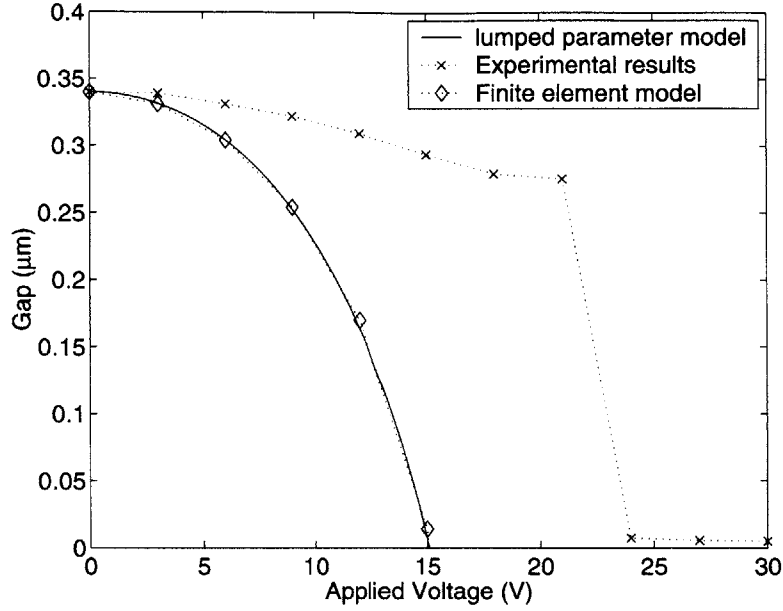


Figure 4-13: Results of fitting the lumped parameter model with no charging to the results of the finite element pull-in analysis.

The values used in the lumped parameter dielectric charging model are shown in Table 4.1. The mass and damping used in the model are inconsequential since the result of interest is the equilibrium (steady state) position of the bridge. For the mass, the generalized mass of the bridge given by the finite element analysis was used. The damping constant was selected to place the system near critical damping (for fast settling of the simulations). The actual area of the fabricated bridge was used for A , and the permittivity values are those of air and silicon oxide, as given in Tables A.6 and A.3 respectively.

The two spring constants k and k_d were selected to match the displacement versus voltage curve of the lumped parameter model with the the displacement versus voltage curve of the finite element pull-in analysis results. The results of the lumped parameter simulation using these parameters is shown in Figure 4-13.

With the lumped parameter model calibrated, the dielectric charging effect was added to the simulation according to the dielectric charging model given in Equation 4.19. The parameters α_0 , α_1 , and Q_{sat} were selected to match the displacement and

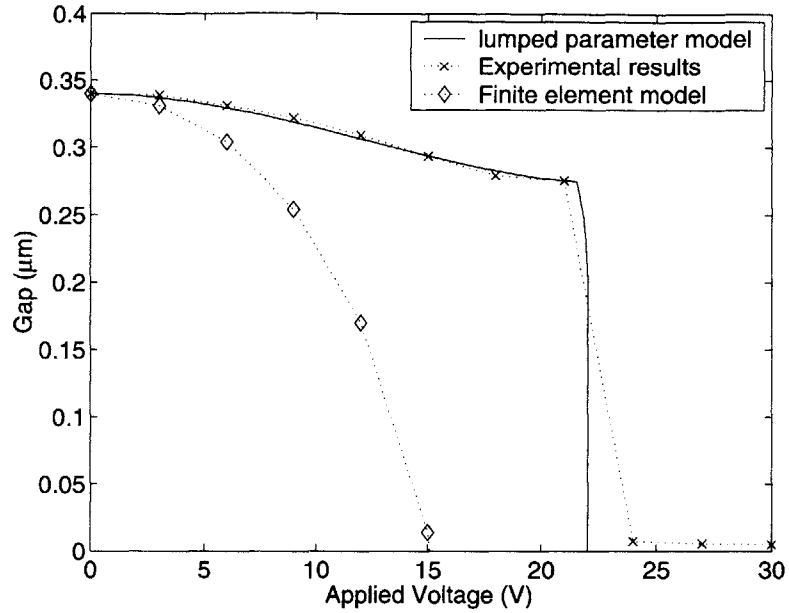


Figure 4-14: Comparison of the results of the experimental actuation results with the finite element actuation model and the lumped parameter model that takes into account dielectric charging using the second order dielectric charging model.

pull-in observed experimentally. The values for these parameters are given in Table 4.1.

The result of the lumped parameter model simulations with the dielectric charging effects included are shown in Figure 4-14. The results from this simulation are a very close match to the experimental results obtained for the wavelength selective switch device. The experimental and modelling results indicate that the trapped charge increases nonlinearly with the applied electric field. The rate of accumulation of the trapped charge increases due to its nonlinear dependency on the applied electric field. As the accumulation rate of the trapped charge increases, the accumulation rate of the charge on the top electrode decreases. Curves of the evolution of the trapped charge Q_0 and the charge on the top electrode Q_t versus applied voltage for the lumped parameter model simulation are shown in Figure 4-15. The result of these accumulation rate dynamics is that the electrostatic attraction force that the top electrode experiences changes little with increasing voltage which leads to the flattening of the displacement versus applied voltage curve seen in Figure 4-14 just

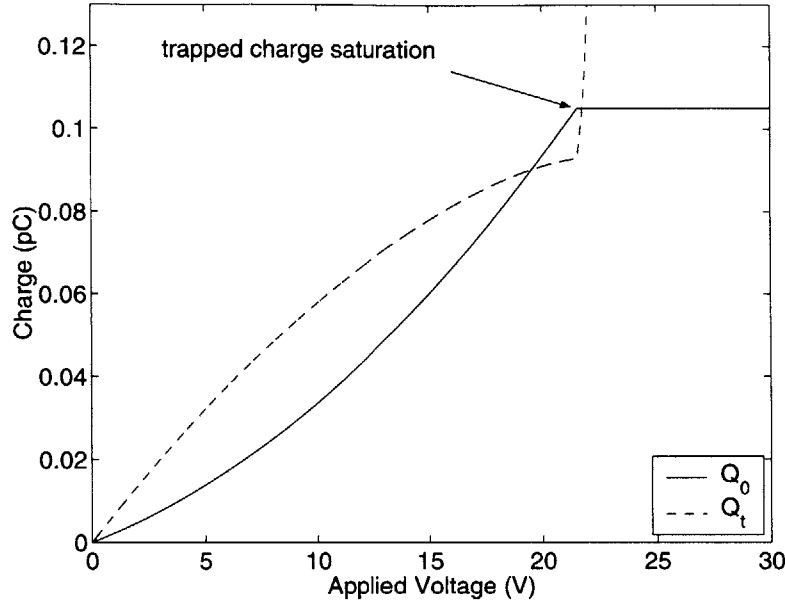


Figure 4-15: Evolution of the top electrode charge and the trapped charge versus the applied voltage for the lumped parameter dielectric charging simulation.

before pull-in occurs.

Pull-in occurs very soon after the charge trap sites of the dielectric material become saturated. At this point, any increase in voltage results only in charge accumulation on the top and bottom electrodes, with no increase in the trapped charge, as seen in Figure 4-15. The charge increases rapidly on the top and bottom electrodes which leads to pull-in very quickly.

The trapped charge density at saturation predicted by the model is 7.4×10^{-5} C/m² and corresponds to a charge trap density of 2.6×10^{10} cm⁻²·eV⁻¹. The charge trap density value compares quite well with published charge trap density values for silicon oxide [59, 70, 123, 149]. For further comparison, the charge trap density for a parallel plate actuator that used parylene as the dielectric material was found to be about eighteen times greater than the value reported here [151]. The fact that the value found for the wavelength selective switch and the device in [151] are only a little more than an order of magnitude different seems like a reasonable difference given that the dielectric materials are quite different (parylene is a polymeric material). The favorable comparison of the trapped charge density of the wavelength selective

switch with these reported values of charge density and charge trap density lends additional validity to this model of dielectric charging.

One of the interesting results of this analysis is that for this particular device, the effects of dielectric charging appeared to dominate the pull-in characteristics of the device. The pull-in voltages of both bridges with etch holes and bridges without etch holes were observed to be essentially the same, although the stiffnesses of the structures were different. In previous work [109], it was shown that etch release holes more strongly affected the mechanical properties of the electrostatic actuators (i.e. stiffness, resonant frequency, and mass). The electric fields created by plates with and without etch holes were found to be fairly similar for small sized etch holes. Because dielectric charging is directly related to the electric fields, it is expected that the dielectric charging characteristics would not be affected greatly by the presence or absence of small etch holes either.

4.2.2 Optical Performance - spectral

Because of the wavelength selective nature of the switch, it was important to test both the wavelength (spectral) response of the switch as well as the temporal response. The spectral response of the switch was tested using the system shown in Figure 4-16.

An image of the optics used to couple the light into the wavelength selective switch and collect the light coming out of the drop and through waveguides is shown in Figure 4-17. The image in Figure 3-5 shows a magnified image of the chip containing the wavelength selective switch with the probes used to introduce the control voltage in contact with the bond pad of a wavelength selective switch.

The edge of the chip where the end facets of the through and drop waveguides were located was imaged and brought to a focus. At the focal plane of the image, an iris was aligned with the bright spot of light coming out of either the through or drop waveguide. Figure 4-18 is an image of the edge of the chip showing the bright spot of light emerging from the waveguide end facet, as seen during testing.

The iris spatially filters the image and allows only the light coming from the drop or through waveguide to pass through to the optical detector. The alignment of the

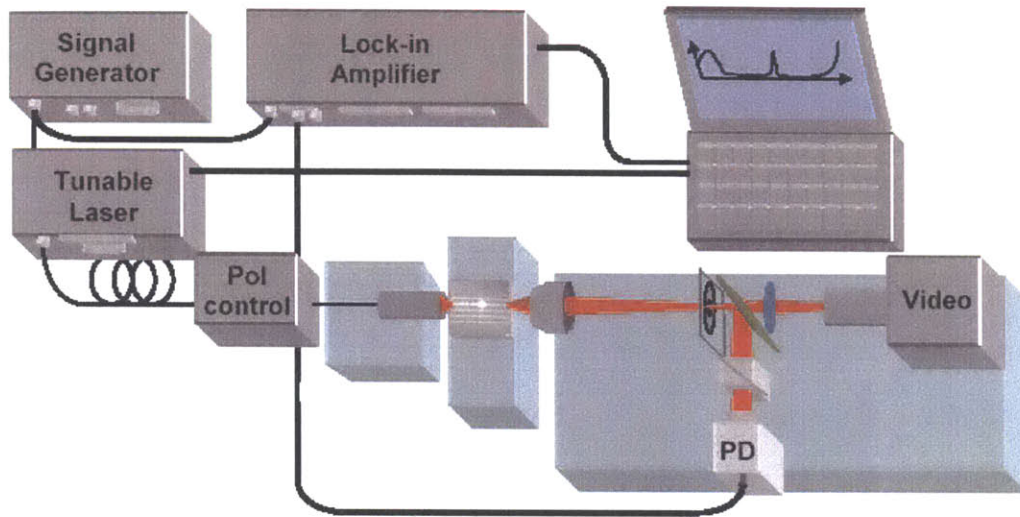


Figure 4-16: Illustration of the set-up to test the spectral response of the wavelength selective switch.

iris is accomplished using the video camera shown in Figure 4-16. When the iris is aligned, a mirror is placed in the optical path routing the light to the optical detector which is subsequently aligned to the light coming from the waveguide.

The light that is input into the device is modulated at a set frequency. The modulated signal that is imposed on the input light is also input into a lock-in amplifier through which the output of the optical detector is also routed. The lock-in amplifier is thus able to filter the output signal to remove noise in the signal.

The experimental results of the spectral response of the drop port are shown in Figure 4-19. The figure shows the response of the switch in both of its states. The different states were achieved by applying either no voltage or 30 volts. The MEMS device changed the optical quality factor of the ring resonator from about 1200 to less than 200, providing a switching contrast in the drop port of 13 ± 1 dB.

The results of spectral testing on the through port are shown in Figure 4-20 for both switch states. The two states were again achieved by applying no voltage or 30 volts. The switching contrast seen in the through port was approximately 1.5 dB.

In Figure 4-21, the results of both through and drop ports in both switch states are plotted together. The insertion loss observed in the drop port is rather high,

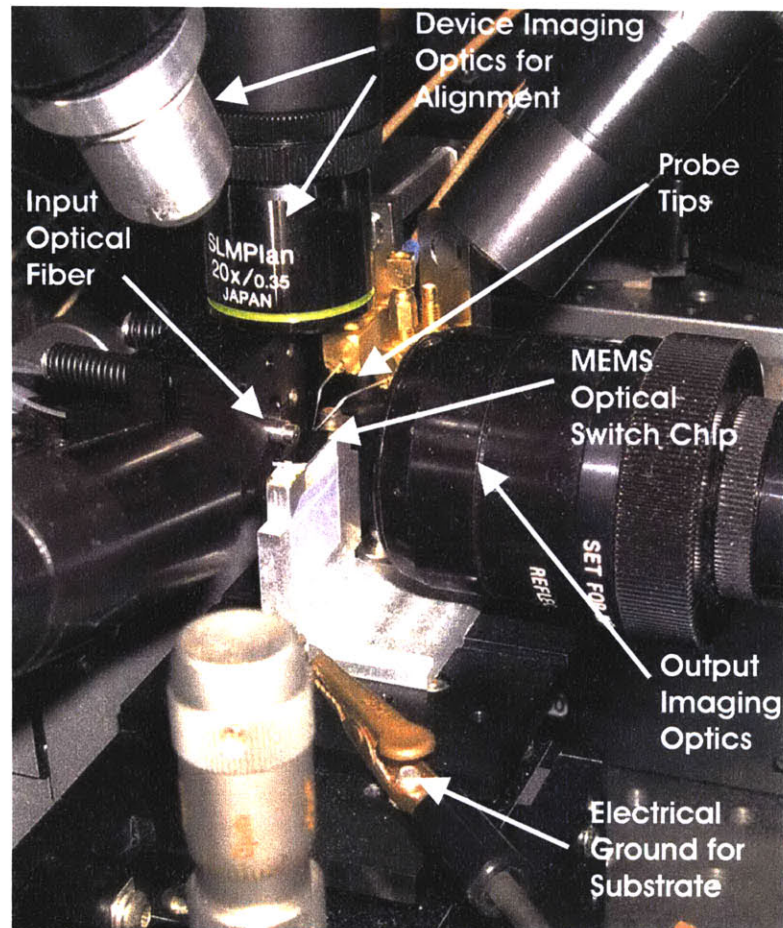


Figure 4-17: Image of the test set-up used to couple light into the input waveguide of the device and image the output light coming from the through and drop ports.

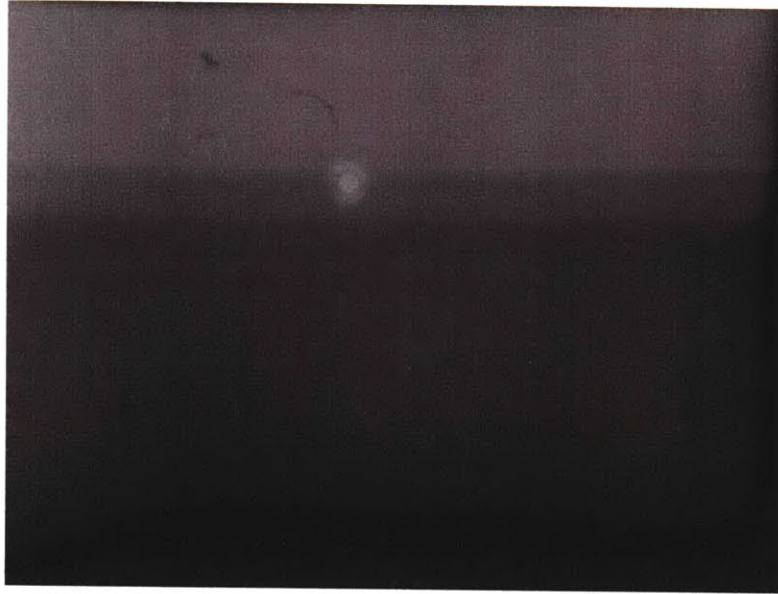


Figure 4-18: Image of the edge of the chip. The bright spot of light is the waveguided light coming out of the end facet of the waveguide at the edge of the chip. The lighter area above the bright spot is the surface of the chip, while the darker area below the bright spot is the chip edges.

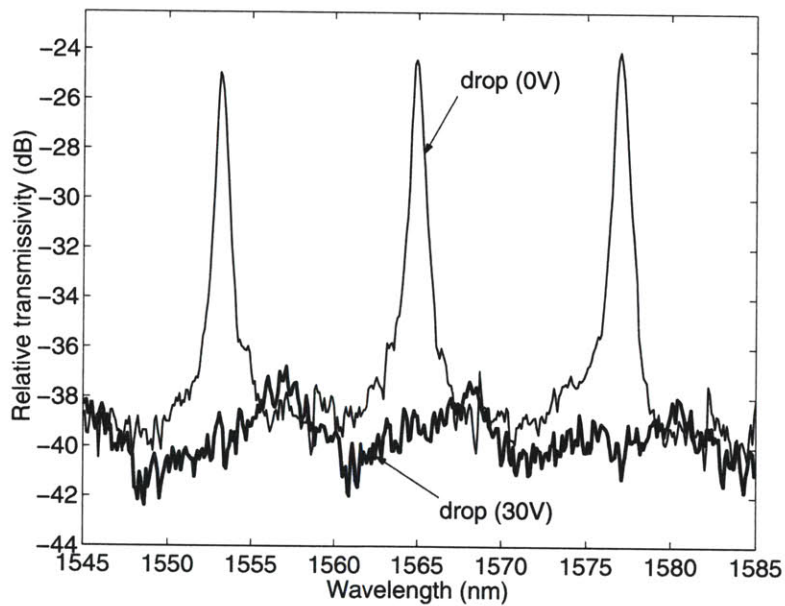


Figure 4-19: Spectral response of the drop port of the wavelength selective switch for both states of the switch.

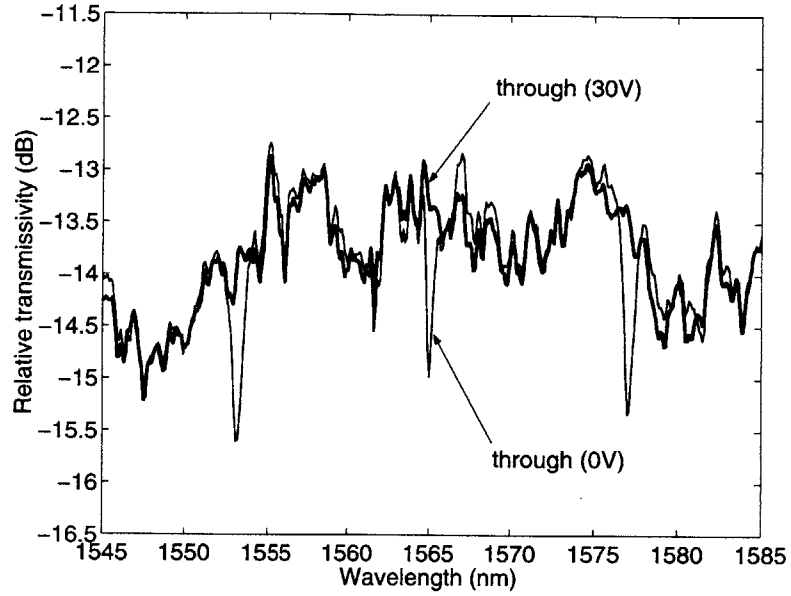


Figure 4-20: Spectral response of the through port of the wavelength selective switch for both states of the switch.

around⁶ 10 to 11 dB. The free spectral range of the ring resonator filter is 12nm.

The high insertion loss seen for the drop port, as well as the low switching contrast seen in the through port are a direct result of the MEMS bridge being partially pulled-in to the evanescent field of the optical ring resonator due to residual stress (see section 4.1.2. However, the test results of the prototype achieved the goal of demonstrating wavelength selective switching by combining an optically lossy MEMS device with integrated optical ring resonator filters. This is the first demonstration of this kind of capability.

Further work on controlling the residual stress should result in devices that perform just like static optical ring resonators when the bridge is up. Light rejection of the switched port and insertion loss in the down state should also improve.

⁶The insertion loss in the through port was not measured but is typically very small (<0.5dB) for ring resonator filters, and should also be very small for this device, since the MEMS device does not directly affect the through port.

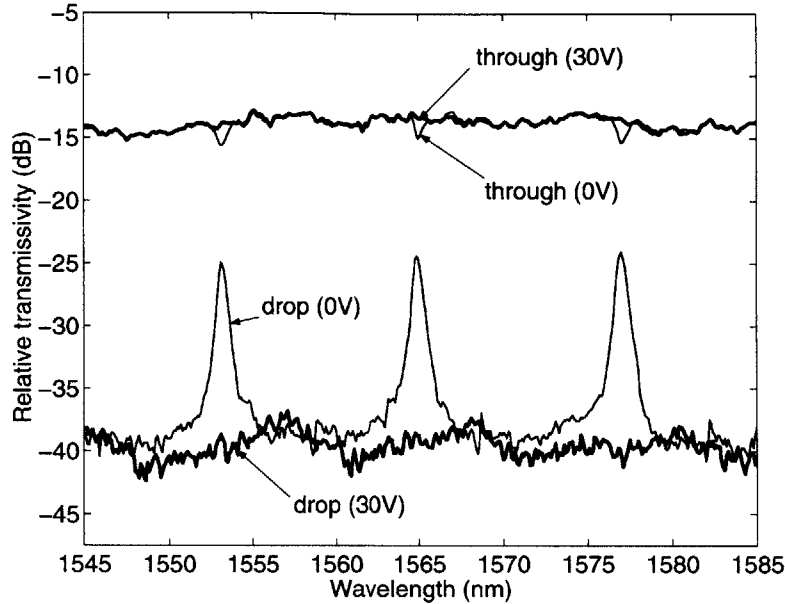


Figure 4-21: Spectral response of both the through port and the drop port of the wavelength selective switch for both states of the switch.

4.2.3 Optical Performance - temporal

Temporal testing of the switch was conducted with a fixed wavelength and a modulated control voltage to allow the evaluation of the switching dynamics of the device. The experimental test set-up for the temporal response of the switch is shown in Figure 4-22.

The tunable laser was set to a wavelength that showed switching contrast for the drop and through ports (i.e., a wavelength at or close to the resonant wavelength of the device). The voltage signal applied to the device by the signal generator and voltage amplifier was a 30 volt (peak-to-peak) square-wave signal with a 15 volt DC bias. It should be noted that the speed of the voltage amplifier was 8kHz. (This actually turned out to be the limiting factor of the switching speed of the device.)

The light detected by the photodetector was modulated according to the motion of the MEMS bridge device. The output of the photodetector was input into a digital oscilloscope in which 512 different samples were collected and averaged to reduce noise. Note that in this set-up the lock-in amplifier was not used, and the only

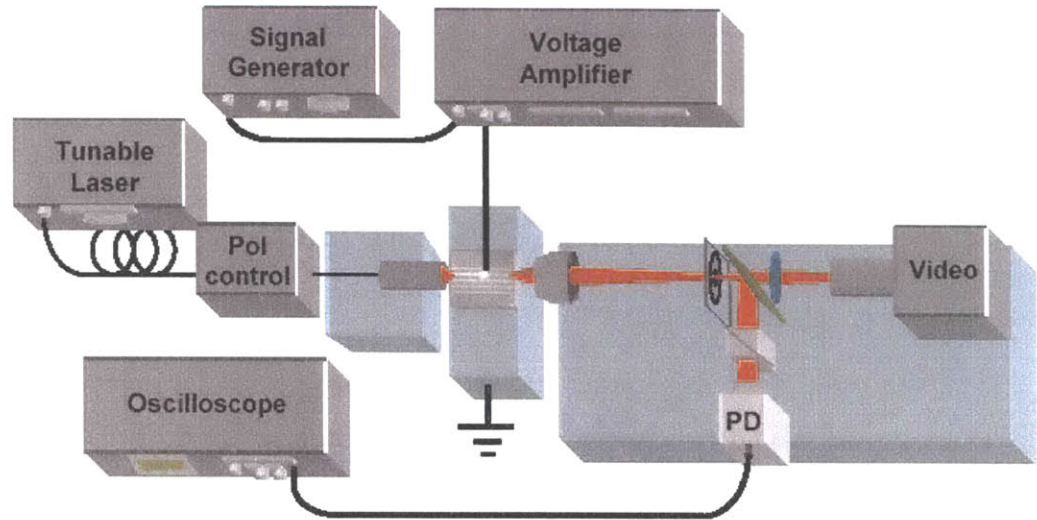


Figure 4-22: Illustration of the test set-up for testing the temporal response of the switch.

modulation to the optical signal came from the wavelength selective switch.

The results of the temporal measurement of the through port are shown in Figure 4-23. The low points in the signal are when the bridge structure is up and the high points are when the bridge structure is down. These results were obtained with the control voltage modulated at 2kHz.

The results of the measurement of the drop port are shown in Figure 4-24. For the drop port, the low points in the signal correspond to the bridge being down and the high points in the signal are when the bridge is up. The control signal in this case was also modulated at 2kHz.

The combined temporal switching results of both the through and drop ports are shown in Figure 4-25.

By analyzing the results of the temporal testing, the switching speed of the device can be obtained. The switching speed was calculated based on a 10% to 90% criteria and was found to be $60 \mu\text{s}$ to pull down and $16 \mu\text{s}$ to pull up. These switching speeds are much slower than those predicted in Chapter 2. At present, speed is only limited by the measurement equipment. The $60 \mu\text{s}$ for the pull-down time is directly related to how long the test equipment takes to reach the pull-in voltage, or one half cycle

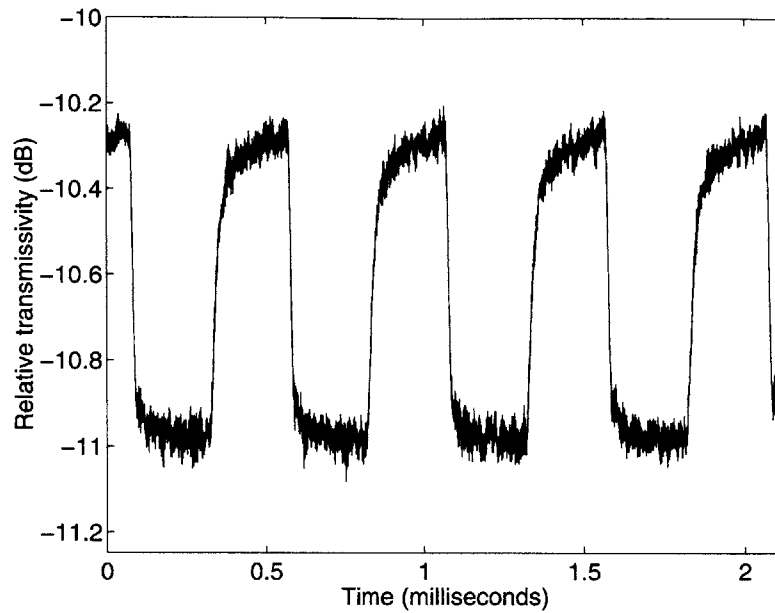


Figure 4-23: Temporal response of the through port of the wavelength selective switch.

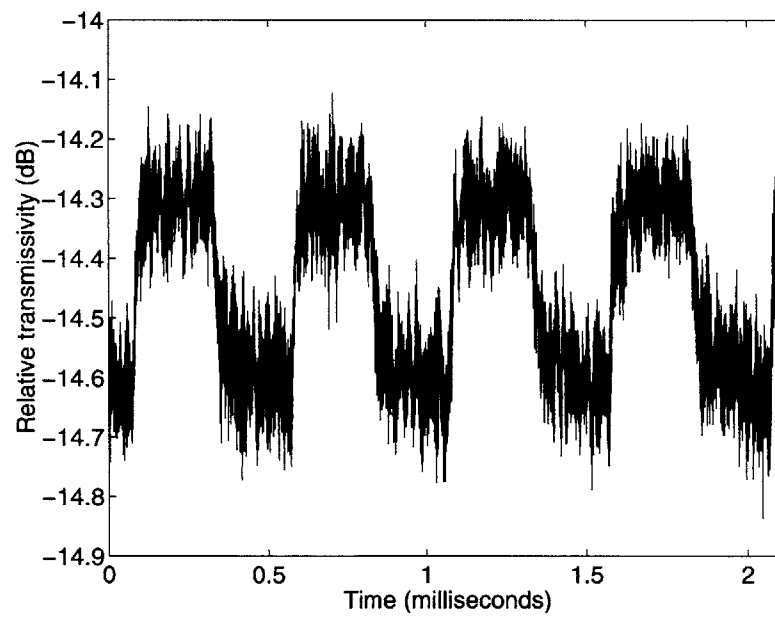


Figure 4-24: Temporal response of the drop port of the wavelength selective switch.

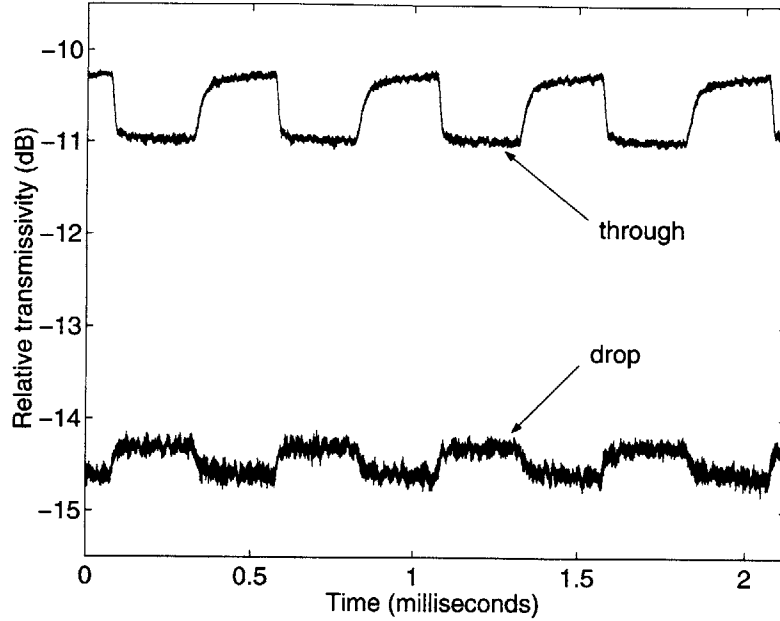


Figure 4-25: Temporal response of both the through port and the drop port of the wavelength selective switch.

at 8 kHz which is $62.5 \mu\text{s}$.

The pull-up time was a little better but only because the effects of dielectric charging caused a strongly binary pull-in effect. This required only a very small drop in voltage for the structure to pop-up to very near its unactuated height. The small voltage drop allowed the switching to occur at a speed faster than the speed of the voltage amplifier.

Although the temporal testing of the device was not intended to constitute a reliability test, the device was cycled more than 5 million times without failing and experienced switching frequencies up to 8kHz (limited by test equipment).

4.3 Discussion of results

The most significant result of the experimental testing of the device was the demonstration of switching an optical ring resonator using induced loss from a MEMS device. This is a very significant new optical switching capability.

The dielectric charging model used to predict the results of the experimental evaluation of the actuation of the device is another significant result. This model provides a method to predict the evolution of the charge on the dielectric surface as a function of applied voltage and bridge displacement. This model should be applicable to all parallel plate electrostatic actuators.

The final significant development is the method used to evaluate the residual stress gradient in microfabricated films. This method is also widely applicable in MEMS and in microfabrication in general to give a more complete understanding of the stress state of thin films.

While the prototype wavelength selective switch fulfilled its primary goal of demonstrating loss-based switching of ring resonator filters, the requirements needed to be integrated with commercial opto-electronic integrated circuits have not yet been met. The primary areas where it did not meet the requirements are in optical performance, actuation voltage, and switching speed.

The optical performance was degraded due to residual stress in the aluminum MEMS structure. In Chapter 5 titanium nitride is identified as a desirable material to replace aluminum as the MEMS bridge material. A fabrication process for the construction of titanium nitride MEMS bridge structures is proposed and tested, demonstrating a significant reduction in residual stress and the resultant deformation. By utilizing titanium nitride as the MEMS bridge structure, the optical performance of the switch should dramatically improve.

In Chapters 6 and 7, two new MEMS switch actuation techniques are described that would allow the switching voltage of the wavelength selective switch to be lowered to IC voltage levels. At the same time, the switching technique in Chapter 7 would allow switching speeds much faster than one microsecond.

By using the techniques developed in Chapters 5, 6, and 7 in conjunction with the induced-loss concept of switching optical ring resonators, a device that is fully compatible with an opto-electronic integrated circuit will become possible.

Chapter 5

Residual stress manipulation and control

In this chapter we consider the issue of residual stress in the aluminum bridge that comprises the optical switch. As explained in Chapter 4, residual stress results in deformation of the bridge, which in turn increases optical loss and degrades optical performance. Therefore, it is critically important to characterize the process of stress emergence and evolution, and understand the parameters upon which this process is dependent. In Section 5.1, the evolution of residual stress in the aluminum film is considered. Next, in Section 5.2, titanium nitride is proposed as a potential material for this, and other MEMS applications. A technique for the control of residual stress in titanium nitride is proposed and demonstrated in Sections 5.3 and 5.5, respectively.

5.1 Residual stress in aluminum films

Like most thin films, the residual stress state of the aluminum film used to create the MEMS device can be altered and controlled by the deposition parameters [54, 71]. However, aluminum and other highly ductile metals (i.e. copper, gold, etc.) can and usually do experience further evolution of the residual stress state of the film due to subsequent processing steps. This evolution of the stress in the film is difficult to work with, although it does appear to be possible as evidenced by Texas Instruments

micromirror array, which is fabricated out of aluminum [35].

The evolution of the stress state in the aluminum film is due to annealing and/or plastic deformation of the film. Because the melting temperature of aluminum is rather low (650°C), the film will anneal even with fairly low temperature processes. If the temperature of the film reaches about half the melting temperature of aluminum, the film will experience significant atomic diffusion (annealing) which will eventually lead to a stress free film at the elevated temperature.

The stress free nature of the film is the desired operating state (i.e. will not deform and introduce undesired loss into the ring resonator); however, upon lowering the temperature of the film back to room temperature, the thermal expansion mismatch between the aluminum film and the silicon substrate very quickly causes the aluminum film to reach its yield point and experience plastic deformation and a new residual stress state [72, 95].

The change in temperature needed to induce plastic deformation in the aluminum film is easily estimated. The strain introduced into a material from a change in temperature is simply

$$\varepsilon = \alpha \Delta T, \quad (5.1)$$

where ΔT is the change in temperature, α is the coefficient of thermal expansion, and ε is the thermally induced strain. If the aluminum film and the silicon substrate were not bonded together, their respective strains would be

$$\varepsilon_{Al} = \alpha_{Al} \Delta T, \quad (5.2)$$

$$\varepsilon_{Si} = \alpha_{Si} \Delta T. \quad (5.3)$$

When the aluminum film and the silicon substrate are combined, the strain of the system is essentially that of the silicon substrate, because the thickness and modulus of the silicon substrate are much greater than the aluminum film. The strain results

in stress developing in the aluminum film, equal to

$$\sigma_{Al} = \frac{E_{Al}}{1 - \nu_{al}} (\alpha_{Si} - \alpha_{Al}) \Delta T. \quad (5.4)$$

where σ_{Al} is the stress in the aluminum film, E_{Al} is the Young's modulus of aluminum, and ν_{Al} is the Poisson ratio for aluminum. It should be noted that $\frac{E_{Al}}{1 - \nu_{Al}}$ is also known as the biaxial modulus and σ_{Al} is actually a biaxial stress.

When σ_{Al} exceeds the yield stress σ_y of aluminum, the film will experience plastic deformation. The result of the plastic deformation is a change in the residual stress state of the aluminum film. By rearranging equation 5.4, the change in temperature needed to induce plastic deformation is found to be

$$\Delta T = \frac{\sigma_y (1 - \nu_{al})}{E_{al} (\alpha_{Si} - \alpha_{Al})}. \quad (5.5)$$

Using the parameters of aluminum and silicon shown in tables A.1 and A.2 found in Appendix A, and assuming no initial residual stress in the aluminum film, the film will begin to experience plastic deformation with a ΔT of only $\pm 47^\circ\text{C}$. This is a very small change in temperature and is experienced routinely during fabrication. Even a process as simple as an oxygen plasma etch to strip photoresist will significantly exceed this ΔT .

One of the most difficult properties of this type of evolution of the stress state in aluminum films is that it does not produce a constant stress through the thickness of the film. A constant stress state can be relieved through the use of flexures that are doubled back, allowing expansion or contraction of the structure to be compensated. Another alternative to deal with a constant residual stress is to use a cantilever beam, which can expand or contract freely to compensate for the constant stress. The stress state that is actually produced by the plastic deformation of the aluminum film is a combination of a constant (mean) stress and a stress gradient through the thickness of the film.

The stress gradient in the film is a result of the aluminum being bonded to a substrate that doesn't allow dislocation flow. Upon reaching the temperature necessary

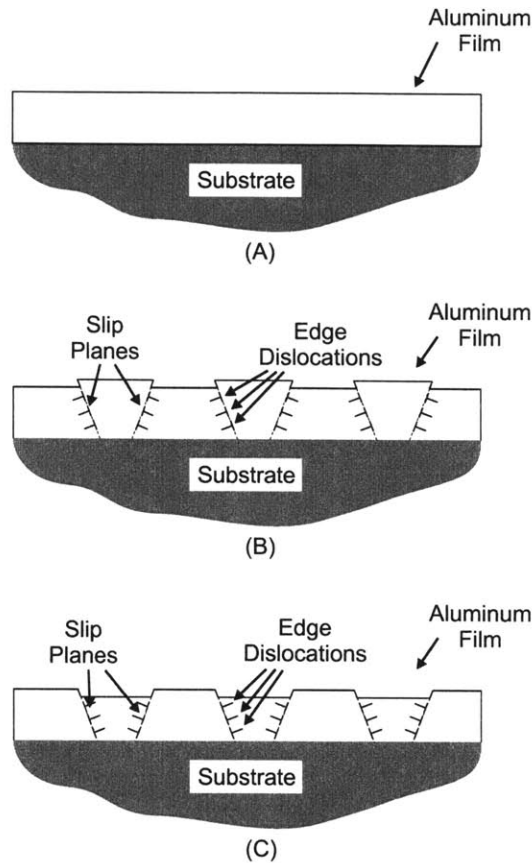


Figure 5-1: Illustrations of the dislocation pile-up experienced by the aluminum film during thermally induced plastic deformation. (A) illustrates the film prior to plastic deformation. (B) illustrates the film after deforming plastically due to temperature increase. (C) illustrates the film after deforming plastically due to a temperature decrease.

for the aluminum film to experience plastic deformation, dislocations flow through the aluminum film but are blocked at the interface of the aluminum film and the silicon substrate. This causes the dislocations to pile up in the aluminum film, creating a gradient in the plastic deformation [72, 95]. Figure 5-1 illustrates the dislocation pile-up effect.

The plastic deformation experienced by the free surface of the film relieves the thermally induced stress that exceeds the yield stress of the aluminum film. The constrained (bottom) surface of the film is not allowed to plastically deform and therefore maintains all of the thermally induced stress. This difference in stress

states between the top of the and bottom surfaces of the film creates a stress gradient through the thickness of the film [72, 95]. As shown in Figure 5-1, the sign of the stress gradient in the film is different depending on whether a temperature increase or a temperature decrease caused the plastic deformation.

5.2 Titanium nitride for MEMS applications

Due to the low temperature change that can induce plastic deformation in aluminum, efforts to modify the deposition parameters to achieve a stress free film appear to be futile since subsequent processing will change the stress state. In addition, efforts to achieve a stress free film by annealing do not succeed either, since the decrease in temperature from the anneal temperature to room temperature would cause a residual stress gradient to develop. For these reasons, a new bridge material was sought whose stress state could be more readily controlled.

In selecting a material that eliminates the evolution of the stress state that was experienced by the aluminum film, several requirements need to be met. First of all, the material needs to be CMOS compatible to allow integration of the optical switch with CMOS integrated circuits. Next, to eliminate the evolution of the stress state, either the coefficient of thermal expansion of the material needs to match that of silicon, or the material needs to not plastically deform. The latter would be the case for a brittle material or a material with a very high yield stress. Moreover, the material needs to be electrically conductive to both function as an electrode for the MEMS actuator and to introduce optical loss into the ring resonator.

Of the materials commonly available in CMOS fabrication, titanium nitride was the best match with the requirements. Although titanium nitride is commonly used in CMOS fabrication [32, 42, 74, 106], this work represents the first use of titanium nitride as an electro-mechanical structural material in MEMS.

5.2.1 Titanium nitride versus other MEMS materials

Titanium nitride has some very appealing mechanical properties for MEMS applications. These properties include a high modulus, high melting temperature, high strength, high stiffness to density ratio, excellent chemical stability, superior anti-stiction characteristics (low surface adhesion energies), high hardness, and wear (abrasion) resistance [75,82,106]. It is due to these outstanding mechanical properties that leads titanium nitride to be used in its second common application area, as a wear resistant coating for machine tools [75,82].

What makes titanium nitride particularly interesting is that, in addition to these mechanical properties, it is also electrically conductive and is thus part of a unique group of materials called electroceramics. This unique combination of electrical and mechanical properties has the potential to be very useful in MEMS devices. To achieve similar properties, usually a bimaterial structure is required. For example, bridges made of a bilayer of silicon nitride and aluminum have been created to achieve a mechanically stiff structure that is electrically conductive [4]. Titanium nitride would allow a simpler bridge constructed of a single material that retains the high mechanical stiffness and is electrically conductive.

5.3 Fabrication techniques for titanium nitride

As mentioned previously, titanium nitride is commonly used in CMOS fabrication as an adhesion layer and diffusion barrier. It is also used as a wear-resistant coating for machine tools. Because of these applications, much is already known about the fabrication processes (deposition, etching, etc.) for titanium nitride.

5.3.1 Deposition

Titanium nitride deposition techniques include sputtering, CVD, evaporation, and arc evaporation [42,64,75,82,106]. Of these deposition techniques, the most common in microfabrication is sputtering, which is also the technique that was used in this

work.

Sputtering of titanium nitride can be accomplished in a number of ways. RF magnetron sputtering or inductively coupled plasma DC magnetron sputtering can be used. In addition, the sputtering target can be either titanium nitride, or, more commonly, a titanium target with a nitrogen gas flow into the chamber. The titanium reacts with the nitrogen and the resulting deposited film is titanium nitride. In addition to the nitrogen, argon is also usually flowed into the chamber. Argon is inert and doesn't participate in the reaction that creates the titanium nitride but does provide a means to control the pressure of the chamber.

Titanium nitride is unique in that many material properties of the film can be varied over a wide range by changing the deposition parameters. Specifically, the Young's modulus can be controllably altered from 100 GPa up to 640 GPa. The density can also be changed from 3700 kg/m³ up to 5700 kg/m³. In addition, similar to many materials, the residual stress can be altered by changing the deposition conditions. For a more complete list of material properties of titanium nitride, see Table A.5 in Appendix A.

5.3.2 Etching

Titanium nitride can be patterned by a number of different techniques including wet etching, reactive ion etching (RIE), and lift-off. Wet etching of titanium nitride can be accomplished using a variety of chemistries. For example, the RCA standard clean 1 (SC1, NH₄OH+H₂O₂+H₂O) can be used to selectively etch titanium nitride [19], or just NH₄OH+H₂O₂ [118]. In addition, dilute HNO₃ can also be used [21] or H₂SO₄+H₂O₂ [19].

RIE of titanium nitride is also widely practiced. Chemistries that have been used for RIE of titanium nitride include BCl₃/Cl₂ [1], SiCl₄ [52], and Cl₂/Ar/CHF₃ [1]. Lift-off has also been used to pattern titanium nitride [153]. In this work, the titanium nitride layer was etched using a BCl₃/Cl₂ RIE chemistry.

5.3.3 Residual stress management

Residual stress can be controlled by adjusting the deposition parameters (i.e., pressure, applied power, field strength, gas flow rates, temperature, etc.) [32, 42, 64, 82]. Residual stress may also be modified by interrupting the columnar grain growth of titanium nitride by depositing a thin amorphous material layer between subsequent titanium nitride depositions [75]. Residual stress has also been diminished by high-energy ion bombardment pulses during the deposition [10].

One of the most interesting techniques involves a low temperature anneal of the titanium nitride. Typically, the temperature required to anneal ceramic materials is roughly half of the melting temperature of the material [95]. However, in the case of sputtered titanium nitride, where there is a high density of defects (vacancies, interstitials, dislocations, etc.) in the crystal lattice, the anneal temperature can be significantly lower than half the melting temperature of titanium nitride. Temperatures anywhere in the range of 100 to 600°C have been reported to allow annealing to occur [32, 42, 74]. The approach to residual stress reduction used in this work was based on this low temperature anneal capability of sputtered titanium nitride.

5.3.4 Sacrificial materials

Since titanium nitride can be deposited at low temperatures (<200°C) [32, 64, 106], polymers are an obvious choice for a sacrificial material for titanium nitride. SU-8, polyimide, and photoresist are all potential candidates. Polymeric sacrificial materials can be removed by oxygen plasma (ashing) or possibly Nano-Strip^{TM1} to leave the titanium structures free standing. Polymers do have some drawbacks as sacrificial materials. In the very high vacuums that titanium nitride is deposited in, the polymers may significantly outgas. Also, if annealing of the titanium nitride is desired to remove residual stress, the polymer material would limit the anneal temperature.

A second option as a sacrificial material for titanium nitride is silicon (amorphous, polycrystal, or single crystal). One possible release etch for a silicon sacrificial material

¹Nano-StripTM is a commercially available solution that removes polymeric material such as photoresist from wafers.

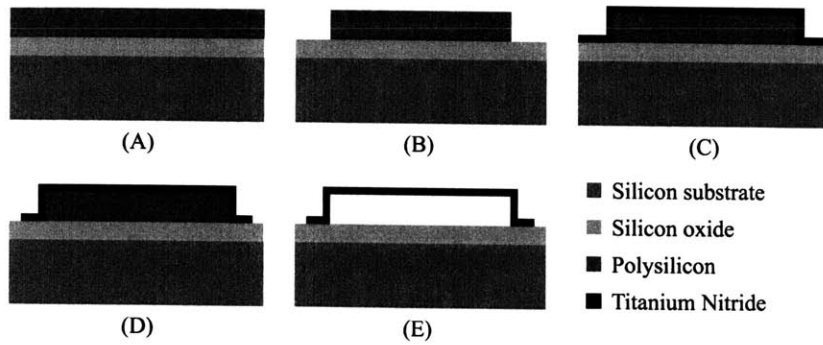


Figure 5-2: Illustration of the fabrication process used to create the titanium nitride MEMS bridges. (A) A silicon oxide film is first grown, followed by deposition of a polysilicon film. (B) The poly-silicon sacrificial layer is patterned and etched with contact photolithography followed by reactive ion etching (RIE). (C) The titanium nitride film is deposited by sputtering. (D) The titanium nitride film is patterned and etched using contact photolithography and etched by RIE. (E) The sacrificial poly-silicon layer is removed using a gas phase xenon difluoride etch.

is a gas phase xenon difluoride etch. Using silicon as the sacrificial material allows for better fabrication compatibility than a polymeric sacrificial material. In addition, the silicon allows higher titanium nitride anneal temperatures to be reached. In addition, if amorphous silicon is used, the deposition temperature can be quite low. For the titanium nitride MEMS bridges fabricated in this work, poly-silicon was used as the sacrificial material.

5.4 Fabrication process

To evaluate titanium nitride as a potential material for MEMS applications, and specifically for use in the wavelength selective optical MEMS switch, some prototype bridge structures were fabricated out of titanium nitride. The fabrication process for the bridge structures was very similar to that used for the aluminum bridges that were integrated with the ring resonator filters. Therefore, direct integration of the titanium nitride bridges with optical ring resonators in the future will be straightforward.

The fabrication process for the titanium nitride prototype bridge structures is shown in Figure 5-2, with details given in Table 5.1. The key differences in this

process as compared with the process for the aluminum device is that RIE was used to etch the titanium nitride rather than a wet etch. Also, the dicing and packaging requirements were much more relaxed because there were no waveguides incorporated in these structures.

The anneal step (step 24) was included for only some of the bridge devices to determine the effects of the anneal on the titanium nitride as compared with unannealed structures.

Table 5.1: Fabrication process for the titanium nitride prototype bridge structures.

Step	Machine	Process Notes
1	Wet station	RCA clean
2	Diffusion tube	Grow 250 nm thermal oxide film
3	Wet station	RCA clean
4	Low-pressure diffusion tube	Deposit 1.1 μm poly-silicon film
5	HMDS oven	Vapor-phase deposition of HMDS
6	Spin coater	Coat wafer with 1.3 μm of photo-resist
7	Oven	Pre-bake photoresist for 30 min at 90°C
8	EV620 Aligner	Align mask and expose photoresist
9	Wet station	Develop photoresist
10	Oven	Post-bake photoresist for 30 min at 120°C
11	Lam 490B	Reactive ion etch (RIE) polysilicon
12	Oxygen plasma asher	Strip photoresist
13	Wet station	Piranha clean and HF dip
14	Endura 5500	Sputter 250nm of titanium nitride
15	HMDS oven	Vapor phase deposition of HMDS
16	Spin coater	Coat wafer with 1.0 μm of photoresist

continued on next page

Table 5.1: *continued*

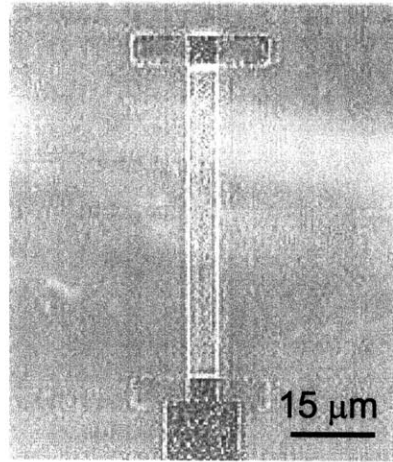
Step	Machine	Process Notes
17	Oven	Pre-bake photoresist for 30 min at 90°C
18	EV620 Aligner	Align mask and expose photoresist
19	Wet station	Develop photoresist
20	Oven	Post-bake photoresist for 30 min at 120°C
21	Lam Rainbow 9600	RIE titanium nitride
22	Oxygen plasma asher	Strip photoresist
23		Cleave wafer
24	<i>KLA Tencor FLX-2320</i>	<i>Anneal titanium nitride film</i>
25	Xenon difluoride etcher	Release etch poly-silicon

5.5 Experimental characterization of titanium nitride

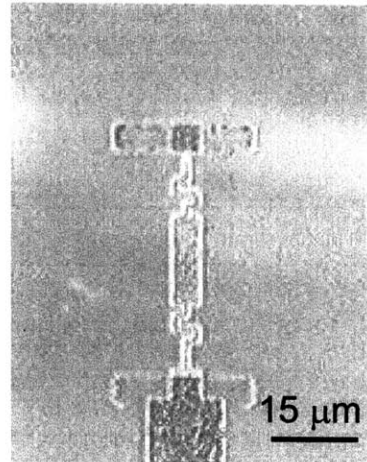
The prototype titanium nitride bridge structures were very encouraging. Optical microscope images of fabricated structures are shown in Figure 5-3 where it can be seen that xenon difluoride etching released very effectively the titanium nitride bridges without noticeable etching of the bridges. Annealing of the titanium nitride was found to be effective for significantly reducing the residual stress of the structure.

5.5.1 Titanium nitride anneal

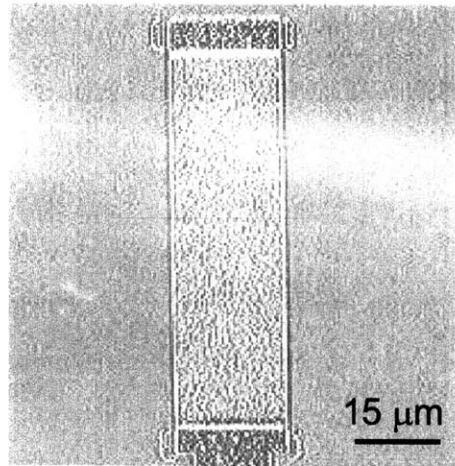
The titanium nitride was annealed in a KLA Tencor FLX-2320 stress measurement machine. This allowed constant monitoring of the stress of the titanium nitride during the anneal process. Figure 5-4 shows a typical result from the anneal process where the temperature was ramped from room temperature up to 500°C at a rate of 2°C per



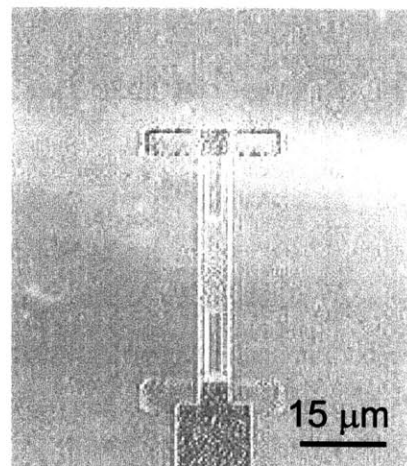
(A)



(B)



(C)



(D)

Figure 5-3: Optical micrographs of a variety of prototype titanium nitride bridges structures.

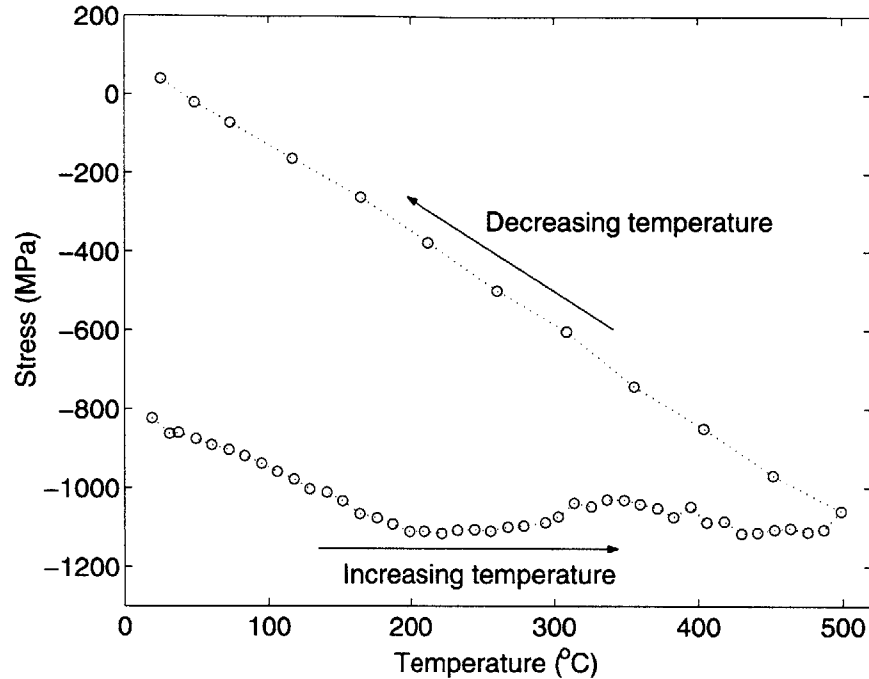


Figure 5-4: Plot of the titanium nitride film stress as a function of temperature during the anneal process.

minute. After reaching 500°C, the temperature was ramped down at 2°C per minute until it reached room temperature. There was no dwell time at 500°C.

As can be seen from Figure 5-4, the initial stress of the titanium nitride film was -822.6 MPa. At the end of the anneal the stress was 40 MPa. The film begins annealing at about 200°C, indicating that the anneal process could thus be run at a temperature as low as 200°C to anneal the titanium nitride film. The lower anneal temperature would require a longer time for the process.

While other researchers have reported success with annealing titanium nitride in air [32], some of our samples (~25%) experienced significant oxidation of the titanium nitride film during the anneal process. Using an atmosphere that does not contain oxygen, such as forming gas, during the anneal process is probably a better approach. Ammonia has also been reported as a beneficial gas for annealing titanium nitride [74].

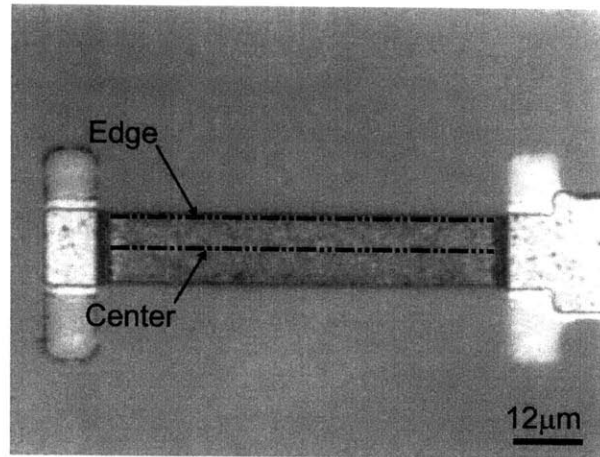
A second challenge associated with the anneal was the formation of a thin layer of titanium silicide at the interface of the titanium nitride and the silicon sacrificial

layer. This was the result of some interdiffusion of silicon and titanium nitride at their interface. The interdiffusion can be minimized by reducing the temperature and increasing the time of the anneal step or by using an appropriate diffusion barrier between the titanium nitride and the silicon.

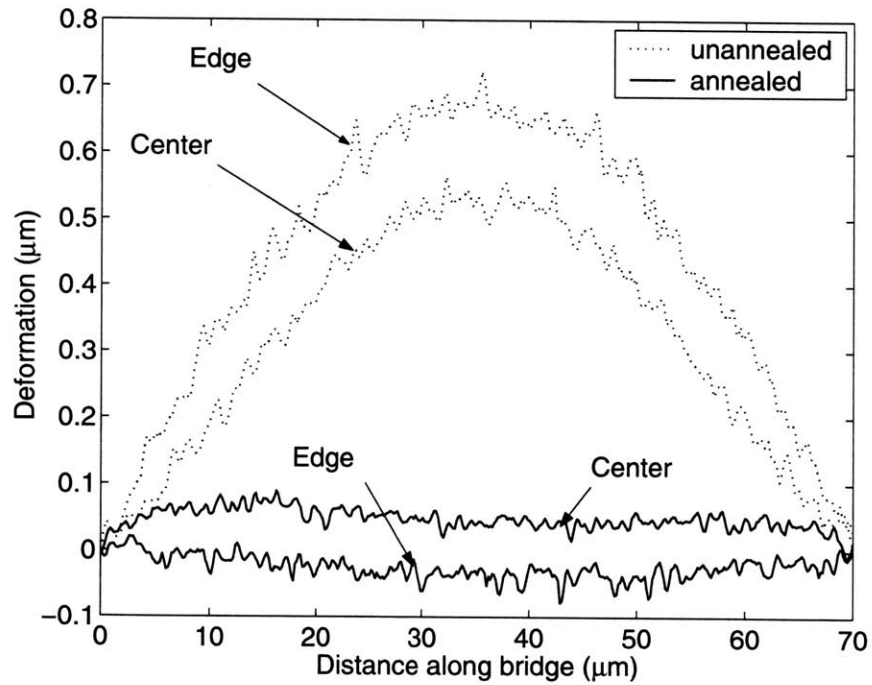
The anneal step had a significant impact on the deformation of the bridge structures. Bridges that were unannealed buckled due to the very high compressive stress in the structures. Annealed bridges were quite flat. Figure 5-5 compares surface contours along the length of annealed and unannealed bridges to illustrate the significant reduction in deformation achieved due to the anneal.

5.6 Discussion

This is the first example of titanium nitride being used as a structural material in a MEMS device. The ability to control the stress state with a low temperature anneal while still possessing all of the very unique properties mentioned in Section 5.2.1 makes titanium nitride a very desirable material for subsequent versions of the wavelength selective switch. In addition, titanium nitride has advantages over most typical MEMS materials for a wide range of other MEMS devices [124]. It is hoped that the preliminary characterization and demonstration of titanium nitride as a structural material for MEMS bridges carried out in this thesis will result in a much wider adoption of this material in future MEMS processes.



(A)



(B)

Figure 5-5: Contours along the center and edge (as illustrated in (A)) of an unannealed and an annealed titanium nitride bridge. The deformation of the annealed bridge is much less than that of the unannealed bridge.

Chapter 6

Dynamic pull-in

One of the requirements to integrate the wavelength selective switch into an optoelectronic integrated circuit is CMOS compatibility, i.e. the actuation voltage should be the same as that used within CMOS integrated circuits. This is typically about five volts. The prototype wavelength selective switch required 24 volts for actuation. In this chapter a new technique is described that makes use of the dynamic characteristics of the mechanical bridge to significantly reduce the required actuation voltage.

Typically the analysis of the pull-in phenomenon associated with parallel plate actuators is performed using quasi-static assumptions. However, it has been experimentally shown that under dynamic conditions, the pull-in voltage can be different from what the quasi-static analysis predicts. Sattler et al, found that for a torsional electrostatic switch, the quasi-static pull-in voltage was 8V; however, when the voltage was applied as a step function, the pull-in voltage was 7.3V [119].

In this chapter, analytical and numerical models exploring *dynamic* pull-in of both parallel plate and torsional actuators are presented. Pull-in due to a step input voltage is first examined and shown to be in agreement with the results of Sattler et al. The analysis is then extended to a case where a modulated voltage is applied and pull-in is experienced after a number of mechanical oscillations.

For pull-in to occur, a certain amount of energy needs to be injected into the system [13,99]. The modulated voltage pull-in technique relies on energy being accumulated in the mechanical system during the pull-in process. This allows the energy

required for pull-in to be input over a number of mechanical oscillations rather than all at once. The modulated pull-in technique thus requires less *power* for pull-in, and leads to substantially lower voltage level requirements. The trade-off for this lower actuation voltage is that the time for pull-in to occur becomes longer.

Our analysis of dynamic pull-in indicates that the pull-in points for both the step voltage case and the modulated voltage case are dependent on dissipation, also represented by the quality factor of the mechanical system. For critically damped or overdamped structures, it is found that the quasi-static analysis adequately describes pull-in, regardless of the applied potential function. However, for underdamped systems, the dynamic behavior can have a significant effect on the pull-in voltage.

6.1 System Model

To explore the dynamic response and pull-in of both parallel plate and torsional electrostatic actuators, lumped parameter models have been used. All of the mechanical terms (inertia, damping, and stiffness) have been assumed to be linear. The electrostatic force term is, of course, nonlinear for both the parallel plate and the torsional actuator cases. The important assumptions made in selecting this model are related to the squeezed film effect, the motion and shape of the moving plate, and, for doubly clamped parallel plate structures, the axial stretching effect. Additionally, the charging and discharging of the capacitor formed by the two plates was assumed to be fast relative to the mechanical system.

The squeezed film effect can cause both the damping and the stiffness terms to become nonlinear [125,135,141]. For the lower quality factors discussed in this chapter ($Q < 10$), the validity of the linear damping and stiffness assumption depends very much on the geometry of the structure. For example, the moving plate needs to have adequate squeeze film damping holes to make the nonlinear squeezed film effects negligible. For the higher quality factors discussed in this chapter, the structures would need to be in a vacuum, which significantly reduces the squeezed film effect regardless of the geometry of the structure.

In the two models that we propose, the motion of the plates has been idealized. It is assumed that the parallel plate only displaces in the dimension perpendicular to the plane defined by the fixed electrode, and that the displacement is the same for all points on the movable plate (i.e., the plate is ideally rigid). The motion for the torsional case is assumed to be strictly rotational about the point where the torsional springs are attached. How well these assumptions hold depends predominantly on the geometry of a particular device [152].

For a doubly clamped plate in a parallel plate actuator, axial stretching can introduce a nonlinear term into the mechanical stiffness of the structure. This nonlinear effect is called the Duffing nonlinearity. The relative significance of this nonlinear term depends on the geometry of the structure, and the residual stress present in the plate [14, 152].

In addition to these assumptions related to the parameters of the mathematical model, there are also assumptions implied by the model about the electrical drive components. The assumption is that the RC time constant of the capacitor formed from the parallel plate actuator is much smaller than the mechanical time constant. This allows the direct application of step voltages and other waveforms. If the electrical and mechanical time constants are similar, the voltage across the parallel plates would have a significant rise time as compared with the mechanical response [13]. In this case, the instantaneous force on the actuator should be calculated from the accumulated charge on the electrodes, rather than the applied voltage.

While these modelling assumptions certainly do leave out a subset of electrostatic structures, the dynamic pull-in analysis provided in this paper should still provide some qualitative intuition into how those structures behave. For many electrostatic structures, the work presented in this paper should be directly applicable.

6.1.1 Parallel Plate Model

The lumped parameter model for the parallel plate actuator is shown in Figure 6-1. It is composed of a movable electrode with mass m , a spring k , a damper b , and a fixed electrode. A voltage is applied across the two electrodes to cause the movable

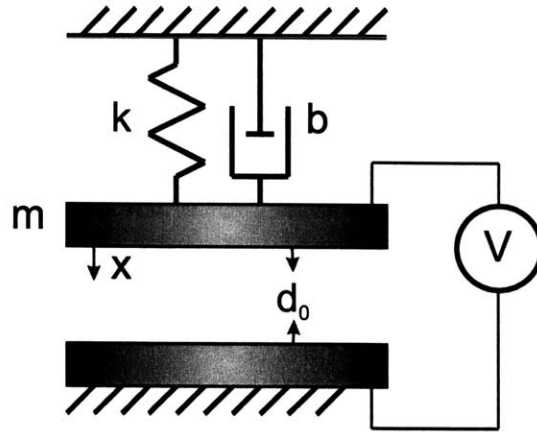


Figure 6-1: Lumped parameter model of a parallel plate actuator.

electrode to displace x . This model includes the assumptions discussed in Section 6.1. The equation of motion associated with this lumped parameter model is

$$m\ddot{x} + b\dot{x} + kx = \frac{\epsilon_0 AV^2}{2(d_0 - x)^2}, \quad (6.1)$$

The quasi-static behavior of this model was analyzed in Section 2.4. The key relationships resulting from that analysis that will be used here are the applied voltage versus displacement equilibrium equation

$$V_0 = \sqrt{\frac{2kx(d_0 - x)^2}{\epsilon_0 A}}, \quad (6.2)$$

and the pull-in voltage equation

$$V_{\text{pi}} = \sqrt{\frac{8kd_0^3}{27\epsilon_0 A}}. \quad (6.3)$$

Equation 6.2 is plotted in Figure 6-2 and indicates the pull-in position and voltage, and illustrates the bifurcation experienced for applied voltages increasing from zero to above the pull-in voltage (this figure is also shown in Figure 2-5).

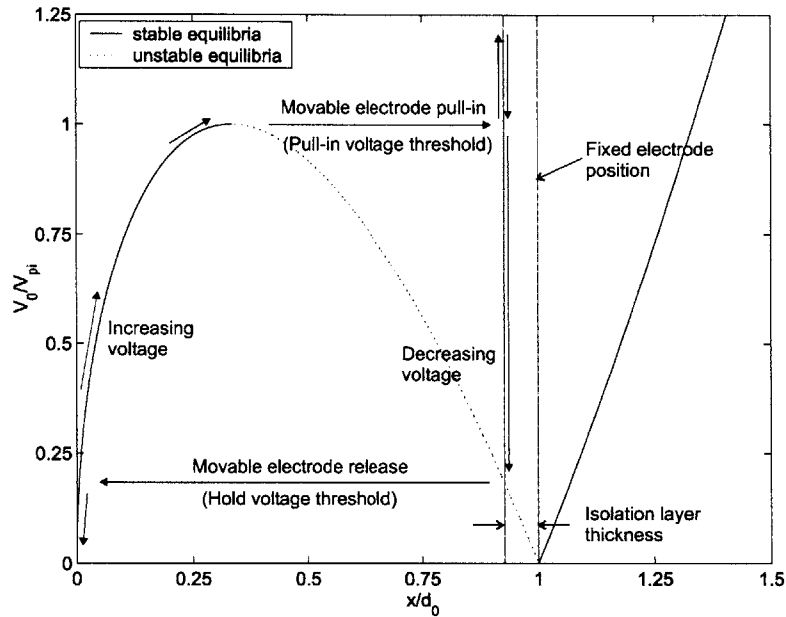


Figure 6-2: Quasi-static equilibrium curve for the parallel plate actuator from Equation 6.2. The arrows showing the evolution of the equilibrium positions for increasing and decreasing voltage indicate the bifurcation in the system. When the pull-in voltage is reached, the movable plate tries to jump to the equilibrium position to the right of the fixed electrode position. The isolation layer between the two electrodes will, of course, limit the plate's displacement so it won't reach the theoretical equilibrium position. The thickness of the isolation layer determines the voltage required to maintain the movable plate in the pulled-in state, referred to as the "hold" voltage [22].

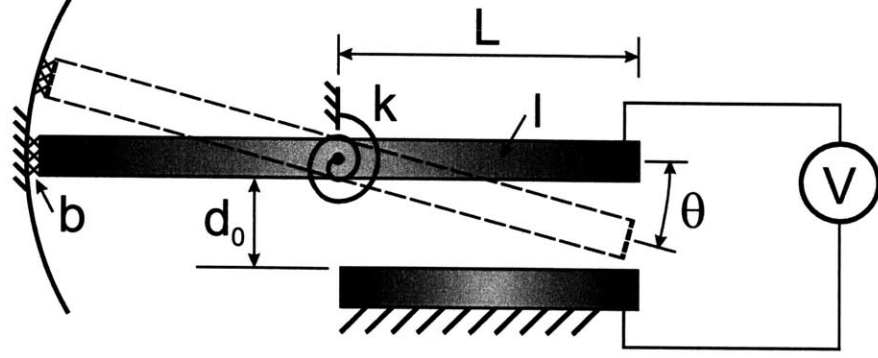


Figure 6-3: Lumped parameter model for a torsional electrostatic actuator.

6.1.2 Torsional Model

Figure 6-3 shows a simple model for a torsional electrostatic actuator with the same assumptions as the parallel plate model. From this model, the following equation of motion can be derived using a small angle approximation ($L_t \gg d_0$) [119],

$$I\ddot{\theta} + b\dot{\theta} + k\theta = \frac{\epsilon_0 w_t V^2}{2\theta^2} \left[\frac{L_t \theta}{d_0 - L_t \theta} + \ln \left(1 - \frac{L_t \theta}{d_0} \right) \right], \quad (6.4)$$

where I is the mass moment of inertia about the center of rotation, w_t is the width of the torsional plate, θ is the rotational displacement, L_t is the length of the plate from the center of rotation to the plate tip, and d_0 is the initial separation of the plates.

The torsional actuator also experiences pull-in. By again using a quasi-static assumption ($\ddot{\theta} = \dot{\theta} = 0$), the following equation describing the voltage required for a given equilibrium position is found,

$$V_0 = \sqrt{\frac{2k\theta^3 (d_0 - L_t \theta)}{\epsilon_0 w_t \left[L_t \theta + (d_0 - L_t \theta) \ln \left(1 - \frac{L_t \theta}{d_0} \right) \right]}}. \quad (6.5)$$

By numerically calculating the maximum of Equation 6.5, the pull-in point is found to be [119]

$$\theta \approx 0.4404\theta_0, \quad (6.6)$$

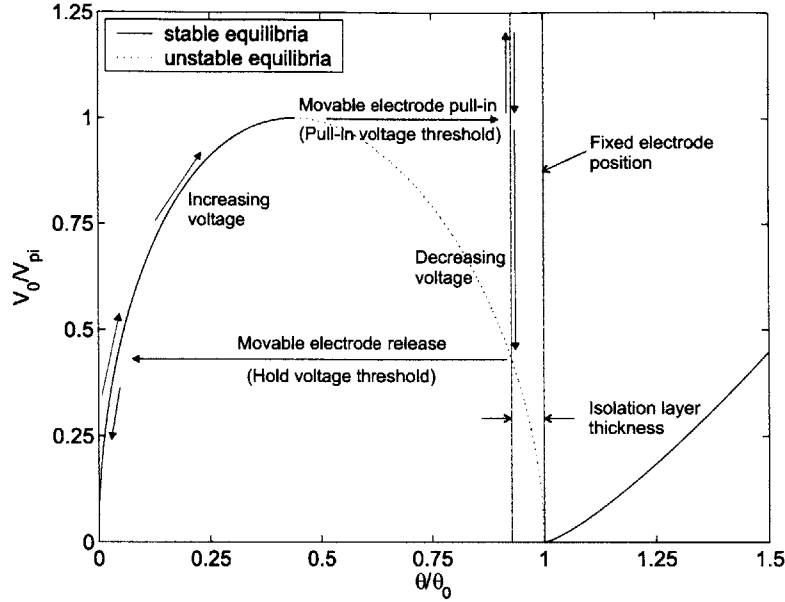


Figure 6-4: Quasi-static equilibrium curve for the torsional actuator from Equation 6.5. The arrows showing the evolution of the equilibrium positions for increasing and decreasing voltage indicate the bifurcation in the system. When the pull-in voltage is reached, the movable plate tries to jump to the equilibrium position to the right of the fixed electrode position. The isolation layer between the two electrodes will, of course, limit the plate's rotation so it won't reach the theoretical equilibrium position. The thickness of the isolation layer determines the voltage required to maintain the movable plate in the pulled-in state, referred to as the "hold" voltage [22].

where θ_0 is the maximum torsional angle ($\theta_0 \approx d_0/L_t$). The pull-in voltage associated with this point is given by

$$V_{pi} \approx \sqrt{0.827 \frac{k d_0^3}{\epsilon_0 w_t L_t^3}}. \quad (6.7)$$

The voltage versus equilibrium curve for Equation 6.5 is shown in Figure 6-4. This curve is in many ways similar to the curve shown in Figure 6-2. The main difference being that the local maximum (indicating the pull-in point) of the torsional curve is shifted slightly to the right of the the maximum for the parallel plate case.

6.2 Step voltage response and pull-in

Perhaps the most common signal applied to parallel plate or torsional electrostatic MEMS devices is a step voltage. For underdamped systems, the response of the structure to a step input causes the structure to overshoot the equilibrium position. If the overshoot is large enough, pull-in could potentially occur at voltages lower than V_{pi} .

For the step response analysis, the applied voltage will take the form

$$V(t) = V_0 U(t), \quad (6.8)$$

where $U(t)$ is a unit step function and V_0 is the magnitude of the voltage.

Due to the nonlinear nature of the parallel plate and torsional models, finding an analytical solution for the step response is difficult. However, by analyzing the energy of the system, the important features of the system response, such as overshoot and pull-in, can be identified.

Initially, the system is at rest and has no stored energy. When the step voltage is applied, energy is injected into the system. The system stores this energy as both kinetic and potential energy. Over time, the stored energy above that associated with the equilibrium position is lost to damping. The energy balance of the system at any instant in time can thus be written as

$$E_{injected} = E_{kinetic} + E_{potential} + E_{dissipated}. \quad (6.9)$$

The lowest possible pull-in voltage occurs when the overshoot has its maximum value. The overshoot can be maximized by setting the damping equal to zero. Under this condition, no energy is lost to dissipation and, hence, the energy dissipation term in Equation 6.9 can be neglected.

When the system is at its point of maximum overshoot, all of the stored energy is in the form of potential energy. The velocity and, therefore, the kinetic energy are zero at that point. By analyzing the energy of the system at this instant, the decrease

in the voltage required for pull-in can be calculated. We will use this technique to analyze pull-in due to a step input for both the parallel plate and the torsional actuators.

6.2.1 Step Voltage System Response - Parallel Plate Case

For the parallel plate actuator case, the stored potential energy can be expressed as

$$E_{\text{potential}} = \frac{1}{2}kx_{\text{max}}^2, \quad (6.10)$$

where x_{max} is the maximum overshoot.

The energy injected into the system by the applied voltage can be found by integrating the force of the actuator over the displacement as

$$E_{\text{injected}} = \int_0^{x_{\text{max}}} \frac{\epsilon_0 AV_0^2}{2(d_0 - x)^2} dx = \frac{\epsilon_0 AV_0^2 x_{\text{max}}}{2d_0(d_0 - x_{\text{max}})}. \quad (6.11)$$

Combining Equations 6.9, 6.10, and 6.11, and setting the kinetic and dissipated energy terms to zero, gives the following expression for the step voltage as a function of maximum overshoot

$$V_0 = \sqrt{\frac{kd_0 x_{\text{max}}(d_0 - x_{\text{max}})}{\epsilon_0 A}}. \quad (6.12)$$

Taking the derivative of Equation 6.12 and setting it to zero ($\frac{dV_0}{dx} = 0$) gives

$$x_{\text{max}} = \frac{d_0}{2}, \quad (6.13)$$

which is the position of the local maximum of Equation 6.12 in the range of $0 < x < d_0$. It turns out that this corresponds to the largest maximum overshoot that can be achieved without pull-in occurring. Any increase in the step voltage would theoretically result in a maximum overshoot above d_0 , due to a bifurcation similar to the quasi-static pull-in analysis. The step voltage associated with this maximum overshoot is, therefore, analogous to the quasi-static pull-in voltage expressed in Equation 6.3. For this reason, we will refer to the step voltage associated with the overshoot

expressed in Equation 6.13 as the step pull-in voltage. It is given by

$$V_{\text{spi}} = \sqrt{\frac{k d_0^3}{4 \epsilon_0 A}}. \quad (6.14)$$

Taking the ratio between the step pull-in voltage, V_{spi} , and the quasi-static pull-in voltage, V_{pi} , gives

$$\frac{V_{\text{spi}}}{V_{\text{pi}}} = \sqrt{\frac{27}{32}} \approx 0.919, \quad (6.15)$$

which indicates that the step pull-in voltage, for the ideal case of no damping, is about 91.9% of the quasi-static pull-in voltage. Since this solution was derived for the ideal case of no damping, it represents a lower limit on the step pull-in voltage levels. The upper limit is provided by the quasi-static pull-in analysis.

Numerical simulations performed in Simulink of the response of the system in Figure 6-1 with non-zero damping to a step voltage signal indicate that for moderate to low damping ($Q > 10$), the step pull-in voltage stays relatively close to the theoretically predicted fraction of 91.9% of the quasi-static pull-in voltage.¹ As the system damping increases, the step pull-in point follows the quasi-static equilibrium curve up until it reaches the quasi-static pull-in point, as shown in Figure 6-5.

6.2.2 Step Voltage System Response - Torsional motion

The approach used to analyze the step response of the torsional actuator is essentially the same as that used with the parallel plate actuator. The energy relation given by Equation 6.9 is again used to examine the energy at the point of maximum overshoot. For the torsional case, the energy injected into the system up to the point of maximum overshoot is given by

$$\begin{aligned} E_{\text{injected}} &= \int_0^{\theta_{\text{max}}} \frac{\epsilon_0 w_t V^2}{2 \theta^2} \left[\frac{L_t \theta}{d_0 - L_t \theta} + \ln \left(1 - \frac{L_t \theta}{d_0} \right) \right] d\theta \\ &= -\frac{1}{2} \epsilon_0 w_t V^2 \left[\frac{1}{\theta_{\text{max}}} \ln \left(1 - \frac{L_t \theta_{\text{max}}}{d_0} \right) + \frac{L_t}{d_0} \right]. \end{aligned} \quad (6.16)$$

¹For example, numerical simulations give the ratio between the step pull-in voltage to the quasi-static pull-in voltage as .937 for a system quality factor of 10.

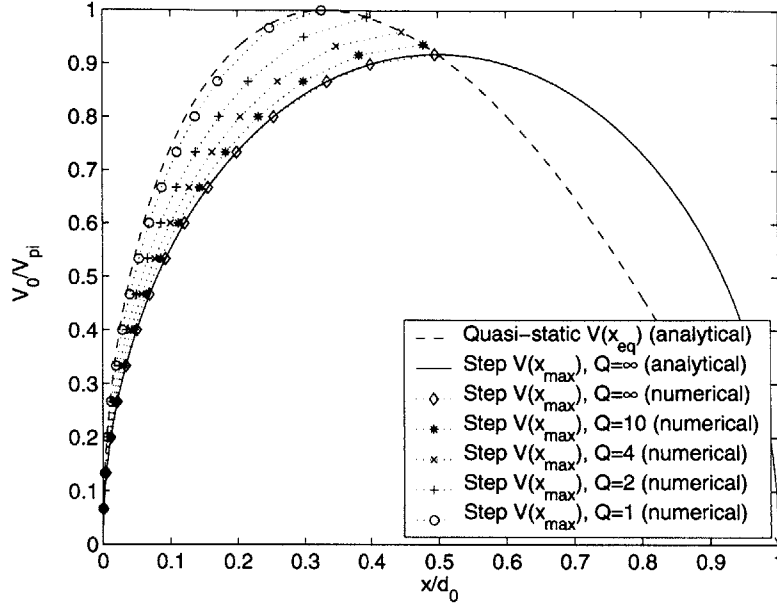


Figure 6-5: Plot of the required voltage for a given maximum overshoot for various levels of damping (Q values). As the quality factor of the system decreases, the step pull-in voltage moves from the ideal step pull-in voltage with no damping to the quasi-static pull-in voltage value.

The energy stored in the system at the maximum overshoot is

$$E_{\text{potential}} = \frac{1}{2} k_t \theta_{\text{max}}^2. \quad (6.17)$$

If we assume no damping in the system, then the energy injected will always equal the energy stored. Solving Equations 6.16 and 6.17 for the voltage gives the following relation between the max overshoot and the step voltage

$$V_0 = \sqrt{\frac{-k\theta_{\text{max}}^3}{\epsilon_0 \omega_t \left[\ln \left(1 - \frac{L_t \theta_{\text{max}}}{d_0} \right) + \frac{L_t \theta_{\text{max}}}{d_0} \right]}}. \quad (6.18)$$

The maximum of Equation 6.18 gives the maximum overshoot achieved before pull-in occurs. The location of this maximum is found numerically to be

$$\theta_{\text{max}} \approx 0.6450\theta_0. \quad (6.19)$$

This overshoot corresponds to a step pull-in voltage of

$$V_{spi} \approx \sqrt{0.6869 \frac{kd_0^3}{\epsilon_0 w_t L_t^3}}. \quad (6.20)$$

The ratio of the step pull-in voltage to the quasi-static pull-in voltage gives

$$\frac{V_{spi}}{V_{pi}} \approx 0.9114. \quad (6.21)$$

Again this solution was developed for a system with no damping and therefore represents a lower boundary on the decrease in pull-in voltage level required due to a step voltage input. Numerical simulations done in Simulink of the torsional system with increasing amounts of damping show that the step pull-in point follows the quasi-static equilibrium curve up until, at about a quality factor of one, the step pull-in occurs at the same point as the quasi-static pull-in, very much like the parallel plate actuator case. Figure 6-6 shows the analytical solution with no damping as well as the numerical solutions for various damping values compared with the quasi-static solution.

Sattler et al. [119] experimentally demonstrated the decreased pull-in voltage required when applying a step voltage to a torsional RF MEMS switch. They found that the quasi-static pull-in voltage for their device was 8.0V while the step pull-in voltage was 7.30V. These values give a ratio of 0.913 between the step pull-in voltage compared to the quasi-static pull-in voltage. As expected, this ratio is above the lower boundary defined by our analysis. However, the step pull-in point appears to be at about $0.58\theta_0$ for their experiments, which, based on our model, corresponds to a quality factor of about 3.75. For this quality factor, our analysis predicts the ratio of the quasi-static pull-in voltage to the step pull-in voltage to be 0.958, an over-prediction of the experimentally observed values by about 4.5%. The small discrepancy is likely due to a combination of small errors due to the assumptions made in our model, a lack of knowledge of the exact experimental conditions used in [119], and general experimental uncertainty.

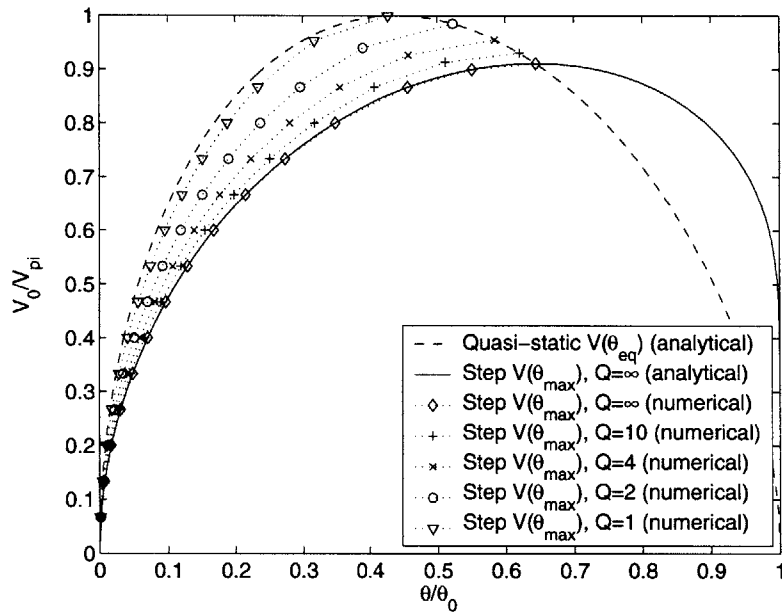


Figure 6-6: Plot of the required voltage for a given maximum overshoot for various levels of damping (Q values) for the torsional actuator. As the quality factor of the system decreases, the step pull-in voltage moves from the ideal step pull-in voltage with no damping to the quasi-static pull-in voltage value.

6.3 Modulated voltage system response and pull-in

The analysis of the step voltage pull-in indicates that by making use of the energy storing capabilities of the mechanical system, pull-in can be achieved at voltages lower than the levels predicted by the quasi-static analysis. This idea of leveraging the energy stored in the mechanical system can be taken even further by applying a voltage signal that is modulated according to the rule

$$V = \begin{cases} V_0 & \text{if the velocity } (\dot{x} \text{ or } \dot{\theta}) > 0 \\ 0 & \text{otherwise.} \end{cases} \quad (6.22)$$

The voltage signal will input energy into the mechanical system over a number of mechanical oscillations. This technique leads to larger displacements than would be possible with an unmodulated actuation signal at the same voltage level [8]. In addition to the injected energy, a certain amount of energy is lost to damping during each cycle. After some number of cycles, there are two possible outcomes. Either the system will reach a limit cycle where the energy input equals the energy lost per cycle [138], or the system will reach a pulled-in state. First let us assume that the system reaches a limit cycle. The energy balance of the system at the limit cycle is

$$E_{\text{injected}} = E_{\text{dissipated}}. \quad (6.23)$$

Deriving expressions for both terms in Equation 6.23 leads to expressions for the modulated voltage levels needed for pull-in to occur. This modulated actuation technique will be explored for both the parallel plate actuator and the torsional actuator.

6.3.1 Modulated Voltage System Response - Parallel Plate Case

For the parallel plate case, the energy injected per period is

$$E_{\text{injected}} = \int_{-x_{\text{max}}}^{x_{\text{max}}} \frac{\epsilon_0 A V_0^2}{2(d_0 - x)^2} dx = \frac{\epsilon_0 A V_0^2 x_{\text{max}}}{(d_0^2 - x_{\text{max}}^2)}, \quad (6.24)$$

where x_{max} refers to the amplitude of the limit cycle.

The energy dissipated is found indirectly by using the definition of the quality factor along with the stored energy in the system. The quality factor definition is

$$Q = 2\pi \frac{E_{\text{stored}}}{E_{\text{dissipated}}}. \quad (6.25)$$

By using this definition in the derivation, we are implicitly assuming that the displacement is sinusoidal in time. Due to the nonlinearities of the system, this is not exactly true. However, for moderate to high quality factors ($Q > 10$), the assumption is quite reasonable.²

The energy stored in the system is, in general, the sum of the kinetic and potential energy at any given instant in time. However, at the point of maximum displacement x_{max} , all of the stored energy is in the form of elastic potential energy. The stored energy can thus be expressed as

$$E_{\text{stored}} = \frac{1}{2} k x_{\text{max}}^2. \quad (6.26)$$

By combining Equations 6.23, 6.24, 6.25, and 6.26, it is possible to find a relationship for the modulated voltage level, V_0 , required for a given amplitude limit cycle. This relationship is

$$V_0 = \sqrt{\frac{\pi k x_{\text{max}} (d_0^2 - x_{\text{max}}^2)}{\epsilon_0 A Q}}. \quad (6.27)$$

The amplitude of the limit cycle that corresponds to the maximum voltage that

²An alternative derivation where a sinusoidal displacement is assumed explicitly and the dissipated energy is calculated directly gives identical results.

leads to a limit cycle can be found by taking the derivative of Equation 6.27 and setting it to zero ($\frac{dV_0}{dx} = 0$). This gives

$$x_{\max} = \frac{d_0}{\sqrt{3}} \approx 0.5774d_0. \quad (6.28)$$

The voltage associated with the limit cycle amplitude in Equation 6.28 is referred to as the modulated pull-in voltage, V_{mpi} . For any voltage V_0 above this voltage the system will pull-in after some number of mechanical oscillations. By combining Equations 6.27 and 6.28, the modulated pull-in voltage is found to be

$$V_{\text{mpi}} = \sqrt{\frac{2\pi k d_0^3}{3\sqrt{3}\epsilon_0 A Q}}. \quad (6.29)$$

The ratio of the modulated pull-in voltage, V_{mpi} to the quasi-static pull-in voltage, V_{pi} , is

$$\frac{V_{\text{mpi}}}{V_{\text{pi}}} = \sqrt{\frac{3\sqrt{3}\pi}{4Q}} \approx 2.02\sqrt{\frac{1}{Q}}. \quad (6.30)$$

This indicates that for a system with a quality factor of 100, the modulated pull-in voltage would be only 20% of the quasi-static pull-in voltage. This is a significant decrease in the required pull-in voltage. Systems with higher quality factors can lead to even lower voltage level requirements. Figure 6-7 gives the curves for the parallel plate actuators response to the modulated voltage for quality factors of 10, 100, and 1000. The quasi-static and ideal (no damping) step response curves are also included for comparison. Figure 6-8 shows displacement with time and phase-space plots from numerical simulations of the parallel plate actuator response to applied modulated voltages that are below and just above the modulated pull-in voltage.

6.3.2 Modulated Voltage System Response - Torsional Case

We now analyze the response of a torsional electrostatic actuator to an applied voltage that follows the rule given in Equation 6.22. The analysis for this case follows the same approach for the parallel plate case. A limit cycle occurs when the energy injected

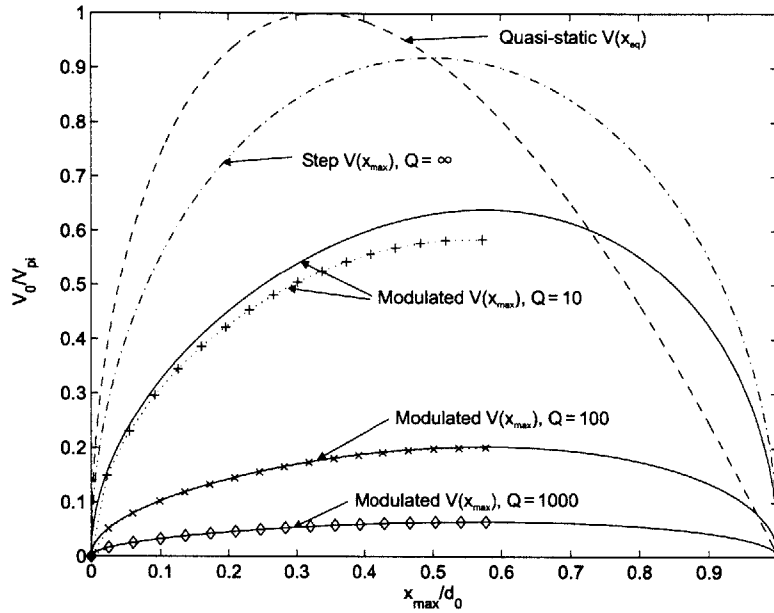


Figure 6-7: Numerical and analytical curves of the modulated voltage required for particular limit cycle amplitudes for parallel plate systems with quality factors of 10, 100, and 1000. The analytical solutions, from Equation 6.27, are the solid lines. The numerical simulation results are given by the data points. For $Q = 10$, the numerical and analytical solution show some discrepancy due to the sinusoidal motion assumption used in the analytical derivation. For comparison, the quasi-static equilibrium curve (Equation 6.2) and the step response curve (Equation 6.12) are also plotted. The peak of each curve defines that curve's pull-in voltage and position.

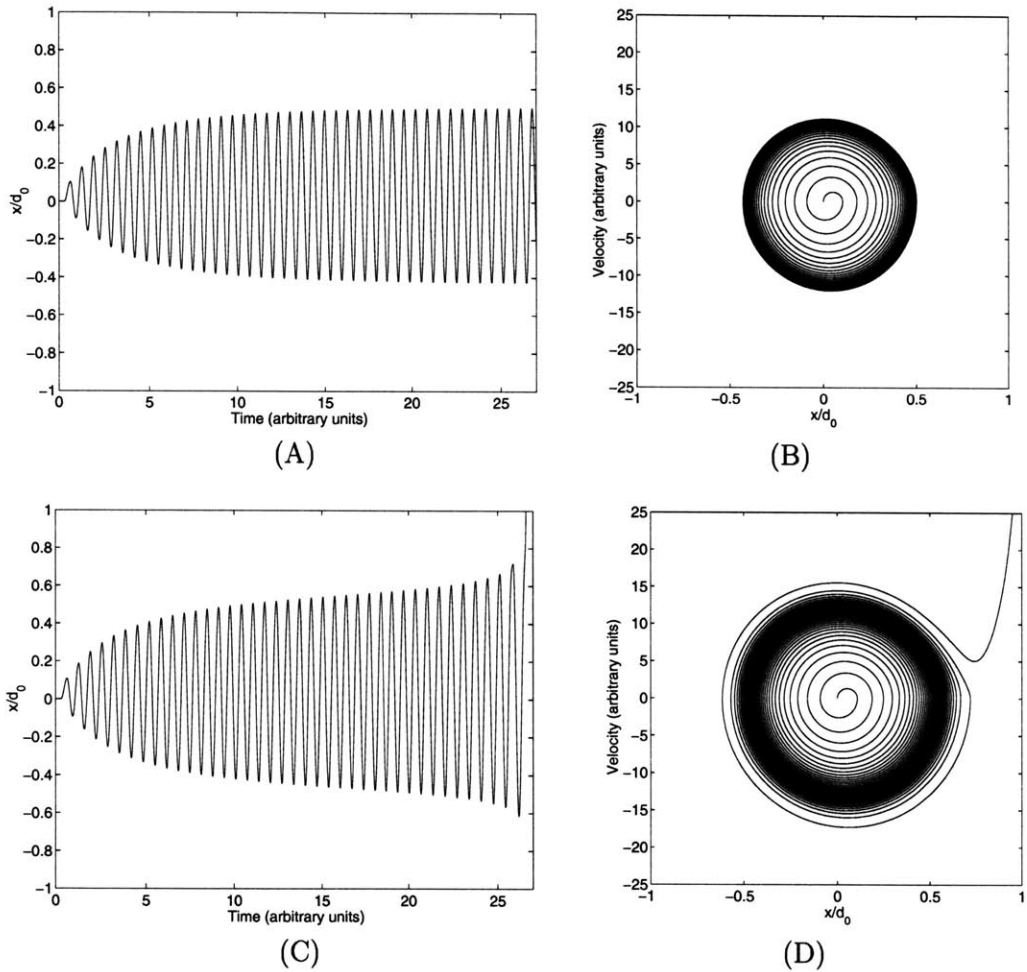


Figure 6-8: Numerical results showing the response of the parallel plate actuator to a modulated input voltage. In A) and B) the applied voltage level is below the modulated pull-in voltage. The system is seen converging to a limit cycle. C) and D) show the system pulling in with an applied voltage just above the modulated pull-in voltage level.

equals the energy dissipated (see Equation 6.23) [138]. The energy dissipated is found indirectly by combining the definition of the quality factor (see Equation 6.25) of the system with the energy stored in the system at the limit cycle. The energy stored at the limit cycle is calculated at the peak amplitude of the oscillation (θ_{\max}), when all the energy is stored as elastic potential energy. The equation for the total stored energy is

$$E_{\text{stored}} = \frac{1}{2}k\theta_{\max}^2 \quad (6.31)$$

The energy injected over one oscillation at the limit cycle is

$$\begin{aligned} E_{\text{injected}} &= \int_{-\theta_{\max}}^{\theta_{\max}} \frac{\epsilon_0 w_t V^2}{2\theta^2} \left[\frac{L_t \theta}{d_0 - L_t \theta} + \ln \left(1 - \frac{L_t \theta}{d_0} \right) \right] d\theta \\ &= -\frac{\epsilon_0 w_t V^2}{2\theta_{\max}} \ln \left(1 - \frac{L_t^2 \theta_{\max}^2}{d_0^2} \right) \end{aligned} \quad (6.32)$$

By combining Equations 6.23, 6.25, 6.31, 6.32, the solution for the voltage required for a given limit cycle is found to be

$$V_0 = \sqrt{\frac{2\pi k \theta_{\max}^3}{\epsilon_0 w_t Q \ln \left(1 - \frac{L_t^2 \theta_{\max}^2}{d_0^2} \right)}}. \quad (6.33)$$

The maximum of this function gives the pull-in point of the torsional actuator. Calculating the maximum of Equation 6.33 numerically indicates that the pull-in limit cycle amplitude is

$$\frac{\theta_{\max}}{\theta_0} \approx 0.7305, \quad (6.34)$$

which corresponds to a modulated pull-in voltage of

$$V_{\text{mpi}} \approx \sqrt{3.21 \frac{k d_0^3}{\epsilon_0 w_t Q L_t^3}}. \quad (6.35)$$

The ratio of the modulated pull-in voltage to the quasi-static pull-in voltage gives

$$\frac{V_{\text{mpi}}}{V_{\text{pi}}} \approx 1.97 \sqrt{\frac{1}{Q}}. \quad (6.36)$$

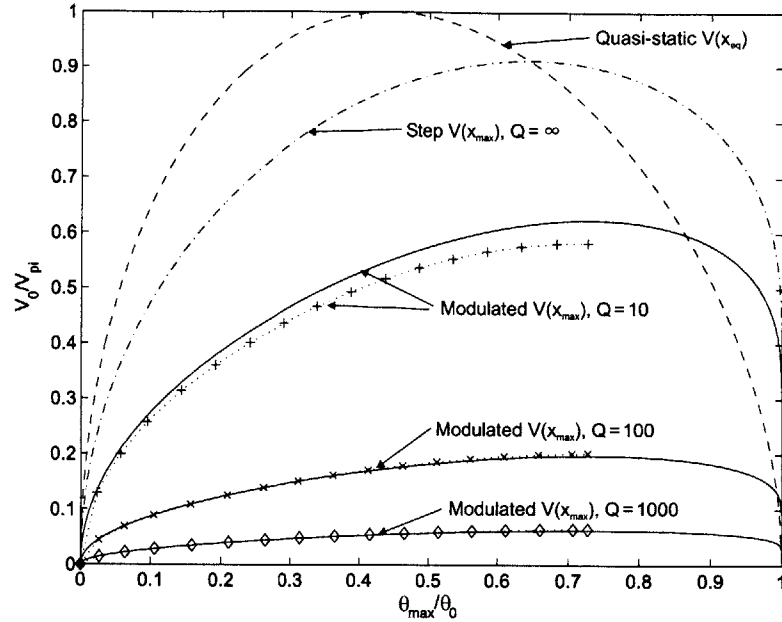


Figure 6-9: Numerical and analytical curves of the modulated voltage required for particular limit cycle amplitudes for torsional systems with quality factors of 10, 100, and 1000. The analytical solutions, from Equation 6.33, are the solid lines. The numerical simulation results are given by the data points. For $Q = 10$, the numerical and analytical solution show some discrepancy due to the sinusoidal motion assumption used in the analytical derivation. For comparison, the quasi-static equilibrium curve (Equation 6.5) and the step response curve (Equation 6.18) are also plotted. The peak of each curve defines that curve's pull-in voltage and position.

Figure 6-9 shows the effect of the quality factor on the limit cycle curves and pull-in points versus the quasi-static equilibrium curve and the system step response. The modulated voltage leads to significant reductions in the voltage requirements for pull-in of the torsional electrostatic actuator, very much like the parallel plate actuator.

6.3.3 Discussion

In torsional and parallel plate modulated pull-in and step pull-in, the quality factor of the system is the key parameter affecting the decrease in required actuation voltage. Figures 6-10 and 6-11 show the effect of the quality factor on the ratio of the dynamic pull-in voltages (step and modulated) with the quasi-static pull-in voltage. It is

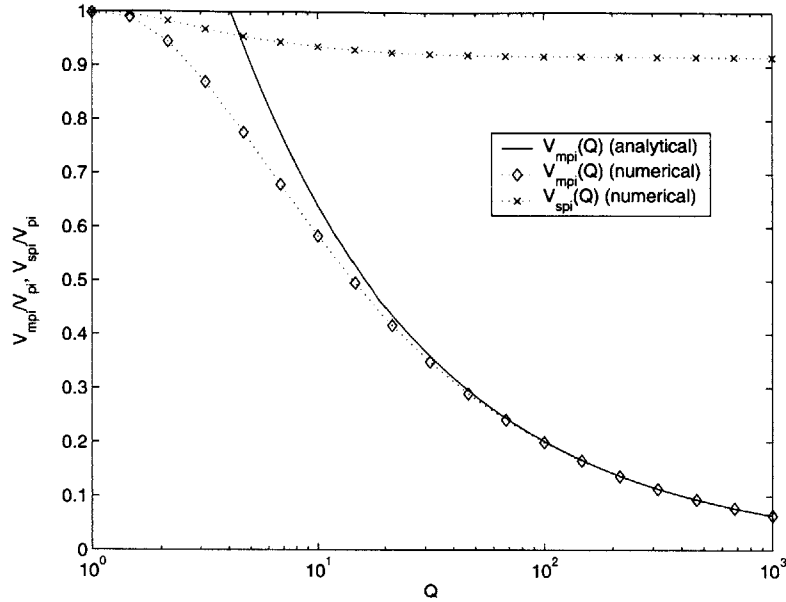


Figure 6-10: V_{spi} and V_{mpi} as a function of the quality factor for a parallel plate electrostatic actuator. For all values of Q greater than one, the modulated pull-in voltage is less than the step pull-in voltage.

interesting to note that for all damping levels the modulated pull-in voltage is less than or equal to the step pull-in voltage.

The modulated pull-in technique described here can lead to pull-in voltages that are significantly lower than the quasi-static pull-in voltage typically used as a minimum actuation voltage. This reduction in voltage needs to be balanced with the thickness of the insulating layer required between the two electrodes to maintain isolation. If the insulating film between the electrodes is too thick, the modulated pull-in voltage level won't be able to hold the structure in the pulled-in state. This is related to the "hold" voltage which is often used in parallel plate actuators and is illustrated in Figures 6-2 and 6-4 [22].

The waveform used in the modulated pull-in analysis provides the greatest transfer of energy, and hence the lowest pull-in voltage, of any waveform in a voltage limited situation; however, in principle any waveform that provides a net positive injection of energy with each cycle could be used. These alternative waveforms should also lead to a decrease in the voltage levels required for pull-in.

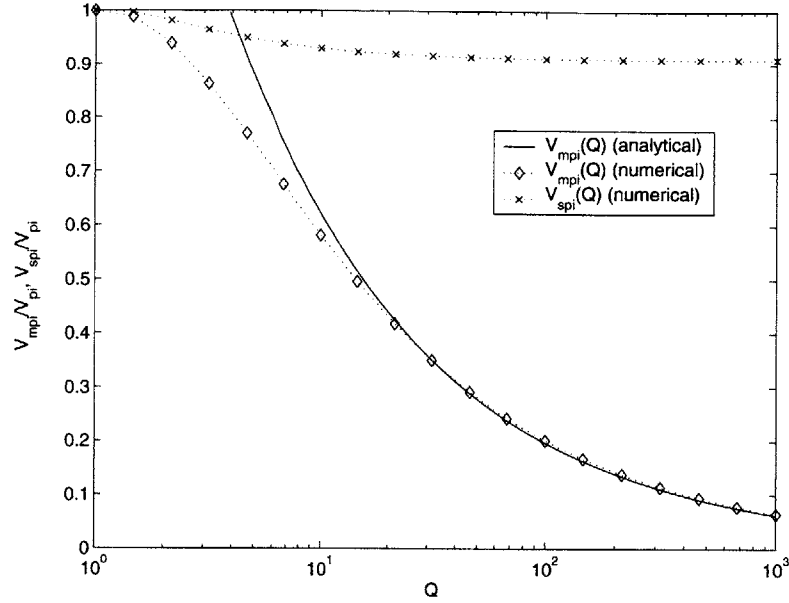


Figure 6-11: V_{spi} and V_{mpi} as a function of the quality factor for a torsional electrostatic actuator. For all values of Q greater than one, the modulated pull-in voltage is less than the step pull-in voltage.

Torsional electrostatic actuators commonly have two fixed electrodes in symmetrically opposite positions, such that the movable electrode can be pulled-in by rotating in either the positive or negative θ directions [119]. In fact, some parallel plate actuators have also been fabricated with top and bottom fixed electrodes, enabling two pulled-in positions as well [107]. For electrostatic switches with two opposing fixed electrodes, the modulated pull-in performance can be enhanced by applying a modulated voltage to both fixed electrodes. This allows energy to be input throughout the entire mechanical oscillation and would lead to a further decrease in the modulated pull-in voltage by a factor of $\frac{1}{\sqrt{2}}$ (for fixed electrodes that are symmetrically located relative to the moving electrode.)

6.4 Conclusions

In this chapter, we have shown that the dynamic nature of parallel plate and torsional electrostatic actuators can have a significant impact on the voltage needed to pull-

in the actuator. In particular, it was shown that for the ideal case of no damping an applied step voltage can achieve pull-in with only 91.9% of the quasi-statically predicted pull-in voltage for parallel plate actuators, and for torsional actuators only 91.2% of the quasi-statically predicted pull-in voltage is required. It was also shown that by applying a voltage that is modulated at the mechanical resonance of the actuator, significant decreases in voltage levels needed for pull-in can be achieved. For instance, for a system with a quality factor of 1000, the voltage level required for pull-in is less than 10% of the quasi-static pull-in voltage for both parallel plate and torsional actuators. The decrease in pull-in voltage for both the step and modulated input voltages is strongly dependent on the damping in the system.

The impact of these dynamic pull-in techniques could be very significant for electrostatic parallel plate and torsional actuators used as switching structures in microwave, RF, or optical MEMS applications. To create reliable switching structures, it has been necessary to have a high actuation voltage, much higher than levels used by integrated circuits. By utilizing these dynamic pull-in techniques, low voltage actuation can be achieved without sacrificing mechanical stiffness and reliability. This would allow direct integration of reliable MEMS switching structures into standard integrated circuits without the need of voltage up-converters.

Chapter 7

Strain-energy MEMS switching

Switching speed is one of the most significant limitations of the MEMS wavelength selective switch, and MEMS switching in general. When compared with semiconductor and opto-electronic switches, MEMS switching is far slower. This is a significant disadvantage for MEMS switching.¹

Another issue for the prototype wavelength selective switch is the operating voltage. To be able to integrate the wavelength selective switch with standard integrated circuits, the operating voltage needs to be at the level of the integrated circuit (i.e. CMOS compatible). The technique described in Chapter 6 allowed the operating voltage of a parallel plate actuator to be reduced significantly below that of a standard parallel plate MEMS actuator, thus allowing actuation voltages at IC levels. However, modulated pull-in technique of Chapter 6 operates over a number of mechanical cycles, leading to a switching time that is slower than actuation by a high DC voltage.

In this chapter, a completely new actuation technique for MEMS will be described that allows significantly faster switching speeds than any other MEMS actuation technique and requires much lower voltage than parallel plate electrostatic actuation².

¹Other important factors in integrated optical switching include fabrication and operation cost, power dissipation, and optical performance. In these categories MEMS based devices are competitive with, and even outperform opto-electronic switches.

²Parallel plate electrostatic actuation was the fastest MEMS actuation technique prior to the development of this technique.

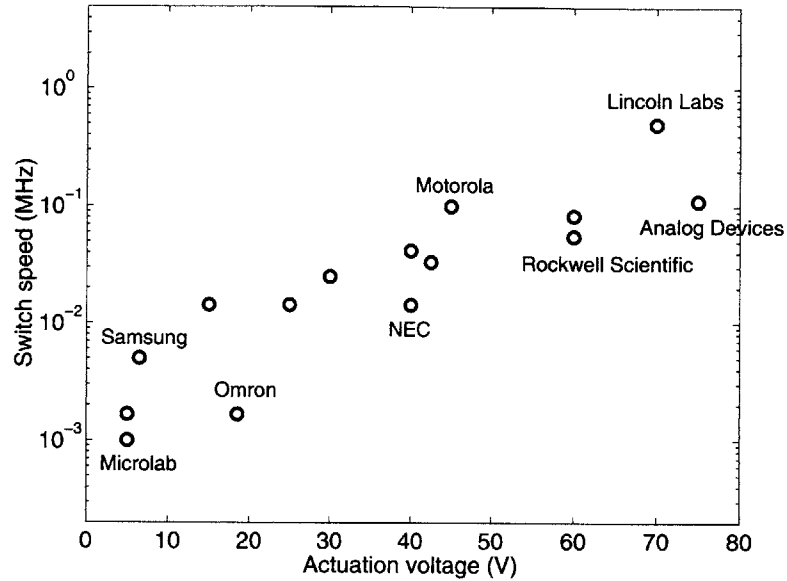


Figure 7-1: Switching voltage versus switching speed for a number of RF MEMS switches that have been developed [111].

The proposed technique is based on using stored elastic potential energy to drive the mechanical switch between stable states. This approach creates an actuator with both high energy and power densities, leading to the extremely fast switching capability at low operating voltage.

7.1 Current parallel plate MEMS switching

For parallel plate electrostatic switching, the required actuation voltage is generally high (typically greater than 20 volts). Figure 7-1 shows the voltage versus switching speed of a number of radio-frequency (RF) MEMS switches that have been developed using parallel plate electrostatic actuation [111].

The switches in Figure 7-1 have displacement requirements that are similar to what is required of the wavelength selective switch ($\sim 1\mu\text{m}$). Because of this, the performance of these RF MEMS switches gives insight into wavelength selective switches based on electrostatic parallel plate actuation.

There is a definite trend in the performance of the MEMS switches seen in Figure

7-1; higher actuation voltage is required to increase the switching speed. This relationship is also obvious from looking at the pull-in voltage equation for parallel plate actuators (see also Equation 6.3)

$$V_{\text{pi}} = \sqrt{\frac{8kd_0^3}{27\epsilon_0 A}}. \quad (7.1)$$

The speed of the switch is directly related to the stiffness, k , through the resonant frequency, $\omega_n = \sqrt{k/m}$. The mass m and the overlap area A effectively cancel each other out. Since the initial gap d_0 for RF MEMS as well as the wavelength-selective optical switch needs to be greater than about one micron, this cannot be decreased to increase switching speed. This means that the only way to get a faster switch is to increase the actuation voltage. This fundamental scaling property of electrostatic parallel plate actuation strictly limits the design space of MEMS electrostatic switches.

There are other MEMS actuation techniques, specifically piezoelectric, thermal, magnetic, and shape memory, that have been used in MEMS devices. However, none of these have achieved the switching speeds at similar displacements that have been demonstrated by parallel plate electrostatic MEMS devices.

7.2 Strain-energy actuation technique

The new actuation technique makes use of stored elastic potential energy to drive the motion of the device during switching. The switching function is accomplished between an equilibrium state and two pull-in states. The actuation principle is shown in Figure 7-2. In operation, the switch is initially pulled in to one of the two fixed electrodes. In this situation, there is a significant amount of elastic potential energy stored in the device. As described in Section 2.4, when the switch is in the pulled-in state, a hold voltage that is less than the pull-in voltage can be used to maintain the switch in the pulled-in state. This arises from the nonlinearities of the electrostatic actuation.

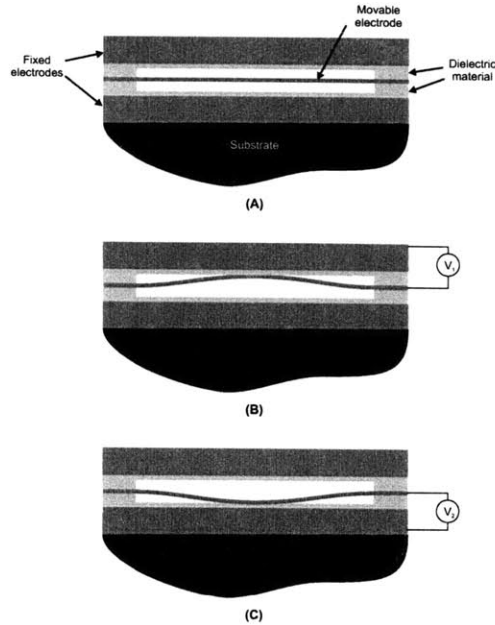


Figure 7-2: Schematic diagram of one possible implementation of the ultra-fast switch. (A) shows the movable electrode in its equilibrium state with no applied voltage. (B) and (C) show the movable electrode in its two switch states during normal operation.

If the mechanical damping of the device is low (i.e. if the device is packaged in vacuum), the movable electrode will significantly overshoot its equilibrium position in-between the two fixed electrodes upon the release of the hold voltage. The overshoot of the moving electrode will bring the moving electrode very close to the second fixed electrode. At this point, a voltage applied to the second fixed electrode that is at or just above the hold voltage level will be able to pull-in and hold the movable electrode. This switching procedure can be repeated indefinitely without ever requiring the application of a high pull-in voltage.

The initial pull-in of the switch can be done by using either a standard high voltage pull-in or by a low voltage using the modulated pull-in technique described in Chapter 6. Beyond that initialization step, the device operates at low voltage, as described earlier.

Using the strain-energy switching principle, several switch designs were developed. Figure 7-3 shows a figure comparing the switching speeds and voltages of the RF MEMS switches shown in Figure 7-1 with those of the strain-energy switch designs.

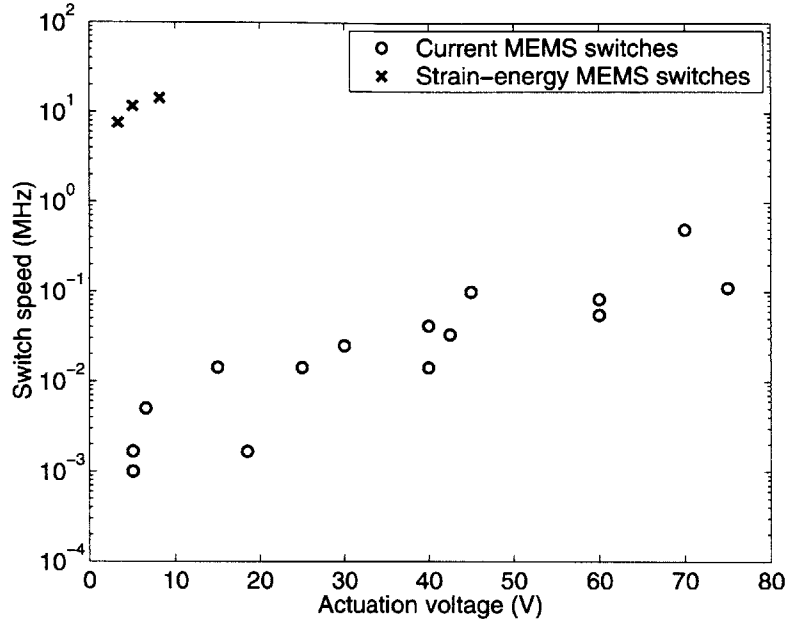


Figure 7-3: Comparison of the switching speed and actuation voltage of a number of RF MEMS switches with switch designs that utilize the strain-energy switching technique.

The three strain-energy switch designs are expected to be 1000 times faster than switches with comparable actuation voltages and 10 times faster than the fastest RF MEMS switch.

A similar macroscale technique has been developed to independently control the valves in an internal combustion engine [16]. For this device, the nonlinearity in the system is achieved by using a unique cam design to catch and hold the valves in their two open and closed states. This device also uses a resonant technique to initially "pull-in" the system (i.e. load the mechanical springs with elastic potential energy).

7.2.1 Strain-energy switch implementations

There are a number of implementations for the strain-energy actuation technique. The basic criterion is that the device needs to have at least two fixed electrodes located relative to the movable electrode in such a way that the fixed electrodes are at the extreme positions of the resonant mode of the movable electrode. This arrangement

can be achieved using a structure very similar to the parallel plate actuator used in the wavelength selective switch by adding a top fixed electrode to the structure, as shown in Figure 7-2. In this arrangement, the movable electrode would switch up and down between the fixed electrode on the substrate and the fixed electrode above the device.

A second implementation of the strain energy switching technique is to use the torsional resonant mode of a device similar to a torsional electrostatic switch. This implementation is shown in Figure 7-4. This structure is essentially identical to standard electrostatic torsional switches, such as Texas Instrument's DMD mirrors [35]. The key differences in design choices would be to reduce the damping significantly, and use the stored elastic potential energy to drive the switching rather than energy introduced from the electrostatic actuator. This arrangement is a simpler structure to fabricate than the parallel plate version shown in Figure 7-2. The simplicity is derived from having only one sacrificial layer, with both fixed electrodes anchored to the substrate.

A third implementation is similar to the parallel plate actuator in Figure 7-2 except it uses side-to-side motion instead of up-and-down. Figure 7-5 is a schematic representation of this device. This approach is the simplest of the three techniques to fabricate. In addition to requiring only one sacrificial layer, only one material layer and one photolithography step is necessary to define the fixed and movable electrodes. This particular arrangement lends itself to fabrication using a silicon-on-insulator (SOI) wafer with the silicon device layer being used to create the fixed and movable electrodes, and the oxide layer creating the sacrificial layer.

The side-to-side device allows more complex structural arrangements. For example, the device can be forced into operating at higher resonant modes, thus increasing speed further. Also, the fixed electrodes can be shaped to mimic the mode shape of the movable electrode. By matching the mode shape, the fixed electrodes require a lower hold voltage and, upon release, the stored elastic potential is more efficiently directed into the desired resonant mode. Figure 7-6 shows a schematic drawing where the fixed electrode is shaped to match the mode shape of the movable electrode.

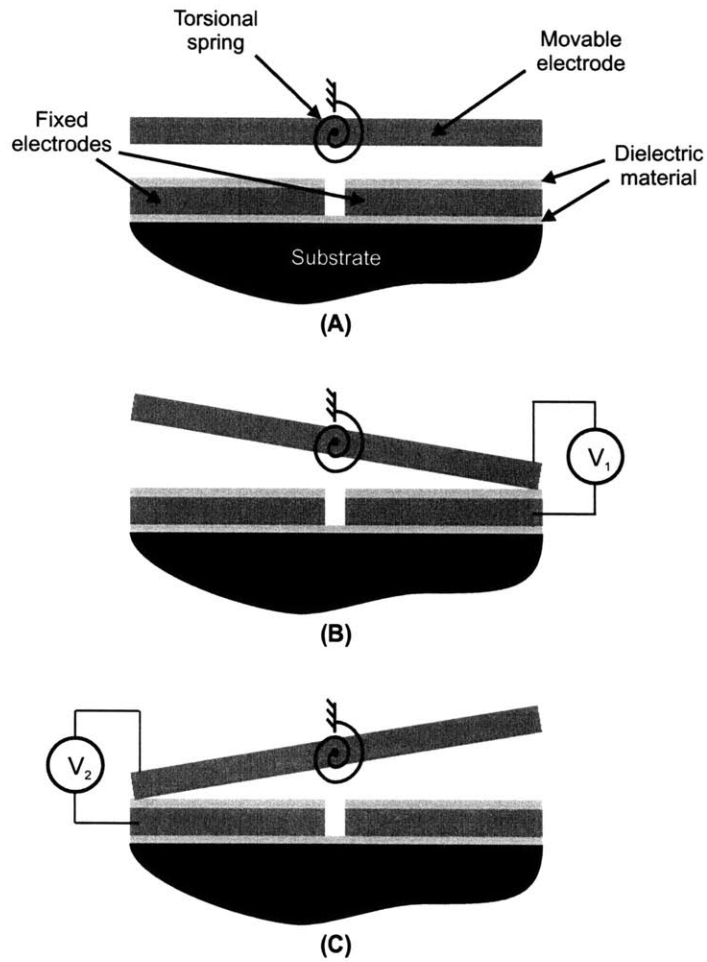


Figure 7-4: Schematic diagram of a torsional implementation of the ultra-fast switching technique. (A) shows the movable electrode in its equilibrium state with no applied voltage. (B) and (C) show the movable electrode in the two switch states used during normal operation.

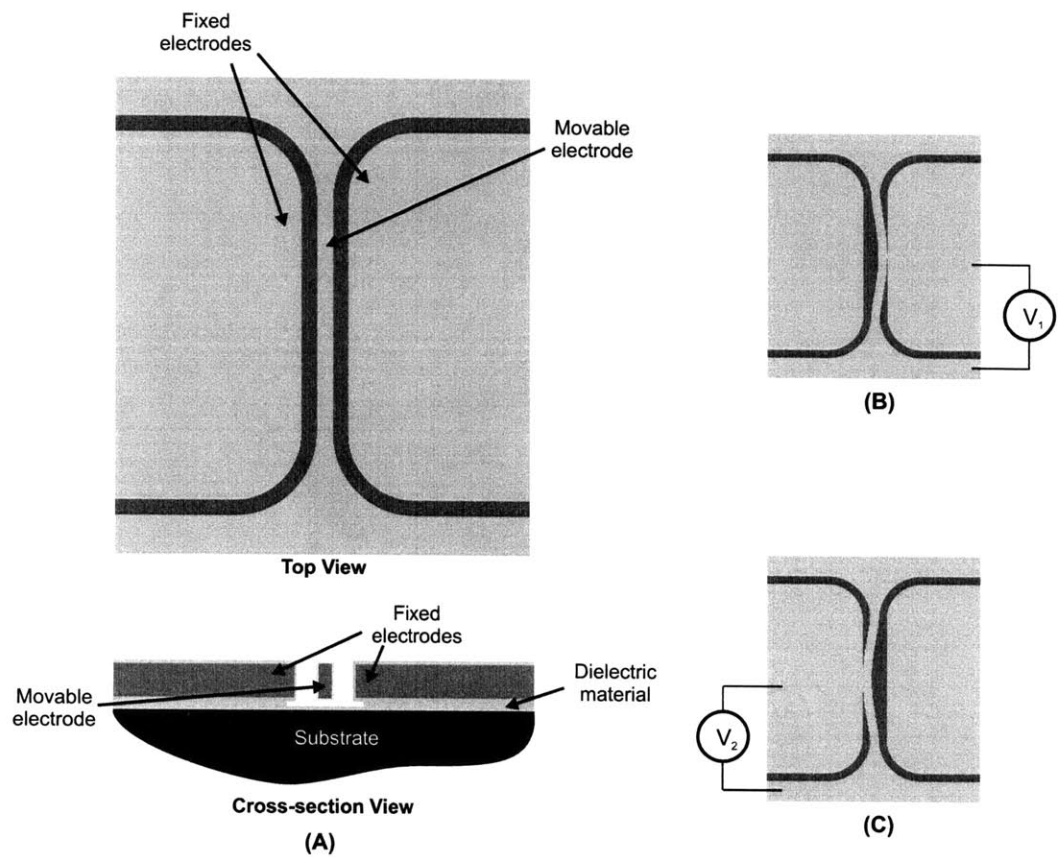


Figure 7-5: Schematic diagram of a side-to-side motion implementation of the ultra-fast switching technique. (A) shows the movable electrode in its equilibrium state with no applied voltage. (B) and (C) show the movable electrode in the two switch states used during normal operation.

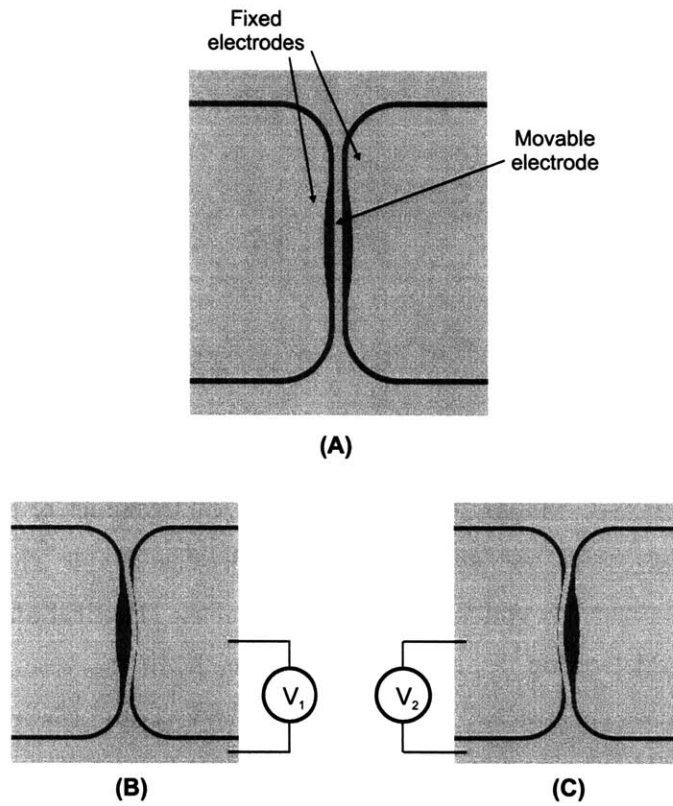


Figure 7-6: Schematic diagram of the side-to-side motion implementation with electrodes that are shaped to match the mode shape of the movable electrode. (A) shows the movable electrode in its equilibrium state with no applied voltage. (B) and (C) show the movable electrode in the two switch states used during normal operation.

Although only fixed-fixed beam implementation have been shown in Figures 7-2, 7-5, and 7-6, cantilever beam implementations of the strain-energy switch can also be realized in both the up-and-down and side-to-side parallel plate implementations. Cantilever beam implementations have an advantage in that they are shorter for a given stiffness, thus minimizing the area of the wafer used. However, the fixed-fixed beams tend to have a better stiffness to area ratio, which allows a lower actuation voltage for a design of a given stiffness.

7.3 Modelling of strain-energy switching

The strain-energy technique takes advantage of the dynamics of the MEMS system to achieve high-speed, low-voltage switching. Because of this, the system needs to be carefully designed to match the performance of the electrical and mechanical sub-systems. In this section, a lumped parameter model of the strain-energy switching technique will be constructed and analyzed as the first step towards the design of a prototype MEMS device that utilizes the strain-energy switching technique.

7.3.1 Lumped parameter model

Figure 7-7 is the lumped parameter model used to analyze the performance of the strain-energy switching technique. The equations of motion for the strain-energy

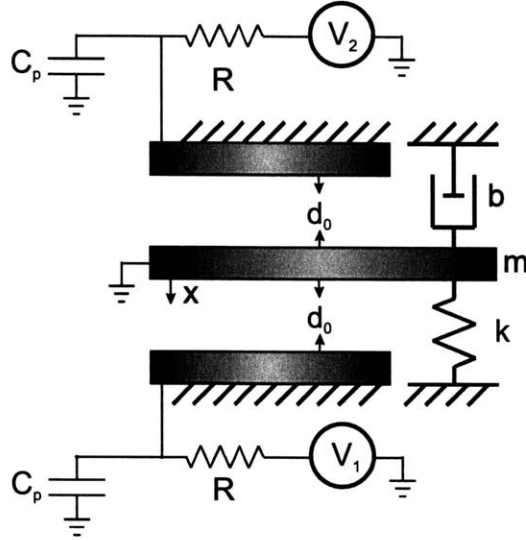


Figure 7-7: Lumped parameter model for the strain-energy actuation technique. Note the switch is designed to be symmetric, therefore the two resistors have the same resistance R and the two parasitic capacitors have the same capacitance C_p .

switch, as derived from the model in Figure 7-7, are

$$\begin{aligned}
 V_1 &= V_{c1} + (\dot{Q}_1 + \dot{Q}_{p1}) R \\
 V_2 &= V_{c2} + (\dot{Q}_2 + \dot{Q}_{p2}) R \\
 m\ddot{x} + b\dot{x} + kx &= \frac{Q_1^2}{2\epsilon_0 A} - \frac{Q_2^2}{2\epsilon_0 A} \\
 Q_1 &= \frac{V_{c1}\epsilon_0 A}{d_0 - x} \\
 Q_2 &= \frac{V_{c2}\epsilon_0 A}{d_0 + x} \\
 Q_{p1} &= C_p V_{c1} \\
 Q_{p2} &= C_p V_{c2},
 \end{aligned} \tag{7.2}$$

where V_{c1} and V_{c2} are the voltages across the two capacitors created by the actuator and the two parasitic capacitors. Q_1 and Q_2 are the charges that are stored in the two capacitors created by the actuator. Q_{p1} and Q_{p2} are the charges that are stored on the two parasitic capacitors. The other parameters are as defined in Figure 7-7.

Many of the same modelling assumptions discussed in Section 6.1 are used here as

well, with the exception of the assumption related to electrical resistance. Resistance was included in this model because the switching speeds that are possible with this technique could become close to speeds of the electronic circuit. Parasitic capacitance was also included in this model for the same reason.

The model also only shows a linear elastic term. For the implementations that used a fixed-fixed beam as the movable electrode, a nonlinear elastic term should be included to capture the effects of the beam stretching as it deforms. The nonlinear term is called a Duffing spring and is $k_d x^3$. For more detailed design involving fixed-fixed structures, this term should be included, however, for the general discussion of the strain-energy switch, this term will be excluded.

7.3.2 Hold voltage

During normal operation, the movable electrode transitions between being pulled in to one fixed electrode to being pulled in to the second electrode. The elastic potential energy stored in the device drives the movable electrode from one position to the other. To hold the electrode in the pulled in position to either of the two fixed electrodes requires a minimum voltage of

$$V_h = \sqrt{\frac{2k \left(d_0 - \frac{t_d}{\epsilon_d}\right) \left(\frac{t_d}{\epsilon_d}\right)^2}{\epsilon_0 A}}, \quad (7.3)$$

where t_d is the thickness of the dielectric layer and ϵ_d is the relative permittivity of the dielectric. To reduce the hold voltage, the thickness of the dielectric layer can be decreased and/or a dielectric with a higher permittivity can be selected. The primary limiting factor for the minimum hold voltage is the point where the dielectric material experiences break-down and allows current to flow. A secondary limiting factor is dielectric charging, which increases as the electric field across the air/dielectric interface increases, as described in Section 4.2.1.

7.3.3 Actuation voltage

During the switch operation, where the movable plate transitions between the two pulled-in states, stored elastic energy is converted to kinetic energy and then back to stored elastic energy. During this process, there is some energy lost to mechanical damping. In addition, since the movable plate and fixed plate do not discharge immediately upon the release of the movable plate, the residual charge acts as a damper to the mechanical motion of the movable plate. Thus, additional energy is lost due to the electrical circuit's resistance.

To compensate for the energy lost to both damping mechanisms, a voltage will need to be applied to the other fixed electrode to inject new energy into the system as the movable electrode moves toward that electrode. Ideally, the electrical and mechanical damping should be minimized so that only a small amount of energy needs to be injected during a switch operation relative to the total energy of the system. Mechanical damping can be minimized by packaging the device in a vacuum. The electrical damping effect can be minimized by making the electrical system much faster than the mechanical system, thereby allowing the charge on the electrodes to be dissipated before substantial mechanical motion is achieved.

The interactions between the mechanical motion and the electrical and mechanical damping are fairly complicated. To allow some level of insight through analytical evaluation, the effects of the mechanical damping will be analyzed separately and then combined with the electrical damping through computational modelling. In these derivations, the fixed electrode to which the movable electrode is initially pulled-in to will be referred to as the first electrode. The electrode to which the movable electrode becomes pulled-in to after the switch operation will be called the second electrode. This is, of course, only for clarification during this discussion since the system is symmetric and switching in either direction is identical.

To analyze the effects of mechanical damping, the speed of the electrical system will be assumed to be much greater than that of the mechanical system. The strength of this assumption will be discussed later when the electrical damping effect is ana-

lyzed. Under these conditions, the energy lost to mechanical damping can be found through the use of the definition of the quality factor

$$Q = 2\pi \frac{E_{\text{stored}}}{E_{\text{dissipated}}}. \quad (7.4)$$

Using this quality factor definition in this analysis implicitly makes the assumption that the velocity of the movable plate during the switching operation is sinusoidal. Similar to the analysis of the modulated pull-in, this assumption is best applied to systems with mechanical quality factors greater than about ten. For quality factors less than ten, the assumption overestimates the energy lost to damping, leading to an overestimate of the voltage needed for actuation. Still, the approximation is useful as an upper bound on the required voltage.

The total energy stored in the mechanical system is

$$E_{\text{stored}} = \frac{1}{2} k x_{\text{max}}^2. \quad (7.5)$$

Since the switching operation lasts only one half of a cycle, the total energy lost is one half of the dissipated energy in the quality factor definition. The energy lost to mechanical damping during switching is, therefore,

$$E_{\text{md}} = \frac{\pi k x_{\text{max}}^2}{2Q}, \quad (7.6)$$

The energy injected into the system by the applied voltage is found by integrating the force over the displacement, and is

$$E_{\text{injected}} = \int_{-x_{\text{max}}}^{x_{\text{max}}} \frac{\epsilon_0 A V_s^2}{2(d_0 - x)^2} dx = \frac{\epsilon_0 A V_s^2 x_{\text{max}}}{(d_0^2 - x_{\text{max}}^2)}. \quad (7.7)$$

For the switch to operate properly, the injected energy must at least equal to the energy lost to damping. By equating Equations 7.6 and 7.7, the minimum voltage

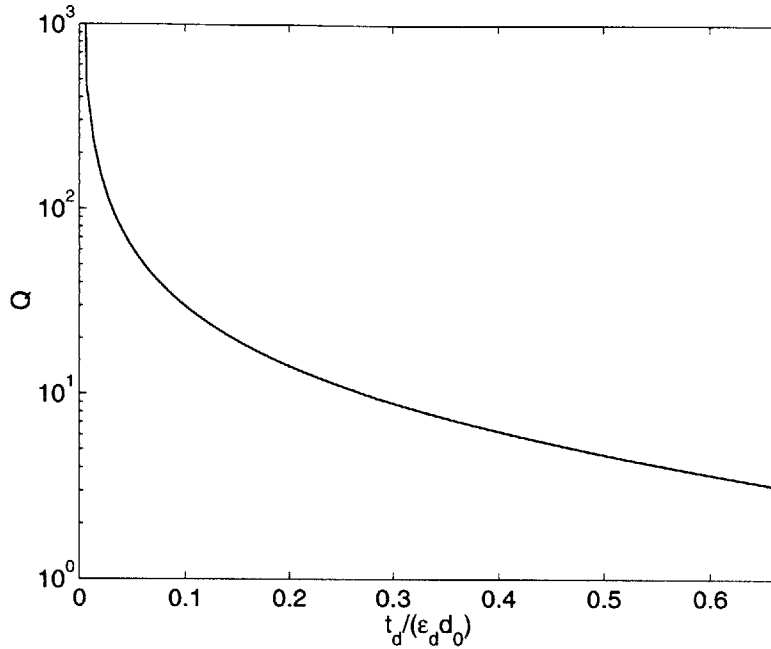


Figure 7-8: Curve of the minimum required quality factor for a given effective dielectric thickness normalized by the total effective gap that allows switching by the use of a voltage no higher than the hold voltage.

required for switching is found to be

$$V_s = \sqrt{\frac{\pi k (d_0^2 - x_{\max}^2) x_{\max}}{\epsilon_0 A Q}}. \quad (7.8)$$

Ideally, the voltage required for switching should be no greater than the hold voltage. This allows the same voltage level to be used both for switching the movable electrode and for holding the electrode in place. This leads to the relationship

$$Q = \frac{\pi \left(2 - \frac{t_d}{\epsilon_d d_0} \right)}{2 \frac{t_d}{\epsilon_d d_0}} \quad (7.9)$$

between the necessary quality factor and the thickness of the dielectric layer separating the electrodes. Figure 7-8 shows the curve given by Equation 7.9. The curve is only shown up to a value of $\frac{t_d}{\epsilon_d d_0} = \frac{2}{3}$ since a dielectric thickness greater than this value would prevent the movable electrode from pulling in.

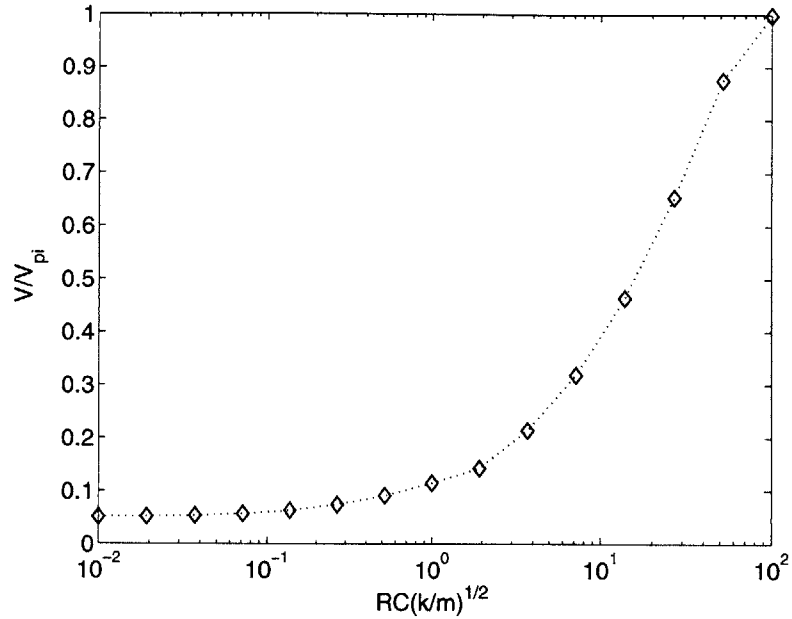


Figure 7-9: Curve of the minimum required actuation voltage for a system with the dimensionless quantity $RC\sqrt{\frac{k}{m}}$, comparing the effect of the RC time constant relative to the resonant frequency of the mechanical structure.

The effect of electrical damping of the mechanical system is more complicated. The charge decreases with time according to the time constant of the circuit, however, the capacitance during the discharge is not constant because the gap is changing. In addition, the velocity of the movable plate will be a complicated function due to the two nonlinear electrostatic forces acting on the plate due to the evolving charges on it and the two fixed plates.

To model the effects of the electrical damping, a model of the strain-energy switch was implemented in Simulink. Simulations were run for a range systems whose dimensionless quantity $RC\sqrt{\frac{k}{m}}$ varied over a range of 0.01 up to 100.0. The results of these simulations are shown in Figure 7-9, where the actuation voltage required for the different systems is shown. The RC time constant begins to have an effect on the overall system when the RC time constant is in the range of 10 to 50% of the mechanical time constant, defined by $\sqrt{\frac{m}{k}}$. Therefore, by designing a system with an RC time constant that is less than 10% of the mechanical time constant, the

electrical damping can be eliminated.

7.3.4 Switch initialization

Prior to the normal operation of the switch, where the stored elastic potential energy drives the switching, the movable electrode needs to be pulled in to one of the two fixed electrodes from its unactuated equilibrium state. This can be done by either applying a DC voltage that exceeds the pull-in voltage of the device or by the modulated pull-in technique described in chapter 6.

Although it requires more control electronics, the modulated pull-in technique has a number of advantages. First of all, the required voltage for pull-in is much lower than a standard DC pull-in voltage and can be essentially the same as the actuation voltage required for the standard operation of the strain-energy switch. This is an important point because it would allow integration of this kind of MEMS switch with integrated electronic circuits. This provides the means to attain the goal of IC level actuation voltage for the wavelength selective switch. Low voltage operation is also important for a number of other MEMS switch applications, for example, RF MEMS switches in cellular phones.

A second advantage of the lower initialization voltage resulting from the modulated pull-in technique is that it allows a much thinner dielectric layer to be used. The dielectric layer needs to be thick enough to withstand the maximum applied voltage. If a thinner dielectric layer is possible because of lower applied voltages, then the hold voltage is also reduced. The result of this is that the actuation and hold voltages can be dramatically reduced compared with standard electrostatic actuation.

7.3.5 Switching speed

Estimating the switching speed of the device is relatively straightforward since it is essentially the time required for one half of an oscillation. This neglects the nonlinear effects in the system resulting from electrostatic forces. However, a well designed switch would minimize the electrostatic forces during switching, thus minimizing the

effect of those on the switching speed.

If the mechanical system is linear, the switching speed base on the resonant frequency is simply

$$t_s = \pi \sqrt{\frac{m}{k}}, \quad (7.10)$$

for zero to 100% switching.

If the mechanical system has a nonlinear term, such as a Duffing spring term, the switching speed is more difficult to calculate and requires knowledge of the maximum displacement of the movable electrode to calculate. The Duffing nonlinear spring results from using a fixed-fixed beam as the moving electrode and can increase the switching speed by as much as 30% or more, depending on the ultimate strength of the materials being used. This method can be effective for increasing the switching speed.

7.4 Strain-energy prototype switch design and fabrication

Because the strain-energy based switching concept is a completely new idea for MEMS actuation, a prototype device was designed and fabricated to demonstrate the actuation technique. Because the device was only for the demonstration of the switching technique, it only required two fixed electrodes and one moving electrode. The approach used for the switch prototype was the implementation shown in Figures 7-5 and 7-6.

7.4.1 Prototype design

The prototype switch structures were designed to be very simple to fabricate. A range of devices were designed with a variety of dimensions for the movable electrode in terms of the width and the length. The gaps between the electrodes was also varied. Finally, some of the devices were designed with curved fixed electrodes, as in Figure 7-6, and some were designed with flat fixed electrodes, as in Figure 7-5.

The SOI wafers used for the fabrication had a $5.0 \pm 0.5 \mu\text{m}$ thick silicon device layer on top of a $3.0 \mu\text{m}$ thick oxide layer. The resistivity of the device layer was given in the wafer specifications as 2.7 - 5.0 $\Omega\text{-cm}$.

The dimensions of the prototype switch structures that were fabricated and tested are given in Table 7.1 along with the shape of the fixed electrode and the resonant frequency of the movable electrode.³

The resonant frequencies of the different beam designs were calculated using finite element analysis. The finite element calculation of the resonant frequencies is based on small deformations. Therefore, it does not take into account the nonlinear Duffing spring effects that these beams experience at the larger deformations that they are subject to. The Duffing spring effect will increase the resonant frequency above the value reported by the finite element analysis.

The finite element analysis also did not take into account the silicon oxide layer grown on the surface of the movable electrode. The thermally grown silicon oxide has a compressive stress of approximately 300 MPa, which tends to decrease the resonant frequency.

The pull-in voltages of these devices were designed to run between 75 and 125 volts with the hold voltage being roughly equal to one half to two thirds of the pull-in voltage. The high hold voltage level was required due to the thick dielectric layer needed to withstand the high pull-in voltages.

The switching speed of these devices can be calculated from their resonance frequency by Equation 7.10. For the devices listed in the Table 7.1, the predicted switching speeds ranged from 98 to 424 ns.

To avoid developing high stresses during the actuation of these devices, the anchors of the movable electrodes were rounded to reduce any stress concentration locations. Through finite element analysis, the maximum stress expected during actuation was about 1 GPa for the device with the highest stress. Most device designs should experience stress levels no greater than 500 MPa.

³A number of other device designs were also fabricated; however, they were unsuitable for testing. Most notably, all of the device designs that had a $1 \mu\text{m}$ -thick movable electrode buckled during the growth of the final thermal oxide film, so they became unusable (see Section 7.5.1).

Table 7.1: Design details of prototype switch structures.

Device	Length (μm)	Width (μm)	Gap (μm)	Electrode shape	Resonant frequency (MHz)
A	120.0	2.0	0.75	curved	1.2
B	120.0	2.0	1.0	flat	1.2
C	120.0	2.0	1.0	curved	1.2
D	100.0	2.0	0.75	flat	1.7
E	100.0	2.0	0.75	curved	1.7
F	70.0	1.5	0.75	curved	2.6
G	60.0	1.5	0.5	flat	3.5
H	60.0	1.5	0.75	curved	3.5
I	60.0	2.0	0.5	flat	4.7
J	50.0	1.5	0.5	flat	5.1
K	80.0	1.5	0.75	flat	2.0
L	70.0	2.0	0.5	flat	3.5
M	70.0	1.5	0.75	flat	2.6

7.4.2 Fabrication

The fabrication process to create the prototype switch was simple due to the use of an SOI wafer. The fabrication process is illustrated in Figure 7-10. A detailed list of steps is given in Table 7.2.

The advantage of using SOI wafers is that both the sacrificial layer and the structural layers are already in place. In addition, the single crystal silicon of the device layer is ideal for MEMS devices since the layer is stress-free, and has the desirable mechanical properties of single crystal silicon.

The design calls for gaps as small as $0.5\mu\text{m}$. To be able to resolve these gaps, a Nikon projection lithography stepper was used. This stepper can resolve down to just under a half micron. For etching the final thermally grown oxide layer, contact lithography was used, since the resolution required was much lower, on the order of tens of microns.

To achieve straight sidewalls for the silicon device layer etch, an STS DRIE machine was used. Straight sidewalls are important for the device, since the sidewalls form the contact surfaces of the movable electrode and the fixed electrodes.

The purpose of the aluminum layer was to allow wirebonding to the bond pads for applying the control signals to the electrodes. The aluminum film had the potential to create short circuits between the bond pads that were intended to be isolated. To avoid this, the aluminum layer was specified to be very thin ($\sim 10\text{nm}$) and to be deposited by electron-beam (E-beam) evaporation. E-beam evaporated films are deposited in a directional manner; therefore, the sidewalls and especially the undercut regions would have very little if any aluminum deposited. Also, by having a very thin film, the film would not be able to coalesce into a completely continuous film. This means that if a short circuit happens to be formed by the aluminum, the short will have a very small cross-sectional area and will quickly, and benignly, burn up as current starts to flow.

Finally, it is noted that the movable electrodes are released fairly early in the fabrication process, as compared with typical MEMS fabrication processes. Typically,

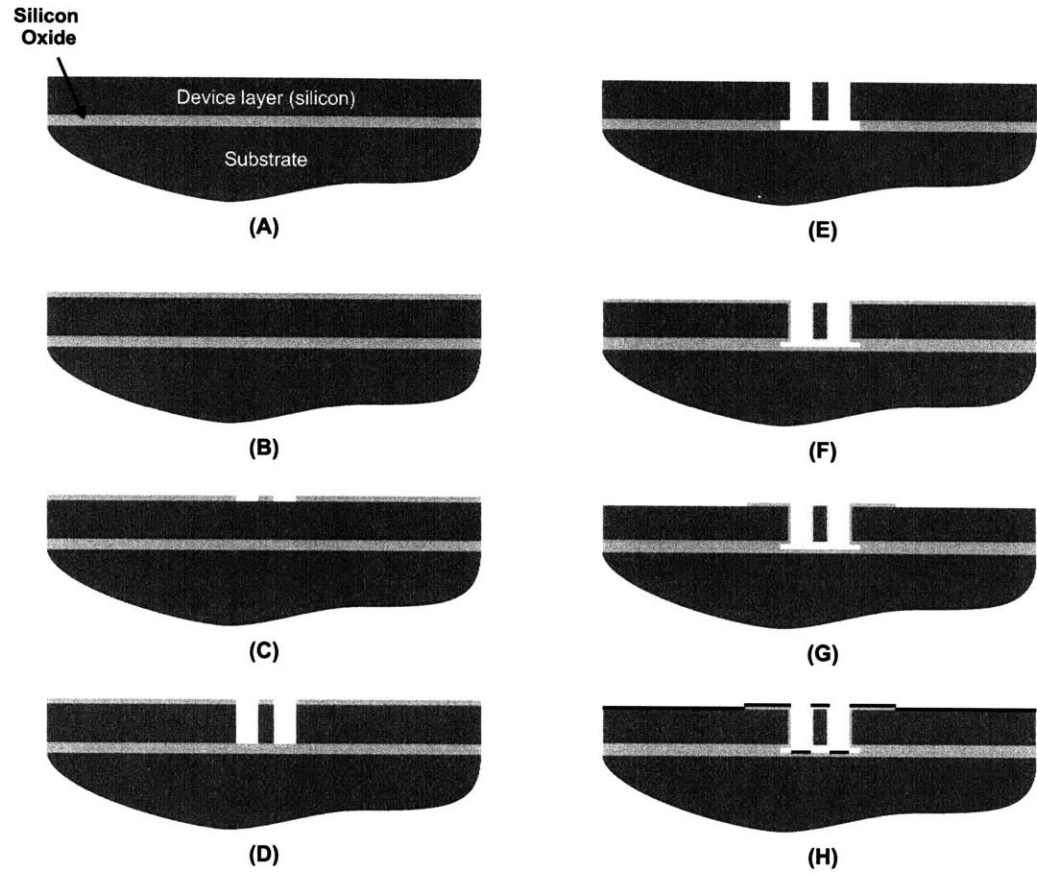


Figure 7-10: Cross-sectional view of the fabrication process used for the strain-energy switching prototype. (A) fabrication process begins with an SOI wafer. (B) thermal oxide is grown on the wafer. (C) thermal oxide is patterned with photolithography and RIE. (D) silicon device layer is etched with Deep RIE (DRIE). (E) thermal oxide mask and oxide sacrificial layer are etched away with BOE. (F) thermal oxide layer is grown to create dielectric layer to separate electrodes. (G) thermal oxide is patterned and etched with photolithography and BOE to provide access to bond pads. (H) thin aluminum film is deposited by electron-beam evaporation.

the release step is the last step before packaging. In this case, the movable electrodes are stiff enough to withstand significant additional processing without any fear of the structures breaking from spin drying, or experiencing stiction due to the surface tension of liquids pulling the electrodes together.

Table 7.2: Fabrication process for the prototype MEMS switch based on the strain-energy technique.

Step	Machine	Process Notes
1	Wet station	RCA clean
2	Diffusion tube	Grow 500 nm thermal oxide film
3	Wet station	RCA clean
4	Coater Track	Apply HMDS and 1.0 μm photo-resist, then soft bake
5	Nikon stepper	Expose photoresist
6	Coater Track	Develop photoresist and hard bake
7	AME Precision 5000	Reactive ion etch (RIE) thermal oxide
8	Oxygen plasma asher	Strip photoresist
9	Wet station	Piranha clean and HF dip
10	STS DRIE	Etch through SOI device (Si) layer
11	Oxygen plasma asher	Remove residual PTFE passivation layer
12	Wet station	Piranha clean and HF dip
13	Wet station	BOE etch oxide mask and SOI oxide layer for release (15 min)
14	Wet station	RCA clean
15	Diffusion tube	Grow 80 nm thermal oxide film
16	Wet station	BOE etch oxide 15nm
17	HMDS oven	Vapor phase deposition of HMDS

continued on next page

Table 7.2: *continued*

Step	Machine	Process Notes
18	Spin coater	Coat wafer with 8.0 μ m of photoresist
19	Oven	Soft-bake photoresist for 30 min at 95°C
20	EV620 Aligner	Align mask and expose photoresist
21	Wet station	Develop photoresist
22	Oven	Post-bake photoresist for 60 min at 95°C
23	Wet station	BOE etch oxide 65nm
24	Oxygen plasma asher	Strip photoresist
25	Wet station	Piranha clean and HF dip
26	E-beam evaporator	Deposit 10nm aluminum
27		Cleave wafer
28	Wire-bonder	Package device in test chip

7.4.3 packaging

The strain-energy switching technique requires low damping for good performance. The only way to reduce mechanical damping to the levels required for optimal performance is to operate the switch in a vacuum. While the initial prototypes of this switch will be tested in vacuum chambers, commercial devices will require some form of vacuum packaging. Vacuum packaging of MEMS devices has been a point of research for a number of years because MEMS resonant filters also require low damping for good performance. These techniques have not yet been applied to MEMS switches.⁴ However, the vacuum packaging techniques that have been developed should be readily applicable to strain-energy switching devices.

Vacuum packaging research has focused on three different approaches. The first

⁴MEMS switches based on current actuation technique typically operate best at near critical damping, where the settling of the switch after it is released is minimized. For this reason, vacuum packaging of MEMS switches has previously not been desired.

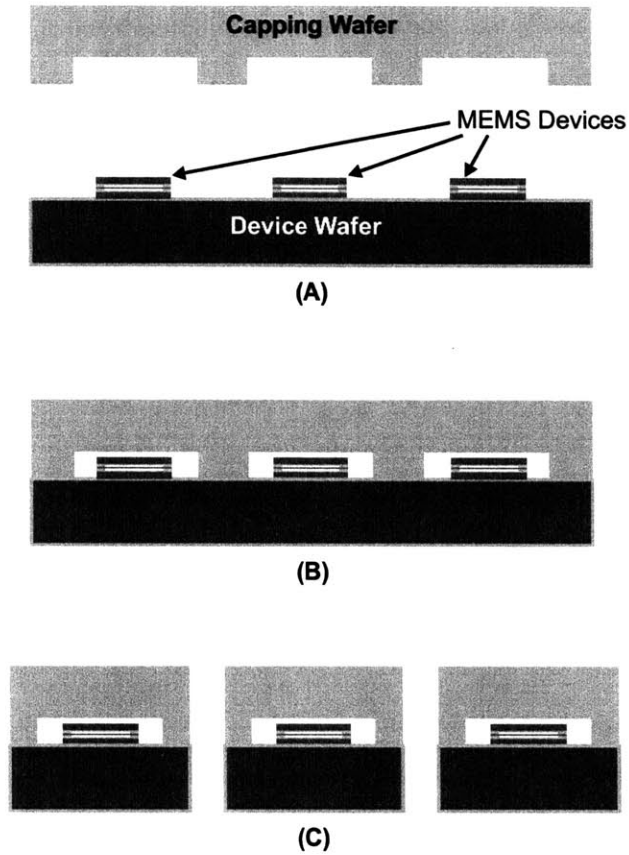


Figure 7-11: Schematic illustration of the wafer bonding vacuum packaging approach. (A) device wafer and capping wafer prior to bonding. (B) wafer stack after bonding. (C) individual chips after bonding and dicing.

is chip level packaging, where the chips are fabricated and diced from a wafer, after which the chips are sealed in a vacuum package [68, 132]. This technique mimics the packaging technique used for most ICs; however, the process and materials are much more expensive.

The second vacuum packaging approach is a wafer-level packaging scheme where the devices are fabricated on a wafer and then a second capping wafer is bonded to the device wafer [20, 60, 76, 77, 133]. The bonding process seals the MEMS devices in a vacuum. After bonding, the wafers are cut into chips with the vacuum seal intact.

The third vacuum packaging approach is also a wafer-level packaging process that

uses thin film deposition to create a vacuum sealed cavity around the device [47, 63, 83, 134]. This is all done on one wafer and uses fairly standard CMOS fabrication steps. After sealing, the chips can be diced from the wafer and packaged in standard plastic IC packages.

Any of these three techniques could be used for devices based on the strain-energy actuation technique. For low-cost applications, such as RF MEMS switches for cellular phones, the thin film deposition or the wafer bonding approaches are likely the best choice. For devices that are required to be very rugged and reliable, and where cost is less of an issue (i.e., military applications and satellite telecommunications), encapsulating the chip in a vacuum package at the chip level is probably the best option.

7.4.4 Control electronics

Because the strain energy based switch utilizes the dynamic behavior of the system to achieve switching, the control electronics need to be well designed so as not to inadvertently alter the dynamics. During the switching process, the electronics need to switch the applied voltages on and off much faster than the mechanical response. In addition, a pathway for the rapid discharge of the electrodes is also required.

The proposed control circuit is shown in Figure 7-13. The speed of the transistors is critical for the strain-energy switch to operate. The switching time of the transistors should be much faster than the mechanical switching time. In addition, the timing of the different control signals V_{cv1} , V_{cv2} , V_{cv3} , and V_{cv4} needs to be carefully controlled. Figure 7-14 illustrates how the control voltages should be manipulated for the strain-energy switch to operate properly. The time delay t_0 between the switching of the control voltages is to give time for the stray capacitances associated with the second electrode to become charged up. This reduces the effects of the stray capacitances on the electrode toward which the movable plate is moving. The parasitic capacitance related to the first electrode will still affect the movable electrode as it moves away from the first electrode.

The control voltage pairs V_{cv1} , V_{cv2} ; and V_{cv3} , V_{cv4} are shown in Figure 7-14 to

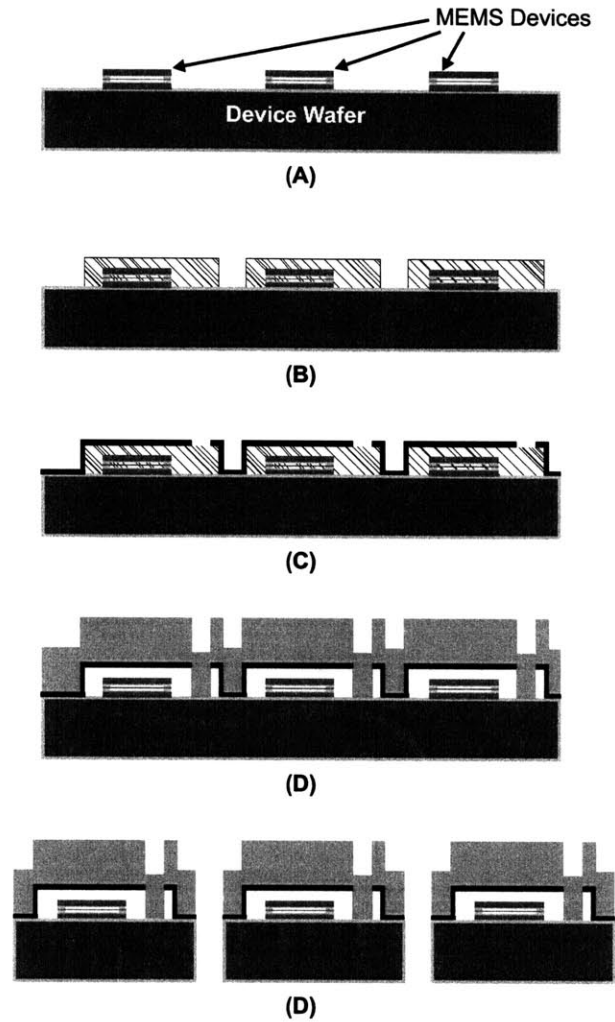


Figure 7-12: Schematic illustration of the thin film vacuum packaging approach. (A) device wafer with the fabricated MEMS devices. (B) wafer after deposition and patterning of the packaging sacrificial material. (C) wafer after deposition and patterning of the first capping thin film. (D) wafer after the removal of the sacrificial material and the deposition of the final capping film. (E) final chips after dicing.

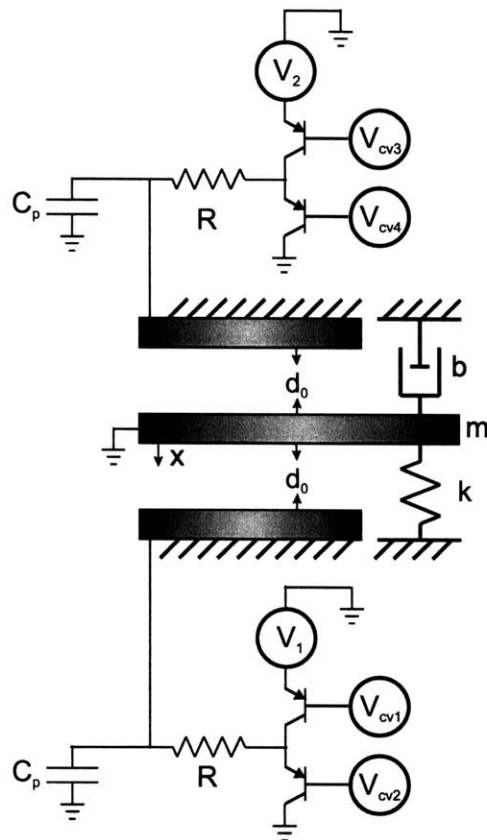


Figure 7-13: Schematic drawing of the switching circuit for the strain-energy actuation technique.

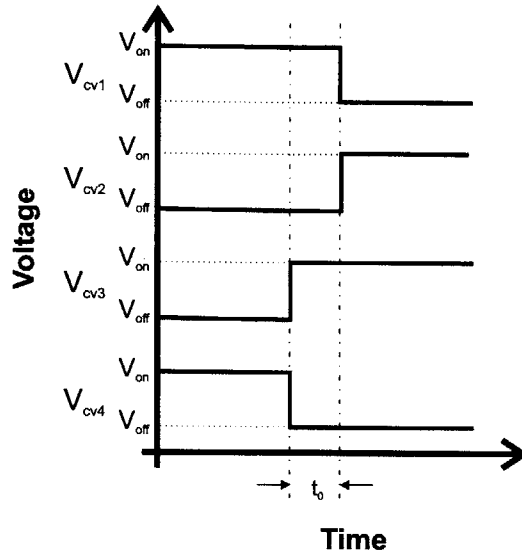


Figure 7-14: Timing of the control voltages for the strain-energy switch circuit for a switch operation where the movable electrode moves from being pulled-in to fixed electrode one to being pulled-in to fixed electrode two.

switch at the same instant. This will work for the circuit but can be relaxed a little bit to be $t_{cv1} \leq t_{cv2}$ and $t_{cv4} \leq t_{cv3}$, as long as the delay between the switching of the two signals is not long enough for the leakage currents of the capacitors to discharge the capacitors enough to cause the movable electrode to release from the pulled-in state. In addition, the two transistors should never both be on at the same time as this would connect voltage sources directly to ground.

7.5 Fabrication and experimental results

The testing of the prototype devices involved characterizing their electrical and mechanical properties. Electrical characterization consisted of measuring resistance to calculate the charge and discharge rates. In addition, the pull-in and hold voltages of the devices were measured in both air and in vacuum. One of the significant, albeit expected, results of these tests was that the dielectric charging experienced during operation in air was not seen in vacuum.

7.5.1 Fabrication results

To evaluate the fabrication results, optical and scanning electron-beam microscopy was used. Through this examination, a number of variations from the ideal process were observed.

One of the variations observed was that the etch of the silicon device layer widened the gaps by 200 to 300 nm over what was designed. The effect of wider gaps was to create devices with thinner movable electrodes and larger displacements. Secondary effects included increasing the resistance of the electrode due to a reduced cross-sectional area, and reducing the resonant frequency. The widening of the gap could have resulted from the lithography, the etching of the oxide mask, the etching of the silicon device layer itself, or a combination of these steps.

Another problem observed with the silicon layer etch was footing, or undercutting of the movable electrodes [81]. Footing became apparent when some of the movable electrodes buckled to the side after the silicon device layer etch. Buckling was a result of being undercut combined with the residual compressive stress in the oxide mask layer. The effect of the undercut on the device is to increase resistance by reducing the cross-section of the movable electrode. The effects of undercut on the stiffness and mass cancel each other out, resulting in zero net change in the resonant frequency. After the oxide mask layer was etched away, the buckled electrodes returned to their unbuckled state.

An additional variation was that the oxide film grown as the dielectric layer in between the electrodes was grown thicker than the design value. This layer was etched back a little (see Table 7.2) to compensate for the overgrowth. The effect of this was minimal, creating a slight increase in the device resistance and a slight decrease in the resonant frequency.

An additional effect of the oxide growth on the electrodes was the introduction of sufficient compressive residual stress into the movable electrodes to cause all of the devices that had been designed with a one micron width to buckle. The buckled structures became unusable at this point.

The aluminum layer performed as anticipated and described earlier. There were some undesired electrical paths created. However, the paths quickly burned up upon application of a voltage. This was observed by the creation of dark patterns in the aluminum film.

7.5.2 Device resistance

The resistance of the moving electrode was measured between the wire-bonded pads on either side of the moving electrode, see Figure 7-5. The movable electrode is the main source of resistance in the device because of its small dimensions. The resistance of the device was predicted using according to

$$R = \frac{L\rho_e}{wt_b}, \quad (7.11)$$

where ρ_e is the resistivity of the silicon, L is the length of the electrode, w is the width of the electrode, and t_b is the thickness of the electrode. Table 7.3 shows the resistance values measured for a number of devices and the predicted values based on the device dimensions as designed, and the resistivity value of the SOI wafer's device layer given by the manufacturer.

The devices that show significantly less resistance than the predicted values have a secondary electrical path created by the thin aluminum film ($\sim 10\text{nm}$) that was deposited on the wafer to enable wirebonding. In the devices that show a comparable resistance to the predicted value, the aluminum does not have a complete path between the bond pads; and thus the resistance increase results from the silicon comprising the movable electrode. A few devices not listed in Table 7.3 were open circuited. This result is likely due to a bad wirebond connection on one of the two bondpads.

7.5.3 Pull-in/hold voltages and dielectric charging

The prototype devices were tested to determine the pull-in and hold voltages of the various designs. Testing consisted of applying a voltage between one fixed electrode

Table 7.3: Resistance measurements and calculations for the prototype strain-energy switching structures.

Device	Measured (Ω)	Predicted (Ω)
B	1.0×10^6	0.6×10^6
D	1.9×10^6	0.5×10^6
E	700	0.5×10^6
G	750	0.4×10^6
I	466	0.3×10^6
J	0.86×10^6	0.33×10^6
K	6.6×10^6	0.53×10^6
M	880	0.47×10^6

and the movable electrode and increasing the voltage until the movable electrode pulled-in. At this point, the voltage was decreased until the movable electrode was released. The test sequence was repeated several times with each device. To observe the effects of dielectric charging, the polarity of the voltage was switched between some pull-in and release cycles during the testing.

Table 7.4 shows the pull-in and hold voltage results of the tested devices. These values given are averaged over a number of pull-in and release testing cycles. For the tests conducted in air, significant dielectric charging was observed, leading to large standard deviations. In some instances, polarity was switched after every pull-in and release cycle. This sequence minimized the effects of dielectric charging. For example, device K was tested in air in this manner, which led to its low standard deviation values. Device K was also tested in vacuum with some random switching of polarity, and it still displayed better stability over a number of iterations than any of the devices tested in air.

It is interesting to compare the ratio of the hold voltage over the pull-in voltage for the different devices. The lowest ratio for any of the devices tested in air was

Table 7.4: Pull-in and hold voltage results of several of the switch prototypes.

Device	Pull-in voltage (V)		Hold voltage (V)		ratio $\frac{V_h}{V_{p1}}$
	mean	standard deviation	mean	standard deviation	
C (air)	66.0	15.5	49.5	14.2	0.75
D (air)	85.5	6.64	69.6	7.27	0.81
E (air)	68.5	7.73	55.7	5.33	0.81
F (air)	71.2	8.44	67.8	8.51	0.95
G (air)	80.0	4.95	70.0	3.50	0.87
K (air)	59.2	3.58	45.6	3.36	0.77
K (vacuum)	86.5	3.81	43.5	3.17	0.50
M (air)	81.3	5.59	72.3	4.86	0.89

0.75, for the device tested in vacuum, the ratio was 0.50. Moreover, that same device (K) tested in air had a ratio of 0.77. One of the effects of dielectric charging in this case is to reduce the contrast between the hold and pull-in voltages. For the strain-energy switch, the contrast between pull-in and hold voltages is important for low voltage operation. For this reason, the fact that the vacuum tested device has a better contrast carries added significance.⁵

Comparing the pull-in and hold voltages of devices D and E is particularly interesting since the two devices have identical lengths, widths, and gaps. The only difference between the two is that in D the fixed electrodes are flat whereas in E the fixed electrodes are curved. The difference in the pull-in and hold voltages shows that the curved electrodes do reduce the pull-in and hold voltages for the device, as expected. The switching speed of the two devices should be essentially the same since the resonant structure have the same dimensions.

As mentioned above, testing the devices in air showed significant dielectric charg-

⁵For a more in depth discussion on the origins of dielectric charging and its effect on parallel plate actuators, see Section 4.2.1.

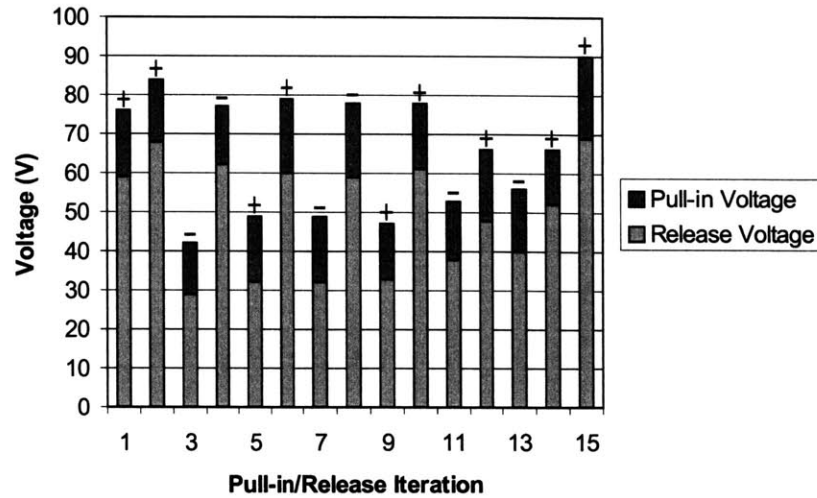


Figure 7-15: Pull-in and hold voltages for a series of switching cycles of device “C.” The + and - signs above the bars indicate the polarity of the iterations. These pull-in and release iterations were performed in air. Note the strong dielectric charging effects.

ing. This was observed by increased or decreased (in the cases of switched polarity) pull-in and hold voltages on subsequent pull-in and release cycles. The following plots show a series of pull-in and release cycles, with some polarity switching for a number of devices. The effects of dielectric charging are significant.

Figure 7-15 shows the results of the testing of device C in air. In this test, there are a series of iterations where two pull-in and release cycles were performed, after which the polarity of the applied voltage was switched. It is seen that the second of the two pull-in voltages during the two pull-in polarity cycle is significantly higher than the first of the two pull-in voltages. This is also true of the release voltages. This increase in the pull-in voltage is due to dielectric charging on the silicon oxide separating the fixed and movable electrodes.

Figure 7-16 shows the results of testing device K where the polarity of the pull-in voltage was switched after each pull-in and release cycle. The interesting thing to note in this case is that the pull-in voltages for both polarities appeared to be converging to a particular value. The convergence results from the charges on the surfaces of

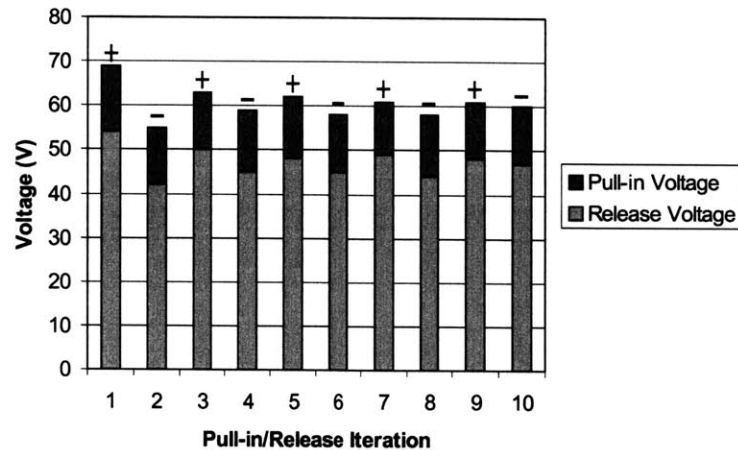


Figure 7-16: Pull-in and hold voltages for a series of switching cycles of device “K.” The + and - signs above the bars indicate the polarity of the iterations. In this case, the polarity is reversed with each cycle and the pull-in and hold voltages for the different polarities appear to be converging to a constant value.

the oxide layers becoming saturated with roughly an equal number of positive and negative charges. These essentially cancel out the effect of the trapped charges, and also prevent the collection of additional charge on the oxide surface.

Figure 7-17 shows testing results for the second fixed electrode of device K. (The first fixed electrode results are shown in Figure 7-16.) The same polarity switching scheme was followed and the same number of pull-in cycles was performed as in the case of the tests on the first electrode. This was done to verify by comparison that the pull-in and hold voltages were essentially the same for the two fixed electrodes. Very similar values and trends were seen between the two tests, validating that the devices were indeed symmetric in terms of electro-mechanical response.

Figure 7-18 shows a series of pull-in and release cycles performed inside an SEM under vacuum. The dramatic dielectric charging seen in the tests performed in air are not seen. This is a very encouraging result, since it indicates that by using one of the vacuum packaging schemes discussed in Section 7.4.3 the performance and reliability problems associated with dielectric charging will be eliminated or significantly reduced. However, the SEM causes a different artifact. If the electron beam impinges

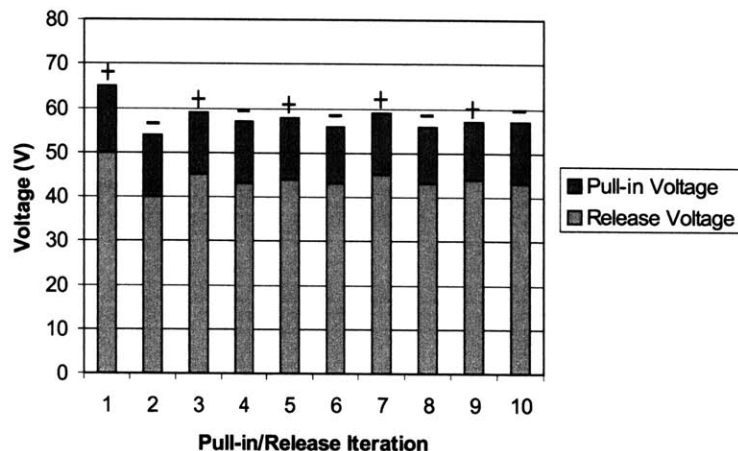


Figure 7-17: Pull-in and hold voltages for a series of switching cycles using the second fixed electrode of device “K” (Figure 7-16 used the first fixed electrode of device “K”). The same polarity cycling strategy was used in this case as in Figure 7-16 and the results are similar. This indicates that the symmetry of device “K” is good.

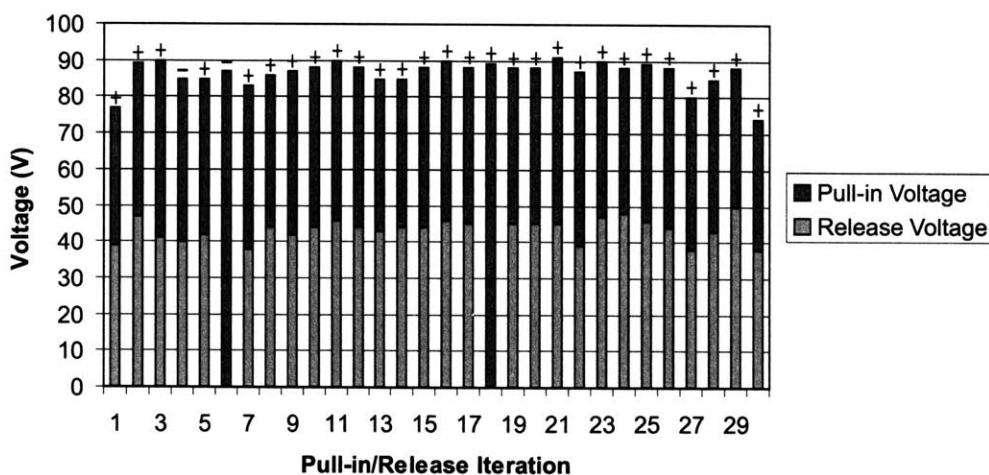


Figure 7-18: Pull-in and hold voltages for a series of switching cycles of device “K.” The + and - signs above the bars indicates the polarity used for that pull-in and release cycle. These pull-in and release tests were conducted in a vacuum within the chamber of an SEM. The dielectric charging seen in Figures 7-15, 7-16, and 7-17 is not observed in these tests. (The release voltages of iterations 6 and 18 were not recorded.)

on the device during operation, it can charge ungrounded parts of the device. This resulted in an artificial increase of the pull-in voltage observed inside the SEM in our experiments (see Table 7.4).

7.5.4 Discussion of results

These particular devices were not tested in a fashion that would allow the demonstration of the strain-energy switching technique. Further development of the control circuit is required before the technique can be demonstrated. However, a number of interesting results were obtained.

First of all, a fabrication process was developed by which strain-energy based switches can be easily fabricated using the device layer of an SOI wafer to create the structure.

It was also shown that by operating in vacuum, dielectric charging is eliminated. This results from having no air to ionize to thus cause dielectric charging. An additional result shown is that the device in the vacuum had a much higher contrast between the pull-in and hold voltages.

Finally, it was shown that by designing the fixed electrodes to be curved to match the mode shape of the movable electrode, the pull-in and hold voltages can be reduced as compared to a device that has flat fixed electrodes. This allows more efficient, and lower voltage operation of the devices.

7.6 Applications of strain energy switching

The strain-energy based actuation technique, allows switching of MEMS devices 10 to 1000 times faster than any other MEMS actuation technique, and at the same time reduces the required voltage and energy for actuation. These performance characteristics are ideal for a number of switching applications. Two of the most significant applications for this switching technique are optical switching and RF switching.

7.6.1 Optical switching

The switching speeds that are possible with the strain-energy based method easily provide the capability to meet the goal of one microsecond switching at IC level voltages. In addition, with either higher voltages or by using smaller displacements, it may be possible to reach switching speeds of 10 ns or less, allowing free-space or integrated optical MEMS switches based on strain-energy switching to be used for packet switching as well as switching for network protection and lightpath provisioning (see Table 2.1). These switches could also be used for optical interconnects for high-performance computing [50].

The benefits of using these MEMS switches for optical switching applications are many. They would be inexpensive to operate since the power consumption is very low. They would be inexpensive to manufacture since they can be made using conventional CMOS fabrication techniques. In addition, because they are CMOS compatible, they can be integrated directly with CMOS electronic chips.

For the wavelength selective ring resonator switch, the capabilities offered by the strain-energy switching method enable the switch to meet or exceed all of the performance requirements identified necessary for the switch to be used as an integrated switch in commercial applications. Indeed, no other switching mechanism provides the same combination of speed, actuation voltage, actuation power, and low cost CMOS compatible manufacturing.

7.6.2 Radio Frequency (RF) switching

RF switching is currently performed by PIN (positive-intrinsic-negative) diodes, FETs (field-effect transistors), or coaxial RF switches. These are either solid-state, semiconductor-based switches; or electromechanical switches with discrete, macroscopic components. Both kinds of switches suffer from natural performance impediments. The semiconductor switches inefficiently transmit current in their closed state because of the limitations of semiconductor materials. This results in dissipated power and insertion loss weakening the signal as it passes through the switch. The macro-electromechanical

switches have much better RF performance but are slow, large, expensive, and use a lot of power. This has led researchers to look toward MEMS technology for RF switching that has good RF performance but is still small and inexpensive [111].

Several RF MEMS switches have been developed over the last 10 years. Unfortunately, technical and cost problems have kept these from being commercialized. Many of the problems RF MEMS switches have faced are directly related to the limitations of the actuation methods they use.

Actuation mechanisms have been electrostatic, piezoelectric, thermal, magnetic, or some combination of these. All of these actuation techniques have advantages and disadvantages. None have yet produced a switch that provides adequate functionality and reliability for widespread commercial application.

As previously mentioned, electrostatic-based switches typically require very high operating voltages (30 to 80 volts). A major limitation is that these voltage levels are not compatible with CMOS integrated circuits. In addition, due to the high operating voltages creating high electric fields, these electrostatic switches have reliability issues related to dielectric charging. Some electrostatic switches have been designed to be mechanically compliant and thus require a lower voltage (10 to 20 volts). However, the low compliance of these switches leads to problems with stiction (when the moving and fixed electrodes stick together) and switching speed.

RF MEMS switches based on other actuation techniques also have limitations. Thermal- and magnetic-based switches require a high current for actuation, which leads to a very high operating power. These types of switches also tend to be very slow. Piezoelectric actuators provide high force, but very small strains. This means the actuators must either be very large or must be coupled to some sort of transmission that amplifies the actuators' motion. Either method leads to relatively slow switching speeds. Additionally, typical materials used in magnetic and piezoelectric actuation are not CMOS compatible.

For all types of RF MEMS switches currently under development, reliability problems have been one of the prime barriers to commercialization. Current RF MEMS switches fail for one or more of the following reasons: contact resistance increase due

to contamination and/or high impact velocities; stiction (moving part becoming stuck to a non-moving surface) due to inadequate mechanical restoring force (stiffness); or dielectric charging, which inhibits the actuation of the switch. The strain-energy actuation technique either directly addresses or significantly minimizes all of these reliability concerns.

Chapter 8

MEMS tuning of Optical ring resonator filters

In addition to switching optical ring resonator filters on and off, it would be very useful in integrated optical circuits to have a tunable ring resonator filter. A tunable filter would allow the circuit to select which wavelength (channel) is dropped from the through waveguide to the drop port. To achieve tuning of an optical ring resonator, the optical path length of the light in the ring resonator needs to change. This can be achieved by changing the index of the material using carrier injection [30, 56, 57, 140]. However, the carriers introduce loss into the ring resonator. This, in turn, changes the filter characteristics (i.e. quality factor) with tuning. Carrier injection also requires a significant amount of energy input to maintain the tuning and the tuning range is quite limited ($\sim 5\text{nm}$).

A second approach uses the thermo-optic effect, where the ring resonator is heated to create the change in the optical path length [88]. The change in path length is due to a combination of thermal expansion and change in refractive index. Thermal tuning does not introduce loss into the ring resonator but does have a limited tuning range and also requires a significant amount of energy to maintain the tuning. Thermal tuning is quite slow, on the order of tens of milliseconds. The range of either the carrier injection technique or thermal tuning can be expanded by using the vernier effect if only one wavelength is of interest in the optical circuit.

A third technique that utilizes MEMS to tune the optical ring resonator filters is proposed here. This technique is similar to the wavelength selective optical switch described previously but, instead of a lossy membrane, a dielectric membrane is suspended over the ring resonator. For tuning, the dielectric membrane would be controllably moved in an analog fashion within the evanescent field of the optical ring resonator. The position of the of the dielectric membrane determines the effective refractive index of the ring resonator. The effective index, in turn, sets the optical path length of the ring resonator filter. Thus, by controlling the position of the ring resonator filter, the ring resonator filter can be tuned through a wide spectral range ($\sim 30\text{nm}$) [145].

By using an electrostatic MEMS actuator, the energy required for tuning is very small compared to both thermal and electro-optic techniques. The response can be up to a thousand times faster than thermal tuning and no loss is introduced into the ring resonators (as is the case with carrier injection). In this chapter, we carry out a feasibility study of this type of MEMS-tunable optical ring resonator filter to determine if the necessary functionality can be achieved and commercialized.

8.1 Design Requirements

For tuning through the entire range of interest of wavelength-division-multiplexed optical communications ($\sim 30\text{nm}$), the dielectric membrane needs a travel range of 50 to 500nm away from the ring resonator. The required displacement stability of the device, at its most strict location of 50nm away from the ring , is ± 0.07 nm. Because of the exponential nature of the evanescent field, the displacement stability becomes much less strict as the gap between the ring resonator and the dielectric membrane becomes larger.

The response time of the tuning device is not as critical as that of the switching device. The desired response time of the filter is 1ms or faster [116]. The actuation voltage is restricted to 5V, the standard voltage available from an integrated circuit.

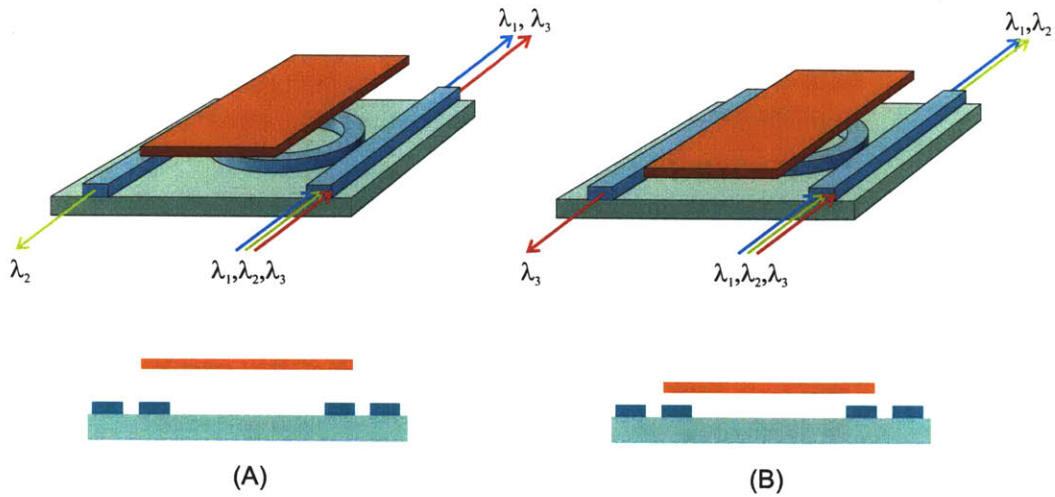


Figure 8-1: Illustration of the operation of the MEMS ring resonator tuning device. (A) and (B) show the ring resonator tuned to drop different channels (wavelengths).

8.2 Device Description

The tuning principle is illustrated in Figure 8.2. As the position of the dielectric membrane is moved within the evanescent field of the ring resonator, the resonant wavelength is changed from one channel to another.

The proposed MEMS structure to control the displacement of the dielectric membrane is illustrated in Figure 8.2. This is the structure that will be used in the feasibility analysis of this chapter. The movable structure consists of the dielectric slab composed of a thin layer of magnesium oxide and a backing layer of silicon oxide. The silicon oxide stiffens the dielectric slab so that it does not deform during actuation. The magnesium oxide provides a higher refractive index than the that of silicon oxide and is thus more effective at tuning the ring resonator than the silicon oxide.

The dielectric slab is suspended by two or more flexures that are electrically conductive. The flexures allow the dielectric slab to displace vertically. The flexures, in conjunction with the top electrodes, provide an electrostatic force that controls the displacement. Together with the bottom electrodes, the flexures are also be used for capacitive displacement sensing. This allows feedback control of the displacement to

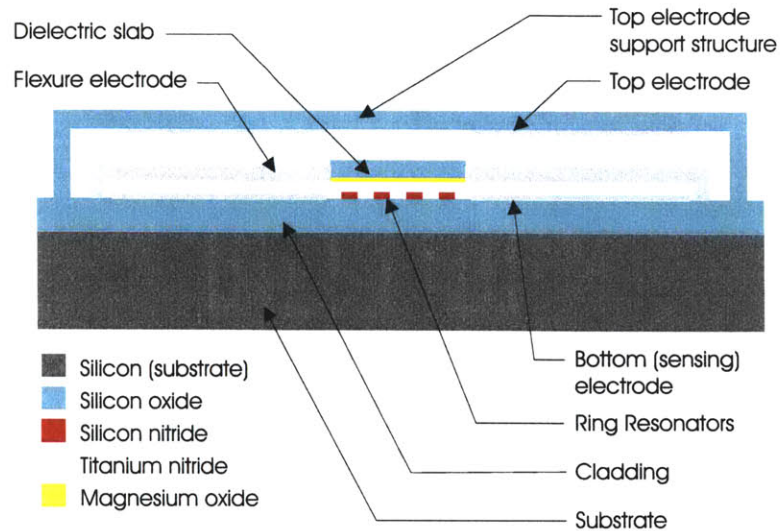


Figure 8-2: Schematic of the MEMS structure, including both the control and sensing electrodes, integrated with the optical ring resonator.

be implemented, rejecting thermal mechanical noise and other disturbances.

The placement of the sensing (bottom) and actuation (top) electrodes takes advantage of the fact that the stability requirement becomes less stringent as the dielectric slab moves away from the ring resonators. Parallel plate electrostatic actuation is nonlinear with the smallest displacement per voltage increment occurring when the structure is at its initial position. Placing the fixed actuation electrode above the moving structure allows the finest control where it is needed most.

The sensing electrode provides the highest sensitivity (large voltage changes for small displacements) when the plates are closest to each other. The sensing electrode is therefore placed underneath the structure to allow the most sensitive measurements where they are needed most.

8.3 Device modelling and design

Figure 8.3 shows a lumped parameter model of the device illustrated in Figure 8.2. This model is used as the basis for the device design and performance analysis. The

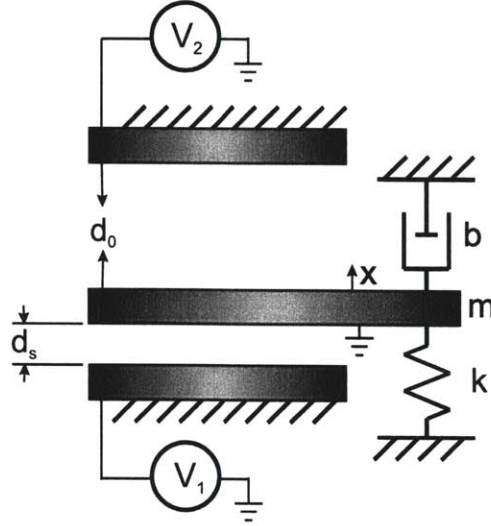


Figure 8-3: Schematic of the lumped parameter model based on the MEMS structure illustrated in Figure 8.2.

equation of motion resulting from this model is

$$m\ddot{x} + b\dot{x} + kx = \frac{\epsilon_0 AV_c^2}{2(d_0 - x)^2} - \frac{\epsilon_0 AV_s^2}{2(d_s + x)^2}, \quad (8.1)$$

Where V_c is the control voltage signal, d_0 is the initial gap between the fixed control electrode and the movable electrodes, V_s is the sensing voltage signal, d_s is the initial gap between the fixed sensing electrode and the movable electrode, A is the overlap area of the sensing and the control electrodes (assumed to be the same), and ϵ_0 is the permittivity of air.

We apply a sensing signal

$$V_s = V_{s0} \sin(\omega_s t), \quad (8.2)$$

where the frequency ω_s is much higher than the mechanical resonant frequency of the structure. The effect of the sensing signal on the bridge is essentially the same as applying a DC voltage at the RMS value of $\frac{V_{s0}}{\sqrt{2}}$. The control voltage will need to compensate for this effect, as well as displace the structure to the desired location.

By assuming quasi-static conditions, the required control voltage is

$$V_c = \sqrt{\frac{2kx(d_0 - x)^2}{\epsilon_0 A} + \frac{V_{s0}^2(d_0 - x)^2}{2(d_s + x)^2}}. \quad (8.3)$$

The total control voltage is a combination of the bias voltage and a voltage signal to displace the structure to the desired location.

To design the structure to operate at a maximum of 5 volts, we set the pull-in voltage of the control signal at 5 volts. In addition, since we know that the maximum displacement needs to be 450 nm from the equilibrium position, we assume this is the pull-in displacement. At this displacement, the gap between the structure and the fixed sensing electrode has increased by a factor of ten (50nm to 500nm). This, combined with the fact that the sensing signal is small, allows us to neglect the effect of the sensing signal on the structure at pull-in. Using these known quantities combined with the pull-in voltage equation

$$V_{pi} = \sqrt{\frac{8kd_0^3}{27\epsilon_0 A}} \quad (8.4)$$

allows the calculation of the required stiffness to area ratio for the device

$$\frac{k}{A} = \frac{27\epsilon_0 V_{pi}^2}{8d_0^3}. \quad (8.5)$$

This will be the same stiffness to area ratio that the sensing electrodes operate with as well. If we require that the sensing signal does not exceed the pull-in voltage in the absence of the control voltage, the maximum sensing signal amplitude would be

$$V_{s0} = \sqrt{\frac{2V_{cpi}d_s^3}{d_0^3}}. \quad (8.6)$$

Since all parameters in Equation 8.6 have been defined already, V_{s0} is calculated to be 50 mV. This value is consistent with our assumption that V_{s0} is small compared with the pull-in voltage of the control signal.

The next design step is to select a structure that provides a stiffness to area ratio

equal to that given in Equation 8.5.

To work off of the success of the wavelength-selective switch, a solid bridge structure will be used. Although it does not take into account the effects of the stepped-up anchors, we will assume that the bridge behaves as a fixed-fixed structure. The stiffness of the fixed-fixed bridge is

$$k = \frac{16Ewt_b^3}{L^3}, \quad (8.7)$$

and the area of the bridge is

$$A = wL. \quad (8.8)$$

The material used for the bridge in this analysis is titanium nitride (see Chapter 5). The value of the Young's modulus E is selected to be 300GPa.¹ Setting the width w of the bridge to $15\mu\text{m}$ and length to $250\mu\text{m}$ on either side of the dielectric slab (i.e. $L = 500\mu\text{m}$) requires that the thickness t_b be $1.58\mu\text{m}$.

The resonant frequency of the movable bridge can be calculated using Rayleigh's energy method [136] which gives

$$\omega_n = \sqrt{\frac{k}{(m_d + \frac{13}{35}m_b)}}, \quad (8.9)$$

where m_d is the mass of the dielectric slab and m_b is the mass of the bridge. Combining the mass of the dielectric slab and the mass of the bridge according to the denominator of Equation 8.9 gives the effective mass m_{eff} for the lumped parameter model. The dielectric slab is composed of silicon oxide and is given dimensions of $45\mu\text{m}$ by $45\mu\text{m}$ by $4\mu\text{m}$. This allows for adequate overlap over the ring resonator so that the edges of the slab do not induce loss. The slab is also thick enough that it should admit very little deformation. As mentioned before, a thin layer ($\sim 100\text{nm}$) of a high index material added on the bottom of the slab for more effective tuning of the ring.

To reduce the effects of Brownian noise² from the system and reduce dielectric charging, the system will be modelled as if it is packaged in a vacuum [36]. A mechanical

¹Titanium nitride gives designers the unique ability to pick a value for the Young's modulus based on the deposition parameters of the film.

²Brownian noise is due to collisions of air molecules with the mechanical structure.

Table 8.1: Mechanical parameters for the ring resonator tuning lumped parameter model.

Parameter	Value
Stiffness k (N/m)	2.28
Area A (m ²)	7.5×10^{-9}
Effective mass m_{eff} (kg)	3.84×10^{-11}
Resonant frequency f_n (kHz)	38.7
Damping constant b (N·s/m)	9.35×10^{-8}

quality factor of $Q = 100$ will be assumed. This estimate is conservative for vacuum packaged MEMS devices. The damping constant is

$$b = \frac{m_{\text{eff}}\omega_n}{Q}. \quad (8.10)$$

Table 8.1 lists the numerical values of all of the mechanical parameters used in the ring resonator tuning lumped parameter model.

8.3.1 Noise sources

Potential noise sources for the mechanical structure include mechanical vibrations, thermal mechanical noise, Brownian noise, and noise resulting from noise in the applied electrical signals. External vibrational noise can be rejected by using proper packaging techniques that only allow low-frequency vibrations to pass through to the device. Low-frequency vibrations will have a very small effect on the device since it has a relatively high resonant frequency. Brownian noise has been significantly reduced through the use of vacuum packaging [36], as already mentioned above. The remaining thermal mechanical noise and the mechanical noise resulting from the noise in the applied control and sensing signals will be the two primary sources of noise in the device.

Thermal mechanical noise is a result of the thermal energy contained within the structure [40, 58, 66, 120]. In each vibration mode, the thermal noise is equal to $\frac{1}{2}k_bT$, where k_b is Boltzmann's constant and T is the absolute temperature of the device. In equilibrium, the thermal energy equals the energy present in the structure in the form of mechanical vibrations, giving

$$\frac{1}{2}k\langle X^2 \rangle = \frac{1}{2}k_bT. \quad (8.11)$$

Using this equation with the stiffness value given in Table 8.1 and a maximum temperature of 125°C gives a RMS noise value of 0.5Å, indicating that the open-loop noise-limited positional accuracy is below specification; i.e., the structure will regularly exceed the 0.7Å range imposed by the optical design. Electronic noise which we have yet to consider would lead to even worse performance.

The thermal noise can be expressed as a stochastic force with RMS value,

$$F_n = \sqrt{4k_bTb\Delta f}, \quad (8.12)$$

where Δf is the frequency band of interest, and combined with the system equation of motion. In this case, Δf is set to the mechanical bandwidth of the system. Equation 8.12 is the mechanical equivalent of the Johnson noise resulting from resistors in electrical circuits.

8.3.2 Feedback control system

In this section we explore the potential of feedback control for bringing the positional of the tuning element back to within specification for our design. In other words, we seek to use feedback to eliminate positional disturbances due to thermal and electrical noise. For this purpose, a linearized model of the system is adequate, since the displacements about the operating position are small.

We linearize the system equations about the operating positions found from Equa-

tion 8.3

$$V_{c0} = \sqrt{\frac{kx_0(d_0 - x_0)^2}{\epsilon_0 A} + \frac{V_{s0}^2(d_0 - x_0)^2}{2(d_s + x_0)^2}}. \quad (8.13)$$

The linearized electrostatic force terms are

$$\begin{aligned} F_{\text{act}}(x, V_c) = & -\frac{\epsilon_0 AV_{c0}^2}{2(d_0 - x_0)^2} + \frac{\epsilon_0 AV_{s0}^2}{4(d_s + x_0)^2} \\ & -\frac{\epsilon_0 Ax_0 V_{c0}^2}{(d_0 - x_0)^3} - \frac{\epsilon_0 Ax_0 V_{s0}^2}{2(d_s + x_0)^3} \\ & + \frac{\epsilon_0 AV_{c0}^2}{(d_0 - x_0)^3}x + \frac{\epsilon_0 AV_{s0}^2}{2(d_s + x_0)^3}x \\ & + \frac{\epsilon_0 AV_{c0}}{(d_0 - x_0)^2}V. \end{aligned} \quad (8.14)$$

For these linearized equations, we have assumed that the noise in the sensing signal is negligible. Since this signal is set at a constant amplitude and frequency, it requires very little bandwidth and can be band-pass filtered to further reduce the noise. This is in contrast to the control signal that needs to be at the bandwidth of the system, and therefore will be subject to much greater noise. For this reason, the assumption that the sensing signal is constant (noiseless) is valid.

The terms that depend on x in Equation 8.14 result in what is called the spring-softening effect in parallel plate actuators. When these linearized terms for the actuator force are combined with the terms describing the dynamics of the mechanical system, the stiffness term becomes

$$\left[k - \frac{\epsilon_0 AV_{c0}^2}{(d_0 - x_0)^3} - \frac{\epsilon_0 AV_{s0}^2}{2(d_s + x_0)^3} \right] x, \quad (8.15)$$

indicating that the stiffness of the system decreases as voltage is applied to the system. This spring softening effect amplifies the stiffness-dependent thermal-mechanical noise of the structure. Amplification of the thermal mechanical noise occurs in all parallel plate actuators, even in the absence of the sensing signal (i.e. $V_{s0} = 0$) [46].³

The point of greatest interest and concern is when the dielectric slab structure

³For a further discussion of the thermal-mechanical noise in parallel plate actuators, see Appendix E.

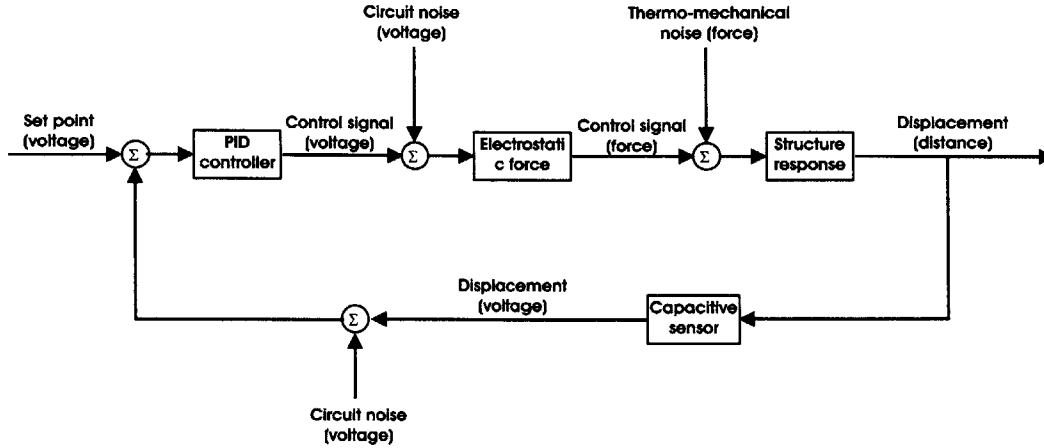


Figure 8-4: Block diagram of the feedback control system used for the tunable ring resonator filter.

is closest to the ring resonator filters (i.e., $x_0 = 0$). It is at this location that the requirements for stability are the strictest.

For $x_0 = 0$, we can combine Equations 8.1, 8.3, and 8.14 to get

$$m\ddot{x} + b\dot{x} + \left(k - \frac{\epsilon_0 AV_{c0}^2 (d_s + d_0)}{d_s d_0^3} \right) x = \frac{\epsilon_0 AV_{c0}}{d_0^2} V. \quad (8.16)$$

This is the linearized equation of motion about the operating point defined by $x_0 = 0$, $V_{s0} = 50\text{mv}$, and $V_{c0} = 0.95\text{V}$. At this operating point, the effective spring constant is 1.56N/m . This increases the RMS thermal noise to 0.6\AA .

This equation is used in the feedback control model shown in Figure 8.3.2. Included in the block diagram are the thermal-mechanical noise as well as the electronic noise from the sensing circuit and the noise from the control circuit. The control circuit used in this analysis is a standard PID controller with transfer function of

$$G_c(s) = K_p + \frac{K_i}{s} + K_d s. \quad (8.17)$$

One possible circuit implementation of a PID controller is shown in Figure 8-5 [103]. The proportional gain, integral gain, and derivative gain resulting from this

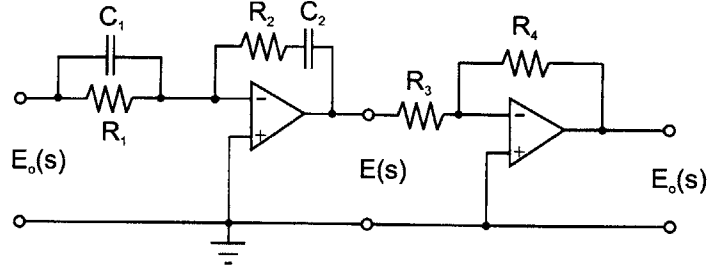


Figure 8-5: PID controller circuit [103].

circuit are

$$K_p = \frac{R_4 (R_1 C_1 + R_2 C_2)}{R_3 R_1 C_2} \quad (8.18)$$

$$K_i = \frac{R_4}{R_3 R_1 C_2} \quad (8.19)$$

$$K_d = \frac{R_4 R_2 C_1}{R_3} \quad (8.20)$$

8.3.3 Capacitive sensing

Sensing for the feedback system is provided by a capacitive sensing circuit. The sensing signal is applied to the capacitor formed between the fixed sensing electrode and the movable bridge electrode. The result of the applied sensing voltage signal is a current flow that is dependent on the capacitance. Since the capacitance depends on the gap between the plates, a measure of the relative position of the movable plate can be obtained indirectly from the current. A simple circuit for the capacitive sensor is shown in Figure 8-6 [7].

The output voltage of the circuit is

$$E_0 = V_s \frac{C_s j \omega_s}{C_f j \omega_s - 1/R_f} \quad (8.21)$$

The maximum output voltage of the circuit should not exceed 5V, because of the CMOS compatibility requirement. Using this constraint, along with the capacitance

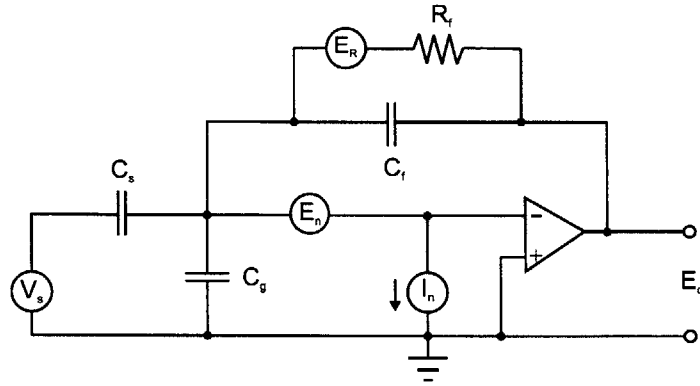


Figure 8-6: Capacitive sensing circuit [7].

Table 8.2: Parameters for the capacitive sensing circuit.

Parameter	Value
C_s	1.3pF
C_f	13fF
R_f	100.0M Ω
C_g	10fF

of the sensing capacitor as determined by the device dimensions selected in Section 8.3, the rest of the parameters were calculated and are shown in Table 8.2. The parasitic capacitance C_g is estimated based on a reasonable value for integrated circuit parasitic capacitance.

The sensing circuit noise is the dominant electronic noise in the closed-loop system because this noise is amplified by both the sensing circuit and the control circuit. The noise from the control circuit is only amplified by the control circuit, and is thus less of a concern, although this noise source was retained in the simulation for safety.

The noise resulting from the sensing circuit is a combination of the Johnson noise from the resistor and the current and voltage noise associated with the op-amp. These noise sources are combined and amplified by the circuit. The total noise in the output

Table 8.3: Simulation results of open-loop and feedback control of the ring resonator tuning structure.

Simulation	Mechanical fluctuations
Open-loop control	0.6 Å
Closed-loop control	2.7pm

signal is

$$\begin{aligned}
 E_{n0}^2 = & \left| \frac{E_n^2 \Delta f (1/R_f + j\omega_s C_s + j\omega_s C_g + j\omega_s C_f)}{1/R_f + j\omega_s C_f} \right|^2 \\
 & + \left| \frac{\sqrt{4k_b T R_f \Delta f}}{1 - j\omega_s C_f R_f} \right|^2 \\
 & + \left| \frac{I_n^2 \Delta f}{1/R_f + j\omega_s C_f} \right|^2. \tag{8.22}
 \end{aligned}$$

Using the values $E_n = 4.5\text{nV}/\sqrt{\text{Hz}}$, $I_n = 1.7\text{pA}/\sqrt{\text{Hz}}$ [102] for the op-amp noise sources along with the parameters given in Table 8.2 gives a total noise at the output of the circuit of $277\mu\text{V}$ at a temperature of 125°C and with a sensing signal frequency of 100MHz . Comparing this noise with the sensitivity of the capacitive sensor indicates that the sensor can resolve a change in capacitance of $7.2 \times 10^{-17}\text{F}$, which corresponds to a displacement of 2.7pm . These results are in line with experimental demonstrations of capacitive sensing [7, 125].

8.3.4 System performance

Using the parameters derived in the preceding sections, the feedback control system model shown in Figure 8.3.2 was implemented in Simulink. The results of the simulations are shown in Table 8.3. The open-loop simulation included only the thermal-mechanical noise of the system and, consistent with the analysis and associated assumptions, the results of the simulation give an RMS value of the displacement noise of 0.6Å .

Table 8.4: PID controller parameters used in closed-loop simulations.

Parameter	Value
K_p	$1 \times 10^{-4} \text{ V/V}$
K_i	$5 \times 10^2 \text{ V/(V}\cdot\text{s)}$
K_d	$2 \times 10^{-5} \text{ V}\cdot\text{s/V}$

For the closed-loop simulation, thermal-mechanical noise and circuit noise for both the sensing circuit and the control circuit was included. The sensing circuit noise was set to $271\mu\text{V}$ (RMS), according to the analysis performed above. The control circuit noise was set to 2.71 mV . The noise from the control circuit should actually be much less. However, our choice represents the value at which the control circuit noise started to influence the mechanical stability of the MEMS structure. The thermal-mechanical noise was same as included in the open-loop simulation.

The parameters selected for the PID controller in the closed loop simulation are shown in Table 8.4. The control signal fluctuations applied to the structure had an RMS value of 100mV . These fluctuations were the result of the feedback control loop, with the PID controller parameters determining the amplitude of the fluctuations. It was necessary to keep the fluctuations in the control signal small since the bulk of the control signal is used to displace the structure to its desired operating position.

8.4 Nonlinear control

MEMS parallel plate actuators are nonlinear systems. In the analysis and simulations performed above, the system was linearized about one particular operating point. Control parameters were selected to minimize the noise of the structure while also meeting the other specifications. However, when the tunable ring resonator structure is desired to be set at a different operating position, the control parameters will need to change to be able to accommodate the changes that occur in the system parameters

due to the nonlinearities of the system.

One way to construct a nonlinear controller is to design a number of PID controllers at a number of operating positions of the system. As the actual operating position of the system moves between the operating positions for which controllers were designed, the parameters for the instantaneous controller can be estimated by interpolation. This kind of nonlinear control is called piecewise linear control [61].

A second nonlinear control method that can be used is to use the controller to compensate for the nonlinearities of the system. For parallel plate actuators, the nonlinearity in the system is created by the dependence of the electrostatic force on the square of the applied voltage and the inverse of the square of the displacement of the plate. The nonlinear dependence of the force on the voltage squared is easily resolved by simply calling the input to the system voltage squared, rather than just voltage. The dependence of the force on the inverse of the displacement squared requires that the controller have a dependence on the square of the displacement as well. This arrangement cancels the nonlinearity of the system.

In theory, this type of nonlinear controller can control the parallel plate actuator in a stable fashion throughout its entire range of motion, even in the range where pull-in would normally occur. Actually achieving the full range of motion is difficult since the calibration of the controller would need to be very accurate. The performance of the controller is further limited by the speed of the controller. The latter also becomes a limiting factor as the movable electrode approaches the fixed electrode.

8.5 Discussion

The primary goal of the analysis provided in this chapter was to determine if a MEMS tunable ring resonator filter is feasible with the strict requirements on the positional accuracy of the bridge structure. Our results indicate that MEMS tuning of integrated optical ring resonators is feasible according to first principles, using closed-loop feedback control. This system would require the integration of the control electronics directly with the MEMS tunable filter in the same chip to be able to achieve

the necessary circuit speed and to reduce stray capacitance to the point where the circuit would perform as designed. The benefit of our feedback scheme is that it can also compensate for variations due to fabrication errors within limits (e.g. lithography resulting in shapes slightly different than predicted), and time variant errors (e.g. due to temperature variations). A complete analysis of such errors and design of the calibration (system identification) procedures and robust control schemes for this goal were beyond the scope of this thesis. These steps would constitute a natural next step in an effort to reduce the proposed devices to practice.

The proposed devices and control methods may have a significant impact on integrated photonics. A tunable filter based on these design parameters would have a very wide tuning range, wide enough to cover an entire 30nm communication band. The speed at which the wavelength could be tuned would be on the order of tens of microseconds. Because the tuning mechanism is independent of the materials used for the cladding and core of the ring resonator filter, the optical performance of the device can be as good as the best performing ring resonator filters currently available.

If the requirements for either the tuning range were relaxed or if the available actuation voltage were increased, the complexity of the control circuitry would be significantly reduced because of the exponential nature of the evanescent field and the dependence of the thermal-mechanical noise on the stiffness of the system. It may even be possible to operate the device using open-loop control to control the device after rigorous calibration, similar to Lucent's micro-mirror arrays [3].

Chapter 9

Conclusions and future work

The purpose of this thesis has been the development of MEMS switchable and tunable ring resonator filters for integrated optical circuits. To this end, a number of contributions have been described herein. A MEMS-switchable ring resonator filter device has been designed, fabricated, and tested to show wavelength-selective switching using MEMS devices combined with ring resonator filters. The switch was operated at 30V (24V pull-in) with switching speeds of $16\mu\text{s}$ to pop-up and $60\mu\text{s}$ for pull-down. The optical switching contrast was 13dB in the drop port and 1.5dB in the through port. The insertion loss in the drop port was 10dB. This is the first demonstration of an integrated wavelength-selective MEMS optical switch and the first demonstration of a ring resonator being switched on and off (rather than detuned).

The work to characterize this particular device led to a better understanding of the residual stress challenges associated with working with aluminum. In addition, a model for dielectric charging has been proposed that shows the trapped charge dependence of the dielectric surface on the electric field applied to the air in the gap between the parallel plates forming the MEMS actuator and matches well with the experimentally observed behavior. The model correctly predicted the behavior of the MEMS bridge during pull-in and provided a measure of the charge trap densities of the silicon oxide that is comparable to values obtained by other experimental means.

Because of the difficulties associated with residual stress in aluminum, titanium nitride was developed as a new material for MEMS applications. Titanium nitride

has a number of appealing properties including high hardness, high stiffness, electrical conductivity, high melting point, chemical inertness, wear resistance, and low surface adhesion (i.e. anti-stiction capacity). Poly-silicon was shown to be an effective sacrificial material for titanium nitride, with xenon difluoride as the etchant to remove the sacrificial material. To control the residual stress in titanium nitride, it was shown that annealing at a relatively low temperature could reduce the residual stress in the titanium nitride to acceptable levels. We expect these contributions to be significant for MEMS applications beyond integrated optics that was the focus of this thesis.

To allow integration of the wavelength selective switch with integrated circuits where the voltage is limited to low values ($\sim 5V$) and to provide switching speeds faster than one microsecond (both key requirements for commercialization of the ring resonator switch), two new complementary actuation techniques for MEMS switching were developed. In the first actuation technique, the mechanical system resonance is excited by a modulated voltage signal until enough energy is stored in the mechanical system to allow pull-in of the movable plate at a significantly reduced voltage as compared to applying a DC voltage to the device.

The second actuation technique switches a movable plate from being pulled-in to one fixed electrode to being pulled-in to an opposing fixed electrode. The energy for switching this device comes from the energy stored in the mechanical system when it is in the pulled-in state. This also allows operation at a much lower voltage than using a standard MEMS parallel plate actuator but it also provides switching speeds that are significantly faster than one microsecond.

MEMS tuning of ring resonator filters was also explored and a feasibility analysis was performed. The proposed design moves a dielectric slab incrementally in the evanescent field of the ring resonator. Different operating positions of the dielectric slab correspond to different WDM channels. For the operating position closest to the ring resonator, the positional accuracy of the dielectric slab for proper optical operation is less than an angstrom. This was demonstrated to be feasible according to first principles by use of capacitive sensing and feedback control. One of the key discoveries from this analysis that has wide application is that for parallel plate MEMS

actuators there is an amplification of the thermal-mechanical noise as the actuator is displaced from its equilibrium position. Therefore, to achieve better stability, it is best to operate the movable electrode as close to its equilibrium point as possible.

9.1 Future work

Much work still needs to be done to apply the results of this thesis towards the creation of practical MEMS switchable and tunable ring resonator filters. The irresistible appeal of integrating guided-wave optics, electronics, and opto-mechanics in the same micro-system is a major driving force for the continuation of this endeavor.

For the wavelength selective switch, the next steps would be to design and fabricate a second generation prototype that incorporates the use of titanium nitride to reduce the negative effects of residual stress, and makes use of the new actuation technique to show both low voltage operation and high-speed switching. In addition, the fabrication process for this device needs to be refined in such a way as to allow integration with a variety of optical elements.

The MEMS tunable ring resonators require a significant amount of work. The next step is to fabricate an initial prototype device to demonstrate filter tuning using the dielectric slab approach. This should be with a simple MEMS device, where the dielectric slab is pulled-down rather than up as shown in the device whose performance was analyzed in Chapter 8. Once demonstrated, a more complex device incorporating more of the design elements of the device in Chapter 8 should be created and tested. After these devices have been demonstrated and refined, an integrated device where the control electronics are integrated together with the device should be created. This is a rather complex system to integrate together. For this reason, the step by step approach described here is the best approach to maximize the chance of success.

As these, and other, integrated optical devices are refined, integrated optical circuits for a variety of functions need to be designed, fabricated, and characterized. Through these optical circuits, the impact promised by the results described herein will be realized.

Appendix A

Material Property Tables

Table A.1: Aluminum (Al) Material Properties

Property	Value	Source
Young's Modulus (E)	70 GPa	[125]
Poisson Ratio (ν)	.33	[12]
Density (ρ)	2697 kg/m ³	[125]
Yield Strength (σ_Y)	17 - 200 MPa	[12, 72]
Coefficient of Thermal Expansion (α)	22.5 - 24.0 μ strain/ $^{\circ}$ C	[12, 117, 125]
Optical Index ($\lambda = 1550\text{nm}$) (n)	1.44+i16	[121]
resistivity	2.74 - 2.78 $\mu\Omega$ -cm	[12, 117]
Melting Point	646 - 658 $^{\circ}$ C	[12, 117]
Specific Heat	0.9 J/g- $^{\circ}$ C	[117]
Thermal Conductivity	210 - 231 W/m- $^{\circ}$ C	[12, 117]

Table A.2: Silicon (Si) Material Properties

Property	Value	Source
Young's modulus ¹	160 GPa	[93]
Poisson ratio	0.22	[93]
Density (ρ)	2400 kg/m ³	[93]
Failure Strength (σ_Y)	7 GPa	[93]
Coefficient of Thermal Expansion (α)	2.6 μ strain/ $^{\circ}$ C	[93]
Optical Index ($\lambda = 1531.941\text{nm}$) (n)	3.4784	[121]
resistivity	varies with doping	
Dielectric Strength ²	3 MV/cm	[93]
Relative Permittivity	11.8	[93]
Melting Point	1415 $^{\circ}$ C	[93]
Specific Heat	0.7 J/g- $^{\circ}$ C	[93]
Thermal Conductivity	157 W/m- $^{\circ}$ C	[93]

Table A.3: Silicon Oxide (SiO₂) Material Properties

Property	Value	Source
Young's modulus	73 GPa	[93]
Poisson ratio	0.17	[93]
Density (ρ)	2300 kg/m ³	[93]
Failure Strength (σ_Y)	8.4 GPa	[93]
Coefficient of Thermal Expansion (α)	0.55 μ strain/ $^{\circ}$ C	[93]
Optical Index ($\lambda = 1469.5\text{nm}$) (n)	1.44497	[121]
Dielectric Strength	5-10 MV/cm	[93]
Relative Permittivity	3.8	[93]
Melting Point	1700 $^{\circ}$ C	[93]
Specific Heat	1.0 J/g- $^{\circ}$ C	[93]
Thermal Conductivity	1.4 W/m- $^{\circ}$ C	[93]

Table A.4: Silicon Nitride (Si_3N_4) Material Properties

Property	Value	Source
Young's modulus	323 GPa	[93]
Poisson ratio	0.25	[93]
Density (ρ)	3100 kg/m ³	[93]
Failure Strength (σ_Y)	14 GPa	[93]
Coefficient of Thermal Expansion (α)	2.8 $\mu\text{strain}/^\circ\text{C}$	[93]
Optical Index ³ ($\lambda = 1239.8\text{nm}$) (n)	1.998	[121]
Dielectric Strength	5 - 10 MV/cm	[93]
Relative Permittivity	4	[93]
Melting Point	1800 $^\circ\text{C}$	[93]
Specific Heat	0.7 J/g- $^\circ\text{C}$	[93]
Thermal Conductivity	19 W/m- $^\circ\text{C}$	[93]

Table A.5: Titanium nitride (TiN) Material Properties

Property	Value	Source
Young's modulus	106 - 640 GPa	[32, 64, 75, 82, 106]
Poisson ratio	0.295	[32]
density	3700 - 5700 Kg/m ³	[64, 74, 82, 106]
residual stress	-10.1 - 5.5 GPa	[10, 32, 64, 75, 82]
resistivity	25 - 40 $\mu\Omega\text{-cm}$	[42]

Table A.6: Properties of air (at standard temperature and pressure).

Property	Value	Source
Viscosity (μ)	1.78×10^{-5} kg/(m*s)	[39]
Density (ρ)	1.23 kg/m ³	[39]
Pressure (p)	101.3 kPa	[39]
Relative Permittivity	1.0	[73]
Optical index	1.00029	[48]

Appendix B

List of Symbols

B.1 List of Symbols

Symbol	Definition
r	Radius of optical ring resonator
n	Refractive index
λ	Wavelength of light
N	Integer value
FSR	Free spectral range
Q_{opt}	Optical quality factor
m	Mass of the moving parallel plate electrode
b	Damping coefficient
k	Spring stiffness
ϵ_0	Permittivity of free space
A	Overlap area of movable and fixed parallel plates
d_0	Initial effective gap between plates
d_a	Air gap between parallel plates
t_d	Thickness of the dielectric material between plates
ϵ_d	Relative permittivity of the dielectric material
V, V_0	Applied voltage

continued on next page

Symbol	Definition
x	Displacement of the movable plate
\dot{x}	Velocity of the movable plate
\ddot{x}	Acceleration of the movable plate
V_{pi}	Quasi-static pull-in voltage
V_h	Hold voltage
f_n	Mechanical resonant frequency in cycles/sec
t_{pi}	Pull-in time
μ	Viscosity
L	Length of the movable plate
W_e	Maximum distance to a free plate edge
ζ	Damping ratio
ω_n	Mechanical resonant frequency in radians/sec
ω_d	Damped mechanical resonant frequency in radians/sec
f_d	Damped mechanical resonant frequency in cycles/sec
t_r	Rise time
Q	Mechanical quality factor
ΔL	Length difference between adjacent cantilevers
ρ	radius of curvature of cantilever beams
θ	Angular measure of difference between cantilever beam tips. Also, angular displacement of the movable torsional plate
$\Delta h_1, \Delta h_2$	Change in heights of cantilever tips
C	Chord length associated with ΔL
ϕ	Angular measure of cantilever tip displacement
M	Bending moment applied to beam
E	Young's modulus
ν	Poisson ratio
I_a	Area moment of inertia

continued on next page

Symbol	Definition
σ_{xx}	Stress in cantilever beam
y	Distance from neutral axis of beam
k_d	Duffing spring constant
Q_0	Trapped charge on dielectric surface
Q_t	Total charge on movable electrode
Q_{ta}	Charge on movable electrode resulting from applied voltage
Q_{tdc}	Charge on movable electrode resulting from charge on dielectric
Q_b	Charge on the bottom electrode
Q_{ba}	Charge on fixed electrode resulting from applied voltage
Q_{bdc}	Charge on fixed electrode resulting from charge on dielectric
C_{tdc}	“Capacitance” between movable electrode and dielectric surface
C_{bdc}	“Capacitance” between fixed electrode and dielectric surface
α_0, α_1	Fitting parameters for dielectric charge model
Q_{sat}	Maximum charge accepted by dielectric surface
ε	Strain
α	Coefficient of thermal expansion
ΔT	Change in temperature
ε_{al}	Strain in aluminum
α_{al}	Coefficient of thermal expansion of aluminum
ε_{si}	Strain in silicon
α_{si}	Coefficient of thermal expansion of silicon
σ_{al}	Stress in aluminum

continued on next page

Symbol	Definition
E_{al}	Young's modulus of aluminum
ν_{al}	Poisson ratio of aluminum
σ_y	Yield stress
$\dot{\theta}$	Angular velocity of the movable torsional plate
$\ddot{\theta}$	Angular acceleration of the movable torsional plate
L_t	Length of the moving torsional electrode from rotation center to tip
w_t	Width of the moving torsional electrode
I	Mass moment of inertia of the moving torsional electrode
x_{\max}	Maximum overshoot (step response) or limit cycle amplitude
θ_{\max}	Maximum overshoot (step response) or limit cycle amplitude
θ_0	Maximum possible angular displacement of movable torsional plate
V_{spi}	Step pull-in voltage
V_{mpi}	Modulated pull-in voltage
E_{injected}	Energy input into the system
E_{kinetic}	Kinetic energy stored in the system
$E_{\text{potential}}$	Elastic potential energy stored in the system
$E_{\text{dissipated}}$	Energy lost from the system due to damping effects
E_{stored}	Total energy stored in the system (kinetic plus elastic potential)
V_1	Voltage source associated with fixed electrode 1

continued on next page

Symbol	Definition
V_{c1}	Voltage across fixed electrode 1 and movable electrode
Q_1	Charge stored on capacitor formed by fixed electrode 1 and movable electrode
Q_{p1}	Charge stored on parasitic capacitor associated with fixed electrode 1
R	Value of the resistances in circuit
V_2	voltage source associated with fixed electrode 2
V_{c2}	Voltage across fixed electrode 2 and movable electrode
Q_2	Charge stored on capacitor formed by fixed electrode 2 and movable electrode
Q_{p2}	Charge stored on parasitic capacitor associated with fixed electrode 2
C_p	Value of the parasitic capacitances in the circuit
V_s	Voltage required for switching strain-energy switch
t_s	Switching time required for strain-energy switch
$V_{cv1}, V_{cv2}, V_{cv3}, V_{cv4}$	Control signals for the strain-energy switch
$t_0, t_{cv1}, t_{cv2}, t_{cv3}, t_{cv4}$	Relative switching times of the strain-energy switch control signals
ρ_e	Electrical resistivity
w	Width of movable beam
t_b	Thickness of movable beam
V_c	Control voltage signal
d_s	Effective gap between movable plate and fixed sensing plate
V_s	Sensing voltage signal
V_{s0}	Sensing signal amplitude

continued on next page

Symbol	Definition
ω_s	Sensing signal frequency
t	Time
V_{cpi}	Pull-in value for the control voltage
m_d	Mass of the dielectric slab
m_b	Mass of the bridge
m_{eff}	Combined effective mass of the bridge and dielectric slab
k_b	Boltzmann's constant
T	Absolute temperature
F_n	Thermal-mechanical noise force
Δf	System bandwidth
x_0	Operating position for linearized system
V_{c0}	Control voltage operating value for linearized system
F_{act}	Linearized electrostatic force
$G_c(s)$	Transfer function of PID controller
$K_p, K_i, K_d,$	Gain parameters of the PID controller
R_1, R_2, R_3, R_4	Resistances of the PID controller circuit
C_1, C_2	Capacitances of the PID controller circuit
E_0	Output signal of sensing circuit
C_s	Capacitance that is measured by sensing circuit
C_f	Feedback capacitance of sensing circuit
C_g	Parasitic capacitance of sensing circuit
R_f	Feedback resistance of the sensing circuit
E_n	Voltage noise source in sensing circuit
I_n	Current noise source in sensing circuit

Appendix C

Residual stress gradient measurements

Table C.1: Radius of curvature, residual stress gradient measurements, and stress difference between top and bottom of aluminum film

Measurement Number	Radius of Curvature (mm)	Residual Stress Stress Gradient (MPa/ μm)	Stress Difference (MPa)
1	-0.7	98.1	34.4
2	-1.0	69.6	24.4
3	-1.3	54.0	18.9
4	-1.3	53.9	18.9
5	-1.0	71.1	24.9
6	-1.7	41.1	14.4
7	-2.2	31.9	11.2
8	-1.8	39.2	13.7
9	-1.1	64.3	22.5

continued on next page

Table C.1: *continued*

Measurement Number	Radius of Curvature (mm)	Residual Stress Stress Gradient (MPa/ μm)	Stress Difference (MPa)
10	-3.1	22.7	7.94
11	-1.8	38.2	13.4
12	-1.0	72.0	25.2
13	-1.3	53.7	18.8
14	-0.7	96.7	33.8
15	-0.5	140.0	48.9
mean	-1.4	63.1	22.1

Appendix D

Linear dielectric charging model

A linear model for the evolution of the trapped charge on the air/dielectric interface is given by

$$Q_0 = \alpha_0 \frac{V \epsilon_0 A}{(d_g - x) + \frac{\epsilon_0 d_d}{\epsilon_d}}. \quad (\text{D.1})$$

This model simply states that the trapped charge increases linearly with the electric field, with α_0 as the proportionality constant.

This model has the advantage of being linear and is sufficient to obtain a rough match to the experimental results. However, the nonlinear model in Section 4.2.1 provides a much better match to the experimental results.

The parameters use in the linear lumped parameter dielectric charging model are shown in Table D.1. The parameter α_0 was assigned such that the pull-in voltage matched up with the pull-in voltage observed in the experimental results. The rest of the parameters are the same as for the simulations done in Section 4.2.1.

The results of the linear dielectric charging simulation are shown in Figure D-1.

The results of the simulation using the linear dielectric charging model given by Equation D.1 are a better match to the experimental results than the results obtained by the finite element and lumped parameter models with no dielectric charging. The pull-in voltage is correctly matched to the experimental results. However, the displacement at pull-in is not accurate, nor is the shape of the displacement versus voltage curve.

Table D.1: Parameters used with the linear dielectric charging lumped parameter model.

Parameter	linear Charging
m (kg)	6.08×10^{-13}
b (N·s/m)	4.8×10^{-7}
k (N/m)	5.23
k_d (N/m ³)	1.3×10^{13}
A (m ²)	1.42×10^{-9}
d_g (m)	3.4×10^{-7}
d_d (m)	3.0×10^{-6}
α_0 (N·s/m)	0.37

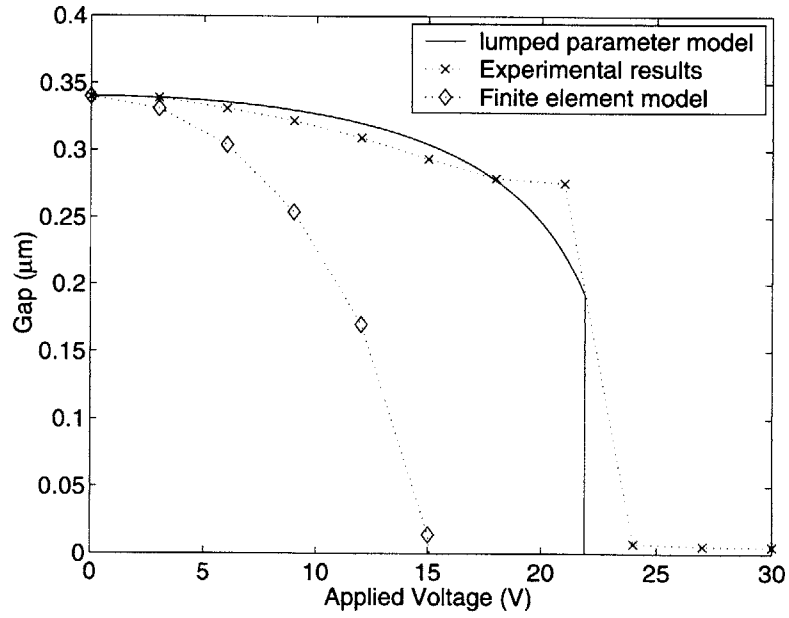


Figure D-1: Comparison of the results of the experimental actuation results with the finite element actuation model and the lumped parameter model that takes into account dielectric charging using the linear dielectric charging model.

Appendix E

Thermal-mechanical noise amplification in parallel plate actuators

An additional result of this analysis that is worthy of note is the amplification of thermal noise experienced by parallel plate actuators as they are displaced. This is an important result for all MEMS devices that use parallel plate actuators to displace the movable plate in an analog fashion (rather than utilizing pull-in to create a binary structure). For a general parallel plate actuator, the thermal noise varies according to

$$\langle X^2 \rangle = \frac{k_b T}{k - \frac{\epsilon A V^2}{(d_0 - x)^2}}. \quad (\text{E.1})$$

The RMS fluctuations due to thermal-mechanical noise are maximum at the pull-in position ($x = d_0/3$). The fluctuations become higher by a factor of $\sqrt{2}$ than when the structure is at its equilibrium position with no voltage applied.

Bibliography

- [1] S. C. Abraham. A new chemistry for a high-density plasma etcher that improves etch rate loading on the TiN ARC layer when geometries are below 0.5 micron. In *Proceedings of the IEEE/SEMI Advanced Semiconductor Manufacturing Conference and Workshop*, pages 328–332, 1996.
- [2] B. Acklin, M. Schienle, B. Weiss, L. Stoll, and G. Müller. Novel optical switches based on carrier injection in three and five waveguide couplers: TIC and SIC. *Electronics Letters*, 30(3):217–218, February 1994.
- [3] V. A. Aksyuk, F. Pardo, D. Carr, D. Greywall, H. B. Chan, M. E. Simon, A. Gasparyan, H. Shea, V. Lifton, C. Bolle, S. Arney, R. Frahm, M. Paczkowski, M. Haueis, R. Ryf, D. T. Neilson, J. Kim, C. R. Giles, and D. Bishop. Beam-steering micromirrors for large optical cross-connects. *Journal of Lightwave Technology*, 21(3):634–642, March 2003.
- [4] R. Apte, F. Sandejas, W. Banyai, and D. Bloom. Grating light valves for high resolution displays. In *Proceedings of the Solid State Sensor and Actuator Workshop*, 1994.
- [5] R. Asquini and A. d’Alessandro. A bistable optical waveguided switch using a ferroelectric liquid crystal layer. In *Proceedings of the IEEE Lasers and Electro-Optics Society Annual Meeting*, volume 1, pages 119–120, 2000.
- [6] T. Barwicz, M. A. Popović, P. T. Rakich, M. R. Watts, H. A. Haus, E. P. Ippen, and H. I. Smith. Microring-resonator-based add-drop filters in SiN: fabrication and analysis. *Optics Express*, 12(7):1437–1442, April 2004.

- [7] L. K. Baxter. *Capacitive Sensors: Design and Applications*. IEEE Press, New York, New York, 1980.
- [8] S. R. Bhalotra, J. D. Mansell, H. L. Kung, and D. A. B. Miller. Parallel-plate MEMS mirror design for large on-resonance displacement. In *Proceedings of the IEEE/LEOS International Conference on Optical MEMS*, pages 93–94, 2000.
- [9] B. Bhushan. Adhesion and stiction: Mechanisms, measurement techniques, and methods for reduction. *Journal of Vacuum Science and Technology B*, 21(6):2262–2296, November/December 2003.
- [10] M. M. M. Bilek, R. N. Tarrant, D. R. McKenzie, S. H. N. Lim, and D. G. McCulloch. Control of stress and microstructure in cathodic arc deposited films. *IEEE Transactions on Plasma Science*, 31(5):939–944, October 2003.
- [11] M. A. Butler, E. R. Deutsch, S. D. Senturia, M. B. Sinclair, W. C. Sweatt, D. W. Youngner, and G. B. Hocker. A MEMS-based programmable diffraction grating for optical holography in the spectral domain. In *International Electron Devices Meeting Technical Digest*, pages 41.1.1 – 41.1.4, 2001.
- [12] W. D. Callister, Jr. *Materials Science and Engineering: an Introduction*. John Wiley & Sons, New York, New York, 3rd edition, 1994.
- [13] L. M. Castañer and S. D. Senturia. Speed-energy optimization of electrostatic actuators based on pull-in. *IEEE Journal of Microelectromechanical Systems*, 8(3):290–298, September 1999.
- [14] E. K. Chan, E. C. Kan, R. W. Dutton, and P. M. Pinsky. Nonlinear dynamic modeling of micromachined microwave switches. In *IEEE MTT-S International Microwave Symposium Digest*, pages 1511–1514, 1997.
- [15] R. Chan, R. Lesnick, D. Becher, and M. Feng. Low-actuation voltage RF MEMS shunt switch with cold switching lifetime of seven billion cycles. *Journal of Microelectromechanical Systems*, 12(5):713–719, October 2003.

- [16] W. S. Chang. *An Electromechanical Valve Drive Incorporating a Nonlinear Mechanical Transformer*. PhD thesis, MIT, 2003.
- [17] R. T. Chen, H. Nguyen, and M. C. Wu. A high-speed low-voltage stress-induced micromachined 2×2 optical switch. *IEEE Photonics Technology Letters*, 11(11):1396–1398, November 1999.
- [18] S. Chen, T. V. Baughn, Z. J. Yao, and C. L. Goldsmith. A new *in situ* residual stress measurement method for a MEMS thin fixed-fixed beam structure. *Journal of Microelectromechanical Systems*, 11(4):309–316, 2002.
- [19] Y. Chen, M. W. Lippitt, H. Chew, and W. M. Moller. Manufacturing enhancements for CoSi_2 self-aligned silicide at the $0.12\text{-}\mu\text{m}$ cmos technology node. *IEEE Transactions on Electron Devices*, 50(10):2120–2125, October 2003.
- [20] Y. T. Cheng, W. T. Hsu, L. Lin, C. T. Nguyen, and K. Najafi. Vacuum packaging technology using localized aluminum/silicon-to-glass bonding. In *Proceedings of the IEEE International Conference on Micro Electro Mechanical Systems*, pages 18–21, 2001.
- [21] H. S. Choe and M. Danek. MOCVD TiN diffusion barriers for copper interconnects. In *Proceedings of the IEEE Conference on Interconnect Technology*, pages 62–64, 1999.
- [22] Y. Choi, K. Kim, and M. G. Allen. A magnetically actuated, electrostatically clamped high current MEMS switch. In *Proceedings of ASME International Mechanical Engineering Congress and Exposition, MEMS*, volume 3, pages 83–87, 2001.
- [23] F. Chollet, M. de Labachellerie, and H. Fujita. Compact evanescent optical switch and attenuator with electromechanical actuation. *IEEE Journal of Selected Topics in Quantum Electronics*, 5(1):52–59, January/February 1999.

- [24] S. T. Chu, B. E. Little, W. Pan, T. Kaneko, and Y. Kokubun. Cascaded microring resonators for crosstalk reduction and spectrum cleanup in add-drop filters. *IEEE Photonics Technology Letters*, 11(11):1423–1425, November 1999.
- [25] S. T. Chu, B. E. Little, W. Pan, T. Kaneko, S. Sato, and Y. Kokubun. An eight-channel add-drop filter using vertically coupled microring resonators over a cross grid. *IEEE Photonics Technology Letters*, 11(6):691–693, June 1999.
- [26] W.-H. Chu and M Mehregany. A study of residual stress distribution through the thickness of p^+ silicon films. *IEEE Transactions on Electron Devices*, 40(7):1245–1250, July 1993.
- [27] T. A. Core, W. K. Tsang, and S. J. Shermann. Fabrication technology for an integrated surface-micromachined sensor. *Solid State Technology*, 36(10):39–47, October 1993.
- [28] P. Dainesi, A. M. Ionescu, L. Thevenaz, K. Banerjee, M. J. Declercq, P. Robert, P. Renaud, P. Fluckiger, C. Hibert, and G. A. Racine. 3-D integrable optoelectronic devices for telecommunications ICs. In *Digest of Technical Papers from the IEEE International Solid-State Circuits Conference*, volume 1, pages 360–361, 473, 2002.
- [29] R. Dangel and W. Lukosz. Electro-nanomechanically actuated integrated-optical interferometric intensity modulators and 2×2 space switches. *Optics Communications*, 156(1):63–76, November 1998.
- [30] K. Djordjev, S.-J. Choi, S.-J. Choi, and P. D. Dapkus. Microdisk tunable resonant filters and switches. *IEEE Photonics Technology Letters*, 14(6):828–830, June 2002.
- [31] M. P. Earnshaw, M. Cappuzzo, E. Chen, L. Gomez, A. Griffin, E. Laskowski, and A. Wong-Foy. Highly-integrated planar lightwave circuit wavelength selective switch. *Electronics Letters*, 39(19):1397–1398, September 2003.

- [32] F. Elstner, A. Ehrlich, H. Giegengack, H. Kupfer, and F. Richter. Synthesis of hard TiN coatings with suppressed columnar growth and reduced stress. *Journal of Vacuum Science and Technology A*, 12(2):476–483, March/April 1994.
- [33] L.-S. Fan, R. S. Muller, W. Yun, J. Huang, and R. T. Howe. Spiral microstructures for the measurement of average strain gradients in thin films. In *Proceedings of IEEE Micro Electro Mechanical Systems*, pages 177–181, 1990.
- [34] W. Fang and J. A. Wickert. Determining mean and gradient residual stresses in thin films using micromachined cantilevers. *Journal of Micromechanics and Microengineering*, 6:301–309, 1996.
- [35] G. A. Feather and D. W. Monk. The Digital Micromirror Device for projection display. In *Proceedings of the IEEE International Conference on Wafer Scale Integration*, pages 43–51, 1995.
- [36] G. K. Fedder and R. T. Howe. Multimode digital control of a suspended polysilicon microstructure. *Journal of Microelectromechanical Systems*, 5(4):283–297, December 1996.
- [37] J. E. Fouquet. Compact optical cross-connect switch based on total internal reflection in a fluid-containing planar lightwave circuit. In *Technical Digest of the Optical Fiber Communication Conference*, volume 1, pages 204–206, 2000.
- [38] J. E. Fouquet, S. Venkatesh, M. Troll, D. Chen, H. F. Wong, and P. W. Barth. A compact, scalable cross-connect switch using total internal reflection due to thermally generated bubbles. In *Proceedings of the Lasers and Electro-Optics Society Annual Meeting*, pages 169–170, 1998.
- [39] R. W. Fox and A. T. McDonald. *Introduction to Fluid Mechanics*. John Wiley & Sons, New York, New York, 4th edition, 1992.
- [40] T. G. Gabrielson. Mechanical-thermal noise in micromachined acoustic sensors. *IEEE Transactions on Electron Devices*, 40(5):903–909, May 1993.

- [41] J. M. Gere and S. P. Timoshenko. *Mechanics of Materials*. PWS Publishing Company, 3rd edition, 1990.
- [42] H. Gilboa, R. Mosely, H. Talieh, and X. S. Guo. Sequential sputter deposition of titanium nitride and aluminum. In *Proceedings of the Seventh International IEEE VLSI Multilevel Interconnection conference*, pages 338–341, 1990.
- [43] C. Goldsmith, J. Ehmke, A. Malczewski, B. Pillans, S. Eschelmann, Z. Yao, J. Brank, and M. Eberly. Lifetime characterization of capacitive RF MEMS switches. In *Proceedings of the IEEE MTT-S International Microwave Symposium*, volume 1, pages 227–230, 2001.
- [44] E. Gros and L. Dupont. Ferroelectric liquid crystal optical waveguide switches using the double-refraction effect. *IEEE Photonics Technology Letters*, 13(2):115–117, February 2001.
- [45] L. Guiziou, P. Ferm, J.-M. Jouanno, and L. Shacklette. Low-loss and high extinction ratio 4×4 polymer thermo-optical switch. In *Proceedings of the European Conference on Optical Communications*, volume 1, pages 84–85, 2001.
- [46] H. A. Haus and G. N. Nielson. Thermal fluctuations of MEMS. *Quantum Electronics and Femtosecond Optics, Internal Memo No. 120*, December 2002.
- [47] R. He, L. Fan, M. C. Wu, and C.-J. Kim. Porous polysilicon shell formed by electrochemical etching for on-chip vacuum encapsulation. In *Proceedings of the Solid-State Sensor, Actuator, and Microsystems Workshop*, pages 332–335, 2004.
- [48] E. Hecht. *Optics*. Addison Wesley, San Francisco, California, 4th edition, 2002.
- [49] P. Heimala, P. Katila, J. Aarnio, and A. Heinämäki. Thermally tunable integrated optical ring resonator with poly-Si thermistor. *Journal of Lightwave Technology*, 14(10):2260–2267, October 1996.

- [50] B. R. Hemenway. High bandwidth, low latency, burst-mode optical interconnect for high performance computing systems. In *Proceedings of the Conference on Lasers and Electro-Optics*, page CTuV2, 2004.
- [51] S. Hengstler, J. J. Uebbing, and P. McGuire. Laser-activated optical bubble switch element. In *Proceedings of the IEEE/LEOS International Conference on Optical MEMS*, pages 117–118, 2003.
- [52] U. Hilleringmann, T. Vieregge, and J. T. Horstmann. Masking and etching of silicon and related materials for geometries down to 25 nm. In *Proceedings of the 25th Annual Conference of the IEEE Industrial Electronics Society*, pages 56–61, 1999.
- [53] A. J. P. Hnatiw, R. G. DeCorby, J. N. McMullin, C. Callender, and R. I. MacDonald. A multimode thermo-optic polymer switch for incorporation in a 4×4 hybrid integrated optoelectronic switch matrix. In *Proceedings of the IEEE Canadian Conference on Electrical and Computer Engineering*, pages 645–650, 1999.
- [54] A. B. Horsfall, K. Wang, J. M. M. dos Santos, S. M. Soare, S. J. Bull, N. G. Wright, A. G. O'Neill, J. G. Terry, A. J. Walton, A. M. Gundlach, and J. T. M. Stevenson. Dependence of process parameters on the stress generation in aluminum thin films. *IEEE Transactions on Device and Materials Reliability*, Accepted for publication 2004.
- [55] J. V. Hryniewicz, P. P. Absil, B. E. Little, R. A. Wilson, and P.-T. Ho. Higher order filter response in coupled microring resonators. *IEEE Photonics Technology Letters*, 12(3):320–322, March 2000.
- [56] T. A. Ibrahim, W. Cao, Y. Kim, J. Li, J. Goldhar, P.-T. Ho, and C. H. Lee. All-optical switching in a laterally coupled microring resonator by carrier injection. *IEEE Photonics Technology Letters*, 15(1):36–38, January 2003.

- [57] T. A. Ibrahim, W. Cao, Y. Kim, J. Li, J. Goldhar, P.-T. Ho, and C. H. Lee. Lightwave switching in semiconductor microring devices by free carrier injection. *Journal of Lightwave Technology*, 21(12):2997–3003, December 2003.
- [58] T. Itoh and T. Suga. Minimum detectable force gradients of piezoelectric micro-cantilever. *Journal of Micromechanics and Microengineering*, 5:231–236, 1995.
- [59] B.-J. Jeon, I.-H. Jung, I.-H. Oh, and T.-H. Lim. Low temperature preparation of the SiO₂ films with low interface trap density using ECR diffusion and ECR CVD method. In *Conference on Optoelectronics and Microelectronics Materials and Devices Proceedings*, pages 259–262, 1996.
- [60] Y. Jin, Z. F. Wang, P. C. Lim, D. Y. Pan, J. Wei, and C. K. Wong. MEMS vacuum packaging technology and applications. In *Proceedings of the Electronics Packaging Technology Conference*, pages 301–306, 2003.
- [61] M. Johansson. *Piecewise Linear Control Systems: A Computational Approach*. Springer-Verlag Heidelberg, New York, 2003.
- [62] T. A. Tumolillo Jr., M. Donckers, and W. H. G. Horsthuis. Solid state optical space switches for network cross-connect and protection applications. *IEEE Communications Magazine*, pages 124–130, February 1997.
- [63] J. W. Kang and K. Simonette. Surface micromachined multi-layer moving gate field effect transistor (MOGFET) pressure switch with integrated vacuum sealed cavity. In *Proceedings of the Twelfth IEEE International Conference on Micro Electro Mechanical Systems*, pages 499–504, 1999.
- [64] A. Karimi, O. R. Shojaei, T. Krumj, and J. L. Martin. Characterisation of TiN thin films using the bulge test and the nanoindentation technique. *Thin Solid Films*, 308-309(1-4):334–339, October 1997.
- [65] N. Keil, C. Weinert, W. Wirges, H. H. Yao, S. Yilmaz, C. Zawadzki, J. Schneider, J. Bauer, M. Bauer, K. Lösch, K. Satzke, W. Wischmann, and J. V. Wirth.

Thermo-optic vertical coupler switches using hybrid polymer/silica integration technology. *Electronics Letters*, 36(5):430–431, March 2000.

- [66] T. Kenney. Nanometer-scale force sensing with MEMS devices. *IEEE Sensors Journal*, 1(2):148–157, August 2001.
- [67] P. F. Van Kessel, L. J. Hornbeck, R. E. Meier, and M. R. Douglass. A MEMS-based projection display. *Proceedings of the IEEE*, 86(8):1687–1704, August 1998.
- [68] R. Keusseyan, J. Sosnowski, M. Doyle, D. Amey, and S. Horowitz. A new approach for opto-electronic/MEMS packaging. In *Proceedings of the Electronic Components and Technology Conference*, pages 259–262, 2002.
- [69] J. Kim, C. J. Nuzman, B. Kumar, D. F. Lieuwen, J. S. Kraus, A. Weiss, C. P. Lichtenwalner, A. R. Papazian, R. E. Frahm, N. R. Basavanhally, D. A. Ramsey, V. A. Aksyuk, F. Pardo, M. E. Simon, V. Lifton, H. B. Chan, M. Haueis, A. Gasparyan, H. R. Shea, S. Arney, C. A. Bolle, P. R. Kolodner, R. Ryf, D. T. Neilson, and J. V. Gates. 1100×1100 port MEMS-based optical crossconnect with 4-dB maximum loss. *IEEE Photonics Technology Letters*, 15(11):1537–1539, November 2003.
- [70] K. Kim, Y. Song, G. S. Lee, and J. Song. Electrical properties of PECVD oxide films deposited at room temperature. *Electronics Letters*, 32(21):2015–2016, October 1996.
- [71] S. P. Kim, H. M. Choi, and S. K. Choi. A study on the crystallographic orientation with residual stress and electrical property of Al films deposited by sputtering. *Thin Solid Films*, 322:298–302, June 1998.
- [72] J. Koike, S. Utsunomiya, Y. Shimoyama, K. Maruyama, and H. Oikawa. Thermal cycling fatigue and deformation mechanism in aluminum alloy thin films on silicon. *Journal of Materials Research*, 13(11):3256–3264, November 1998.

- [73] J. A. Kong. *Electromagnetic Wave Theory*. EMW Publishing, Cambridge, Massachusetts, 2000.
- [74] K. Kushida-Abdelghafar, K. Torii, S. Takatani, Y. Matsui, and Y. Fujisaki. Mechanism of TiN barrier-metal oxidation in a ferroelectric random access memory. *Electronics Letters*, 13(11):3265–3269, November 1998.
- [75] M. M. Lacerda, Y. H. Chen, B. Zhou, M. U. Guruz, and Y. W. Chung. Synthesis of hard TiN coatings with suppressed columnar growth and reduced stress. *Journal of Vacuum Science and Technology A*, 17(5):2915–2919, September/October 1999.
- [76] B.-L. Lee, C.-H. Oh, S. Lee, Y.-S. Oh, and K.-J. Chun. A vacuum packaged differential resonant accelerometer using gap sensitive electrostatic stiffness changing effect. In *Proceedings of the IEEE International Conference on Micro Electro Mechanical Systems*, pages 352–357, 2000.
- [77] D.-J. Lee, B.-K. Ju, Y.-H. Lee, J. Jang, and M.-H. Oh. Glass-to-glass anodic bonding for high vacuum packaging of microelectronics and its stability. In *Proceedings of the IEEE International Conference on Micro Electro Mechanical Systems*, pages 253–258, 2000.
- [78] B. Li and S.-J. Chua. Reflection-type optical waveguide switch with bowtie electrode. *Journal of Lightwave Technology*, 20(1):65–70, January 2002.
- [79] B. Li and S.-J. Chua. Two-mode interference photonic waveguide switch. *Journal of Lightwave Technology*, 21(7):1685–1690, July 2003.
- [80] J. Li, Q. X. Zhang, and A. Q. Liu. Advanced fiber optical switches using deep rie (drie) fabrication. *Sensors and Actuators A*, 102:286–295, 2003.
- [81] J. Li, Q. X. Zhang, A. Q. Liu, W. L. Goh, and J. Ahn. Technique for preventing stiction and notching effect on silicon-on-insulator microstructure. *Journal of Vacuum Science and Technology B*, 21(6):2530–2539, November/December 2003.

- [82] J.-W. Lim, H.-S. Park, T.-H. Park, J.-J. Lee, and J. Joo. Mechanical properties of titanium nitride coatings deposited by inductively coupled plasma assisted direct current magnetron sputtering. *Journal of Vacuum Science and Technology A*, 18(2):524–528, March/April 2000.
- [83] L. Lin, R. T. Howe, and A. P. Pisano. Microelectromechanical filters for signal processing. *Journal of Microelectromechanical Systems*, 7(3):284–294, September 1998.
- [84] Y.-C. Lin, J.-C. Chiou, W.-T. Lin, Y.-J. Lin, and S.-D. Wu. The design and assembly of surface-micromachined optical switch for optical add/drop multiplexer application. *IEEE Transactions on Advanced Packaging*, 26(3):261–267, August 2003.
- [85] B. E. Little. Advances in microring resonators. In *Proceedings of the Integrated Photonics Research Conference*, 2003.
- [86] B. E. Little, S. T. Chu, H. A. Haus, J. Foresi, and J.-P. Laine. Microring resonator channel dropping filters. *Journal of Lightwave Technology*, 15(6):998–1005, June 1997.
- [87] B. E. Little, H. A. Haus, J. S. Foresi, L. C. Kimerling, E. P. Ippen, and D. J. Ripin. Wavelength switching and routing using absorption and resonance. *IEEE Photonics Technology Letters*, 10(6):816–818, 1998.
- [88] Little Optics, Inc. Optical application specific integrated circuits (ASICs). whitepaper, June 2003.
- [89] Y. L. Liu, E. K. Liu, S. L. Zhang, G. Z. Li, and J. S. Luo. Silicon 1×2 digital optical switch using plasma dispersion. *Electronics Letters*, 30(2):130–131, January 1994.
- [90] J. P. Lorenzo and R. A. Soref. $1.3\mu\text{m}$ electrooptic silicon switch. *Applied Physics Letters*, 51(1):6–8, July 1987.

- [91] M. J. Madou. *Fundamentals of Microfabrication: the Science of Miniaturization*. CRC Press LLC, Boca Raton, Florida, 2nd edition, 2002.
- [92] S. Majumder, J. Lampen, R. Morrison, and J. Maciel. MEMS switches. *IEEE Instrumentation & Measurement Magazine*, pages 12–15, March 2003.
- [93] N. Maluf. *An Introduction to Microelectromechanical Systems Engineering*. Artech House, Inc., Norwood, Massachusetts, 2000.
- [94] B. Maune, R. Lawson, C. Gunn, A. Scherer, and L. Dalton. Electrically tunable ring resonators incorporating nematic liquid crystals as cladding layers. *Applied Physics Letters*, 83(23):4689–4691, December 2003.
- [95] F. A. McClintock and A. S. Argon. *Mechanical Behavior of Materials*. Addison-Wesley Publishing Company, Reading, Massachusetts, 1966.
- [96] R. J. Mears, W. A. Crossland, M. P. Dames, J. R. Collington, M. C. Parker, S. T. Warr, T. D. Wilkinson, and A. B. Davey. Telecommunications applications of ferroelectric liquid-crystal smart pixels. *IEEE Journal of Selected Topics in Quantum Electronics*, 2(1):35–46, April 1996.
- [97] S. Mechels, L. Muller, G. D. Morley, and D. Tillett. 1D MEMS-based wavelength switching subsystem. *IEEE Communications Magazine*, pages 88–94, March 2003.
- [98] M. Mehregany, R. T. Howe, and S. D. Senturia. Novel microstructures for the in situ measurement of mechanical properties of thin films. *Journal of Applied Physics*, 62(9):3579–3584, 1987.
- [99] J. B. Muldavin and G. M. Rebeiz. Nonlinear electro-mechanical modeling of MEMS switches. In *IEEE MTT-S International Microwave Symposium Digest*, volume 3, pages 2119–2122, 2001.
- [100] G. Müller, L. Stoll, G. Schulte-Roth, and U. Wolff. Low current plasma effect optical switch on InP. *Electronics Letters*, 26(2):115–117, January 1990.

- [101] E. J. Murphy, T. O. Murphy, A. F. Ambrose, R. W. Irvin, B. H. Lee, P. Peng, G. W. Richards, and A. Yorinks. 16×16 strictly nonblocking guided-wave optical switching system. *Journal of Lightwave Technology*, 14(3):352–358, March 1996.
- [102] National Semiconductor. LMH6654/55 Datasheet, August 2001.
- [103] K. Ogata. *Modern Control Engineering*. Prentice Hall, Englewood Cliffs, New Jersey, 2nd edition, 1990.
- [104] E. Ollier. Optical MEMS devices based on moving waveguides. *IEEE Journal on Selected Topics in Quantum Electronics*, 8(1):155–162, January/February 2002.
- [105] P. M. Osterberg and S. D. Senturia. M-TEST: a test chip for MEMS material property measurement using electrostatically actuated test structures. *Journal of Microelectromechanical Systems*, 6(2):107–118, 1997.
- [106] P. Patsalas, C. Charitidis, and S. Logothetidis. The effect of substrate temperature and biasing on the mechanical properties and structure of sputtered titanium nitride thin films. *Surface and Coatings Technology*, 125(1-3):335–340, March 2000.
- [107] D. Peroulis, S. P. Pacheco, K. Sarabandi, and L. P. B. Katehi. Electromechanical considerations in developing low-voltage RF MEMS switches. *IEEE Transactions on Microwave Theory and Techniques*, 51(1):259–270, January 2003.
- [108] M. L. Povinelli, R. E. Bryant, S. Assefa, S. G. Johnson, S. Fan, A. A. Erchak, G. S. Petrich, E. Lidorikis, J. D. Joannopoulos, L. A. Kolodziejski, and E. P. Ippen. Compact evanescent optical switch and attenuator with electromechanical actuation. *IEEE Photonics Technology Letters*, 15(9):1207–1209, September 2003.
- [109] V. L. Rabinovich, R. K. Gupta, and S. D. Senturia. The effect of release-etch holes on the electromechanical behaviour of MEMS structures. In *Proceedings*

of the *International Conference on Solid State Sensors and Actuators*, volume 2, pages 1125–1128, 1997.

- [110] R. Ramaswami and K. N. Sivarajan. *Optical Networks: A Practical Perspective*. Morgan Kaufmann Publishers, Inc., San Francisco, California, 1998.
- [111] G. M. Rebeiz. *RF MEMS Theory, Design, and Technology*. John Wiley & Sons, Hoboken, New Jersey, 2003.
- [112] G. M. Rebeiz and J. B. Muldavin. RF MEMS switches and switch circuits. *IEEE Microwave Magazine*, pages 59–71, December 2001.
- [113] G. T. Reed. The optical age of silicon. *Nature*, 427:595–596, February 2004.
- [114] J.-K. Rhee, F. Garcia, A. Ellis, B. Hallock, T. Kennedy, T. Lackey, R. G. Lindquist, J. P. Kondis, B. A. Scott, J. M. Harris, D. Wolf, and M. Dugan. Variable passband optical add-drop multiplexer using wavelength selective switch. In *Proceedings of 27th European Conference on Optical Communication*, pages 550–551, 2001.
- [115] N. A. Riza and S. Yuan. Reconfigurable wavelength add-drop filtering based on a banyan network topology and ferroelectric liquid crystal fiber-optic switches. *Journal of Lightwave Technology*, 17(9):1575–1584, September 1999.
- [116] M. Romagnoli, M. Tormen, and G. Gorni. Personal communication, 2002.
- [117] R. B. Ross. *Metallic Materials Specification Handbook*. E. & F. N. Spon Ltd., New York, New York, 3rd edition, 1980.
- [118] G. S. Sandhu, S. G. Meikle, and T. T. Doan. Metalorganic chemical vapor deposition of TiN films for advanced metallization. *Applied Physics Letters*, 62(3):240–242, January 1993.
- [119] R. Sattler, F. Plötz, G. Fattinger, and G. Wachutka. Modeling of an electrostatic torsional actuator: demonstrated with an RF MEMS switch. *Sensors and Actuators A*, 97-98:337–346, April 2002.

- [120] P. R. Saulson. Thermal noise in mechanical experiments. *Physical Review D: Particles and Fields*, 42(8):2437–2445, October 1990.
- [121] E. F. Schubert. <http://www.rpi.edu/~shubert/>. website, April 2004. (Educational Resources, Materials - refractive index).
- [122] R. E. Scotti, C. Madsen, C. H. Henry, G. Lenz, Y. P. Li, H. Presby, and A. White. A hitless reconfigurable add-drop multiplexer for WDM networks utilizing planar waveguides, thermo-optic switches and UV induced gratings. In *Technical Digest of the Optical Fiber Communication Conference*, pages 142–143, 1998.
- [123] K. Sekine, Y. Saito, M. Hirayama, and T. Ohmi. Highly reliable ultrathin silicon oxide film formation at low temperature by oxygen radical generated in high-density krypton plasma. *IEEE Transactions on Electron Devices*, 48(8):1550–1555, August 2001.
- [124] D. Seneviratne, G. N. Nielson, G. Barbastathis, and H. L. Tuller. Functional Material for Micromechanical Systems. United States Patent Application, July 2004.
- [125] S. D. Senturia. *Microsystem Design*. Kluwer Academic Publishers, Norwell, Massachusetts, 2001.
- [126] S. D. Senturia. Diffractive MEMS: the polychromator and related devices. In *Proceedings of the IEEE Conference on Optical MEMS*, pages 5–6, 2002.
- [127] W.-C. Shih, C. W. Wong, Y. B. Jeon, S.-G. Kim, M. A. Schmidt, S. Desai, D. M. Freeman, A. Sinha, G. Nielson, and G. Barbastathis. Analog tunable diffractive grating with milliradian resolution. In *Technical Digest of the Optical Fiber Communication Conference*, pages 189–190, 2002.
- [128] K.-C. Shu, Y. Lai, and D.-W. Huang. A novel S-shape 1×2 thermo-optic polymer waveguide switch. In *Technical Digest of the Optical Fiber Communication Conference*, pages 697–698, 2002.

- [129] S. Sohma, T. Goh, H. Okazaki, M. Okuno, and A. Sugita. Low switching power silica-based super high delta thermo-optic switch with heat and insulating grooves. *Electronics Letters*, 38(3):127–128, January 2002.
- [130] O. Solgaard, S. F. A. Sandejas, and D. M. Bloom. Deformable grating optical modulator. *Optics Letters*, 17(9):688–690, May 1992.
- [131] R. A. Soref. Silicon-based optoelectronics. *Proceedings of the IEEE*, 81(12):1687–1706, December 1993.
- [132] D. R. Sparks, L. Jordan, and J. H. Frazee. Flexible vacuum-packaging method for resonating micromachines. *Sensors and Actuators, A*, 55(2-3):179–183, July 1996.
- [133] D. R. Sparks, S. Massoud-Ansari, and N. Najafi. Chip-level vacuum packaging of micromachines using nanogetters. *IEEE Transactions on Advanced Packaging*, 26(3):277–282, August 2003.
- [134] B. H. Stark and K. Najafi. A low-temperature thin-film electroplated metal vacuum package. *Journal of Microelectromechanical Systems*, 13(2):147–157, April 2004.
- [135] J. B. Starr. Squeeze-film damping in solid-state accelerometers. In *Technical Digest of the Solid-State Sensor and Actuator Workshop*, pages 44–47, 1990.
- [136] R. F. Steidel, Jr. *An Introduction to Mechanical Vibrations*. John Wiley & Sons, New York, 3rd edition, 1989.
- [137] N. Tas, T. Sonnenberg, H. Jansen, R. Legtenberg, and M. Elwenspoek. Stiction in surface micromachining. *Journal of Micromechanics and Microengineering*, 6:385–397, 1996.
- [138] J. M. T. Thompson and H. B. Stewart. *Nonlinear Dynamics and Chaos*. John Wiley & Sons, West Sussex, England, 2nd edition, 2002.

- [139] L. Tong, M. Mehregany, and L. G. Matus. Mechanical properties of 3C silicon carbide. *Applied Physics Letters*, 60(24):2992–2994, June 1992.
- [140] V. Van, T. A. Ibrahim, K. Ritter, P. P. Absil, F. G. Johnson, R. Grover, J. Goldhar, and P.-T. Ho. All-optical nonlinear switching in GaAs-AlGaAs microring resonators. *IEEE Photonics Technology Letters*, 14(1):74–76, January 2002.
- [141] T. Veijola, H. Kuisma, and J. Lahdenpera. Model for gas film damping in a silicon accelerometer. In *Proceedings of the International Conference on Solid-State Sensors and Actuators*, volume 2, pages 1097–1100, 1997.
- [142] S. Venkatesh, J. E. Fouquet, R. Haven, M. DePue, D. Seekola, H. Okano, and H. Uetsuka. Performance improvements in bubble-actuated cross-connect switches. In *Proceedings of the IEEE Lasers and Electro-Optics Society Annual Meeting*, pages 39–40, 2002.
- [143] S. Venkatesh, R. Haven, D. Chen, H. L. Reynolds, G. Harkins, S. Close, M. Troll, J. E. Fouquet, D. Shroeder, and P. McGuire. Recent advances in bubble-actuated cross-connect switches. In *Proceedings of the 4th Pacific Rim Conference on Lasers and Electro-Optics*, volume 1, pages I-414 – I-415, 2001.
- [144] M. R. Watts. Wavelength switching and routing through evanescently induced absorption. Master’s thesis, MIT, 2001.
- [145] M. R. Watts and M. A. Popović. Personal communication, 2002.
- [146] J. R. Whinnery, C. Hu, and Y. S. Kwon. Liquid-crystal waveguides for integrated optics. *Optics Communications*, 13(4):262–267, April 1977.
- [147] J. Wibbeler, G. Pfeifer, and M. Hietschold. Parasitic charging of dielectric surfaces in capacitive microelectromechanical systems (MEMS). *Sensors and Actuators A*, 71:74–80, November 1998.

- [148] C. W. Wong. *Strain-Tuning of Periodic Optical Devices: Tunable Gratings and Photonic Crystals*. PhD thesis, MIT, 2003.
- [149] H. Wong and Y. C. Cheng. Study of the electronic trap distribution at the SiO₂-Si interface utilizing the low-frequency noise measurement. *IEEE Transactions on Electron Devices*, 37(7):1743–1749, July 1990.
- [150] T. Yaji, S. Kurita, Y. Tejima, A. Horinouchi, and M. Koyanagi. Integrated optical devices using amorphous As₂S₃ thin film. *IEEE Transactions on Components, Hybrids, and Manufacturing Technology*, 6(1):134–135, March 1983.
- [151] T.-J. Yao, K. Walsh, and Y.-C. Tai. Dielectric charging effects on parylene electrostatic actuators. In *Proceedings of the IEEE International Conference on Micro Electro Mechanical Systems*, pages 614–617, 2002.
- [152] M. I. Younis and A. H. Nayfeh. A study of the nonlinear response of a resonant microbeam to an electric actuation. *Nonlinear Dynamics*, 31(1):91–117, January 2003.
- [153] F. Yuan, J. Wiler, K. Wise, and D. Anderson. Micromachined multi-channel microelectrodes with titanium nitride sites. In *Proceedings of the First Joint BMES/EMBS Conference*, volume 1, page 379, 1999.